ABSTRACT

Title of Document: EMISSIONS, TRANSPORT, AND EVOLUTION OF ATMOSPHERIC POLLUTANTS FROM CHINA: AN OBSERVATIONAL STUDY

Can Li, Doctor of Philosophy, 2008

Directed By: Professor Russell R. Dickerson
Professor Zhanqing Li
Department of Atmospheric and Oceanic Science

China's air pollution issue, a byproduct of recent phenomenal economic growth, has received increasing attention in light of its local and large-scale impacts. I investigated the emissions, transport, and evolution of pollutants from China using measurements near some source regions in northern China in 2005. Surface pollution near Beijing in March was overall heavy but changed dramatically, as passing mid-latitude cyclones led to fast transitions between polluted prefrontal and clean postfrontal conditions. Large differences found between measurements and inventories suggest substantial uncertainties in emission estimates. Small, coal-fired boilers are shown unlikely to be the major source of inventory error; experiments measuring traffic emissions are called for. Ground-level aerosols absorb light and are from both wind-blown dust and anthropogenic emissions. Their effects on climate are to be further studied.

Pollutants at higher altitudes are more likely to have large-scale impact than pollutants that remain near the surface. The aircraft campaign in April was among the first efforts to measure the vertical distribution of pollutants over inland China. The largest pollutant levels observed in the free troposphere during the campaign were related to dry convective lofting over an industrial region. This differs from earlier experiments over the Pacific, which recognized the warm conveyor belt (WCB) as the main lofting mechanism. Dry convection over the continent may be followed by WCB lifting as the systems move out over the ocean. Their relative roles are yet to be determined.

Analyses of meteorological and satellite cloud data reveal the importance of in-cloud processing in oxidizing SO_2 transported behind cold fronts. Through integration of satellite sensors, in-situ measurements, trajectory and chemical transport models, I tracked a pollution plume as it traveled away from source region. The decay of SO_2 in the plume over three days was quantified, suggesting an SO_2 lifetime of 1-4 d. Formation of sulfate and loss of dust together changed the aerosol loading of the plume. This analysis showcases the potential for employing satellites to trace transport events and pollutant evolution, and highlights the main uncertainties in quantitative application of satellite data.

EMISSIONS, TRANSPORT, AND EVOLUTION OF ATMOSPHERIC POLLUTANTS FROM CHINA: AN OBSERVATIONAL STUDY

By

Can Li

Dissertation submitted to the Faculty of the Graduate School of the
University of Maryland, College Park, in partial fulfillment
of the requirements for the degree of
Doctor of Philosophy
2008

Advisory Committee:
Professor Zhanqing Li, Chair/Advisor
Professor Russell R. Dickerson, Advisor
Professor Sheryl H. Ehrman
Dr. Nickolay A. Krotkov
Professor Ross J. Salawitch
Dr. Jeffrey W. Stehr

© Copyright by
Can Li
2008

Dedication

To My Fellow Countrymen

Acknowledgements

First and foremost, I wish to thank my advisors, Professors Russ Dickerson and Zhanqing Li, for their guidance, patience, and support over the years. Working with them has been a truly "eye-opening" experience for me. I enjoyed close collaboration with Drs. Lackson Marufu, Jeff Stehr, Brett Taubman, Jennifer Hains, and many others of Russ's air chemistry group. I was also privileged to have some of the best colleagues and officemates in Wen Mi, Hye Lim Yoo, Feng Niu, Maureen Cribb, Drs. Tianle Yuan, Kwon-Ho Lee, and others in Zhanqing's team.

My deepest gratitude goes to my colleagues at IAP/CAS and Liaoning Meteorological Administration, without whom this research would have been impossible. Dr. Tianxue Wen and Yanan Liu of IAP analyzed the aerosol composition. I cannot thank Drs. Nick Krotkov and Kai Yang of NASA/GSFC/UMBC enough for their help on OMI data and lots of insightful discussion. Dr. Mian Chin of NASA/GSFC kindly helped me with GOCART output. Drs. David Streets and Q. Zhang of ANL provided emission inventory data. Dr. Shimizu of NIES, Japan provided lidar data.

My thank goes out to all the faculty and staff of AOSC and ESSIC for their help. I am indebted to my fellow students and friends, especially Drs. Haifeng Qian, Junjie Liu, and Jie Liu, for five delightful years of my life.

Last but not least, I would like to thank my parents for supporting me and giving me courage to pursue my dream. I owe a great deal to my always caring, understanding, and loving wife, Chen. She has been my greatest inspiration and will always be.

Table of Contents

Dedication ii
Acknowledgements iii
Table of Contents iv
List of Tables vi
List of Figures vii
Chapter 1: Introduction 1
1.1 Background 1
1.2 Some Important Atmospheric Pollutants 5
1.3 Air Pollution in China 9
1.3.1 Industrialization, urbanization, and air pollution 9
1.3.2 Air pollution in China: State of the issue 13
1.3.3 Air pollution in China: impacts 15
1.4 Overview of Research 17
1.4.1 Emission inventory: method, uncertainties, and evaluation 17
1.4.2 Long-range transport of atmospheric pollutants: mechanisms 19
1.4.3 Aerosol chemical composition in China 25
1.4.4 EAST-AIRE: an international regional experiment 26
1.4.5 Outline of research 27
Chapter 2: Experimental Methods 29
2.1 Sampling Site and Platform 29
2.1.1 Xianghe site 29
2.1.2 Y-12 aircraft 30
2.2 Measurements of Trace Gases 32
2.2.1 Carbon monoxide 32
2.2.2 Sulfur dioxide 34
2.2.3 Ozone 35
2.2.4 Total reactive nitrogen oxides 37
2.3 Aerosol Optical Properties 38
2.3.1 Aerosol scattering coefficients 38
2.3.2 Aerosol absorption coefficient 40
2.4 Aerosol Chemical Composition 42
2.4.1 Aerosol sampling 42
2.4.2 Chemical analysis 43
Chapter 3: Xianghe Ground Experiment 45
3.1 Abundance of Pollutants: Statistics and Variations 45
3.1.1 Concentrations of trace gases 45
3.1.2 Aerosol optical properties and composition 46
3.1.3 Diurnal variation of pollutants 49
3.1.4 Synoptic variation of pollutants 52
3.2 Pollutant Ratios and Implications for Regional Emissions 61
3.2.1 Pollutant ratios from correlation analysis 61
3.2.2 Implications for CO and SO_2 emissions 65
3.2.3 Cluster analysis and implications for regional emission inventory 67

3.2.4 Some other issues of inventory evaluation 72
3.2.5 Black carbon emissions 74
3.3 Enrichment of Elements and Ions in Aerosols 76
3.3.1 Enrichment factors and enrichment of lead 76
3.3.2 Enrichment of chloride ion 80
3.4 Characterize Emissions from a Small Coal-Fired Boiler 81
3.4.1 The boiler 81
3.4.2 Method 83
3.4.3 Emission characteristics of the boiler and implications 84
3.5 Summary 89
Chapter 4: Shenyang Aircraft Campaign 95
4.1 Overview of the Aircraft Campaign 95
4.1.1 Weather 95
4.1.2 Flight routes 97
4.1.3 Synoptic variation of air pollution during the aircraft campaign 99
4.1.4 Vertical distribution of pollutants: comparison to the Northeastern U.S. 103
4.2 Upwind Dry Convection and Long-Range Transport: A Case Study 107
4.2.1 Prefrontal flight on April 5, 2005 107
4.2.2 Postfrontal flight on April 7, 2005 115
4.2.3 Discussion 119
4.3 Summary 121
Chapter 5: Evolution of Pollutants during Transport: A Perspective from Space ... 125
5.1 In-Cloud Processing of Upwind Sulfur Dioxide 125
5.1.1 The relative nitrate-to-sulfate ratio in Xianghe aerosol samples 125
5.1.2 Synoptic change in $[NO_3^-]/[SO_4^{2-}]$ 127
5.1.3 SO_4^{2-}/SO_x and NO_3^-/NO_y mole ratios 129
5.1.4 In-cloud processing of SO_2 134
5.1.5 Implications for regional atmospheric chemistry 138
5.2 Transport and Evolution of a Pollution Plume from Northern China: A Satellite-Based Case Study 139
5.2.1 Introduction 139
5.2.2 Data and models 140
5.2.3 AMF correction for OMI operational SO_2 product 144
5.2.4 Transport and evolution of the plume 150
5.2.5 Changes in AOD and total mass of SO_2 158
5.2.6 Discussion 160
5.2.7 Summary 167
Chapter 6: Conclusions 169
6.1 Summary of Results 169
6.2 Recommendations 175
Appendix I 179
Appendix II 185
Appendix III 189
Bibliography 190

List of Tables

Table 1.1. National Ambient Air Quality Standards for some atmospheric pollutants 9
Table 1.2. Concentration limits for some pollutants in the National Ambient Air Quality Standard of China 14

Table 3.1. Statistics of trace gases and aerosol optical properties in Xianghe 47
Table 3.2. Statistics of water-soluble inorganic ions in aerosol samples from Xianghe ($\mu g/m^3$) 48
Table 3.3. Statistics of elements in aerosol samples from Xianghe ($\mu g/m^3$) 49
Table 3.4. Concentrations of some elements and water-soluble ions in daytime and nighttime samples (average ± standard deviation, $\mu g/m^3$) 52
Table 3.5. Results of the pollutant concentration correlation analysis 61
Table 3.6. Observed and national inventory pollutant ratios (ppbv/ppbv) 65
Table 3.7. Regional inventory pollutant ratios within different areas around Xianghe (ppb/ppb) 69
Table 3.8. Results of correlation analysis for different trajectory groups 69

Table 4.1. Summary of weather conditions during the Shenyang aircraft campaign. 97
Table 4.2. Summary of the flights during the Shenyang aircraft campaign 98
Table 4.3. Statistics of Ångström exponents (440-675 nm) in 2005 at three AERONET sites in China and the U.S. 106

Table 5.1. Average nitrate and sulfate concentrations from this study and some previous studies 126

List of Figures

Figure 1.1. Some examples of the impacts of atmospheric pollutants on climate, ecosystem, and humans. 5
Figure 1.2. GDP and percentage contribution from industry for China during 1978-2004. 11
Figure 1.3. Correlation between annual growth rate of GDP and industry of China during 1989-2004. 11
Figure 1.4. Coal production and percentage contribution to total energy consumption of China during 1978-2004. 12
Figure 1.5. Total SO_2 emissions, industrial SO_2 emissions, and industrial output value of China during 1995-2005. 12
Figure 1.6. Schematic of major pathways for pollutant outflows from East Asia and inflows into North America 22
Figure 1. 7. Major air streams associated with a mid-latitude cyclone. 23
Figure 1. 8. Schematic of CO redistribution by a deep convection process. 24

Figure 2.1. Location of the Xianghe site. 30
Figure 2.2. Y-12 aircraft used for the aircraft campaign. 32
Figure 2.3. Schematic diagram of the modified CO analyzer. 34
Figure 2.4. Schematic diagram of the modified SO_2 analyzer 35
Figure 2.5. Schematic diagram of the TEI O_3 analyzer 36
Figure 2.6. Schematic diagram of the modified NO/NO_y detector 38
Figure 2.7. Schematic diagram of the TSI 3563 integrating nephelometer 40
Figure 2.8. Schematic diagram of the PSAP 42
Figure 2.9. Left: setup of the bulk aerosol sampler during the Xianghe experiment; **Right**: schematic diagram of the bulk aerosol sampler. 43

Figure 3.1. Diurnal cycles of CO, NO_y, aerosol absorption SO_2, aerosol scattering, and O_3 at the Xianghe site. 51
Figure 3.2. Hourly averaged aerosol scattering, aerosol absorption, relative humidity, temperature, surface pressure, wind direction, and wind speed observed at the Xianghe site. 54
Figure 3.3. Hourly averaged concentrations of SO_2, CO, NO_y, and O_3 observed at the Xianghe site. 55
Figure 3.4. Time series of some water-soluble ions in aerosol samples from Xianghe. 58
Figure 3.5. Time series of some pollutant tracer metal elements in aerosol samples from Xianghe. 59
Figure 3.6. Time series of some crustal elements in aerosol samples from Xianghe. 60
Figure 3.7. Correlations of CO and NO_y, CO and SO_2, aerosol scattering and SO_2, aerosol scattering and aerosol absorption at the Xianghe site. 62

Figure 3.8. Inventory ratios of CO/SO_2 and CO/NO_x in March, 2001. 68
Figure 3.9. Correlation between BC and CO at the Xianghe site. 75
Figure 3.10. Box and whisker chart of the enrichment factors.. 79
Figure 3.11. Enrichment factor of Pb and hourly averaged CO. 79
Figure 3.12. Scatter plot of Cl^- and Na^+ concentrations..... 81
Figure 3.13. The coal-fired boiler at the Xianghe site. 82
Figure 3.14. One plume from the boiler detected on March 14, 2005. 84
Figure 3.15. Correlations of ΔCO, ΔSO_2, ΔNO_y, and ΔCO_2 for all plume data.85
Figure 3.16. Same as Figure 3.14 but for cold start data. 86

Figure 4.1. Meteorology records from the airport near Shenyang. 96
Figure 4.2. Flight altitudes and SO_2 concentrations along the flight tracks..... 100
Figure 4.3. Flight altitudes and aerosol scattering along the flight tracks. 102
Figure 4.4.Surface measured aerosol optical thickness over Shenyang. 103
Figure 4.5. a) Mean vertical profiles of SO_2 during the Shenyang experiment. **b)** Mean vertical profiles of aerosol scattering. 105
Figure 4.6. Vertical profiles of Ångström Exponents over N China in spring and over the NE U.S. in summer. 106
Figure 4.7. Surface analysis for 00 UTC April 5, 2005. 109
Figure 4.8. Vertical profiles of ozone, RH, and temperature S of Shenyang on April 5. 110
Figure 4.9. Vertical profile of aerosol scattering coefficients for flight S of Shenyang on April 5. 110
Figure 4.10. Vertical profile of SO_2, for flight S of Shenyang on April 5..... 111
Figure 4.11. Vertical distribution of CO from the flight of April 5..... 111
Figure 4.12. Backward trajectories for the location of southern spiral. 113
Figure 4.13. GOES-9 IR image for 00 UTC April 4, 2005..... 114
Figure 4.14. MODIS true color image for 04 UTC April, 4, 2005. 115
Figure 4.15. Surface weather analysis for 00 UTC April 7, 2005. 117
Figure 4.16. Backward trajectories for the southern spiral on April 7..... 118
Figure 4.17. Profiles of temperature, trace gases and aerosol scattering N of Shenyang on April 7. 118
Figure 4.18. Profiles of temperature, trace gases and aerosol scattering S of Shenyang on April 7. 119
Figure 4.19. Climatology of precipitation near Baltimore and Beijing 120

Figure 5.1. Nitrate and sulfate in bulk aerosol samples from Xianghe..... 129
Figure 5.2. SO_4^{2-}/SO_x and NO_3^-/NO_y mole ratios as a function of CO. 130
Figure 5.3. Scatter plots of SO_4^{2-}/SO_x and NO_3^-/NO_y mole ratio 132
Figure 5.4. Upper: 72-hr backward trajectories from Xianghe at 04 UTC on March 17, 2005. **Middle**: MODIS-retrieved cloud properties along the trajectories. **Lower**: histograms of MODIS cloud properties..... 136
Figure 5.5. Percentage of "cloud", "dust", "cloud and dust", and "unexplained" samples..... 138

Figure 5.6. Histograms of MODIS cloud top pressure near the plume 147
Figure 5.7. Normalized trajectory-projected and GOCART SO_2 vertical profile over N Japan on April 6, 2005. 148
Figure 5.8. Normalized trajectory-projected and GOCART SO_2 vertical profile over N Pacific on April 7, 2005. 148
Figure 5.9. Upper: aerosol extinction coefficients in Sapporo, Japan on April 6, 2005; **Lower**: vertical profile of aerosol extinction by spherical, non-spherical, and total aerosols 149
Figure 5.10. Normalized trajectory-projected and GOCART aerosol vertical profile over N Pacific on April 7, 2005. 150
Figure 5.11. OMI-retrieved and trajectory-calculated SO_2 from April 5 to 7. 151
Figure 5.12. MODIS-retrieved AOD, OMI aerosol index, and trajectory projected AOD from April 5 to 7, 2005..... 152
Figure 5.13. GOCART simulated SO_2, and AOD at 06 UTC, April 5, 2005.. 153
Figure 5.14. Same as Figure 5.13 but for 03 UTC, April 6, 2005 156
Figure 5.15. Same as Figure 5.13 but for 03 UTC, April 7, 2005 157
Figure 5.16. Total SO_2 mass of the plume and average AOD near the main body of the plume.. 160
Figure 5.17. Trajectory-projected AOD on April 6. 162
Figure 5.18. Total SO_2 mass of the plume, and MODIS and trajectory AOD. 163
Figure 5.19. Decay plot of SO_2 in the plume from April 5 to 7, 2005..... 165
Figure 5.20. Change of AOD of aerosol species in GOCART model. 166

Appendix I.1. Surface weather analysis at 00 UTC on April 1, 2005. 179
Appendix I.2. Surface weather analysis at 00 UTC on April 2, 2005. 179
Appendix I.3. Surface weather analysis at 00 UTC on April 3, 2005. 180
Appendix I.4. Surface weather analysis at 00 UTC on April 4, 2005. 180
Appendix I.5. Surface weather analysis at 00 UTC on April 5, 2005. 181
Appendix I.6. Surface weather analysis at 00 UTC on April 6, 2005. 181
Appendix I.7. Surface weather analysis at 00 UTC on April 7, 2005. 182
Appendix I.8. Surface weather analysis at 00 UTC on April 8, 2005. 182
Appendix I.9. Surface weather analysis at 00 UTC on April 9, 2005. 183
Appendix I.10. Surface weather analysis at 00 UTC on April 10, 2005. 183
Appendix I.11. Surface weather analysis at 00 UTC on April 11, 2005. 184
Appendix I.12. Surface weather analysis at 00 UTC on April 12, 2005. 184

Appendix II.1. Vertical profiles of RH, aerosol scattering, and wet-bulb potential temperature north of Shenyang on April 5, 2005. 185
Appendix II.2. Vertical profiles of RH, SO_2, and wet-bulb potential temperature north of Shenyang on April 5, 2005. 185
Appendix II.3. Vertical profiles of SO_2, temperature, aerosol scattering, and relative humidity on April 10, 2005..... 186
Appendix II.4. Vertical profiles of SO_2, temperature, aerosol scattering, and relative humidity on April 11, 2005..... 187

Appendix II.5. Vertical profiles of SO_2, temperature, aerosol scattering, and relative humidity on April 12, 2005..... 188

Appendix III.1. Polygon boxes used to sample pollution plume on April 6... 189
Appendix III.2. Polygon boxes used to sample pollution plume on April 7... 189

Chapter 1: Introduction

1.1 Background

Atmospheric pollutants refer to chemical or biological substances introduced into the atmosphere directly or indirectly by anthropogenic activities, existing in such amounts as to adversely impact the living environment and well-being of humans and other living organisms [*Williamson*, 1973]. Atmospheric pollutants can be classified into two categories: primary pollutants that are emitted directly; and secondary pollutants that are not emitted directly but formed in the atmosphere. Air pollution, a situation in which one or more atmospheric pollutants produce measurable adverse effects, has long been noted [*Williamson*, 1973]. Prior to the industrial era, scarce accounts in a handful of large population centers blamed coal or wood burning for foul odor and reduced visibility, generally the first noticed aspects of air pollution [*Williamson*, 1973]. Industrialization and urbanization that followed the Industrial Revolution brought irreversible changes to air quality. A series of deadly air pollution disasters from the 1880s to the 1950s called attention to the acute health effects of high concentrations of sulfur-containing pollutants. From the 1940s, expansion of the motor vehicle fleet led to pollution characteristic of high ozone levels in some cities with bright sunshine [*Seinfeld and Pandis*, 1998]. Later epidemiological studies revealed more subtle health effects of aerosols, or small condensed particles suspended in the air, at their common ambient abundance [e.g., *Pope III et al.*, 1995]. The late 1980s saw chlorofluorocarbons (CFCs), a class of man-made substances

previously believed harmless, undergo regulation amid worries about their role in depleting stratospheric ozone, which protects life from harmful solar ultraviolet radiation [*UNEP*, 2000]. More recently, carbon dioxide (CO_2), safe to breathe at ambient concentrations, has raised concerns regarding its greenhouse effect [*IPCC*, 2007].

Two major types of air pollution have been recognized. The first type or "London smog" is characterized by high concentrations of sulfur compounds, usually found in metropolitan areas with intense coal burning when cold and stagnant weather suppresses dilution of pollutants [*Seinfeld and Pandis*, 1998]. The second type or "photochemical smog" occurs in cities with heavy automobile traffic as hot and sunny weather favors the generation of ozone and other secondary pollutants [*Seinfeld and Pandis*, 1998]. Traditionally air pollution was viewed as a local problem for metropolitan or industrialized regions where strong emissions greatly exceed the capacity of natural cleansing mechanisms such as dry and wet deposition, chemical reaction, and ventilation. But it is now accepted that air pollution is not just limited to these "hot spots". The motion of the atmosphere conveys pollutants far away from their emission sources, in some cases all over the globe. Photochemical smog may span over a few hundred kilometers, with peak ozone found in suburban areas [e.g., *T. Wang et al.*, 2006]. Sulfur and nitrogen compounds convert to acidic species during transport, and can harm forests a few thousand kilometers downwind. There has been accumulating observational evidence on the intercontinental transport of pollutants across the Atlantic and the Pacific. The Antarctic "ozone hole" in association with

CFCs is a perfect example that trace amounts of long-lived atmospheric pollutants can cause global environmental problems [*Seinfeld and Pandis*, 1998].

An imminent global issue is the change of climate caused by anthropogenic activities, particularly emissions of greenhouse gases. With CO_2 increasing from about 280 ppm (parts per million) pre-industrial to 379 ppm in 2005, the global surface temperature rose by 0.76ºC from 1850-1899 to 2001-2005, and is projected to go up by another 0.4ºC in the next two decades [*IPCC*, 2007]. Some aspects of air pollution will change or have already changed in this global warming scenario. A warmer climate and the associated change in precipitation can affect ecosystems and the emissions of biogenic hydrocarbon compounds [e.g., *Steiner et al.*, 2006], important precursors in the photochemical production of ozone. At the regional scale, the weakening of monsoon systems or mid-latitude cyclones in some regions can lower surface wind speed and build up pollutants near their emission sources [e.g., *Mickley et al.*, 2004]. Forest fires may increase in some regions [*Westerling et al.*, 2006]; so would emissions from the fires. A warmer climate can also affect temperature-dependent chemical processes of the atmosphere. Air pollution, in turn, by altering the composition of the atmosphere may also impact the climate system. Some atmospheric pollutants are themselves direct or indirect radiative forcing agents. CFCs and ozone are important greenhouse gases [*IPCC*, 2007]. Aerosols, through scattering and absorbing light [e.g., *Charlson et al.*, 1992] and interacting with clouds [*Twomey*, 1959], can change the Earth's radiation budget, and remain the one of the largest sources of uncertainties in climate studies [*IPCC*, 2007]. Atmospheric pollutants influence ecosystems and the biosphere-atmosphere exchange of CO_2. It

has been proposed that nitrogen deposited to the northern hemispheric mid-latitude forests may have turned them into a net carbon "sink", assimilating CO_2 from the atmosphere [*Reay et al.*, 2008]. Cloud-aerosol interaction may affect precipitation [e.g., *Rosenfeld et al.*, 2008], another factor regulating the land-atmosphere carbon flux. Export of nutrients to the oceans can possibly impact maritime ecosystems as well [*Reay et al.*, 2008]. High ozone levels near ground on the other hand can damage plants [*Chameides et al.*, 1994]. Air pollution may also enhance the oxidizing capacity of the atmosphere, affecting the budget of some reactive greenhouse gases (e.g., methane, [*Karlsdóttir and Isaksen*, 2000]). Listed above and illustrated in Figure 1.1 are some examples of the possible connections between air pollution and a changing climate. In addition, human activities in response to climate change or air pollution can also affect air quality. For example, shifting energy use from fossil fuels to renewable energy (e.g., hydro power and wind farms) can cut the emissions of CO_2 and NO_x at the same time.

Anthropogenic emissions are closely related to the economic and social status of a region; so is air pollution, which could be distinctly different between developed and developing areas. Therefore understanding air pollution under global warming circumstances requires examining the emissions, distribution, and evolution of atmospheric pollutants on a region-by-region basis. To study air pollution in any given region, observations from close range are highly desired. It is based on this notion that the studies presented in this dissertation have been formulated. This observational research focuses on China, an emerging economic power and the most populous country in the world, and delivers a data set that lends some insights into

China's air pollution and its impact on the composition of the atmosphere on local and global scales.

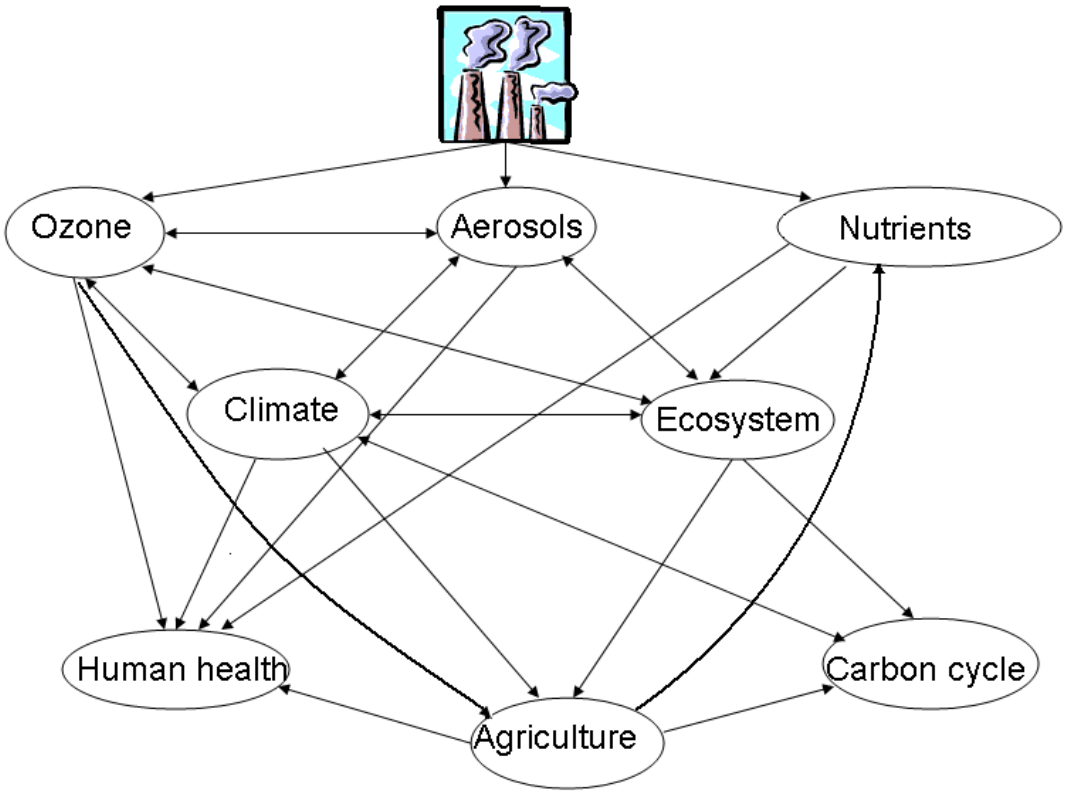

Figure 1.1. Some examples of the impacts of atmospheric pollutants on climate, ecosystems, and humans.

1.2 Some Important Atmospheric Pollutants

In this section, I briefly review the sources, sinks, and residence times (or lifetimes) of some atmospheric pollutants discussed in more detail in this dissertation. Sources of atmospheric pollutants refer to locations, facilities, or mechanisms releasing pollutants to the atmosphere or producing secondary pollutants. Sinks of atmospheric pollutants are processes that remove pollutants from the atmosphere (or a portion of the atmosphere) or convert pollutants to other species [*Seinfeld and Pandis*,

1998]. Regarding the entire atmosphere as a reservoir for a certain pollutant with total abundance Q, its rate of change is determined by the rate the pollutant is introduced into (P) and removed from (R) the atmosphere, and can be expressed as

$$\frac{dQ}{dt} = P - R \qquad (1.1)$$

Assuming a steady state under which P = R, the average residence time of the pollutant, τ, is

$$\tau = \frac{Q}{R} = \frac{Q}{P} \qquad (1.2)$$

The residence time can be used to estimate how far certain pollutants may travel before being removed from the atmosphere. Long-lived species (e.g., CO_2) are generally well-mixed around the globe. Short-lived species are unevenly distributed, and are usually more abundant where strong emissions exist.

Carbon monoxide (CO) is a poisonous trace gas [*Seiler and Junge*, 1970] limited by a National Ambient Air Quality Standard (NAAQS). CO participates in photochemical processes that form ozone in the air. Three major sources of CO are oxidation of methane (CH_4), biomass burning, and combustion of fossil and domestic fuels, each contributing about 650-800 terragrams (10^{12} g) CO per year (Tg CO/yr) [*IPCC*, 2001]. Reaction with hydroxyl radicals (OH) is the most important sink of CO, consuming 1500-2700 Tg CO/yr. The chemical lifetime of tropospheric CO is around 30-90 days [*Seinfeld and Pandis*, 1998].

Nitrogen Oxides ($NO_x = NO + NO_2$) play a central role in the photochemical processes of the atmosphere. They are mainly from high-temperature combustion of fossil fuels (33 Tg N/yr). Soil emissions, lightning, and biomass burning add

considerable but less NO_x to the atmosphere (in total about 19 Tg N/yr [*IPCC*, 2001]). The major sink of NO_x is reaction between NO_2 and OH to form nitric acid (HNO_3), which ultimately is scavenged from the atmosphere. Compared to CO, NO_x has a shorter lifetime of hours to few days [*Seinfeld and Pandis*, 1998]. The sum of NO_x and its atmospheric oxidation products is total reactive nitrogen oxides (NO_y), including NO_x, HNO_3, nitrous acid (HONO), the nitrate radical (NO_3), dinitrogen pentoxide (N_2O_5), peroxynitric acid (HNO_4), peroxyacetyl nitrate (PAN), alkyl nitrates ($RONO_2$), and peroxyalkyl nitrates ($ROONO_2$).

Sulfur dioxide (SO_2) arises predominantly from anthropogenic sources (~70 Tg S/yr, [*Seinfeld and Pandis*, 1998; *Chin et al.*, 2000] including combustion of sulfur-containing fossil fuels and industrial processes, although occasional large volcanic eruptions inject large amount of SO_2 into the atmosphere in a short period of time. Dry deposition accounts for almost half of the total SO_2 sink [*Chin et al.*, 2000]. In-air oxidation of SO_2 (by OH, R1.1) and in-cloud reaction (by hydrogen peroxide, H_2O_2, R1.2) are other important SO_2 sinks; the latter mechanism is faster [*Chin et al.*, 1996]. Sulfate particles generated from SO_2 chemical conversion scatter radiation and can be activated as cloud condensation nuclei (CCN). Estimates of SO_2 lifetime vary, from around one day [*Chin et al.*, 2000] to a few days [*Koch et al.*, 1999].

$$SO_2 + OH(g) \rightarrow H_2SO_4 + \ldots \qquad \text{(R1.1)}$$

$$SO_2 + H_2O_2(aq) \rightarrow H_2SO_4 + \ldots \qquad \text{(R1.2)}$$

Ozone (O_3) is a product of complex photochemical reactions involving two precursors: NO_x and volatile organic compounds; the two determine ozone concentration in a nonlinear way. Exchange between troposphere and stratosphere is

another source of tropospheric ozone. Ozone in the stratosphere is "good", in terms of its absorption of harmful UV radiation. On the contrary, ozone near ground is "bad", with adverse effects on the health of both humans and plants. Ozone near the tropopause acts as a greenhouse gas [*IPCC*, 2007]. Photolysis of ozone generates OH, an important player in atmospheric chemistry (R1.3).

$$\begin{aligned} O_3 + h\upsilon &\rightarrow O(^1D) + O_2 \\ O(^1D) + H_2O &\rightarrow 2OH \end{aligned} \qquad \text{(R1.3)}$$

Aerosols or particulate matter are known for their complicated composition and origins. Directly emitted or formed in the atmosphere, these condensed particles suspended in the air can come from both natural (e.g., sea spray, volcanoes) and anthropogenic sources (e.g., combustion). Dust, if mobilized from areas where human activities have caused desertification, may also be considered "anthropogenic". Of great concern in recent years is the aerosol radiative forcing (ARF), the biggest uncertainty in climate change studies. Some proposed ARF mechanisms are: absorption and scattering of radiation (direct forcing), change of cloud reflectivity, alteration of cloud fraction and lifetime (indirect forcing), change in atmospheric stability due to aerosol heating and cloud formation (semi-direct forcing). Another issue drawing much attention is the health effects of aerosols. Aerosol size ranges from a few nanometers (nm) to up to few hundred micrometers (μm). Smaller aerosols with aerodynamic diameter below 2.5 μm ($PM_{2.5}$), also referred to as fine particles, could be of great harm, as their size allows for deeper penetration into the respiratory system. Coarse mode aerosols (> 2.5 μm in aerodynamic diameter) usually consist of dust, sea salt, and plant particles, and have a lifetime shorter than that of fine particles (days to about a week) due to gravitational sedimentation

[*Seinfeld and Pandis*, 1998]. Studies also demonstrate the association between aerosols and reduced visibility [e.g., *Dzubay et al.*, 1982]. Table 1.1 lists the U.S. NAAQS standards for some pollutants.

Table 1.1. U.S. National Ambient Air Quality Standards for some atmospheric pollutants

	Primary standards		Secondary standards	
Pollutant	Level	Averaging time	Level	Averaging time
CO	9 ppm[a]	8-hour	None	
	35 ppm	1-hour	Same as Primary	
NO_2	0.053 ppm	Annual	Same as Primary	
PM_{10}[b]	150 μg/m^3	24-hour	Same as Primary	
$PM_{2.5}$[c]	15.0 μg/m^3	Annual	Same as Primary	
	35 μg/m^3	24-hour	Same as Primary	
O_3	0.075 ppm	8-hour	Same as Primary	
	0.12 ppm	1-hour	Same as Primary	
SO_2	0.03 ppm	Annual	0.5 ppm	3-hour
	0.14 ppm	24-hour		

Source: EPA website: http://www.epa.gov/air/criteria.html; Primary standards protect people from health risk; Secondary standards prevents unacceptable effects on the public welfare, for example unacceptable damage to buildings and crops.
[a] Parts per million.
[b] Particulate matter with aerodynamic diameter below 10 μm.
[c] Particulate matter with aerodynamic diameter below 2.5 μm.

1.3 Air Pollution in China

1.3.1 Industrialization, urbanization, and air pollution

With her economy soaring at unprecedented pace, products swarming into global market, and cities expanding faster than ever, China has become arguably the second largest economic entity in the world, as measured by purchasing power parity

(PPP) [*World Bank*, 2006]. However, such dazzling achievement does not come without a cost. Among many challenges for this country is the deteriorating atmospheric environment, a byproduct of fast industrialization and urbanization.

Contributing over 40% of the gross domestic product (GDP, Figure 1.2), industry is the locomotive driving economic growth in China (Figure 1.3), but also consumes about 70% of China's energy, mostly from coal (Figure. 1.4). Annual coal production in China has increased almost by a factor of three since 1978 (Figure 1.4, [*Chinese CBS*, 2005]), accounting for more than 60% of total energy consumption. SO_2 emissions, mostly from coal-burning, have recovered from a decline in mid-1990s [*Larssen et al.*, 2006] and been on the rise over the past several years (Figure 1.5). NO_x emissions from China have also increased [*Richter et al.*, 2005], as power generation grows [*Chinese CBS*, 2005]. CO emissions, largely from the residential sector, were projected to be relatively steady, as more efficient combustion techniques cancel out growing energy demand [*Streets and Waldhoff*, 2000], although emissions from steel mills may continue to go up.

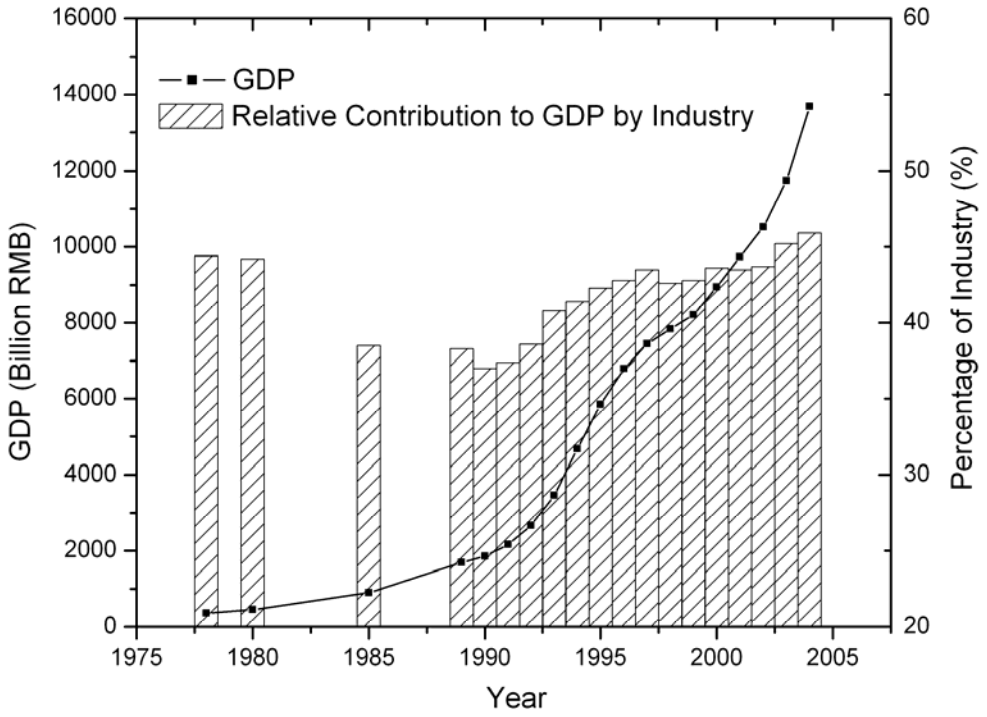

Figure 1.2. GDP (line and dots) and percentage contribution from industry (shaded columns) for China during 1978-2004 (source: [*Chinese CBS*, 2005]).

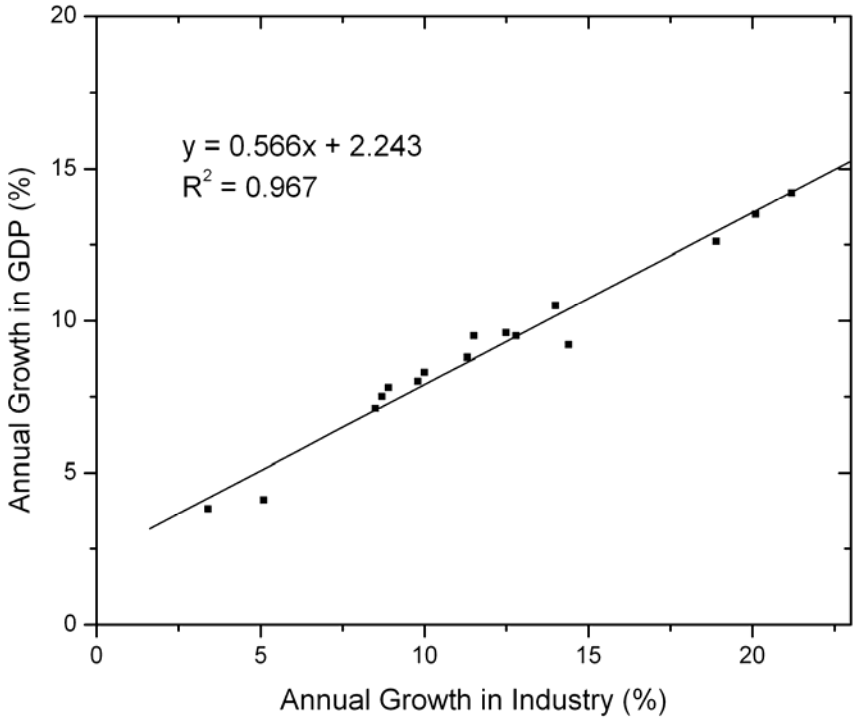

Figure 1.3. Correlation between annual growth rate of GDP and industry of China during 1989-2004 (source: [*Chinese CBS*, 2005]).

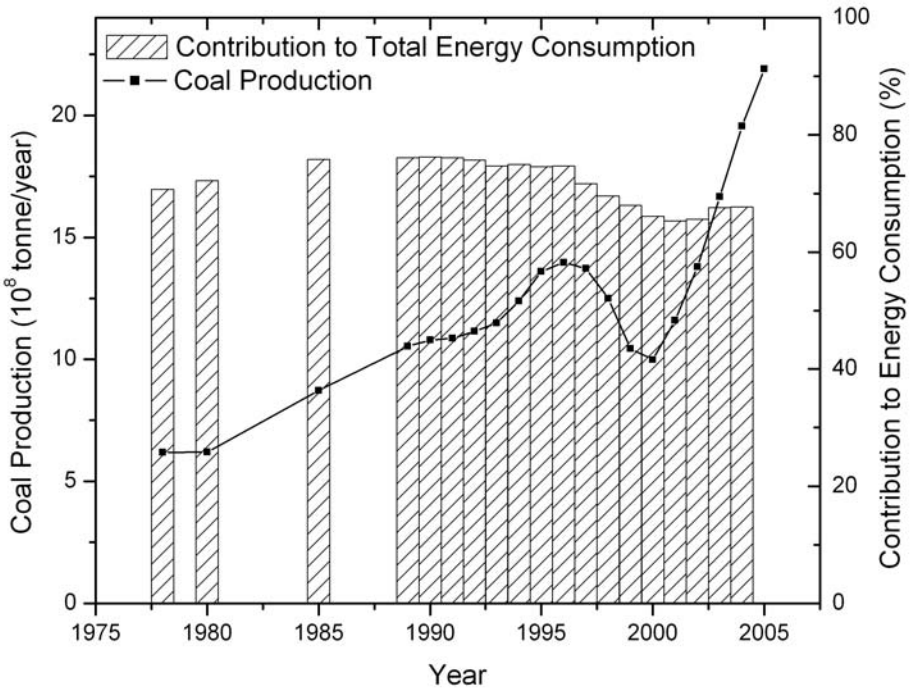

Figure 1.4. Coal production (line and dots) and percentage contribution to total energy consumption (shaded columns) of China during 1978-2004 (source: [*Chinese CBS*, 2005]).

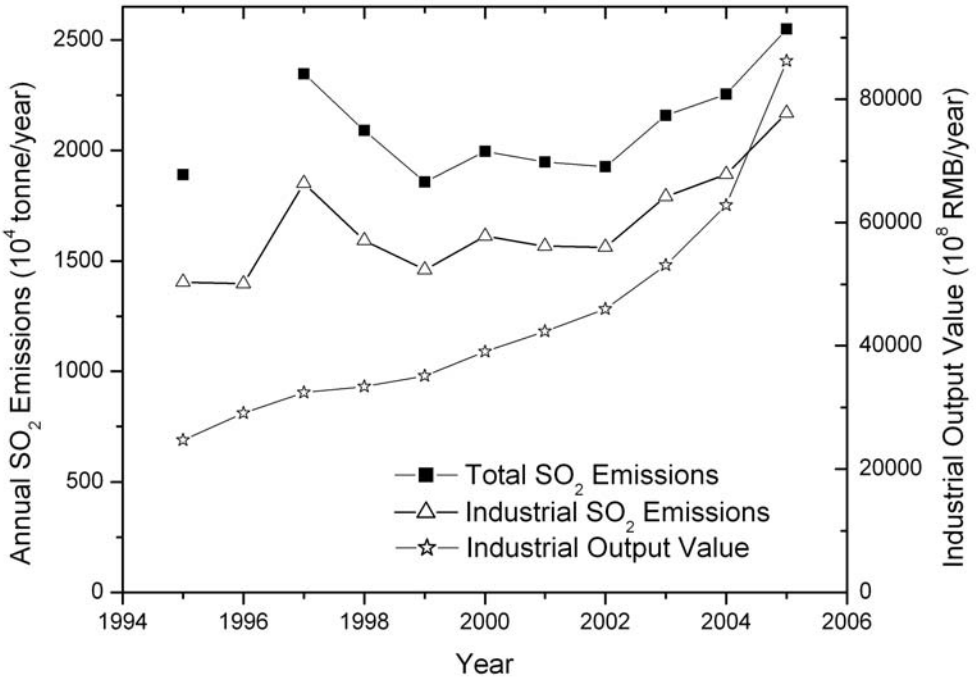

Figure 1.5. Reported total SO_2 emissions (line and squares), industrial SO_2 emissions (line and triangles), and industrial output value (line and stars) of China during 1995-2005 (source: [*Chinese CBS*, 2005]).

Air pollution, previously considered a local problem for industrialized big cities in China [*Tang et al.*, 1990], has developed into a regional problem [e.g., *He et al.*, 2002; *Shao et al.*, 2006]. From 1985 to 2002 the urban population in China doubled, and the urbanized area nearly tripled [*Guo*, 2004, document available online at http://www.drcnet.com.cn/]. Fast urbanization processes turn agricultural land into city clusters and mega cities [*Shao et al.*, 2006]. Industry in rural areas is booming: in 2004, one in every five of China's 650 million person labor force worked for factories built in the countryside [*Chinese CBS*, 2005]. These numerous and mostly small factories are substantial sources of atmospheric pollutants [*Streets et al.*, 2003]. In addition to industrialization and urbanization, other factors such as the 20-fold growth of the motor vehicle fleet since 1978 [*Chinese CBS*, 2005] may also have exacerbated the air quality issue in China.

1.3.2 Air pollution in China: State of the issue

In 2002, only about one third of the 343 monitored cities met the Class II National Ambient Air Quality Standard of China (Table 1.2) [*Hao and Wang*, 2005]. In cold winter, indoor heating and stagnant meteorological conditions build up heavy pollution in cities across northern China [e.g., *He et al.*, 1999; *Liu and Song*, 2001; *Ma et al.*, 2003; *Wu et al.*, 2002]. In spring, dust storms pick up in the arid northern China; some particularly strong ones can have widespread effects [e.g., *Sun et al.*, 2005]. Higher temperature and stronger sunshine in summer are conducive to the formation of ozone and secondary aerosols, causing photochemical smog and haze in big cities [e.g., *Bergin et al.*, 2001; *Liu and Shao*, 2004]. Ozone violations in the cities

in the warmer south may occur from late spring until early fall [e.g., *X. Wang et al.*, 2003]. Acid deposition has become a serious problem in southern China, where the buffering capacity of soil is weak [e.g., *Wang and Wang*, 1995, 1996].

Experiments at a number of rural or "background" sites demonstrate the extent of the air pollution issue in China. Almost 700 ppb (parts per billion) CO was measured at a rural site in the Yangtze River Delta (YRD) region in spring [*T. Wang et al.*, 2004], far higher than the normal range seen in the Northern Hemisphere [*Seinfeld and Pandis*, 1998]. At a mountainous site 50 km north of downtown Beijing, *T. Wang et al.* [2006] recorded maximum O_3 of 286 ppb in the summer of 2005. $PM_{2.5}$ monitoring in winter 2002 shows comparable aerosol loadings at eight urban and suburban sites in the Pearl River Delta region [*Cao et al.*, 2003]. Similarly, great $PM_{2.5}$ levels were found both downtown and in the outskirts of Beijing [*Zheng et al.*, 2005].

Table 1.2. Concentration limits for some pollutants in the National Ambient Air Quality Standard of China (adapted from [*He et al.*, 2002]). (Unit: mg/m^3)

Pollutants	Averaging Time	Class I[a]	Class II[b]	Class III[c]
TSP	Daily	0.12	0.3	0.5
	Annual	0.08	0.2	0.3
PM_{10}	Daily	0.05	0.15 (0.15)	0.25
	Annual	0.04	0.1	0.15
SO_2	Daily	0.05	0.15 (0.37[d])	0.25
	Annual	0.02	0.06 (0.08[d])	0.1
NO_2	Daily	0.08	0.08	0.12
	Annual	0.04	0.04 (0.1)	0.08
NO_x	Daily	0.1	0.1	0.15
	Annual	0.05	0.05	0.1
CO	Daily	4	4 (10[e])	6
O_3	Hourly	0.12	0.16 (0.24[f])	0.2

Numbers in parenthesis are the U.S. EPA NAAQS values.

[a] Set for natural conservation, resort, or tourist areas.

[b] Set for urban residential, commercial, or rural areas.
[c] Set for industrial districts or traffic centers.
[d] Unit converted assuming 20°C, 101.325 kPa (NIST standard temperature and pressure).
[e] 8-hour concentration for the U.S. standard.
[f] Unit converted assuming 20°C, 101.325 kPa, hourly concentration standard only applied in limited areas.

1.3.3 Air pollution in China: impacts

Elevated pollutant levels lead to various problems. Ozone in rural China, projected to rise further in the future [*Chameides et al.*, 1999a], may reduce the yield of some crops by almost 20% [*Aunan et al.*, 2000]. High aerosol loading in eastern China (aerosol optical thickness, AOT: ~0.5, [*Xin et al.*, 2007]) can diminish solar radiation reaching the surface, and may cost China ~10% of total crop production [*Chameides et al.*, 1999b]. Acid deposition can affect ecosystems and contaminate water bodies [e.g., *Yang et al.*, 2001]. As discussed earlier, high ozone and aerosol levels also adversely impact human health, causing increased morbidity [*Wang and Mauzerall*, 2006], and over 300,000 estimated excess deaths every year in China [*WHO and UNDP*, 2001]. Strongly absorbing aerosols (particles that absorb solar radiation) may influence atmospheric heating rates [*Z. Li et al.*, 2007a] and affect the evolution of the planetary boundary layer (PBL) [*Yu et al.*, 2002]. Some studies attribute the recently documented weakening of the East Asian summer monsoon [*Xu et al.*, 2006], reduced cloudiness [*Qian et al.*, 2006] and precipitation [*Zhao et al.*, 2006], and "north drought south flood" climate anomaly [*Menon et al.*, 2002; *Xu,* 2001] over China to aerosol forcing. Changes in precipitation may further affect ecosystems and agriculture. In 2006, the first ever "Green GDP" report issued by

Chinese EPA and Chinese CBS [2006] estimated that the economic loss due to air pollution in China was more than 25 billion U.S. dollars in 2004, or 1.2% of GDP. The *World Bank* [1997] suggested that air pollution cost a much higher fraction of China's GDP (7%).

Once vented into the free troposphere and driven by strong westerly winds aloft, pollutants can potentially travel over long distances [e.g., *Berntsen et al.*, 1999; *Chatfield and Crutzen*, 1984; *Dickerson et al.*, 1987, *Jaffe et al.*, 1999, 2003a; *Husar et al.*, 2001; *Prospero et al.*, 2003; *Allen et al.*, 2004; *Mari et al.*, 2004; *Guttikunda et al.*, 2005], turning a local air pollution issue into a large scale problem. While the average intercontinental transport time was estimated to be 2-4 weeks [*Liu and Mauzerall*, 2005]; in some episodic transpacific events, pollution plumes from East Asia could reach North America in just days [e.g., *Husar et al.*, 2001; *Jaffe et al.*, 1999; *Stohl et al*., 2003]. Pollutants from East Asia could increase surface ozone [e.g., *Fiore et al.*, 2002; *Hudman et al.*, 2004; *Jaffe et al.*, 2003b; *Lin et al.*, 2000] and particle concentrations, and reduce visibility [*Park et al.*, 2004; *Fairlie et al.*, 2007] in the U.S. Transboundary transport of pollutants from China into Korea and Japan also has been documented in both observational and numerical studies [e.g., *Kim et al.*, 2001; *Arimoto et al.*, 2006]. Aerosols (or precursors) from China might impact the climate over large areas, such as the cloud system in the northern Pacific storm track [*R. Zhang et al.*, 2007].

1.4 Overview of Research

1.4.1 Emission inventory: method, uncertainties, and evaluation

Usually constructed with "bottom-up" methods, emission inventories estimate the amount of certain pollutants released into the atmosphere from a certain area during a certain period of time. Emissions of a specific pollutant j are calculated as:

$$E_{j,k,l} = \sum_{m}\sum_{n} A_{j,k,l,m,n} EF_{j,k,l,m,n} \qquad (1.3)$$

where E represents emissions, A is the activity rate (e.g., fuel consumption), and EF is emission factor after abatement (e.g., pollutant release from unit mass of fuel). *k* represents an area; *l* stands for a sector; m is fuel or activity, and n represents emission abatement [*X. Wang et al.*, 2005]. Total emissions of the species j from the whole inventory region would be:

$$E_j = \sum_{k}\sum_{l} E_{j,k,l} \qquad (1.4)$$

In practice, anthropogenic and natural contributions are often treated separately [e.g., *Streets et al.*, 2003], with the former classified into three categories: large point sources (LPS) with strong emissions from a small fixed area (e.g., stacks of power plants), area sources including all stationary sources not identified as LPS, and mobile sources mainly consisting of on-road vehicles [*X. Wang et al.*, 2005]. Activity rate (or fuel consumption) data are normally from government statistics, and emission factors are from in-lab or field experiments. The quality of the A and EF largely determines the reliability of an emission inventory.

For a large developing country like China, collecting information to compile a "bottom-up" inventory takes tremendous effort. Bias and inconsistency in government statistics, as pointed out by *Sinton* [2001], *Streets et al.* [2003], and *X.*

Wang et al. [2005], require extra caution when using the data. Coexistence of advanced and primitive technologies, in addition to the wide variety of fuels, adds to the uncertainties in emission estimates. Emission factors are derived from scarce in-lab experiments [e.g., *Chen et al.*, 2006], which are far from sufficient considering the many distinct combinations of combustion devices and fuels in China. Even existing emission factors deviate [*Streets et al.*, 2003], sometimes by a factor of five (e.g., CO emission factors from small stoves given by *Zhang et al.* [1999] vs. *Venkataraman and Rao* [2001]). Field experiments can characterize emissions from some processes such as biomass burning [e.g., *Andreae and Merlet*, 2001], but can introduce bias when results are extrapolated to a much larger area. Yet another source of uncertainty for emission inventories is the abatement technique employed: some big cities like Beijing may have more stringent emission control measures in place [e.g., *Beijing EPA*, 2002], although a national clean air act (China's Air Pollution Prevention Law) gives general guide. Additional uncertainties stem from rapid economic growth, which makes the air pollution issue of China a "moving target" [*Q. Zhang*, personal communication].

Large uncertainties exist in current emission inventories of China, especially for pollutants mainly from low-efficiency combustion processes such as CO and black carbon (BC). *Streets et al.* [2003] put error bars of 150% and 400% on their "bottom-up" estimates of CO and BC emissions from China, respectively. This CO emission inventory [*Streets et al.*, 2003], along with some others [e.g., *Streets and Waldorf*, 2000], has been tested extensively [*Streets et al.*, 2006]. In general, observations in eastern China [*T. Wang et al.*, 2002, 2004; *Wen et al.*, 2008] and its

downwind region [e.g., *Huebert et al.*, 2003], inverse [*Arellano et al.*, 2004; *Heald et al.*, 2004; *Palmer et al.*, 2003; *Tan et al.*, 2004; *Y. Wang et al.*, 2004] and forward modeling [*Allen et al.*, 2004; *Carmichael et al.*, 2003; *Heald et al.*, 2003; *Kurata et al.*, 2004], and more recently four-dimensional variational data assimilation (4DVAR, [*Yumimoto and Uno*, 2006]) all suggest an underestimate of China's CO emissions in these inventories. A new inventory [*Streets et al.*, 2006], with updated activity rate and emission factors for some industrial sources, adjusts the CO emitted from China up by about 60%, but still has an uncertainty of almost 70%. Observational and numerical studies also help evaluate emissions of other pollutants from East Asia, including mercury [*Jaffe et al.*, 2005], ammonia [*Kim et al.*, 2006], and black carbon [*Huebert et al.*, 2003]. *Ma and van Aardenne* [2004] reported large discrepancies in NO_x, non-methane hydrocarbon compound (NMHC), and CO emissions from China between three emission inventories.

1.4.2 Long-range transport of atmospheric pollutants: mechanisms

Key factors determining the potential for long-range pollutant transport are the lifetime of a certain pollutant [e.g., *Liu et al.*, 2005; *Liu and Mauzerall*, 2005] and meteorological conditions. As previously discussed, the pollutant lifetime is determined by the rate it is removed from atmosphere via dry deposition, wet removal, and photochemical reactions [*Seinfeld and Pandis*, 1998]. These removal processes are all somewhat influenced by meteorological conditions: atmospheric stability affects deposition; relative humidity, precipitation, and cloudiness control wet removal; temperature and radiation regulate photochemical processes. Pollutants at

higher altitudes, above the boundary layer, tend to exist longer as lower temperature slows chemical reactions and deposition diminishes.

Direction and speed of winds determine the destination of pollutants before their removal from the atmosphere. Strong winds in the middle and upper troposphere promote long-range transport of pollutants, in some cases driving pollutant plumes across ocean basins in just days [e.g., *Husar et al.*, 2001]. In comparison, the timescale of transpacific transport in the lower troposphere is typically 2-3 weeks [e.g., *Holzer et al.*, 2003, 2005; *Liu and Mauzerall*, 2005; *Liu et al.*, 2005]. Given a longer lifetime and stronger advection, pollutants ventilated from the polluted PBL into the free troposphere (FT) can potentially be carried far away from their emission sources. The mechanisms lifting pollutants to higher altitudes are therefore crucial for long-range transport.

Long-range transport of pollutants from mid-latitude (30-60º north and south) continental regions is related to eastward moving mid-latitude wave cyclones [e.g., *Berkowitz et al.*, 1996; *Bethan et al.*, 1998; *Bey et al.*, 2001; *Cooper et al.*, 2001; *Esler et al.*, 2003; *Hannan et al.*, 2003; *Kaneyasu et al.*, 2000; *Liang et al.*, 2004, 2005; *Mari et al.*, 2004; *Prados et al.*, 1999], which are under the control of the large-scale atmospheric circulation. Long-range transport events from East Asia are episodic [e.g., *Berkowitz et al.*, 1996; *Jaffe et al.*, 2003b; *Mari et al.*, 2004; *Yienger et al.*, 2000], and show seasonal variability in association with the East Asian monsoon. The dominant Siberian anticyclone in winter traps pollutants over East Asia at lower altitudes [*Newell and Evans*, 2000], until prevailing northwesterly winds convey them to the southeast, where they are lifted to the upper troposphere by convection and

transported further in the upper branches of Hadley cell circulation [*Liu et al.*, 2003; *Liang et al.*, 2004]. With cyclone activities intensifying and convection picking up, spring is the peak season for eastward transport of pollutants from East Asia [e.g., *Holzer et al.*, 2003; *Igarashi et al.*, 2006; *Jaffe et al.*, 1999; *Liu et al.*, 2003; *Liang et al.*, 2004]. Summer months see weaker mid-latitude cyclones; and surface winds from the ocean prevail. But strong convection over the hot land surface can sometimes vent pollutants into upper troposphere [e.g., *Kiley and Fuelberg*, 2006], although some of the uplifted pollutants are transported around the Tibetan anticyclone to the Middle East [*Liu et al.*, 2003]. Eastward transport of Asian pollutants is not as strong in fall as in winter [*Gregory et al.*, 1997], as northeasterly winds push pollutants southwestward [*Liu et al.*, 2003]. Factors controlling the interannual variability of transpacific transport include the strength of Pacific high and Aleutian low [*Liang et al.*, 2005; *Liu et al.*, 2005], and El Niño and La Niña events, whose influence on atmospheric circulation may alter the frequency of mid-latitude wave cyclones [e.g., *Fuelberg et al.*, 2003; *Liu et al.*, 2003; *Liu et al.*, 2005].

Liang et al. [2004, 2005] summarized the major pathways for pollutants to leave East Asia, and to enter North America (Figure 1.6). The outflow pathways shown in the figure include convective uplift (E1), slantwise ascent in the warm conveyor belt (E2), postfrontal boundary layer transport (E3), and low-level prefrontal jet transport (E4). Import mechanisms to North America include advections in the free troposphere westerly flow (I1), boundary layer transport (I2), large-scale subsidence in the Pacific high (I3), subsidence in the postfrontal dry air stream (I4), and subsidence due to mountain waves (I5). E2, E3 and E4 associated with mid-

latitude cyclones are of synoptic scale. Convective lifting (E1) is of relatively small scale, but is often induced by or embedded in frontal systems [e.g., *Dickerson et al.*, 2007; *Kiley and Fuelberg*, 2006]. A pollutant lofting mechanism not illustrated in the figure is orographic lifting [e.g., *Hanna et al.*, 2003; *Liu et al.*, 2003], which happens when air flows interact with uneven terrain.

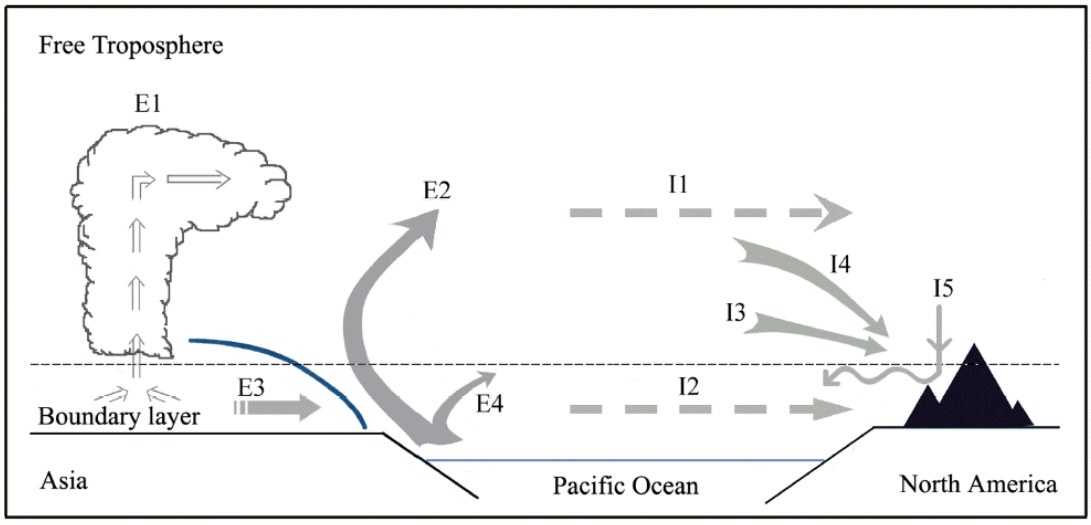

Figure 1.6. Schematic of major pathways for pollutant outflows from East Asia (E1, E2, E3, and E4) and inflows into North America (I1, I2, I3, I4, and I5) [*Liang et al.*, 2005].

As depicted in Figure 1.6, convection and the warm conveyor belt lifting are two major mechanisms ventilating PBL air into free troposphere. The warm conveyor belt (WCB) refers to large scale ascending motion ahead of the surface cold front of a mid-latitude cyclone system (Figure 1.7). The air stream originating from low altitudes in the warm sector of the cyclone sends warm, moist air northward and upward along isentropic surfaces, reaching the middle and upper troposphere before turning anticyclonically at higher altitudes over the surface warm front [*Cooper et al.*, 2001; *Mari et al.*, 2004]. As condensation occurs along the way, the warm conveyor

belt can often be identified with a synoptic scale cloud band on satellite images. Upward motion in WCB's is generally slow, typically lifting air from PBL to upper troposphere (300 mb) in 2-3 days [*Stohl et al.*, 2002]. The chemical properties of a WCB largely depend on its origin [e.g., *Bethan et al.*, 1998]. A WCB originating from the PBL over a pollutant source region [e.g., *Stohl et al.*, 2003] is more polluted than one initially from a clean marine boundary layer [e.g., *Mari et al.*, 2004], and more likely to transport pollutants downwind.

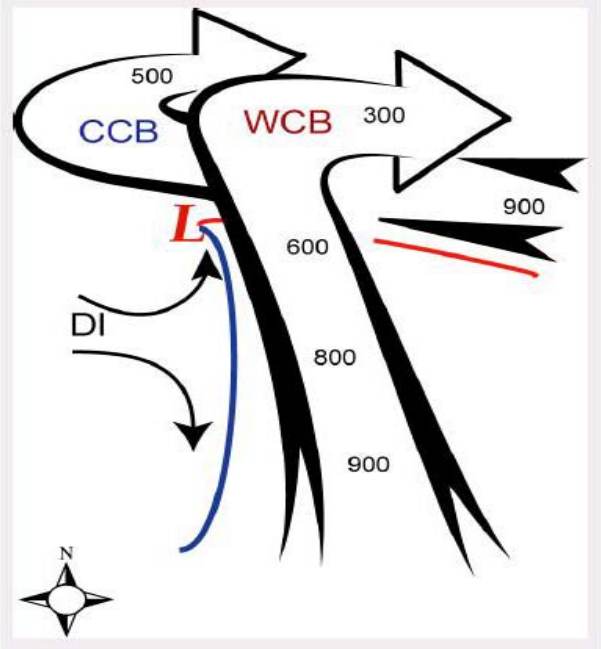

Figure 1. 7. Major air streams associated with a mid-latitude cyclone: cold conveyor belt (CCB), warm conveyer belt (WCB), and dry intrusion (DI) [*Kiely and Fuelberg*, 2006].

Convection is induced by atmospheric instability, and occurs most frequently in summer in mid-latitudes [e.g., *Hartmann*, 1994; *Horowitz et al.*, 2003; *Liang et al.*, 2004]. Strong updrafts up to tens of meter per second associated with these local or mesoscale processes makes them very efficient in lofting pollutants (Figure 1.8). The role of convection in the long-range transport of pollutants has been identified in

observational and numerical experiments [*Bertram et al.*, 2007; *Chatfield and Crutzen*, 1984; *Dickerson et al.*, 1987; *Donnell et al.*, 2001; *Pickering et al.*, 1988; 1990].

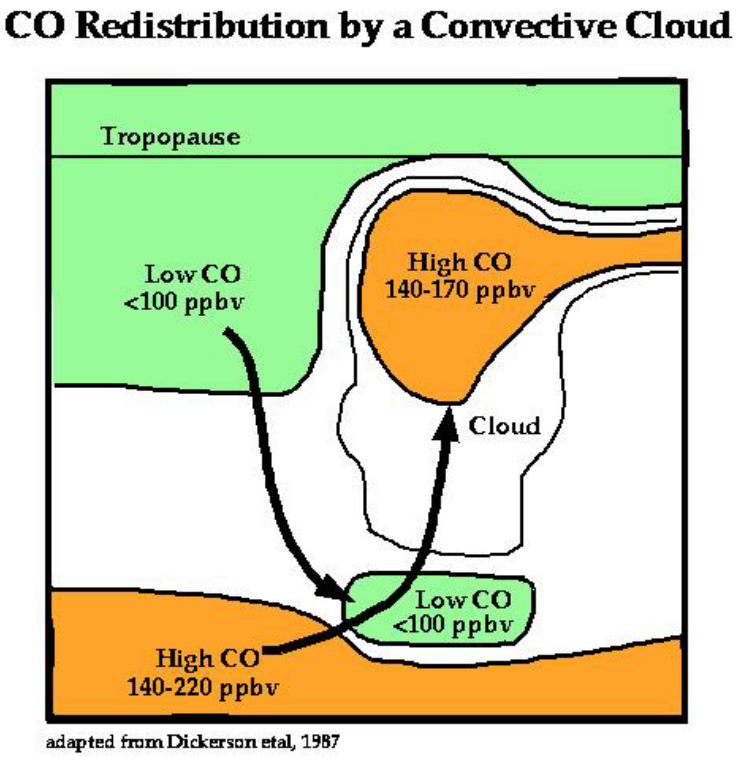

Figure 1. 8. Schematic of CO redistribution by a deep convective process [*Dickerson et al.*, 1987].

Yet to be determined is the relative importance of the warm conveyor belt ascent and rapid convection in exporting pollutants from East Asia. Aircrafts measurements off the east and west coasts of the Pacific during PEM-West A/B [*Gregory et al.*, 1996, 1997], TRACE-P [*Jacob et al.*, 2003], ACE-Asia [*Huebert et al.*, 2003], and ITCT 2K2 [*Parrish et al.*, 2004] measured the chemical properties of air flows from Asian continent, particularly China. Many studies recognize warm conveyor belt lofting as the principal mechanism lifting and transporting pollutants emitted from East Asia [e.g., *Cooper et al.*, 2004; *Jaffe et al.*, 1999; *Kaneyasu et al.*,

2000; *Martin et al.*, 2002; *Miyazaki et al.*, 2003]. But these studies rely on data collected downwind of China. The backward trajectory models and/or chemical transport models employed in these studies can explicitly simulate synoptic-scale features like WCB, but need to parameterize convective processes. The coupling of the WCB and convection further complicates this issue. Deep convective processes embedded in a WCB could either dilute [e.g., *Mari et al.*, 2004] or enrich [e.g., *Donnell et al.*, 2001] the pollutants within the rising air stream of a WCB.

1.4.3 Aerosol chemical composition in China

In recent years, there has been a lot of effort analyzing aerosol chemical composition in China. Bulk [e.g., *Wang, Zhuang et al.*, 2006] and size segregated [e.g., *Lun et al.*, 2003] samples have been collected from rural and urban sites [e.g., *Zheng et al.*, 2005], from the dust-laden west [e.g., *Zhang et al.*, 2003; *Xu et al.*, 2004] to the industrialized east [e.g., *Xu et al.*, 2002], and from various platforms including surface stations [e.g., *Sun et al.*, 2004], towers [e.g., *Chan et al.*, 2005], balloons [e.g., *Xu et al.*, 2001], and aircraft [e.g., *Hatakeyama et al.*, 2005]. Inorganic ions [e.g., *Yao et al.*, 2003], elements [e.g., *Ning et al.*, 1996], and carbonaceous compounds [e.g., *Cao et al.*, 2003; *Yang et al.*, 2005] are among the most commonly studied species. Dust storms in spring draw a lot of attention, in light of their severe regional environmental effects [e.g., *Sun et al.*, 2005; *Zhang et al.*, 2002]. Generally, sulfate has been found to be more abundant than nitrate [e.g., *He et al.*, 2002; *Yao et al.*, 2003; *Hu et al.*, 2008], a phenomenon often attributed to the relatively large contribution from coal-burning stationary sources vs. mobile sources, although the

latter are growing quickly [*Wang, Zhuang et al.*, 2006]. In winter and spring in N China, the cold environment slows gas-phase (OH) oxidation from SO_2 to sulfate, the proposed major wintertime SO_2 conversion pathway in some studies [e.g., *Yao et al.*, 2003]. Interaction between dust particles and pollutants, via absorption of gases, surface reaction, and particle coagulation, has been suggested as another important mechanism producing secondary aerosols in spring, particularly in dust storms [e.g., *Sun et al.*, 2005; *Wang, Zhuang et al.*, 2007; *Yuan et al.*, 2008]. Single particle analysis [e.g., *Gao and Anderson*, 2001; *Sullivan et al.*, 2007] has found traces of S and N compounds on the surface of some airborne dust particles sampled in the region.

1.4.4 EAST-AIRE: an international regional experiment

East Asian Study of Tropospheric Aerosols: an International Regional Experiment (EAST-AIRE) is a scientific project jointly conducted and supported by both American and Chinese institutes and agencies. The major goals of EAST-AIRE are to understand better the origins, transport, physical, chemical, and optical properties of dominant natural and anthropogenic aerosols and gases in China, as well as to gain preliminary insights into the direct and indirect effects of these aerosols and gases on radiation, clouds, and precipitation [*Z. Li et al*, 2007b]. In view of the urgent need for high-quality observational data of aerosols and precursor gases from China, a special focus of EAST-AIRE is to make measurements within or near major aerosol source regions of China, using instruments traceable to international standards [*Z. Li et al*, 2007b]. Routine measurements of aerosols and radiation parameters are

provided by a nationwide surface remote sensing network, comprised of more than twenty stations and three super sites distributed in various climate zones and source regions of different aerosol types in China. This long-term monitoring network is supplemented by intensive field experiments involving in-situ measurements of trace gases and aerosols, from surface sites and instrumented aircraft.

From February to April 2005, a U.S.-China joint Intensive Field Campaign (IFC) was conducted under the auspices of EAST-AIRE. This dissertation benefits from the data set from this IFC. Surface measurements of SO_2, CO, NO/NO_y, O_3, aerosol absorption, and aerosol scattering were made in Xianghe, a rural site about 70 km ESE and generally downwind of Beijing in March. Bulk aerosol samples were collected during and beyond the ground experiment (results presented in Chapter 3). The April aircraft campaign measuring CO, SO_2, O_3, and aerosol scattering over Shenyang, an industrialized city of 6 million residents ~600 km NE of Beijing, determined the vertical distribution of pollutants up to 4500 m altitude under a variety of synoptic conditions (results given in Chapter 4).

1.4.5 Outline of research

Some of the specific questions I try to address in this dissertation include:

1) Current estimates of pollutant emissions from China: how good are they?

2) What are some of the important meteorological mechanisms lifting pollutants from their sources in China into the free troposphere, where they can potentially move far downwind?

3) How do some of the pollutants evolve during transport, and can their evolution be tracked with state-of-the-art satellite sensors?

I start with ground measurements of trace gases, aerosol optical properties, and aerosol chemical composition. I evaluate a few current emission inventories for China by comparing observed and inventory pollutant ratios. Emissions of gaseous pollutants from a local small-scale coal-fired boiler are characterized as well. I calculate the enrichment factors of some elements in aerosol samples, which provide some insights into the origins of aerosols in the region.

I also analyze the synoptic variation of pollutants, observed from the ground as well as from the aircraft. Backward trajectories and weather analysis will help determine the sources of our sampled air parcels. Focusing on two research flights measuring the chemical properties of the atmosphere around a frontal system, a case study reveals the role of upwind dry convection in lofting and transporting pollutants.

The conversion of SO_2 to sulfate aerosols during transport is studied using satellite data. An analysis combining aerosol composition, backward trajectories, and satellite cloud product studies the conversion process as pollutants are carried into northern China by NW flows behind cold fronts. A second analysis makes use of forward trajectories, a chemical transport model, and multiple satellite sensors to track the evolution of a large pollution plume as it leaves China and moves into the northern Pacific, and estimates the decay of SO_2 and change of aerosols in the plume.

Chapter 2: Experimental Methods

2.1 Sampling Site and Platform

2.1.1 Xianghe site

The Xianghe Atmospheric Observatory (39.75ºN, 116.96ºE; 35 m above sea level), a supersite of the EAST-AIRE project, is located about 70 km east-southeast and generally downwind of the Beijing metropolitan area. This area of plains is surrounded by agricultural land, densely occupied residences and light industry. Sitting between two mega-cities (with Beijing to the northwest and Tianjin to the southeast, shown in Figure 2.1) and less than 5 km west of the local township (population: ~50,000), the site sees pollutants of urban, rural, or mixed origins, depending on wind direction. A small coal-fired boiler about 50 m east of the four-story main facility building provides heating in winter months.

Routinely measured at the site are aerosol optical thickness, direct and diffuse radiation, and sky conditions by instruments installed about 15 m above ground, on the top of the main facility building. During the first IFC of EAST-AIRE in March, 2005, trace gas detectors measuring CO, NO/NO_y, SO_2, and O_3, and instruments detecting aerosol absorption and scattering coefficients were deployed in the same location, with sampling inlets mounted on the top of the building, ~10 m away from the radiation instruments. A high-volume sampler near the aerosol instruments collected bulk aerosol samples from March to April.

Instruments on a 32-m meteorological tower about 50 m southwest of the main facility building measured ambient temperature, relative humidity (RH), and wind speed at five levels (2, 4, 8, 16, and 32 m above ground) every 10 min. A weather vane at the top of the tower determined the wind direction, and a barometer monitored local atmospheric pressure. During the ground experiment, the area was generally cold and dry, with average temperature of ~4.4ºC, RH of ~36%, and very little precipitation (~0.1 mm in total).

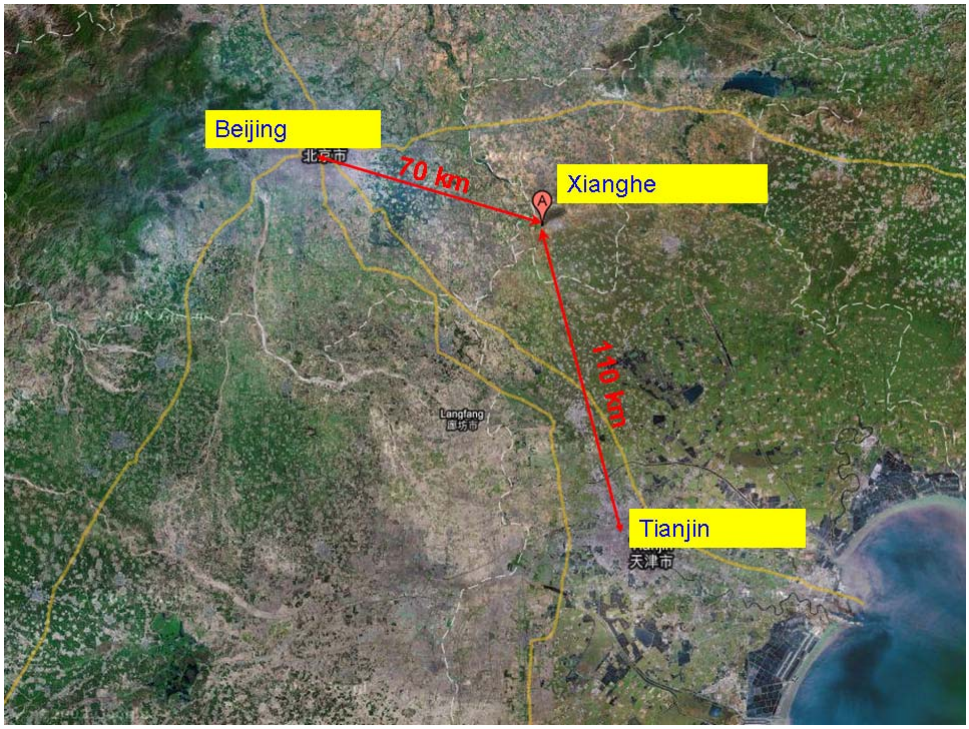

Figure 2.1. Location of the Xianghe site.

2.1.2 Y-12 aircraft

A modified Chinese Y-12 twin engine turboprop aircraft (Figure 2.2) was used in the aircraft experiment. The Y-12 has a cruise speed of about 200 km/hr and a ceiling of about 7000 m. A forward-facing isokinetic inlet mounted on the top of the

cockpit, ahead of the engines, directs samples into aerosol instruments. Conductive rubber tubing minimizes loss of small aerosol particles. An aft-facing inlet at the same spot supplies sampling flow to trace-gas instruments. Teflon inlet line was used to avoid ozone loss. Due to losses of coarse aerosol particles to the aerosol sampling line, aerosol data collected from the aircraft represent mainly fine particles. The sampling efficiency of the inlet for aerosols of different sizes has not been quantitatively characterized.

A RH/T probe (EIL Instruments Inc. Rustrak RR2-252, Hunt Valley, MD) installed in between the aerosol and trace gas inlets measured ambient temperature and relative humidity, with a precision of 0.5ºC in temperature and 2% in RH [*Taubman*, 2004]. A Rosemount Model 2008 pressure transducer provided static pressure readings during flight, which were compared to surface meteorological records at the airport upon takeoff and landing. The corrected pressure data were then converted into pressure altitude (*palt*) using the 1976 standard atmosphere equation:

$$palt = 8303.951372 \times \ln(1013.25/pressure) \qquad (2.1)$$

where pressure is in mb. Flight positions were recorded with the Global Positioning System (Garmin GPS-90) and validated with known geographic reference points.

During the airborne campaign, theY-12 aircraft was instrumented with CO, SO_2, and O_3 monitors, and an integrating nephelometer measuring aerosol scattering coefficients. Taoxian International Airport (41.64ºN 123.49ºE), where the aircraft was based, is ~20 km south-southeast of downtown Shenyang, the capital of China's northeastern province of Liaoning, and a big city (population: 6 million) ~600 km NE

of Beijing. Within 80-km radius of Shenyang are five more industrialized cities of 400,000 or more residents (Fushun, Benxi, Liaoyang, Tieling, and Anshan).

Figure 2.2. Y-12 twin engine turboprop research aircraft used for the aircraft campaign.

2.2 Measurements of Trace Gases

2.2.1 Carbon monoxide

Carbon monoxide (CO) was measured with a modified (Figure 2.3, [*Dickerson and Delany*, 1988]) commercial non-dispersive infrared (NDIR) gas filter correlation (GFC) analyzer (Thermo Environmental Instruments, Model 48, Franklin, MA). This instrument utilizes the absorption by CO at its vibration-rotation band of 4.67 μm. Radiation from the IR source alternately passes through two gas filters before entering the sample cell of ~30 m effective optical path. The gas filter filled

with high concentration of CO produces the reference beam, and the other filter with CO-free nitrogen (N_2) produces the sample beam. The difference between the two beams is used to calculate CO concentration in the sample cell.

Interference from carbon dioxide (CO_2) and water vapor complicates CO measurements. The response of the detector also drifts as temperature changes, by as much as 200 ppb in 24 hr [*Dickerson and Delany*, 1988]. Beads of palladium/alumina (Pd/Al_2O_3) heated to about 250ºC are used as a catalyst to convert CO to CO_2, providing a chemical zero. A 3-way solenoid valve, manually activated or timer controlled, directs the sample flow to go through (zero mode) or bypass (sample mode) the CO zero, generating a dynamic baseline of the detector. During the field experiment, filters were placed ahead of trace gas instruments (except for the catalytic converter of the NO_y detector) to remove particles. On the aircraft, no particle filters were used.

During the ground experiment, the instrument was operated with a 60-minute cycle switching between 48 min of sample and 12 min of zero. CO concentration was logged with 1-minute resolution and processed into 10-min and hourly averages. When deployed onboard the Y-12 aircraft, the zero and sample modes were manually controlled, and data were recorded at 10-s resolution. The detector was calibrated with CO working standard gas (~1 ppm CO in nitrogen, Scott-Marrin Inc., Riverside, CA) traceable to a NIST (National Institute of Standards and Technology) standard reference material before and after the field campaign. Its calibration-determined detection limit is 40 ppb (signal-to-noise ratio S:N = 2:1 for $\pm 1\sigma$ noise), for 1-min means of 10-s data.

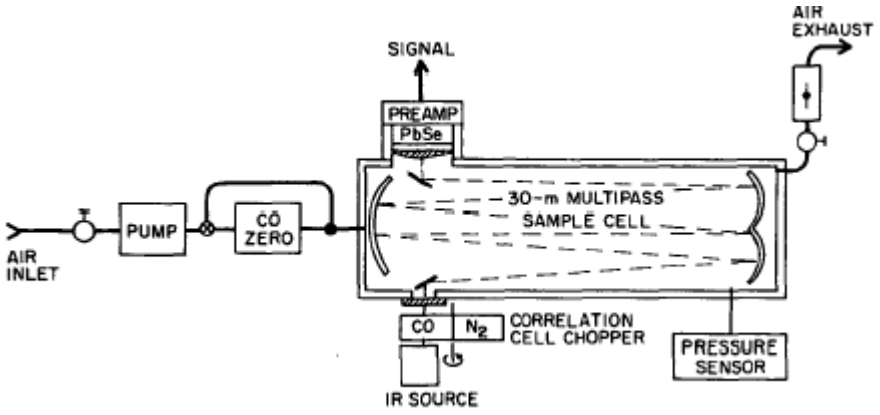

Figure 2.3. Schematic diagram of the modified CO analyzer (adapted from [*Dickerson and Delany*, 1988]).

2.2.2 Sulfur dioxide

A modified (Figure 2.4, [*Luke*, 1997]) commercial pulse-fluorescence detector (Thermo Environmental Instruments, Model 43, Franklin, MA) measured sulfur dioxide (SO_2). The instrument works on the principle that SO_2 molecules, electronically excited after absorption of UV radiation, can decay back to the ground state through fluorescence emission, quenching, or dissociation. Fluorescence emission dominates if SO_2 molecules are activated by UV radiation in the wavelength range of 190-230 nm. The ambient concentration of SO_2, over a wide range of temperature and atmospheric conditions, is proportional to the fluorescence intensity.

Aromatic hydrocarbons could interfere with SO_2 measurements as they respond to UV radiation in a similar manner. These compounds are removed as the sample air flows through a hydrocarbon "kicker" ahead of the fluorescence chamber. The sample flow intermittently passes through a potassium carbonate (K_2CO_3) filter,

which reacts with SO_2 and generates a dynamic zero to correct for the baseline drift of the instrument.

During the ground experiment, the SO_2 instrument worked on the same zero/sample cycle as the CO instrument, with data logged at 1-min resolution and averaged into 10-min and hourly means. In the aircraft campaign, the zero/sample modes of the SO_2 instrument were in synchronization with CO. SO_2 concentration was recorded with 10-s resolution. The instrument was calibrated with a NIST traceable standard material (~5 ppm SO_2 in air, Scott-Marrin Inc., Riverside, CA) before and after the field deployment, and has a detection limit of 80 ppt (parts per trillion, signal-to-noise ratio S:N = 2:1 for $\pm 1\sigma$ noise) for 1-min means of 10-s data.

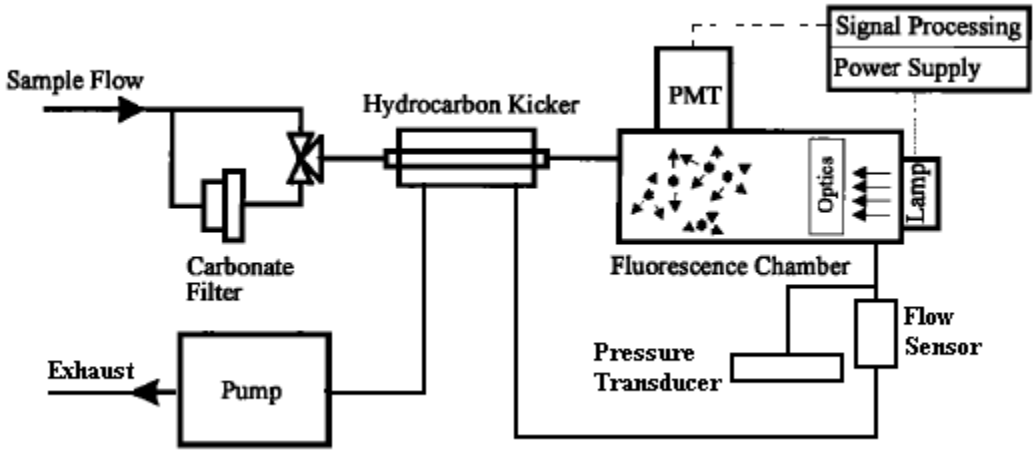

Figure 2.4. Schematic diagram of the modified SO_2 analyzer (adapted from [*Luke*, 1997]).

2.2.3 Ozone

Ozone (O_3) concentration was determined employing a commercial analyzer (Thermo Environmental Instruments, Model 49, Franklin, MA) based on the ozone

UV absorption at 254 nm. The sample flow is divided into two streams (Figure 2.5), one drawn through an ozone scrubber as the reference and the other directly into the optical cell as the sample. Regulated by the solenoid valves, the reference and sample streams alternately flow into optical cells A and B. The intensity difference between the two cells is used to calculate ozone concentration. O_3 data were stored at 1-min and 10-s resolutions during the ground and aircraft experiments, respectively. Calibration with an in-house primary standard (Thermo Environmental Instruments, Model 49 PS) before and after the field deployment shows the instrument has a detection limit of 4 ppb (signal-to-noise ratio S:N = 2:1 for $\pm 1\sigma$ noise) for 10-s data.

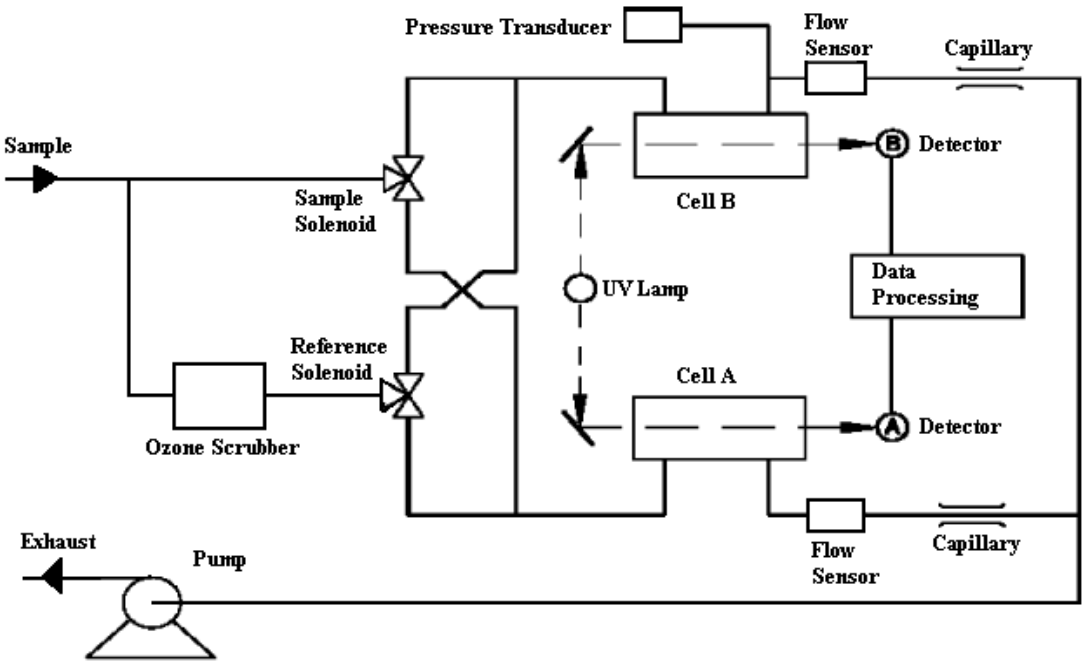

Figure 2.5. Schematic diagram of the TEI O_3 analyzer (adapted from [*Taubman*, 2004]).

2.2.4 Total reactive nitrogen oxides

A modified [*Fehsenfeld et al.*, 1987; *Stehr et al.*, 2000] commercial chemiluminescence detector (Thermo Environmental Instruments, Model 42, Franklin, MA) was employed to measure nitric oxide (NO) and total reactive nitrogen oxides (NO_y). The instrument measures NO based on the quick reaction between NO and O_3 (generated in the instrument). A fraction (~10%) of the NO_2 molecules produced in the reaction ($NO + O_3 \rightarrow NO_2 + O_2$) are excited, and release a characteristic luminescence in the wavelength range of 600-3000 nm, which is then detected by a photomultiplier. NO_y species other than NO (e.g., NO_2, PAN, and nitrate) are first reduced to NO by a molybdenum catalyst, and then measured with the same detector. A solenoid valve (Figure 2.6) controls the sample flow to alternately go through (NO_y mode, 18 min) and bypass (NO mode, 12 min) the converter. Very short tubing ahead of the converter minimizes the line losses of nitric acid and nitrate aerosols.

The instrument was calibrated with a working standard (~4.5 ppm n-propylnitrate in nitrogen, and NO in nitrogen; Scott-Marrin Inc., Riverside, CA) before the field experiment. In China the instrument was calibrated with Chinese NO standards and via gas-phase titration [e.g., *Dickerson et al.*, 1984]. The NO detection limit of the detector is 150 ppt (signal-to-noise ratio S:N = 2:1 for $\pm 1\sigma$ noise) for 1-min mean of 10-s data. The conversion efficiency for NO_2 exceeds 95% and is assumed unity for all NO_y compounds. This assumption probably leads to an underestimate of some nitrate aerosols that are more difficult to convert to NO [*Chen*, 2002]. The overall uncertainty of NO_y measurements using this technique is about

±30% [e.g., *Stehr et al.*, 2000]. NO and NO_y were only measured during the ground experiment, with 1-min resolution and averaged into 10-min and hourly data.

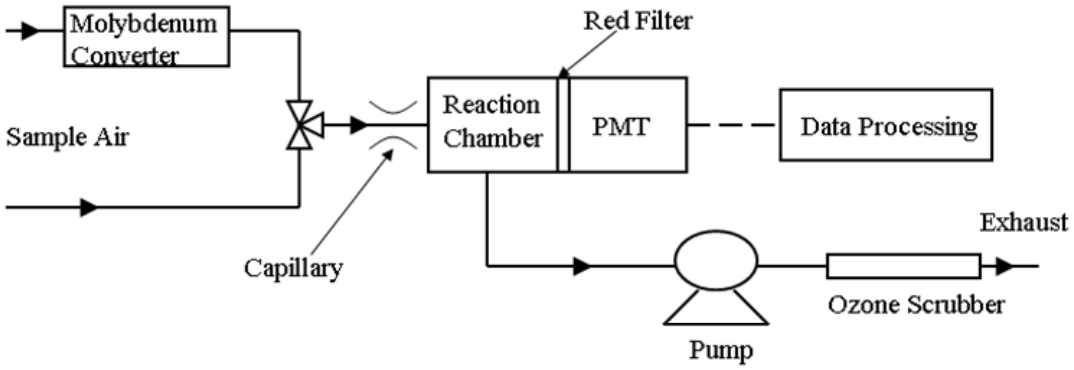

Figure 2.6. Schematic diagram of the modified NO/NO_y detector (adapted from [*Chen*, 2002]).

2.3 Aerosol Optical Properties

2.3.1 Aerosol scattering coefficients

An integrating nephelometer (TSI Model 3563, Shoreview, MN) was used for measurements of aerosol scattering coefficients (b_{sp}) at three wavelengths (450, 500, and 700 nm). A Lambertian light source (and an orthogonal light detector allow for a geometrical integration of the angular distribution of scattered light, from 7º to 170º in scattering angle. A bypass aerosol filter is periodically switched inline with the inlet to supply a particle-free sample, thereby allowing the instrument to account for the light scattered by gases and internal surfaces of the instrument, which is then subtracted from the total scattering. Straight conductive tubing less than 1 m in length conducted sample flow into the nephelometer. The instrument was calibrated with CO_2 and particle-free air before and after the field campaign. 5-min records were

saved during ground deployment and processed into 10-min and hourly averages. When operated on the aircraft, the instrument output was logged with 30-s resolution. For an averaging interval of 5 min, the detection limits of the instrument at 450, 550, and 700 nm are 0.44×10^{-6} m^{-1}, 0.17×10^{-6} m^{-1}, and 0.26×10^{-6} m^{-1}, respectively (signal-to-noise ratio S:N = 2:1, [*Anderson et al.*, 1996]). The major source of uncertainty, especially when the sampled particles are dominated by coarse-mode particles, is the non-ideal forward-scattering truncation of 0-7º [*Anderson et al.*, 1996]. Following *Anderson and Ogren* [1998], wavelength-dependent correction factors can be calculated using the Ångström exponent (α) to represent changes of b_{sp} with wavelength. A measure of the wavelength-dependence of particle scattering, α is defined as:

$$\alpha = -\frac{\log\left[b_{sp}(\lambda_1)/b_{sp}(\lambda_2)\right]}{\log(\lambda_1/\lambda_2)}. \qquad (2.2)$$

where $b_{sp}(\lambda_1)$ and $b_{sp}(\lambda_2)$ are the aerosol scattering coefficients at wavelengths λ_1 and λ_2, respectively. Aerosol scattering measurements with this instrument have an estimated uncertainty of ~10% [*Anderson et al.*, 1996]. The heat of the instrument reduces the RH below ambient level. The RH in the integrating volume was 17.5% ± 17.5% (±2σ) and never exceeded 42.5% during the ground experiment. The actual aerosol scattering in the atmosphere changes with environmental humidity and is often determined with the growth factor, an empirically derived relationship between b_{sp} and the environmental RH [*Charlson et al.*, 1992; *Jeong et al.*, 2006]. The growth factor depends on the aerosol composition and can be very different between different areas. For this study, no correction of the humidity effect was performed because there is little information available concerning the aerosol growth factors in this area.

The generally dry atmospheric conditions during the ground experiment kept the humidity effect to less than 20% most of the time (from a rough estimate).

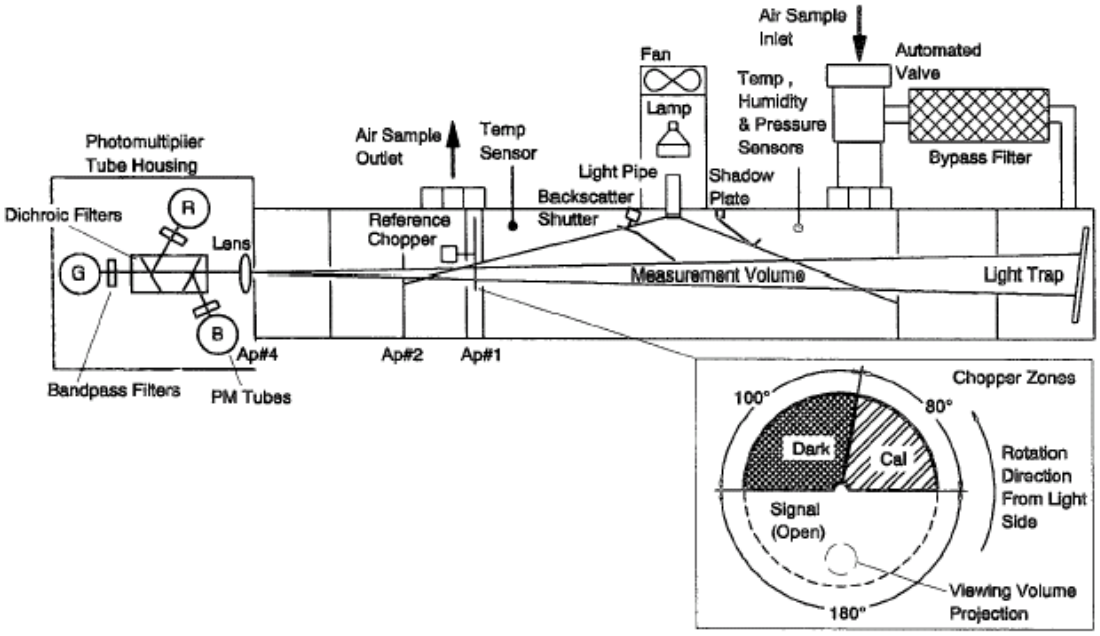

Figure 2.7. Schematic diagram of the TSI 3563 3-wavelength integrating nephelometer (adapted from [*Anderson et al*., 1996]).

2.3.2 Aerosol absorption coefficient

Aerosol absorption coefficient (b_{ap}) was determined with a Particle/Soot Absorption Photometer (PSAP, Radiance Research, Seattle, WA). This filter-based instrument collects aerosols to a filter, and continuously monitors the transmittance of the filter (Figure 2.8). The absorption coefficient, with units of m^{-1}, is calculated with the following equation:

$$b_{ap} = \frac{A}{V}\ln\left(\frac{I_0}{I}\right) \qquad (2.3)$$

where A is the area of the sample spot, V is the volume of sample air that passes through the filter during the averaging period (one minute in this study), I_0 and I are

transmittances of the filter during the previous and current averaging periods, respectively. The particle-free reference flow (Figure 2.8) helps detect the constancy of the LED light source. Nonlinearity in instrument response and magnification of absorption by the filter are corrected for with manufacturer's calibration [*Bond et al.*, 1999]. Routine calibration of PSAP is not applicable due to lack of standard material.

Under its typical configuration (1-min averaging period), the instrument has a detection limit of 1.8×10^{-6} m^{-1} (signal-to-noise ratio S:N = 2:1 for $\pm 1\sigma$ noise) [*Bond et al.*, 1999]. Due to high aerosol loadings in Xianghe, I decreased the sampling flow from ~2 L/min to ~0.2 L/min to improve the filter-change interval to a manageable level (every 2-3 hr on a polluted day). The actual flow rate was calibrated with an electronic bubble flow meter (DC-2, Bios International Corp., Butler, NJ). The influences of flow rate, spot size, and the interference from non-absorbing aerosols were corrected following the method of *Bond et al.* [1999], which is valid for filter transmittance above 0.7. In data processing, data with filter transmittance larger than 0.65 were kept to maintain the sample size, particularly in early morning hours. This introduces some uncertainties to the aerosol absorption data. The corrected aerosol absorption coefficient at 574 nm is then extrapolated to 550 nm [*Virkkula et al.*, 2005] for comparison with scattering measurements at the same wavelength. It is also assumed that the ambient RH has negligible effects on the absorption measurements, as RH was mostly relatively low during the experiment. The uncertainty of the absorption measurement is about 30% at a 95% confidence level.

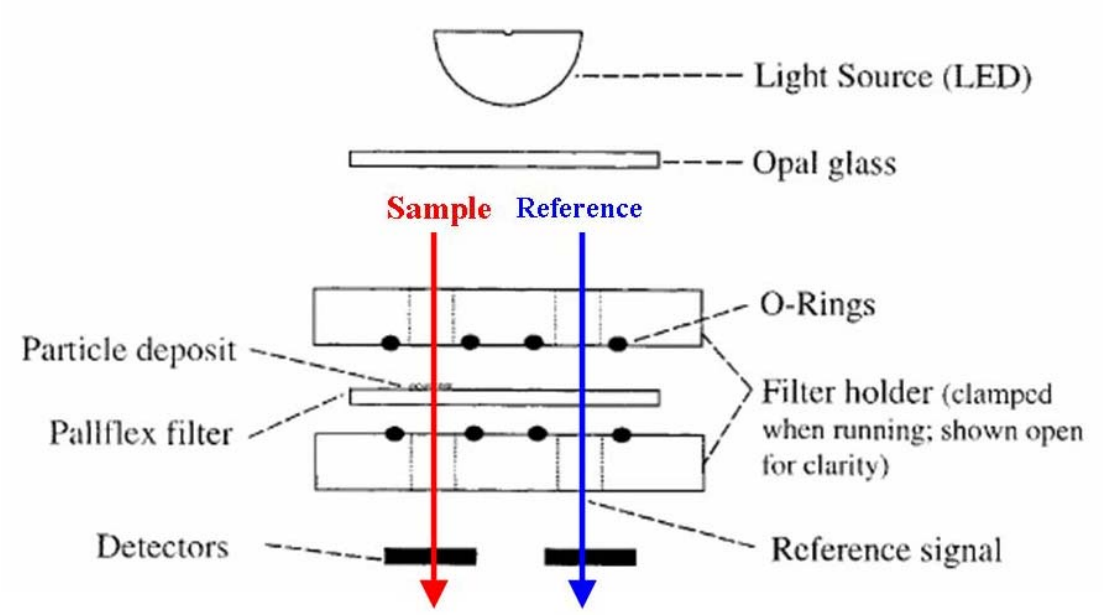

Figure 2.8. Schematic diagram of the PSAP (adapted from [*Bond et al.*, 1999]).

2.4 Aerosol Chemical Composition

2.4.1 Aerosol sampling

A University of Miami high-volume aerosol sampler (Figure 2.9, [*Prospero et al.*, 2003]) collects particles (total aerosols without size cut) on Whatman 41 quantitative filter paper (8 by 10 in, or 20.32 by 25.4 cm), at about 15 m above ground. A manometer measures the pressure drop as the sampling flow passes through an orifice plate. The recorded pressure drop is used to calculate the flow rate, which starts at about 800 L/min initially upon filter change and drops as the filter becomes loaded with particles. Depending on aerosol loading, the total volume of air sampled by each filter ranges from 400 to 500 m^3 during the 12-hr sampling period (08:00-20:00 local time for daytime samples and 20:00-08:00 for nighttime samples). From March 1 to April 13, 85 samples were collected along with blank samples taken

every 10 days. Both exposed and blank filters were stored in a freezer until chemical analysis.

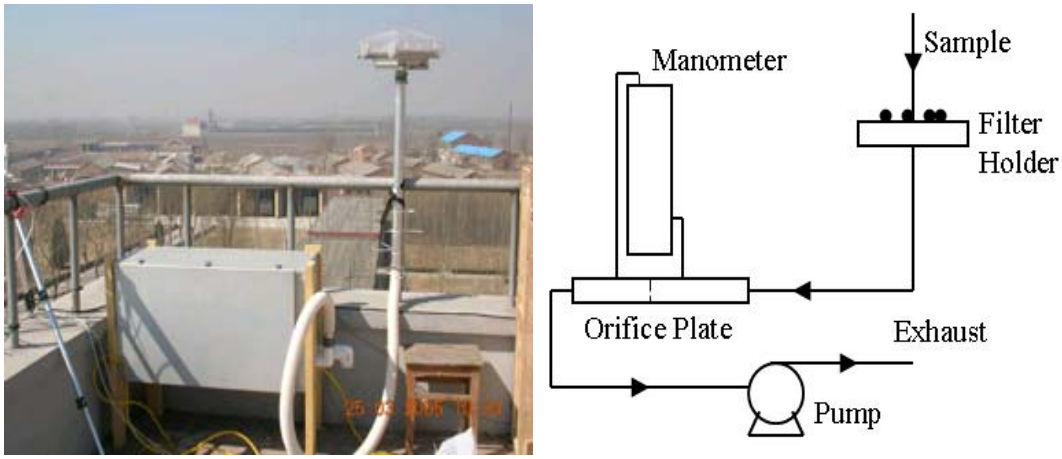

Figure 2.9. Left: setup of the bulk aerosol sampler during the Xianghe experiment; **Right**: schematic diagram of the bulk aerosol sampler.

2.4.2 Chemical analysis

The chemical analysis of the aerosol samplers was conducted by our colleagues at the Institute of Atmospheric Physics (IAP), Chinese Academy of Sciences (CAS), and is only briefly described here. For element analysis, one-fourth of the filters were first digested in concentrated HNO_3 (6 mL) and HCl (2 mL), using a microwave sample digestion system (PerkinElmer Life and Analytical Sciences, Inc., Model Multiwave 3000, Waltham, MA). An inductively coupled plasma mass spectrometer (ICP-MS, Agilent Technologies, Inc., Model 7500a, Santa Clara, CA) was used to analyze elements including Be, Na, Mg, Al, K, Ca, V, Mn, Fe, Ni, Cu, Zn, As, Mo, Ag, Cd, Ba, Tl, Pb, Th, and U.

One-fourth of each filter was ultrasonically extracted in 50 mL deionized water (resistivity: 18 MΩ/cm) for about 30 min. The filtrate, after passing through a microporous membrane (0.45 μm in pore size), was then analyzed with an ion

chromatograph (IC, Dionex Corporation, Model ICS-90, Sunnyvale, CA) for the concentrations of F^-, Cl^-, NO_3^-, SO_4^{2-}, NH_4^+, Ca^{2+}, Na^+, Mg^{2+}, and K^+. All ions have detection limits below 0.01 $\mu g/m^3$. Quality control and quality assurance procedures were routinely applied. More detailed descriptions are available in other studies employing the same analysis system [*Xu et al.*, 2007a, b].

Chapter 3: Xianghe Ground Experiment

3.1 Abundance of Pollutants: Statistics and Variations

Some results of this chapter, including the measurements of trace gases and aerosol optical properties, comparison to emission inventories, and estimate of black carbon emissions have been presented in the *Journal of Geophysical Research* special section on EAST-AIRE [*C. Li et al.*, 2007]. Aerosol chemical composition and the emissions from the local small coal-fired boiler were not included in that paper.

3.1.1 Concentrations of trace gases

One prominent feature of air pollution in Xianghe is the high pollutant levels for a non-urban site. Hereafter, results are presented as average ± one standard deviation (σ) unless otherwise noted. The hourly averaged SO_2 (17.8 ± 15.7 ppb, maximum: 96.5 ppb), CO (1.09 ± 1.02 ppm, maximum: 6.59 ppm), and NO_y (26.0 ± 24.0 ppb, maximum: 184 ppb) concentrations observed in Xianghe are much higher than at a rural site about 50-60 km east of the urban center of Baltimore, MD, USA (SO_2: 2.8 ± 3.2 ppb, CO: 0.219 ± 0.087 ppm, NO_y: 8.1 ± 6.3 ppb; [*Stehr et al.*, 2000]). The springtime ambient temperature (average: 4.4ºC) and solar flux (due to large solar zenith angle and heavy aerosol loading) in Xianghe were too low to be conducive to the photochemical production of O_3, and its concentration was only 29.1 ± 16.5 ppb, with an hourly maximum of 73.4 ppb.

For comparison, during the TRACE-P and ACE-Asia field campaigns in the spring of 2001, *T. Wang et al.* [2004] observed high levels of trace gases at a rural site in Yangtze Delta Region, about 1000 km SSE of Xianghe. Their reported CO (0.68 ppm), SO_2 (15.9 ppb), and NO_y (13.8 ppb) concentrations were lower than, but comparable to, this study. High pollutant levels observed at rural sites in different areas probably reflect the large extent of the air pollution issue in China, particularly in the more developed and populated East.

3.1.2 Aerosol optical properties and composition

Heavy aerosol loadings were observed at the Xianghe site. The average aerosol scattering (b_{sp}) and absorption coefficients (b_{ap}) at 550 nm are (358 ± 363) × 10^{-6} m^{-1}, and (65 ± 75) × 10^{-6} m^{-1}, respectively. Aerosol optical properties measured with the same type of instruments in Bondville, IL, USA, a continental site at similar latitude, by *Delene and Ogren* [2002] recorded aerosol scattering ((57.7 ± 17.7) × 10^{-6} m^{-1}) and absorption ((4.66 ± 2.27) × 10^{-6} m^{-1}) almost an order of magnitude smaller. Note that aerosol loadings in Bondville are lower in March than in other months [*Delene and Ogren*, 2002]. At a site NE of Beijing, farther away from the city than Xianghe, *Yan et al.* [2008] found lower but comparable aerosol scattering ((154 ± 160) × 10^{-6} m^{-1}) and absorption ((18.3 ± 14.0) × 10^{-6} m^{-1}) coefficients in spring. Table 3.1 summarizes the statistics of trace gases and aerosol optical properties observed during the ground experiment.

Table 3.1. Statistics of trace gases and aerosol optical properties in Xianghe

	Mean	Standard Deviation	Median	10^{th} Percentile	25^{th} Percentile	75^{th} Percentile	90^{th} Percentile
CO[a]	1.09	1.02	0.766	0.252	0.350	1.43	2.34
SO_2[b]	17.8	15.7	13.8	2.11	4.74	26.9	37.8
NO_y[b]	26.0	24.0	18.8	4.09	7.04	37.4	56.3
O_3[b]	29.2	16.5	30.3	5.55	13.7	41.9	49.1
Scattering[c]	358	363	323	45.0	87.0	507	814
Absorption[d]	65.4	74.9	38.7	11.3	16.5	84.9	115

[a] Unit: ppm;
[b] Unit: ppb;
[c] Unit: 10^{-6} m^{-1} or Mm^{-1}, wavelength: 550 nm;
[d] Unit: 10^{-6} m^{-1} or Mm^{-1}.

The statistics of water-soluble ions are given in Table 3.2, which shows fairly high concentrations of secondary aerosol species such as sulfate (SO_4^{2-}, 7.2 ± 6.2 μg/m^3), nitrate (NO_3^-, 9.5± 9.2 μg/m^3), and ammonium (NH_4^+, 5.4 ± 4.2 μg/m^3). Most interestingly, in contrast to a number of previous studies in northern China, our observed NO_3^- mass concentration ($[NO_3^-]$) is higher than that of SO_4^{2-} ($[SO_4^{2-}]$). I further discuss the $[NO_3^-]/[SO_4^{2-}]$ ratio in Chapter 5. For comparison, *Chen* [2002] found on average 3.3 μg/m^3 of SO_4^{2-}, 4.1 μg/m^3 of total nitrate (HNO_3 + all particulate NO_3^-) and 1.92 μg/m^3 of total ammonium (NH_3 + particulate NH_4^+) in April $PM_{2.5}$ samples collected at a traffic-influenced site in Fort Meade, Maryland.

Table 3.3 summarizes the statistics of element concentrations for aerosol samples from Xianghe. High loadings of crustal elements including Al (9.6 ± 5.3 μg/m^3), Mg (3.1 ± 1.6 μg/m^3), Ca (9.8 ± 4.7 μg/m^3), and Fe (6.5 ± 3.4 μg/m^3) indicate existence of soil particles in springtime aerosols in the region. Aerosol samples in New Castle, NH, a coastal site in the northeastern U.S. contain much lower Al (0.21 μg/m^3) and Fe (0.15 μg/m^3) [*Pike and Moran, 2001*]. Comparing the two sites also shows much greater concentrations of some pollutant tracer elements in Xianghe (e.g.,

Pb: 0.28 μg/m^3 vs. 0.005 μg/m^3; Cd: 4.5 ng/m^3 vs. 0.17 ng/m^3; Ag: 0.59 ng/m^3 vs. 0.031 ng/m^3; Cu: 75 ng/m^3 vs. 2.1 ng/m^3). For reference, the U.S. EPA NAAQS standard for lead is 0.15 μg/m^3 for a rolling 3 month average and 1.5 μg/m^3 for a quarterly average [*U.S. EPA*, 2006]. The ratio between the 90th percentile (the concentration below which 90% of the observations fall) and the 10th percentile of each element is calculated to estimate its variability. Crustal elements in general have ratios between 3 and 5, but the ratios of some pollutant tracer elements (e.g., Cu, Ag, As, and Pb) exceed 10, showing large variation in their loadings. Water soluble ions such as sulfate, nitrate, and ammonium, aerosol scattering and absorption, as well as traces gases including CO, SO_2 and NO_y are also found to be very variable. Aerosol optical thickness (AOT) at the same site fluctuated over a wide range of 0.2-4 during the experiment [*Z. Li et al*, 2007a]. In sections 3.1.3 and 3.1.4, I discuss in more details the variations of pollutant levels observed in Xianghe.

Table 3.2. Statistics of water-soluble inorganic ions in aerosol samples from Xianghe (μg/m^3)[a]

Element	Mean	Standard Deviation	Median	10th Percentile	25th Percentile	75th Percentile	90th Percentile
F^-	1.5×10^{-1}	1.2×10^{-1}	1.1×10^{-1}	1.2×10^{-2}	3.1×10^{-2}	2.2×10^{-1}	3.4×10^{-1}
Cl^-	3.4	2.6	3.2	7.0×10^{-1}	1.1	4.6	6.4
NO_3^-	9.5	9.2	6.4	9.6×10^{-1}	2.1	13.0	21.1
SO_4^{2-}	7.2	6.2	5.2	1.7	2.7	8.9	14.3
Na^+	6.5×10^{-1}	3.8×10^{-1}	6.2×10^{-1}	2.2×10^{-1}	4.0×10^{-1}	8.6×10^{-1}	1.1
NH_4^+	5.4	4.2	4.4	1.2	1.8	7.4	11.5
K^+	1.4	1.0	1.1	3.4×10^{-1}	6.0×10^{-1}	2.1	3.1
Ca^{2+}	3.4	1.6	3.1	1.2	2.1	4.6	5.3
Mg^{2+}	3.0×10^{-1}	1.5×10^{-1}	2.8×10^{-1}	1.2×10^{-1}	1.8×10^{-1}	4.0×10^{-1}	4.8×10^{-1}

[a] Part of the Na, Ca, K, and Mg exist in minerals that are not very water-soluble, the concentrations of the ions are thus generally lower than the corresponding elements (Table 3.3). Uncertainties in both analysis methods may also contribute to the differences between water-soluble ions and elements.

Table 3.3. Statistics of elements in aerosol samples from Xianghe (μg/m^3)

Element	Mean	Standard Deviation	Median	10th Percentile	25th Percentile	75th Percentile	90th Percentile
Be	3.9×10^{-4}	1.7×10^{-4}	3.6×10^{-4}	1.9×10^{-4}	2.6×10^{-4}	4.8×10^{-4}	6.4×10^{-4}
Na	1.2	5.7×10^{-1}	1.1	4.6×10^{-1}	0.8	1.6	2.0
Mg	3.1	1.6	2.7	1.1	2.2	4.0	5.0
Al	9.6	5.3	8.4	3.5	5.8	11.9	15.5
K	3.6	2.0	3.2	1.2	2.0	5.2	6.8
Ca	9.8	4.7	9.5	3.5	6.3	13.6	16.2
V	1.2×10^{-2}	6.5×10^{-3}	1.1×10^{-2}	3.7×10^{-3}	6.5×10^{-3}	1.5×10^{-2}	2.0×10^{-2}
Mn	1.7×10^{-1}	8.3×10^{-2}	1.6×10^{-1}	6.9×10^{-2}	1.0×10^{-1}	2.2×10^{-1}	2.8×10^{-1}
Fe	6.5	3.4	5.8	2.3	4.1	8.9	11.4
Ni	1.2×10^{-2}	3.6×10^{-2}	7.3×10^{-3}	3.3×10^{-3}	4.6×10^{-3}	1.1×10^{-2}	1.6×10^{-2}
Cu	7.5×10^{-2}	1.6×10^{-1}	2.6×10^{-2}	6.9×10^{-3}	1.3×10^{-2}	7.7×10^{-2}	1.7×10^{-1}
Zn	4.4×10^{-1}	3.6×10^{-1}	3.9×10^{-1}	4.9×10^{-2}	8.6×10^{-2}	6.3×10^{-1}	9.0×10^{-1}
As	1.8×10^{-2}	1.4×10^{-2}	1.4×10^{-2}	3.1×10^{-3}	5.7×10^{-3}	2.6×10^{-2}	3.6×10^{-2}
Mo	2.8×10^{-3}	2.3×10^{-3}	2.5×10^{-3}	4.8×10^{-4}	9.2×10^{-4}	4.1×10^{-3}	5.6×10^{-3}
Ag	5.9×10^{-4}	4.8×10^{-4}	5.6×10^{-4}	6.6×10^{-5}	1.6×10^{-4}	8.5×10^{-4}	1.2×10^{-3}
Cd	4.5×10^{-3}	3.7×10^{-3}	3.8×10^{-3}	4.4×10^{-4}	8.1×10^{-4}	6.6×10^{-3}	9.6×10^{-3}
Ba	9.2×10^{-2}	5.3×10^{-2}	7.9×10^{-2}	3.8×10^{-2}	5.8×10^{-2}	1.1×10^{-1}	1.8×10^{-1}
Tl	2.2×10^{-3}	2.1×10^{-3}	1.6×10^{-3}	3.5×10^{-4}	5.9×10^{-4}	3.3×10^{-3}	4.6×10^{-3}
Pb	2.8×10^{-1}	2.4×10^{-1}	2.3×10^{-1}	2.9×10^{-2}	5.4×10^{-2}	4.5×10^{-1}	6.6×10^{-1}
Th	1.4×10^{-3}	7.6×10^{-4}	1.3×10^{-3}	5.4×10^{-4}	9.0×10^{-4}	1.8×10^{-3}	2.4×10^{-3}
U	4.5×10^{-4}	2.2×10^{-4}	4.2×10^{-4}	1.9×10^{-4}	2.9×10^{-4}	6.0×10^{-4}	7.7×10^{-4}

3.1.3 Diurnal variation of pollutants

Diurnal cycles of CO, NO_y, SO_2, and O_3, aerosol scattering (550 nm) and absorption are given in Figure 3.1. The error bars are 10th (lower bars) and 90th (upper bars) percentiles of the data. With the exception of O_3, all parameters show minima at around 3 pm local standard time (LST) and accumulate until reaching maxima during the rush hour (7-9 am LST) on the following day. Aerosol absorption from 11 pm to 6 am LST may be underestimated due to filter saturation (fewer measurements on more polluted days as filters saturate quickly and cannot be replaced in time). Both meteorological conditions and emissions contribute to these diurnal cycles. A nocturnal inversion forms near ground on cold nights, trapping locally emitted pollutants near ground until around 8 am LST the next morning, when sunlight heats

the surface and breaks up the inversion (cf. meteorological records available at: http://www.atmos.umd.edu/~zli/EAST-AIRE/station.htm). Emissions may be strong during the morning rush hour, when rural households set up stove fires for cooking and heating [*X. Wang et al.*, 2005], and local factories start running. As the temperature increases during the day, stronger surface winds and active convection dilute pollutants near the surface. Needs for heating reduce, too.

The error bars in Figure 3.1 demonstrate that CO, NO_y, SO_2, and aerosol scattering are more variable in the morning and evening than at mid-day. The sample size for each hour of the day is similar (e.g., 120 and 122 10-min averages during 7-8 am and 3-4 pm LST for CO, respectively); and the diurnal change in error bars probably reflects the emission sources detected by the instruments. Local emission sources are diverse, as noticed by the author of this dissertation, who identified coal-fired boilers, two-stroke, four-stroke and diesel vehicles, biofuel, liquefied propane, and agricultural burning near the site. In stagnant morning and evening hours, various nearby sources may dominate the pollutants captured by the instruments. Stronger mixing and winds during daytime transport mixed plumes from a larger region to the site, reducing variability. The variability of aerosol absorption cannot be properly determined between 11 pm and 6 am because of the filter saturation issue mentioned above.

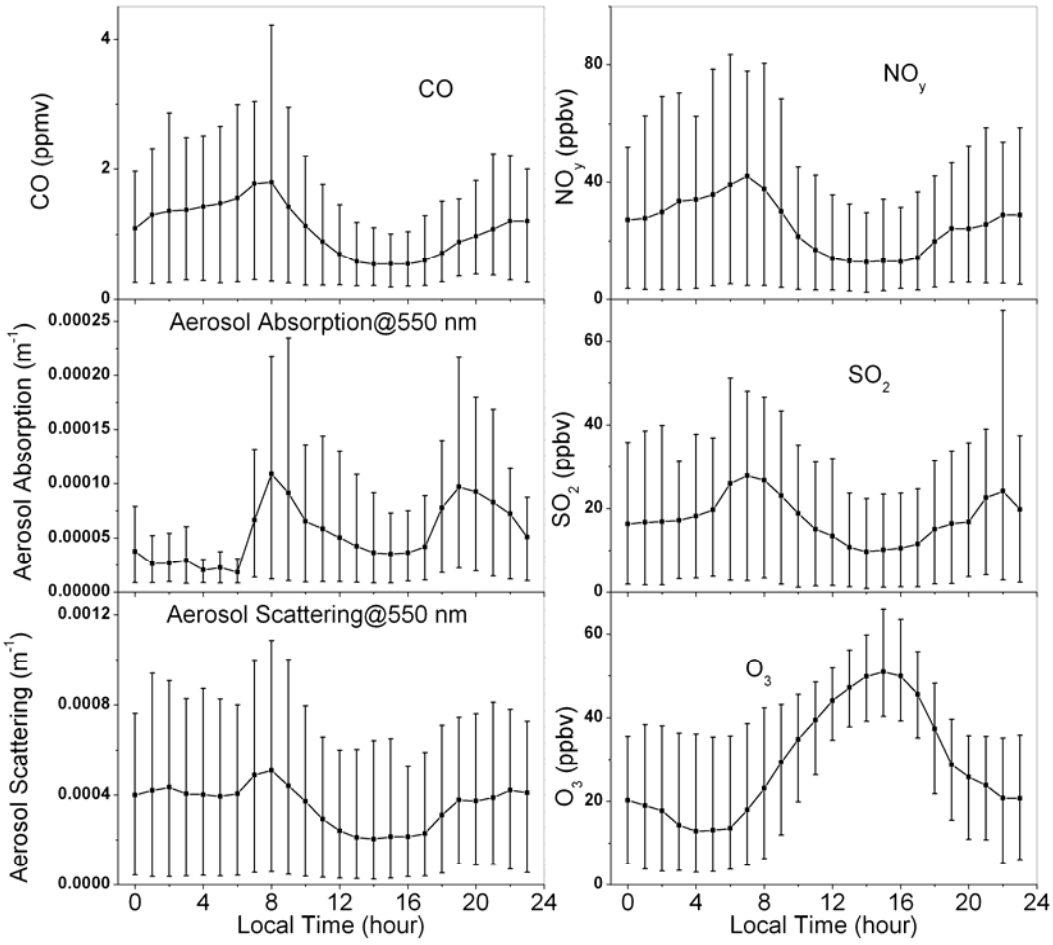

Figure 3.1. Diurnal cycles of CO, NO_y, aerosol absorption, SO_2, aerosol scattering (550 nm), and O_3 at the Xianghe site. Lines show the median; error bars are 10^{th} (lower bars) and 90^{th} (upper bars) percentiles of the data. Note that the value and variability of the aerosol absorption during 11 pm-6 am LST cannot be properly determined due to saturation of the filter in the instrument.

Table 3.4 compares some elements and water-soluble ions in the daytime and nighttime samples. Secondary aerosol species such as sulfate (SO_4^{2-}) and nitrate (NO_3^-) are slightly more abundant in nighttime samples. The shallow nocturnal boundary layer may accumulate pollutants near ground at night, but photochemical production of these components is stronger in daylight. Pollution-related elements (Cu, As, Ag, Cd, and Pb, cf. section 3.3 for their enrichment factors) are all higher at

night as well. Crustal elements including Mg, Al, K, Fe, and Ca, on the other hand, are less consistent, with slightly more K and Fe at night but more Mg and Al in daytime. Note that the so-called "daytime" samples were mostly collected from 8 am to 8 pm LST, thus incorporating the valley as well as part of the peak in the diurnal cycles of aerosols as shown in Figure 3.1.

Table 3.4. Concentrations of some elements and water-soluble ions in daytime and nighttime samples (average ± standard deviation, μg/m^3)

	Daytime	Nighttime
Cl^-	2.7 ± 2.0	4.1 ± 3.0
NO_3^-	8.6 ± 9.2	10.4 ± 9.2
SO_4^{2-}	6.9 ± 7.1	7.4 ± 5.4
Na^+	$(5.6 \pm 3.1) \times 10^{-1}$	$(7.4 \pm 4.3) \times 10^{-1}$
NH_4^+	4.8 ± 4.5	5.9 ± 4.0
K^+	1.3 ± 1.0	1.5 ± 1.0
Ca^{2+}	3.4 ± 1.6	3.3 ± 1.6
Mg	3.1 ± 1.6	3.0 ± 1.6
Al	10.0 ± 5.8	9.2 ± 4.8
K	3.4 ± 2.0	3.8 ± 2.1
Ca	9.8 ± 4.6	9.8 ± 4.9
Fe	6.3 ± 3.3	6.7 ± 3.4
Cu	$(6.1 \pm 10.9) \times 10^{-2}$	$(8.8 \pm 19.2) \times 10^{-2}$
As	$(1.5 \pm 1.5) \times 10^{-2}$	$(2.0 \pm 1.4) \times 10^{-2}$
Ag	$(5.2 \pm 4.4) \times 10^{-4}$	$(6.7 \pm 5.2) \times 10^{-4}$
Cd	$(4.0 \pm 3.8) \times 10^{-3}$	$(5.0 \pm 3.6) \times 10^{-3}$
Pb	$(2.3 \pm 2.2) \times 10^{-1}$	$(3.3 \pm 2.4) \times 10^{-1}$

3.1.4 Synoptic variation of pollutants

Hourly averaged aerosol absorption coefficient and scattering coefficients at 450, 550, and 700 nm are shown in Figure 3.2, along with locally-recorded temperature, relative humidity, surface pressure, wind direction, and wind speed. Hourly mean trace gas (CO, SO_2, NO_y, and O_3) concentrations are given in Figure 3.3, as is the AOT measured with the co-located sun photometer [*Z. Li et al*, 2007a]. The

gaps in both plots are due to a power failure (on March 7, day of year (DOY) 66), routine maintenance of instruments, and instrument malfunctions. PSAP filter saturation due to heavy aerosol loadings causes most of the gaps in PSAP data in early morning hours (11 pm -6 am LST).

Fast transitions between highly polluted and relatively clean episodes are seen in both figures. Surface weather analysis (Korean Meteorological Administration: available at http://abc-gosan.snu.ac.kr/sfc.html) identifies five cold-front passages on March 5-6 (DOY 64-65), March 10-11 (DOY 69-70), March 16-17 (DOY 75-76), March 19-20 (DOY 78-79), and March 21-22 (DOY 80-81). These frontal passages led to an abrupt change in wind direction (from generally south to generally north), an increase in atmospheric pressure, and a decrease of temperature and relative humidity.

Shaded areas roughly representing the analyzed cold front passages in Figures 3.2 and 3.3, by no coincidence, also mark dramatic changes in air quality. Pollutants accumulate before cold front passages and quickly disperse afterward, as prefrontal continental tropical (cT) air mass is replaced by postfrontal continental polar (cP) air mass. The high wind speed behind cold fronts facilitates ventilation and vertical mixing, reducing surface pollution. Descending air from less populated northern regions (Mongolia and Siberia) also brings in relatively clean air. Postfrontal morning ozone, on the other hand, is higher than under average conditions (~40 ppb vs. few ppb), while CO (a few hundred ppb), SO_2 (a few ppb) and NO_y (a few ppb) are lower. The high wind speeds behind cold fronts dilute primary pollutants and increase the thickness of the nocturnal PBL, resulting in reduced titration of O_3 by local pollutants.

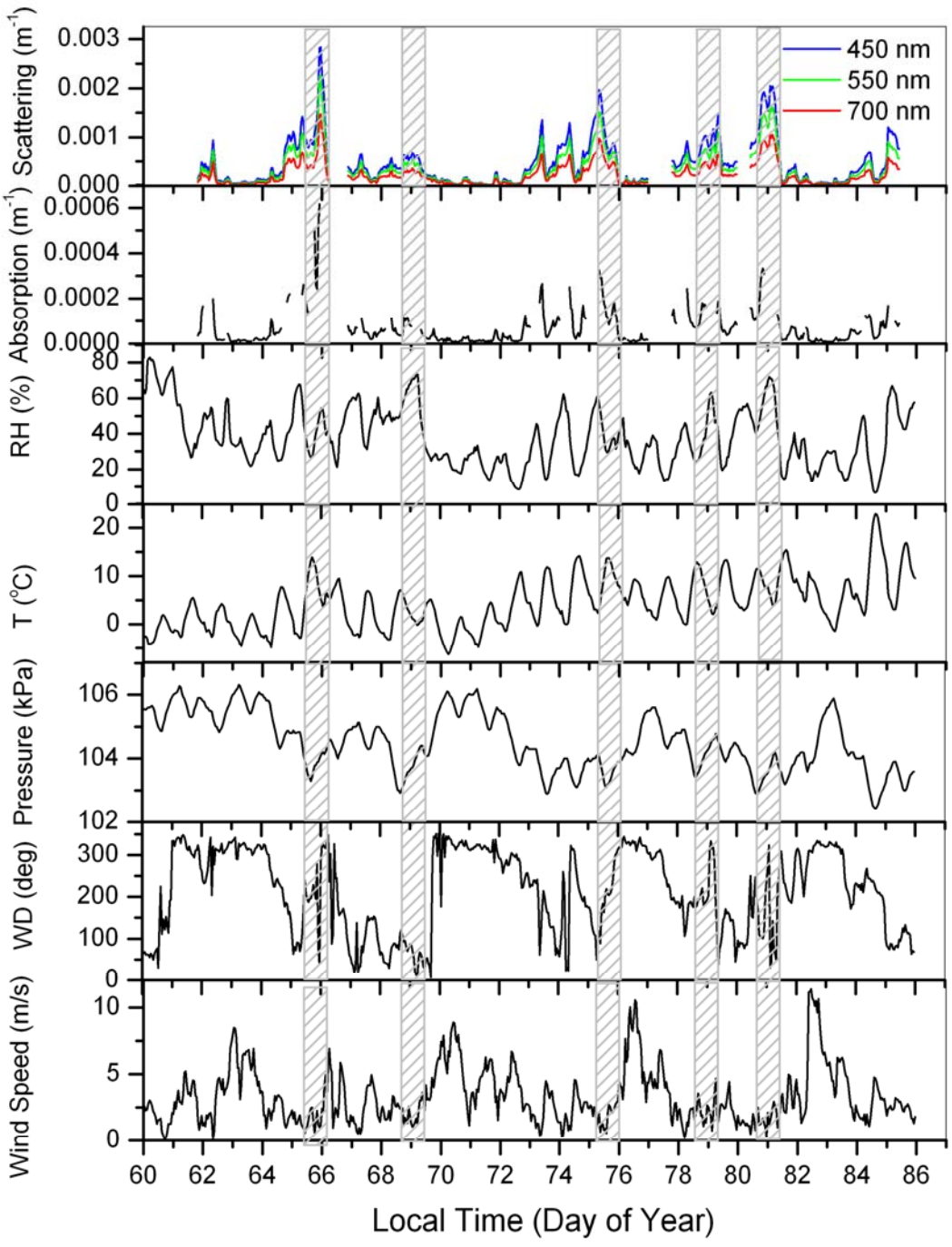

Figure 3.2. Hourly averaged aerosol scattering (450, 550, and 700 nm), aerosol absorption (550 nm), relative humidity (RH, %), temperature (T, °C), surface pressure (kPa), wind direction (WD, degree), and wind speed (m/s) observed at the Xianghe site. Time periods with analyzed cold front passages are indicated approximately with hatched areas.

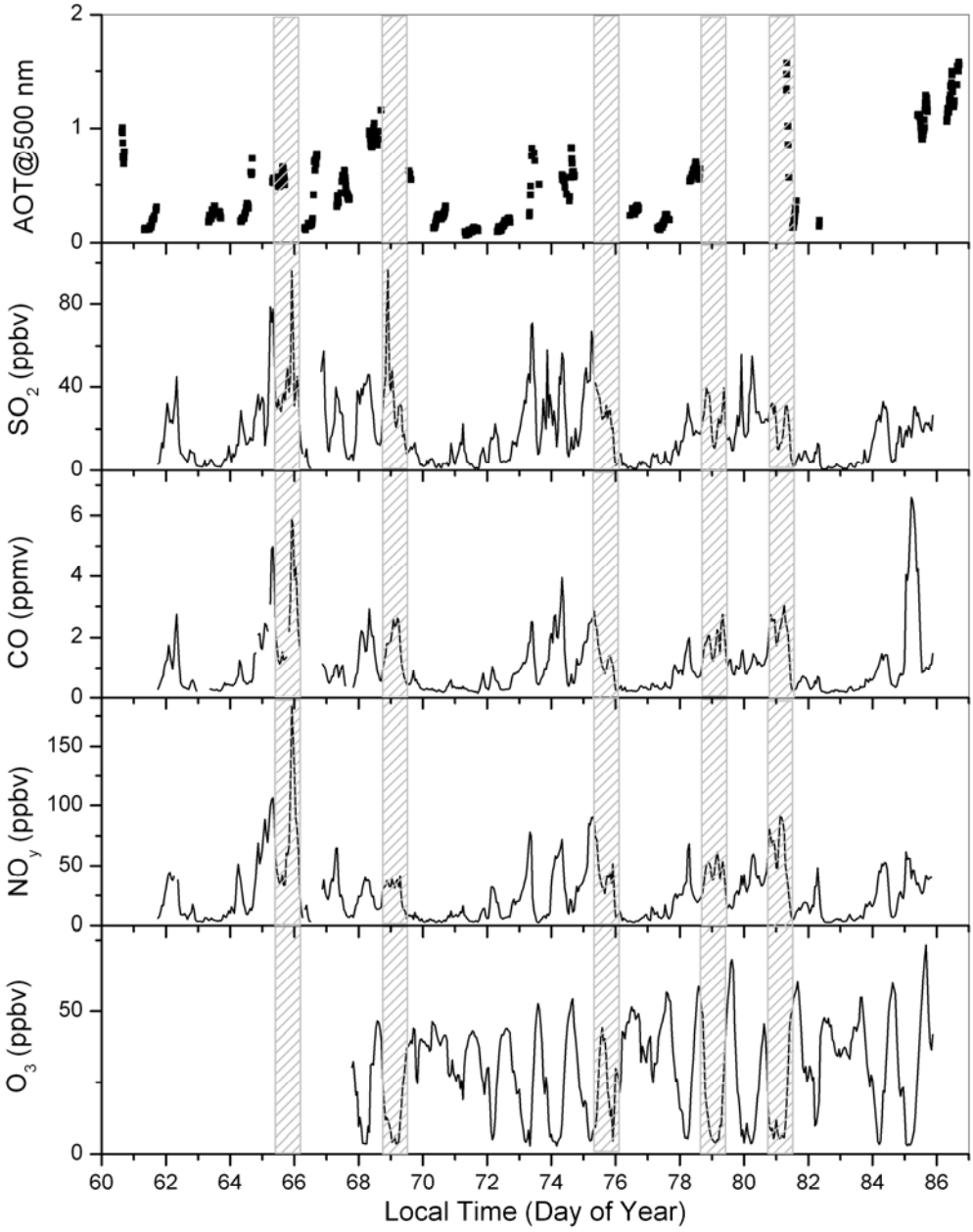

Figure 3.3. Hourly averaged concentrations of SO_2, CO, NO_y, and O_3 observed at the Xianghe site. Time periods with analyzed cold front passages are indicated approximately with hatched areas. The top panel shows the aerosol optical thickness (at 500 nm) determined with the co-located Cimel sun photometer.

Figures 3.4 and 3.5 present the time series of some water soluble ions (SO_4^{2-}, NO_3^-, NH_4^+, Cl^-, and K^+) and pollutant tracer elements (Cu, Zn, As, Cd, and Pb). CO

is shown in the two figures as a reference. The good correlation between these aerosol compounds and CO (R^2: CO and NH_4^+, 0.43; CO and Cl^-, 0.66; CO and SO_4^{2-}, 0.47; CO and NO_3^-, 0.48; CO and K^+, 0.32; CO and Cu, 0.35; CO and As, 0.52; CO and Zn, 0.50; CO and Cd, 0.33; CO and Pb, 0.50) suggests that they are likely mainly related to anthropogenic sources, and largely controlled by synoptic conditions. The exceptionally large peaks in Cl^- and Cu on DOY 100-101 remain unaccounted for, but are probably from certain special aerosol sources. The synoptic variation in the relative ratio between sulfate and nitrate is another interesting feature and will be discussed in Chapter 5.

Given in Figure 3.6 are time series of some crustal elements as well as CO and wind speed. Red shaded areas in the plot mark periods of high wind speed or relatively low CO level (DOY 66). With a few exceptions, an outbreak of strong surface winds is usually accompanied by a peak in Al and a drop in CO, as strong winds mobilize dust, either locally or from upwind desert regions (average wind speed for Al above 75th percentile: 3.5 m/s, for Al below 25th percentile: 3.2 m/s, for 5 highest Al concentration: 5.6 m/s). Note that the high Al peak sometimes lasts only 1-2 aerosol samples or 12-24 hr, shorter than the entire period during which CO is maintained low by high wind speed. High dust levels are sometimes but not always observed under windy postfrontal conditions. Mg has a variation similar to Al (correlation coefficient $R^2 = 0.77$). Strong winds sometimes also boost the loadings of Ca, Fe, and K, but overall these elements are more abundant under calm and polluted conditions (weak winds and high CO, average wind speed for Ca above 75th percentile: 2.9 m/s, for Ca below 25th percentile: 3.1 m/s; for K above 75th percentile:

2.8 m/s, for K below 25th percentile: 3.4 m/s; for Fe above 75th percentile: 2.8 m/s, for Fe below 25th percentile: 3.7 m/s), likely due to substantial local sources related to anthropogenic activities. A fraction of K is probably from biomass burning, as evidenced by the correlation between CO and water-soluble K^+. Construction sites could release calcium-containing particles to the atmosphere [*Wang, Zhuang et al.*, 2005]. Local sources of crustal elements in airborne particles also include traffic, agriculture, and some other activities. Figure 3.6 appears to suggest that Al would serve as a better tracer for dust transported into the region than other crustal elements.

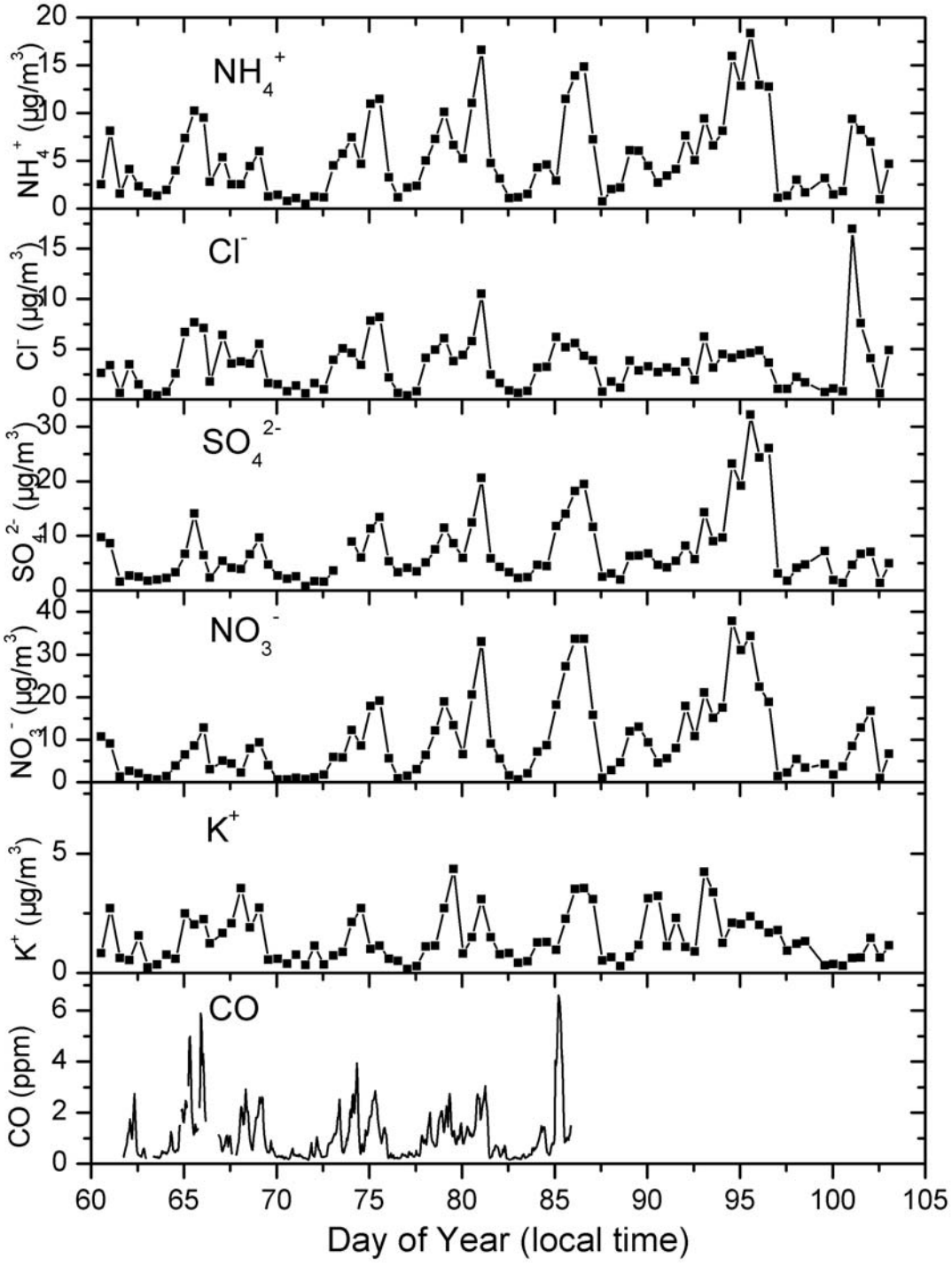

Figure 3.4. Time series of some water-soluble ions (NH_4^+, Cl^-, SO_4^{2-}, NO_3^-, and K^+) in aerosol samples from Xianghe.

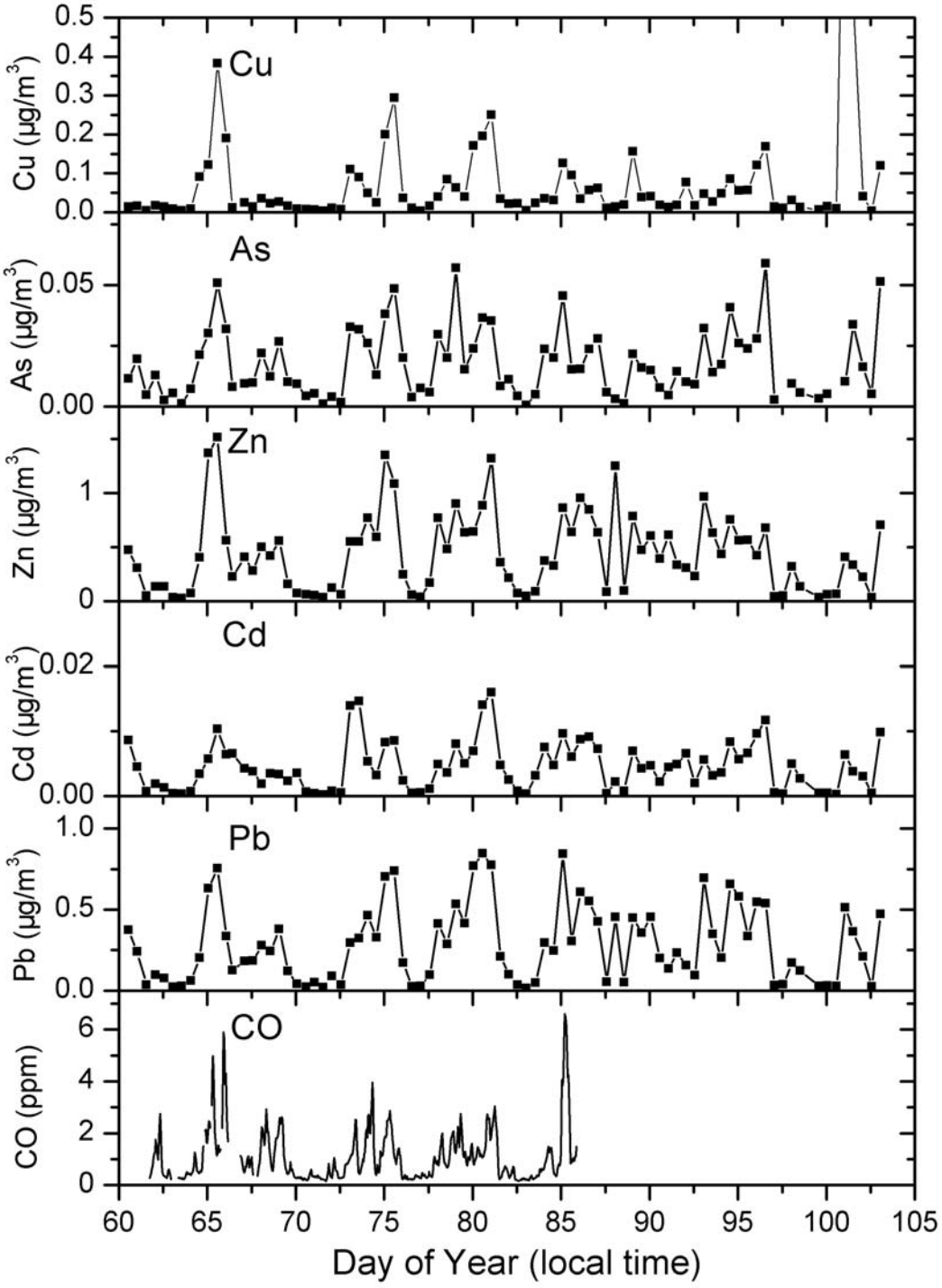

Figure 3.5. Time series of some pollutant tracer metal elements (Cu, As, Zn, Cd, and Pb) in aerosol samples from Xianghe. Cu concentration for the samples from DOY 101-101.5 is 1.26 and 0.55 μg/m^3, respectively.

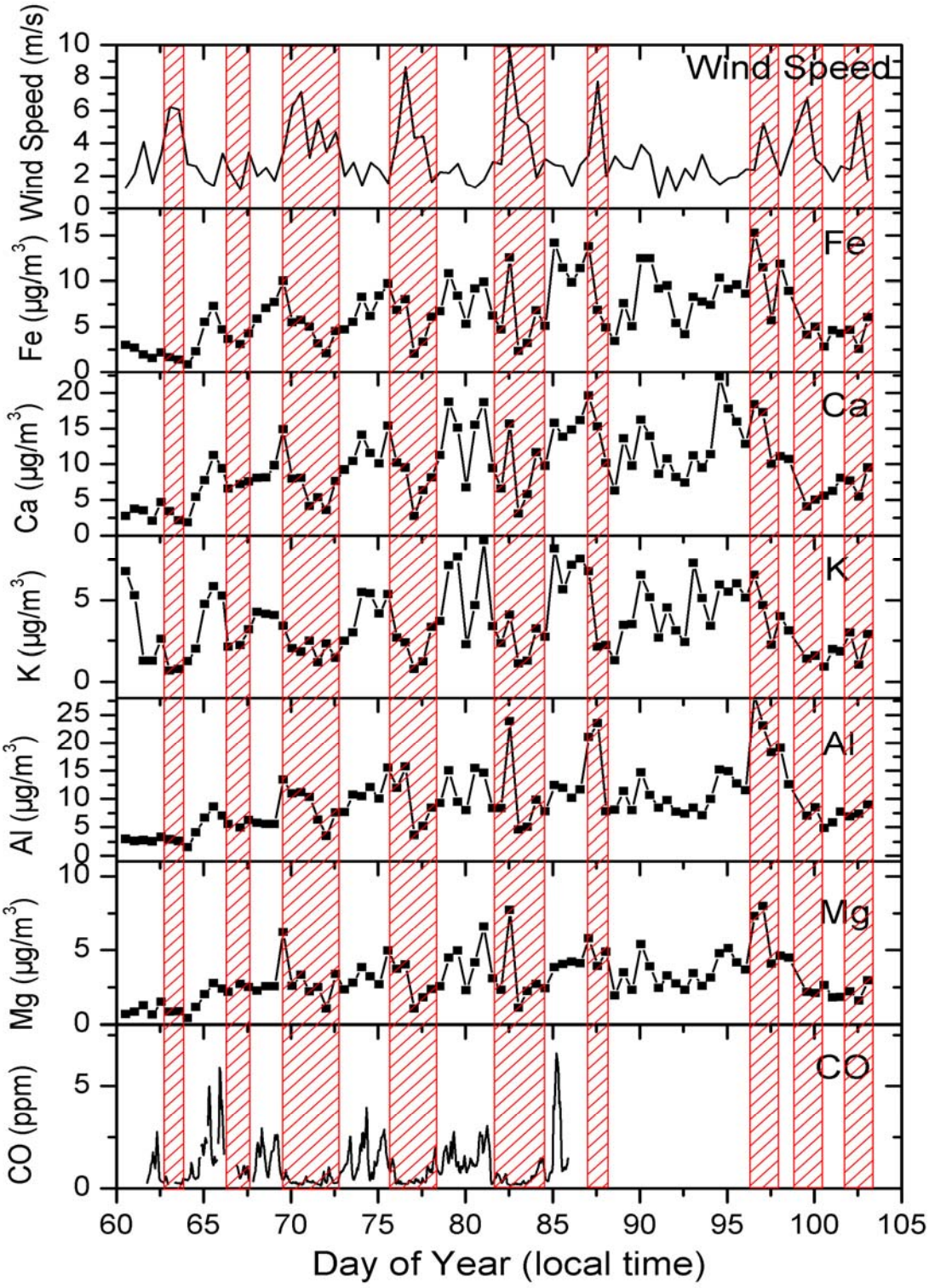

Figure 3.6. Time series of some crustal elements (Fe, Ca, K, Al, and Mg) in aerosol samples from Xianghe. 10-m wind speed averaged to sampling time is shown in the top panel. Shaded areas indicate outbreaks of strong winds or drop in CO concentration (DOY 67).

3.2 Pollutant Ratios and Implications for Regional Emissions

3.2.1 Pollutant ratios from correlation analysis

Different types of emissions sources often have distinct emission profiles. For instance, a boiler used in electricity generation has a high flame temperature and excess air supply, emitting a lot of NO_x but little CO. On the other hand, a coal-burning stove for household heating usually has a lower flame temperature and limited ventilation, releasing substantial CO but less NO_x. Simultaneous measurements of NO_x and CO can help characterize the emission sources. Once emitted into atmosphere, NO reacts rather quickly, and in this study the ratio between CO and NO_y is used.

The ratios of CO/NO_y, CO/SO_2, b_{sp}/SO_2, and b_{sp}/b_{ap} during the morning rush hour (7-9 am LST) and mid-day (2-4 pm LST) are obtained via correlation analysis of simultaneous measurements (10-min means). As shown in Figure 3.7, the correlation coefficients (R^2) for CO/NO_y, CO/SO_2, b_{sp}/SO_2, and b_{sp}/b_{ap} are higher in the afternoon than in the morning. This supports the argument that the afternoon data draw information from better-mixed and more "regional" plumes, while the early morning data contain information from less-mixed and more "local" plumes. Table 3.5 summarizes the results of the correlation analysis.

Table 3.5. Results of the pollutant concentration correlation analysis[a].

	CO/NO_y		CO/SO_2		b_{sp}/SO_2[b]		b_{sp}/b_{ap}	
	AM	PM	AM	PM	AM	PM	AM	PM
slope	35.4	27.2	50.0	35.8	1.4×10^{-5}	2.3×10^{-5}	4.4	5.8
y-intercept	304.0	180.7	330.4	181.6	9.0×10^{-5}	-1.6×10^{-5}	5.1×10^{-6}	-1.7×10^{-5}
R^2	0.44	0.79	0.47	0.83	0.54	0.88	0.85	0.92

[a]About 100 data points (10-min means) for each correlation analysis; [b]Unit: m^{-1}/ppb.

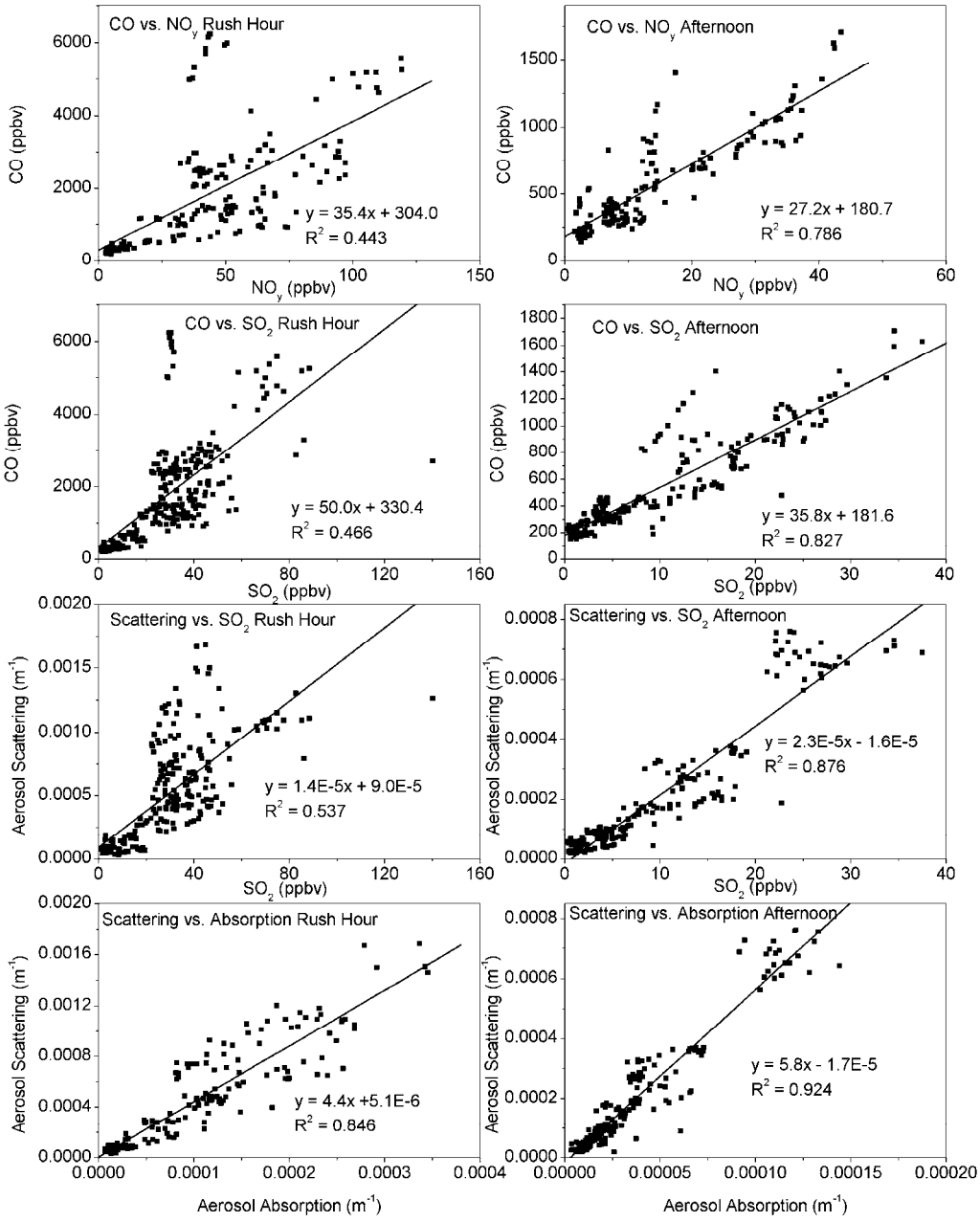

Figure 3.7. Correlations of CO and NO_y, CO and SO_2, aerosol scattering (550 nm) and SO_2, aerosol scattering (550 nm) and aerosol absorption (550 nm) in the morning rush hour (7-9 am LST, left panels) and in the mid-afternoon (2-4 pm LST, right panels) at the Xianghe site. All data points are 10-min averages. The equations shown in the plots are the best-fit lines through the data.

The CO/NO_y ratio is 35.4 in the morning and 27.2 in the afternoon. Industrialized regions in China have more of high-efficiency combustion sources

releasing little CO but much NO_y (e.g., large point sources), whereas rural areas have more of low-efficiency sources emitting CO but little NO_y (e.g., residential stoves). The CO/NO_y ratio in the more "regional" afternoon data is thus smaller. Small-scale boilers (~1 MW) operate during daytime in local factories, with a high flame temperature and excess air supply to optimize burning efficiency [*D. Zhou*, personal communication], may also emit flue gas with a relatively low CO/NO_y ratio. Later in this chapter (section 3.4), I determine the emission factors for the small coal-fired boiler that heats the site.

CO and SO_2 have some emission sources in common. Coal is the dominant energy source in China and is widely used in the north for household heating and cooking. *He and Chen* [2002] reported that the average sulfur content of coal in China is 1.1-1.2% by weight, but can be as high as 3%. Low-efficiency stoves burning sulfur-containing coal emit both SO_2 and CO in substantial amounts. Most thermal power plants in China run on coal, and are likely important sources of SO_2 but not CO. The CO/SO_2 ratio in more "regional" data (35.8) is lower than that in more "local" morning data (50.0), reflecting the difference in source composition.

Compared to previous studies, the y-intercepts of the afternoon CO/NO_y and CO/SO_2 scatter plots are about 180 ppb, close to the mid-latitude continental background [*Novelli et al.*, 1998]. The slopes (CO/NO_y and CO/SO_2 ratios) of the afternoon scatter plots are similar to those observed in rural eastern China (CO/NO_y: 35 vs. 37; CO/SO_2: 36 vs. 29, the latter values are from *T. Wang et al.,* [2002; 2004]). During the TRACE-P campaign in spring 2001, downwind aircraft measurements found a similar CO/SO_x (SO_2 + sulfate) ratio (~27) but much higher CO/NO_y ratio

(~55) in plumes from the Beijing area (altitude < 2 km, air mass age < 1 day) [*Carmichael et al.*, 2003].

Aerosol scattering is fairly well-correlated with SO_2. As shown in section 3.1 and earlier chemical composition researches [e.g., *He et al.*, 2001; *Zheng et al.*, 2005], sulfate is one of the major aerosol compounds in the region. The b_{sp}/SO_2 ratio is ~50% higher in the afternoon than in the morning, probably showing the aging of primary pollutants. Also, the relative role of organic aerosols is likely higher in the morning when emissions from vehicles and biofuel burning are more important. Additionally, strong mixing within the daytime PBL may bring "yesterday's pollutants" in the residual layer (the layer above the shallow nocturnal boundary layer) down to the ground level. The pollutants from the residual layer are often of greater chemical age [e.g., *Taubman et al.*, 2004] and more thoroughly reacted. Lack of vertical profiles of pollutants prevents further investigation of this mechanism.

The b_{sp}/b_{ap} ratio is slightly higher in the afternoon than in the morning. This could be explained with BC emitted from numerous local low-efficiency stoves. Photochemical conversion from precursor gases to non-absorbing aerosols (e.g., sulfate and nitrate) can also improve b_{sp}/b_{ap} ratio over time. Aged aerosols in the residual layer, possibly mixed down to ground level during daytime as discussed above, are often "brighter" (more scattering). The single scattering albedo (SSA), a critical parameter in aerosol radiative forcing research, is defined as the ratio between aerosol scattering and aerosol extinction (scattering + absorption). Based on the b_{sp}/b_{ap} correlation, the SSA at 550 nm is near 0.81 in the morning and around 0.85 in the afternoon. SSA retrieved with the co-located Cimel sun photometer was about 0.9

during the same period [*Z. Li et al*, 2007a]. The difference originates presumably from the aerosols actually detected by the two methods, since the Cimel retrieval is sensitive to aerosols in the whole atmospheric column, while the PSAP and nephelometer measure surface values. Compared to the other experiments in China, SSA derived from this experiment is lower than in the Yangtze delta region (0.93, [*Xu et al.*, 2002]), but similar to that in Guangzhou (0.86, [*Andreae et al.*, 2005]) and Beijing (0.81, [*Bergin et al.*, 2001]). Overall, measurements conducted in recent years agree that aerosols near the surface in the eastern part of China are light-absorbing.

3.2.2 Implications for CO and SO_2 emissions

As discussed in Chapter 1, emission inventories can be evaluated by comparing observed and inventory pollutant ratios [e.g., *T. Wang et al.*, 2002, 2004]. Here I further examine some contemporary emission inventories for China, by contrasting the observed CO/SO_2 and CO/NO_y ratios from this study to inventory values.

Table 3.6. Observed and national inventory pollutant ratios (ppbv/ppbv)

	This study	*Wen et al.* [2008]	*Streets et al.* [2003]	*Streets et al.* [2006][a]	*X. Wang et al.* [2005][b]
CO/SO_2	35.8	72.1	13.0	17.5	7.7
CO/NO_x	27.2	25.4	16.7	22.7	8.6

[a] Using SO_2 and NO_x emission data for 2000, from *Streets et al.* [2003]. The base year for CO emissions is 2001.
[b] Emission inventory is regional.

Table 3.6 lists the CO/SO_2 and CO/NO_x (CO/NO_y) ratios from this study, an experiment carried out at street level in downtown Beijing [*Wen et al.*, 2008], an

inventory study for East Asia [*Streets et al.*, 2003], an updated CO emission inventory for China after TRACE-P field campaign [*Streets et al.*, 2006], and a high-resolution regional inventory covering eastern China [*X. Wang et al.*, 2005]. Afternoon ratios from this experiment, presumably reflecting more "regional" emission characteristics, are used in the comparison. The different ratios between the two experimental studies probably reflect the difference between rural and urban emission sources. The lower CO/NO_x ratio and higher CO/SO_2 ratio observed by *Wen et al.* [2008] in downtown Beijing are attributed to mobile sources, which emit CO and NO_x (but with a lower CO/NO_x ratio than residential sources [*X. Wang et al.*, 2005]), and little SO_2. Also, high-sulfur coal has been gradually replaced by low-sulfur fuels in Beijing since 1998, as part of the government's efforts to improve air quality [*Brajer and Mead*, 2003], but not in rural areas like Xianghe and smaller cities/towns. Despite these differences, rural and urban sites both record higher CO/SO_2 ratios than the inventories. The CO/SO_2 ratio derived from our experiment is a factor of three higher than *Streets et al.* [2003] and a factor of four higher than *X. Wang et al.* [2005], implying an underestimate of CO emissions by these earlier inventory studies. SO_2 emissions in inventories are considered more robust than CO [*Streets et al.*, 2003], but can also be biased, as the NO_y/SO_2 ratio from this experiment (1.18) is about 40% higher than the inventories (0.78 [*Streets et al.*, 2003] and 0.89 [*X. Wang et al.*, 2005]). Another possibility is that SO_2 emissions in this region went down from 2000 to 2005. However, this is in contrast with government statistical data (Chapter 1). Given a 36% boost in their estimated CO from China, the new inventory by *Streets et al.* [2006] has a greater CO/SO_2 ratio, but is still only half of our observed value. Note

that quantitatively evaluating emission inventories with our current observations is subject to uncertainties. Mismatch in spatial coverage between bottom-up and in-situ methods is one such uncertainty, and will be discussed in section 3.2.3. Some other uncertainty sources are addressed in section 3.2.4.

3.2.3 Cluster analysis and implications for regional emission inventory

Figure 3.8 presents the inventory ratios of CO/SO_2 and CO/NO_y for March 2001, calculated from the updated CO inventory by *Streets et al.* [2006] and their earlier estimates of SO_2 and NO_x emissions [*Streets et al.*, 2003]. Estimated CO emissions from each 0.5×0.5º grid cell shown in the figure exceed 10000 tonne for the month (The Xianghe cell, 39.5-40ºN, 116.5-117ºE, emits ~30000 tonne CO). The blue and red lines in the upper panel of the figure are 24-hr backward trajectories calculated using the NOAA Air Resource Lab (ARL) HYSPLIT model [*Draxler and Rolph*, 2003] and NCEP reanalysis meteorological data. Trajectories are initiated daily at 3 pm LST, 500 m above ground level over Xianghe; and could be classified into two groups: one from west and southwest and often relatively polluted (red lines: DOY 65, 68, 73-75, 78, 80, and 85), and the other from north and northwest and sometimes relatively clean (blue lines: DOY 61-64, 66-67, 69-72, 76-77, 79, and 81-84). A few trajectories passing over the grid cell of downtown Beijing (39.5-40ºN, 116-116.5ºE) are marked in green in the lower panel (DOY 65, 74-75, 78, and 80).

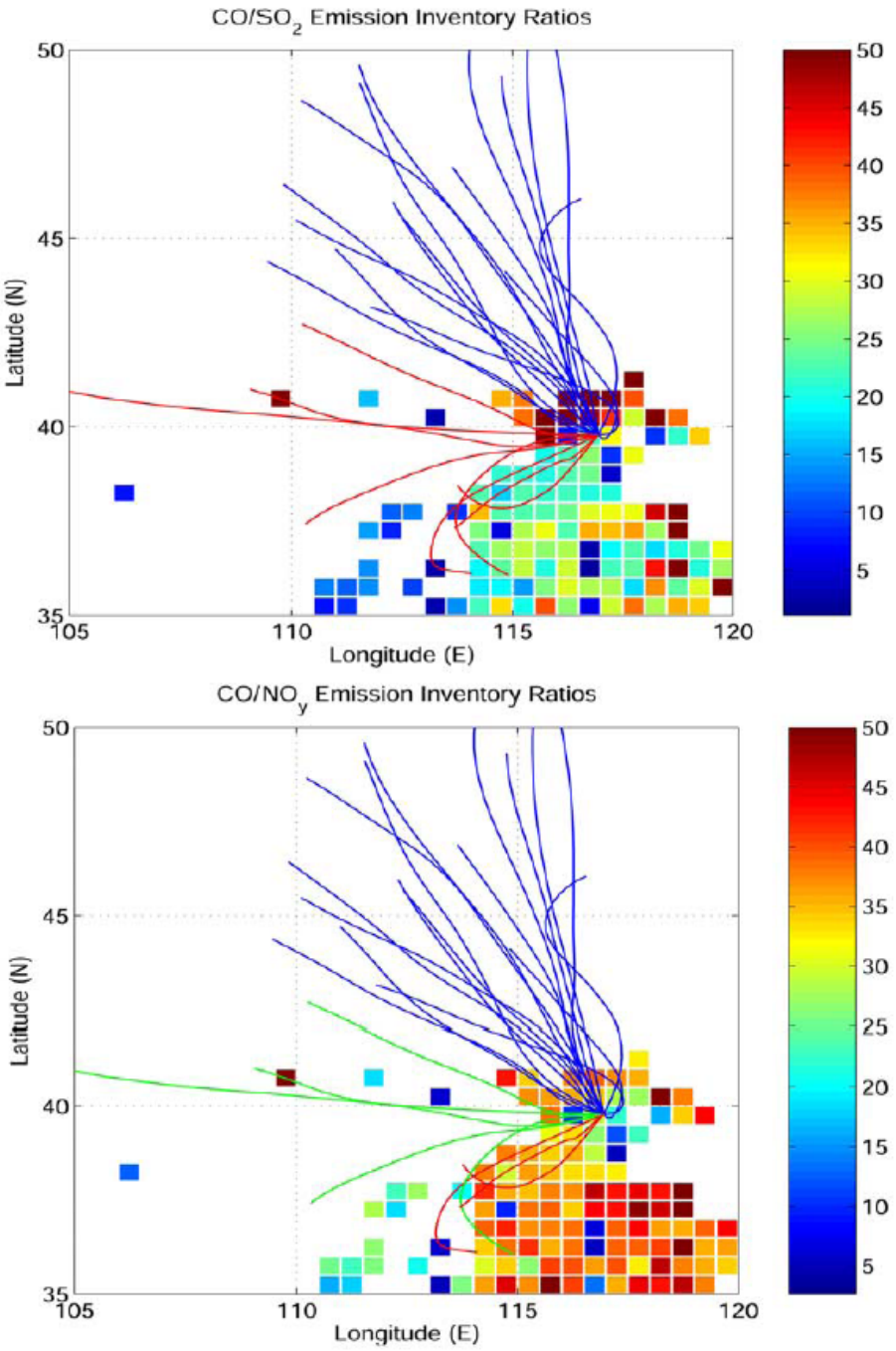

Figure 3.8. Emission inventory ratios of CO/SO_2 (upper panel) and CO/NO_x (lower panel) in March, 2001 [*Streets et al.*, 2003, 2006]. Only grid cells with CO emissions exceeding 10000 tonne/month are shown. The upper limit of color scale is set at 50 for clearer view of the spatial patterns, although some grid cells have ratios higher than 50. Blue, red and green lines are 24-hr backward trajectories started at 3 pm LST each day, 500 m above ground over Xianghe, calculated with the HYSPLIT model, using NCEP global reanalysis data. Blue lines, red lines (upper panel), and green lines (lower panel) represent trajectories passing over different areas (area to the N & NW

of Xianghe with high CO/SO_2 inventory ratios, area to the W & SW of Xianghe with low CO/SO_2 inventory ratios, and the grid cell containing Beijing).

The CO/SO_2 inventory ratios demonstrate an obvious spatial pattern over the region around Xianghe, with the ratios in the north (higher than 45) more than twice as high as in the south (around 20). The CO/SO_2 ratio for the Beijing grid cell is even lower at about 12.5, while the same ratio for the Xianghe grid cell is 22.4. CO/NO_y (NO_x) inventory ratios have a different spatial pattern, lower in the Beijing grid cell and the area immediately to the southeast of Xianghe. Table 3.7 lists the pollutant inventory ratios for areas north and northwest of Xianghe, west and southwest of Xianghe, the Beijing grid cell, and the Xianghe grid cell. Results of correlation analysis for different trajectory groups are summarized in Table 3.8.

Table 3.7. Regional inventory pollutant ratios within different areas around Xianghe (ppb/ppb)

Area	Latitude Range	Longitude Range	*Streets et al.* [2003]		*Streets et al.* [2006][a]	
			CO/SO_2	CO/NO_x	CO/SO_2	CO/NO_x
N & NW	40 – 41 ºN	114.5 – 117.5 ºE	45.7	28.2	57.2	35.3
W & SW	37.5 – 40 ºN	114 – 117 ºE	10.1	14.7	16.5	24.0
Beijing	39.5 – 40ºN	116 – 116.5 ºE	10.9	16.3	12.5	18.7
Xianghe	39.5 – 40 ºN	116.5 – 117 ºE	15.0	19.1	22.4	28.6

[a] Use SO_2 and NO_x emission data from *Streets et al.* [2003].

Table 3.8. Results of correlation analysis for different trajectory groups

y/x	North and Northwest			Southwest and West			Beijing		
	a	b	R^2	a	b	R^2	a	b	R^2
CO/SO_2	33.1	193.6	0.469	36.7	167.5	0.847	41.4	48.4	0.842
CO/NO_x	40.6	64.4	0.525	21.8	335.4	0.758	36.5	-91.6	0.908
NO_x/SO_2	0.71	3.7	0.665	1.47	-3.8	0.832	1.05	5.65	0.775

a: slope (ppb/ppb), b: y-intercept

Air parcels from N & NW of Xianghe can have very different chemical characteristics at times; SO_2, NO_y, and CO from that sector (blue lines, upper panel Figure 3.8) are only moderately correlated. Brisk descending flows from north or northwest bring clean air with background level CO (~200 ppb) and very little SO_2 and NO_y. Weak winds from the same direction (e.g., on March 20), on the other hand, can build up ~1 ppm CO and ~10 ppb SO_2 and NO_y, probably emitted by local agricultural burning. Such diverse conditions complicate direct comparison between emission inventories and measurements. The measurement-derived CO/SO_2 ratio of 33 is lower than the inventory ratio (57), but the CO/NO_y ratios (observation: 41, inventory: 35) are close. The high CO/SO_2 inventory ratios in the region are due to traffic sources, estimated to contribute more than 70% of total CO emissions in the area [*Streets et al.*, 2006], even for the mountainous areas of 40.5-41ºN, 116-117ºE. Total estimated traffic CO emissions from these two grid cells are 310000 tonne (in 2001), only slightly lower than from downtown Beijing (386000 tonne) [*Streets et al.*, 2006]. Reexamining mobile sources in China is called for to reduce the uncertainties revealed here.

CO is well-correlated with both SO_2 and NO_y in air from west and southwest of Xianghe (red lines, upper panel Figure 3.8). The observed CO/SO_2 ratio associated with these trajectories is 36.7, more than a factor of two higher than the inventory value (W & SW, Table 3.7). The y-intercept of ~170 ppb is close to the background CO concentration. As for the CO/NO_y ratio, the observed value (21.8) is not far from the inventory value of 24.0, but the y-intercept is more than 300 ppb of CO. The CO/SO_2 ratio under windy conditions (wind speed > 3 m/s) is also calculated to

minimize influence from nearby sources; the resulting R^2 (0.656) and y-intercept (138.5 ppb) are lower, but the CO/SO_2 ratio remains about the same (38.6). A couple of trajectories might have passed over a grid cell about 600 km west of Xianghe, where CO emitted from the large steel mills in the city of Baotou could affect our measurements. But excluding the data of these two trajectories does not significantly change the observational CO/SO_2 ratio (35.6, R^2: 0.752, y-intercept: 192.9 ppb). In short, our CO/SO_2 correlation analysis for air from west and southwest of Xianghe consistently derives CO/SO_2 ratio over 100% higher than the inventory, lending us some confidence concluding that CO emissions might be underestimated for the area. Or SO_2 emissions could be overestimate or SO_2 emissions have decreased since 2000.

For the trajectories passing over the Beijing grid cell, the CO/SO_2 ratio (41.4) from our measurements is not as high as what is directly observed downtown (Table 3.6, [*Wen et al.*, 2008]), but still a factor of three higher than the inventory value (12.5). The grid cell west of downtown Beijing (39.5-40ºN, 115.5-116ºE) has a higher CO/SO_2 ratio, but only emits one fifth as much CO. Our CO/NO_y ratio from this trajectory group (36.5) is higher than *Wen et al.* [2008], and is double the corresponding inventory ratio (18.7). During 2000-2004, CO/SO_2 and CO/NO_x ratios based on Beijing EPA's yearly average data from their urban monitoring network were 89 and 56, respectively [*T. Wen*, personal communication]. These ratios could be biased high, however, as SO_2 and NO_x would be removed through fast photochemical processes in summer months. The CO/SO_2 inventory ratio for the grid cell immediately north of Beijing (40-40.5ºN, 116-116.5ºE) is greater (Figure 3.8), with strong traffic CO emissions. This is probably true as the city has expanded

rapidly northward in recent years. Even after combining inventory emissions from this northern grid cell with the downtown grid cell (i.e. consider the area of 39.5-40.5ºN, 116-116.5ºE as the urbanized area of Beijing), the resulting inventory CO/SO_2 (17.0) and CO/NO_y (22.3) ratios are still considerably smaller than observations. Thus I conclude that CO emissions from Beijing are likely underestimated (or SO_2 emissions are overestimated) by inventory studies. Detailed analysis of pollutant emissions in downtown Beijing is given by *Wen et al.* [2008]. Worth noting is that current emission inventories [*Streets et al.*, 2003, 2006] tend to have rather low CO/SO_2 (NO_x) ratios in Chinese mega cities such as Beijing, Tianjin (Figure 3.8, 39-39.5ºN, 117-117.5ºE), Shanghai, and Guangzhou. Characterizing emissions from mobile sources and/or small-scale boilers [*Streets et al.*, 2006] may help reduce the uncertainties in emission inventories for big cities in China. In section 3.4, I present a case study on the trace gas emissions from a small coal-fired boiler.

3.2.4 Some other issues of inventory evaluation

Besides the spatial issue discussed above, some other issues could also complicate the comparison between inventories and measurements. Measurements are normally only available for a limited period of time, whereas emission inventories are often based on annual activity data. The vertical distribution of pollutants could be another issue for pollutants with different release heights. Losses of pollutants during transport need to be taken into account as well.

As discussed in Chapter 1, CO has a lifetime much longer (30-90 days) than SO_2 and NO_x (hours to days), and as a result the observed CO/SO_2 and CO/NO_y ratios

are expected to be greater than those of actual emissions. However, the effects of chemical reactions are likely small in this study, due to the proximity of our site to heavily populated areas and emission sources. Trajectory analysis (Figure 3.8) suggests that in some cases plumes from Beijing could reach Xianghe in hours. In addition, chemical conversion of locally emitted SO_2 and NO_x during our experiment is slowed by the relatively cold and dry environment, and limited sunshine, as evidenced by the observed ozone level. As will be detailed in Chapter 5, the mole ratio between sulfate and SO_x (sulfate + SO_2) is less than 10% most of the time. Taking sulfate into consideration, the CO/SO_x ratio is above 30 for W & SW trajectories, still almost double the inventory value.

Surface measurements may not exactly mirror all emissions in an area if pollutants are emitted from different heights and have distinct vertical distributions. In China, a large fraction of CO is from area sources near the surface, though steel mills inject CO at relatively high altitudes. SO_2 is different; large point sources emit a substantial part of total SO_2. Therefore the CO/SO_2 ratios measured at the surface would be higher than inventory values. This sampling bias is partly avoided in this study, as I select measurements from local afternoon for comparisons, when vertical mixing in the PBL is most vigorous. As a test, I calculated the regional CO/SO_2 inventory ratio, excluding large point sources of CO and SO_2. The resulted surface-source-only-ratio for the area W & SW of Xianghe (37.5-40ºN, 114-117ºE) is about 20.8 [*Streets et al.*, 2006], 25% larger than the all-source-ratio (16.5), but still 70% smaller than our value from afternoon observations.

The inventory studies compared here are based on statistics for the whole years of 2000-2001, while this experiment only lasted one month in 2005. This mismatch can also hinder direct comparison between observations and inventories, although the inventory emissions of trace gases in March are close to annual averages [*Streets et al.*, 2003], and no discernable change occurred in the monitored CO/SO_2 ratio in Beijing from 2000 to 2004 [*T. Wen,* personal communication]. In summary, different spatial and temporal coverage, losses of pollutants, and uncertainties in measurements and emission estimates all contribute to the discrepancies discussed in this section. Reducing the gap between observations and bottom-up estimates helps improve emission inventories. The better agreement between the new CO inventory for China [*Streets et al.*, 2006] and our measurements reflects an important achievement of the TRACE-P experiment. More extensive field experiments and direct measurements of emission factors should help improve understanding of pollutant emissions from China.

3.2.5 Black carbon emissions

The correlation between CO and BC, both products of inefficient combustion, can be used to estimate BC emissions based on known CO emissions. Data (Figure 3.9) from the afternoon hours (2-4 pm LST) are used to avoid sampling gaps at night and to get a more regionally representative ratio. The mass concentration of BC is calculated using PSAP aerosol absorption data, assuming that BC is the dominant absorbing compound at 550 nm. The specific absorption coefficient (10 m^2/g) determined by *Barnard et al.* [2005] is adopted for the calculation. The mass

concentration of CO is computed with locally measured ambient pressure and temperature.

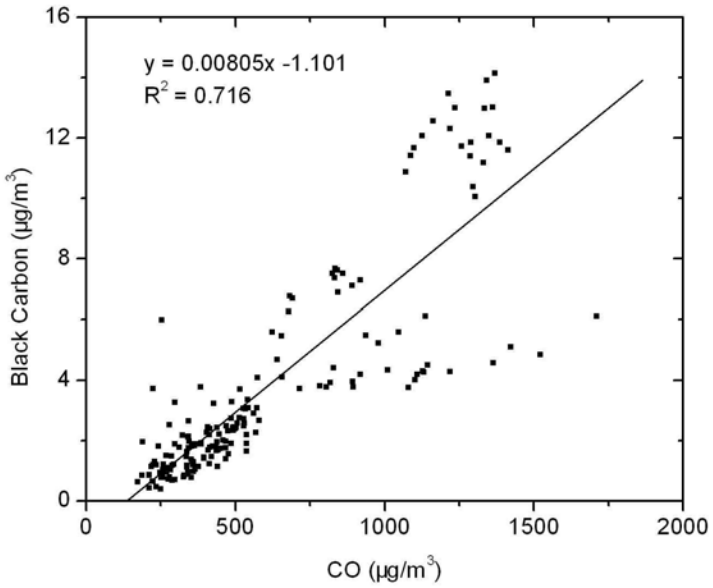

Figure 3.9. Correlation between 10-min average BC and CO during the afternoon hours (2-4 pm LST) at the Xianghe site. Data points with relatively low BC/CO ratio probably reflect emissions from agricultural burnings (spotted during the experiment) during the smoldering stage.

The BC/CO ratio from this study is 8.05×10^{-3} ($\mu g/m^3$ BC vs. $\mu g/m^3$ CO), lower than observed over the Indian Ocean during the INDOEX experiment (12.5×10^{-3}, [*Dickerson et al.*, 2002]) but higher than that for the eastern U.S. (3.4×10^{-3}, [*Chen et al.*, 2001]). Despite the uncertainties in sampling and measurements, the different ratios likely reflect differences in energy consumption of these regions. Among the three regions, India probably has the most intense emissions from biomass burning, followed by China. The inefficient combustion of other fuels and high-emission vehicle fleets in India and China could also contribute to the high BC/CO ratios observed. Using the ratio in Figure 3.9 and the CO emissions estimated

by *Streets et al.* [2006], BC emitted from China in 2001 is estimated at ~1300 Gg/yr, in agreement with the inventory (1049 Gg/yr, [*Streets et al.*, 2003]). If as suggested in previous sections, the actual CO emissions could be twice as much as estimated, the resulted BC emissions could be up to 2600 Gg/yr. The relative uncertainty of this estimate is large (at least a factor of two) and ill-constrained, due to sizeable uncertainties in BC measurements, CO inventories, and spatial and temporal coverage of the experiment (BC/CO ratio from a single location used for a large region and assumed constant in all seasons). Nonetheless, bottom-up estimates and observational results are in good agreement in this study, compared to a similar study for India [*Dickerson et al.*, 2002].

3.3 Enrichment of Elements and Ions in Aerosols

3.3.1 Enrichment factors and enrichment of lead

Using Al as the reference element, the enrichment factor of an element X in aerosols can be calculated with the following equation:

$$EF_X = \left(\frac{X}{Al}\right)_{Aerosol} \Big/ \left(\frac{X}{Al}\right)_{Crust} \qquad (3.1)$$

where $\left(\frac{X}{Al}\right)_{Aerosol}$ is the mass ratio between X and Al in aerosols, while $\left(\frac{X}{Al}\right)_{Crust}$ is the same ratio in the crustal material, taken from *Lide* [1998]. The concentrations of elements in different types of soil vary, but normally by less than a factor of 5 [e.g., *Chen et al.*, 1991]. If EF_x is close to one, X in aerosols mainly comes from soil sources. On the other hand if EF_x is much higher than unity, X in aerosols may have

important sources other than soil particles. Elements with high EF have been used as tracers of anthropogenic aerosols [e.g., *Sun et al.*, 2005].

Shown in Figure 3.10 are EF's of different elements in aerosol samples from Xianghe. Elements abundant in the Earth's crust like Ca, Fe, and Mg generally have EF below 5, and are mostly from soil sources, although as discussed in section 3.2, substantial sources of Ca and Fe are related to human activities. Compared to other crustal elements, the EF of K is more variable, probably due to emissions from biomass burning. The EF of V is close to one, showing little evidence of oil combustion [*Rahn*, 1981]. As, Ag, Pb, and Cd have EF's above 100, and are largely from anthropogenic pollution sources. For example, As may be from coal burning, incinerators, and smelters; Cd may be emitted from incinerators, smelters, and during manufacture of pigments [*Pacyna*, 1998]. EF's of pollution elements are generally more variable than crustal elements, due to large synoptic fluctuations in pollutant levels discussed earlier.

Lead (Pb) is highly enriched, with an EF over 100. Our average Pb level (0.28 $\mu g/m^3$) is comparable to the loadings near busy roads of downtown Beijing (0.24-0.31 $\mu g/m^3$, spring 2002-2004) [*Sun et al.*, 2006] and higher than the spring average concentration of 0.0036 $\mu g/m^3$ found in Fort Meade, MD [*Chen et al.*, 2002]. During the 1970s leaded gasoline was the major source of Pb in particulate matter in the U.S., although point sources such as incinerators, battery manufacturing, and glass manufacturing also emit Pb [e.g., *Pekney et al.*, 2006]. In recent years after the phasing out of leaded gasoline, resuspension of lead-containing particles (due to deposition of previously emitted Pb) has been suggested to be an important source of

lead in aerosols in the U.S. [e.g., *Ehrman et al.*, 1992; *Harris and Davidson*, 2005]. Leaded gasoline was phased out in China in 2000 [*Chinese EPA*, 1999]. But the good correlation between the EF of Pb and CO in our data (Figure 3.11) implies that substantial anthropogenic sources may still exist in the region. The concentration of Pb is correlated with CO ($R^2 > 0.5$, and higher under stagnant conditions) but not with Al (tracer of soil particles). Our site is ~500 m away from the nearest major road with limited traffic. Traffic in Chinese cities grows fast recently, but in the mid 1990s the total lead added to gasoline in China was only ~900 tonne/yr, about 1/3 of that in Australia [*Thomas*, 1995]. The mean concentration of Pb in soil in parks in Beijing [*Chen et al.*, 2005] is 66.2 $\mu g/m^3$, only a factor of 3-4 higher than the background crustal concentration. Therefore resuspension of Pb-enriched soil particles may merely be a minor source of Pb in this study. Pb can poison the catalytic converter of cars [*Thomas*, 1995] resulting in higher CO emissions; old cars used to run on leaded gasoline may emit both CO and Pb in substantial amounts, and this might explain the observed correlation between CO and Pb. Considering that the phasing out of gasoline took a long period in the U.S. [*Nadim et al.*, 2001], it is also possible that leaded gasoline may still be in use in China. Regardless of its origin, the high concentrations of Pb in China exceed the new U.S. EPA standard [*U.S. EPA*, 2006] and require more detailed analysis.

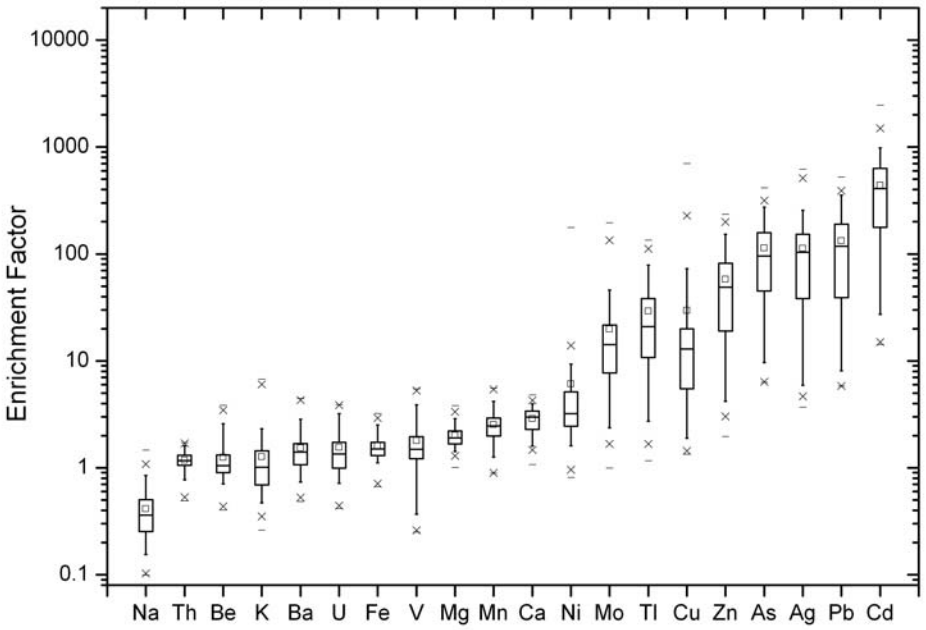

Figure 3.10. Box and whisker chart of the enrichment factors. The center horizontal line, lower edge, and upper edge of the box represent the median, the 25th and 75th percentiles, respectively. Lower and upper whiskers are the 10th and 90th percentiles. Crosses stand for the 1st (lower) and 99th (upper) percentiles. Maximum (upper) and minimum (lower) EF's are marked with horizontal lines outside the box body.

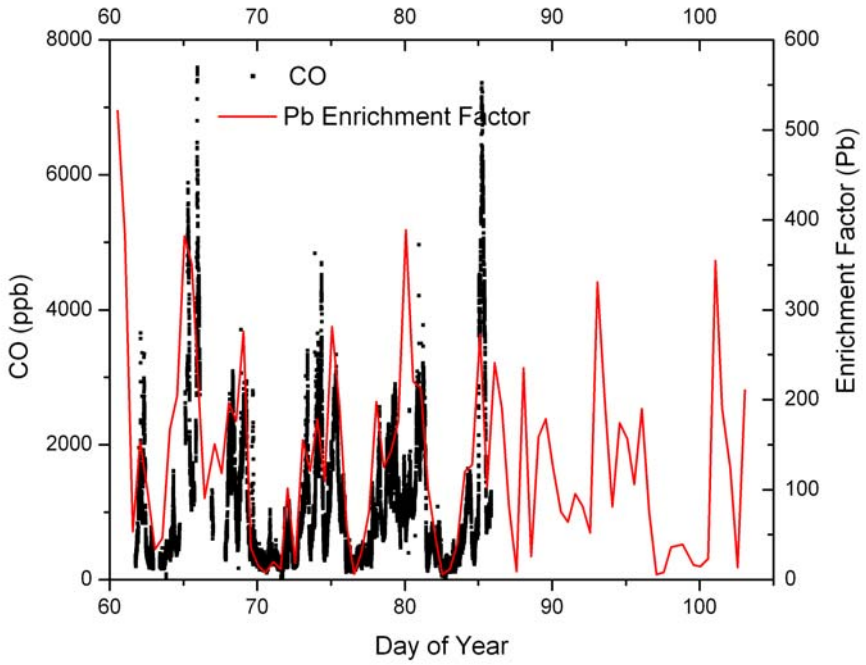

Figure 3.11. Enrichment factor of Pb (red solid line) and hourly averaged CO concentration (black dots).

3.3.2 Enrichment of chloride ion

Figure 3.12 is a scatter plot of the concentrations of Na^+ (0.65 ± 0.38 μg/m^3) and Cl^- (3.4 ± 2.4 μg/m^3) ions in aerosol samples, as a function of ambient SO_2. It appears that the samples could be divided into two groups, one with high SO_2 concentration (>10 ppb) and enriched in Cl^- with respect to sea water, and the other with low SO_2 (<10 ppb) and a Cl^-/Na^+ ratio close to that of sea water (blue line in Figure 3.12, slope ~1.8, [*Prospero et al.*, 2003]), although the two ions are only weakly correlated in both groups. Coal burning, the dominant energy source in China, emits both SO_2 [*Streets et al.*, 2003] and HCl. The latter could enrich Cl^- in aerosols through interactions with soil particles [*Wang, Zhuang et al.,* 2005]. The Cl/S mass ratio in coal used in six power plants in China ranges from 3.5×10^{-2} to 0.12, but only a fraction of Cl is emitted during combustion [*Chen et al.*, 2007]. Cl^--enriched aerosols could be a potential chlorine source for atmospheric chemical processes in the region.

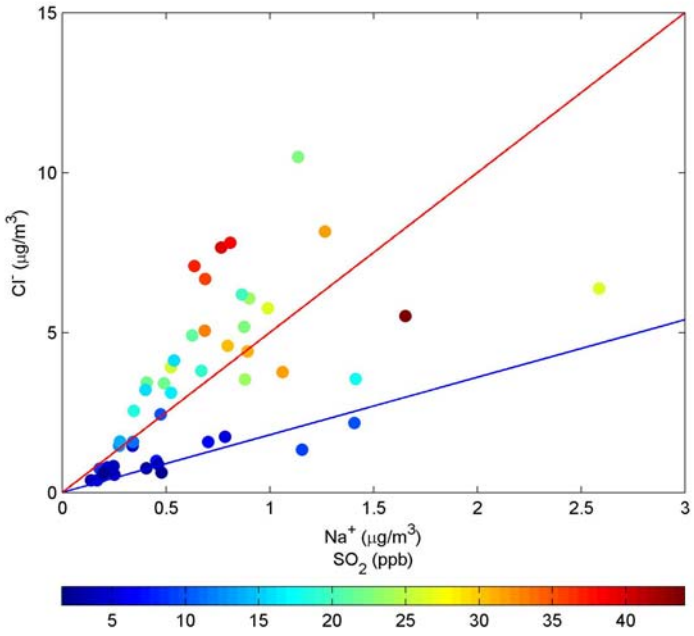

Figure 3.12. Scatter plot of Cl^- and Na^+ concentrations. The color of the dots represents the average SO_2 for the corresponding samples. Blue (slope = 1.8) and red (slope = 5) solid lines are for reference only.

3.4 Characterize Emissions from a Small Coal-Fired Boiler

3.4.1 The boiler

The boiler studied (Figure 3.13), as mentioned in Chapter 2, is located ~50 m east of the major facility building where all trace gas instruments were deployed during the Xianghe experiment. This hot water boiler made in 1996 has a rating of 0.7 MW and a working pressure of 0.2 MPa. At its full capacity, the boiler burns 220 kg coal every hour; during the experiment, the actual coal consumption was about 100 kg/hr. This may influence the emissions (e.g., less CO) from the boiler due to possible enhancement in the air-fuel ratio. But the boiler is equipped with induced-draft and forced-draft fans, so lean combustion conditions are probably achieved even when the boiler runs at its maximum capacity. Without detailed information about the

configuration and conditions of the boiler, I will not further discuss this issue in this dissertation. A cyclone separator with unknown efficiency removes particles in the flue gas, which is emitted through a 15-m chimney. There is no control on emissions of trace gases. In winter, it provides heating for the whole Xianghe observatory, roughly 3000 m^2 in four buildings. The boiler normally runs 2-3 times in the morning and evening a day, each time for 1-3 hr, depending on outdoor temperature. A detailed running record was kept during the experiment. No element analysis was performed for the raw coal in chunks (0-50 mm in size) used; this type of coal from Datong, China is usually bituminous, consisting of 70-90% carbon and 0.5-3% sulfur [*Chen et al.*, 2006, *Ge et al.*, 2001]. I picked out the plumes from the boiler by looking for pollutant peaks that were observed when the boiler was running under weak east winds (wind speed < 2 m/s), and when maximum SO_2 exceeded 80 ppb. In total, six such events were recorded in the 4-week experiment.

Figure 3.13. The coal-fired boiler at the Xianghe site.

3.4.2 Method

CO_2 was measured with a Thermal Environment Instruments, Model 41C analyzer (Franklin, MA) operated by IAP, CAS. As an example, Figure 3.14 shows a plume from the boiler observed near midnight, March 14, 2005. Peaks of CO_2 (450 ppm), NO_y (90 ppb), SO_2 (500 ppb), and CO (4500 ppb) appeared almost simultaneously as the boiler started running at 9:35 pm LST. I derive the "background" through linearly interpolating the concentrations before and after the peaks (shown as red lines in the plot), assuming that the background pollutant levels (controlled by all other local emission sources) change slowly and linearly in the short period, and that the peaks appear as fresh boiler emissions are superimposed on the background. ΔCO_2, ΔCO, ΔSO_2, and ΔNO_y are calculated by subtracting background from the peaks. CO_2 is relatively smooth, as the instrument has a longer averaging time (5 min) than the others (1 min). Because the CO peak lasted for a shorter period of time than other trace gases (~15 min into the boiler run, or 9:50 pm LST), I define the first 15 min of each boiler run as a "cold start", marked by the area between two vertical dashed lines in Figure 3.14. As the boiler just starts running, unstable or less-than-optimized combustion conditions may result in emission characteristics different from normal combustion conditions.

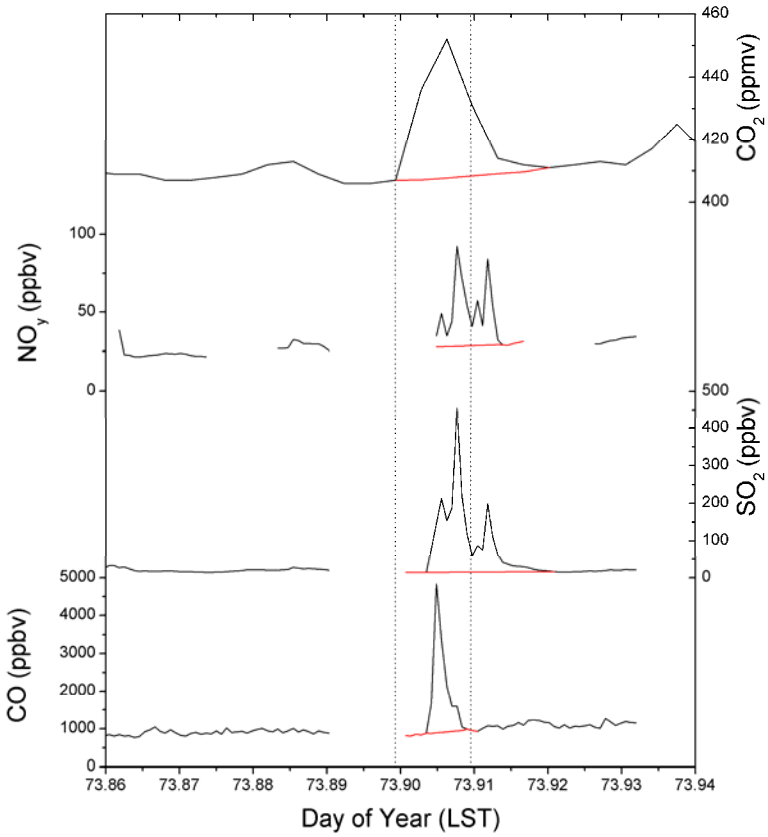

Figure 3.14. One plume from the boiler detected on March 14, 2005. Red lines are baselines derived through linear interpolation of measurements before and after the peak. The "cold start" period of the boiler run (from the starting time to 15 min into the run) is marked with two vertical dashed lines.

3.4.3 Emission characteristics of the boiler and implications

Results of correlation analysis for data of all six boiler plumes and the subset of cold-start only data are given in Figures 3.15 and 3.16, respectively. 1-min data are used for the correlation of $\Delta CO/\Delta SO_2$ and $\Delta NO_y/\Delta SO_2$; 5-min data are used for CO_2. Too few simultaneous NO_y and CO_2 data points are available for a meaningful correlation analysis.

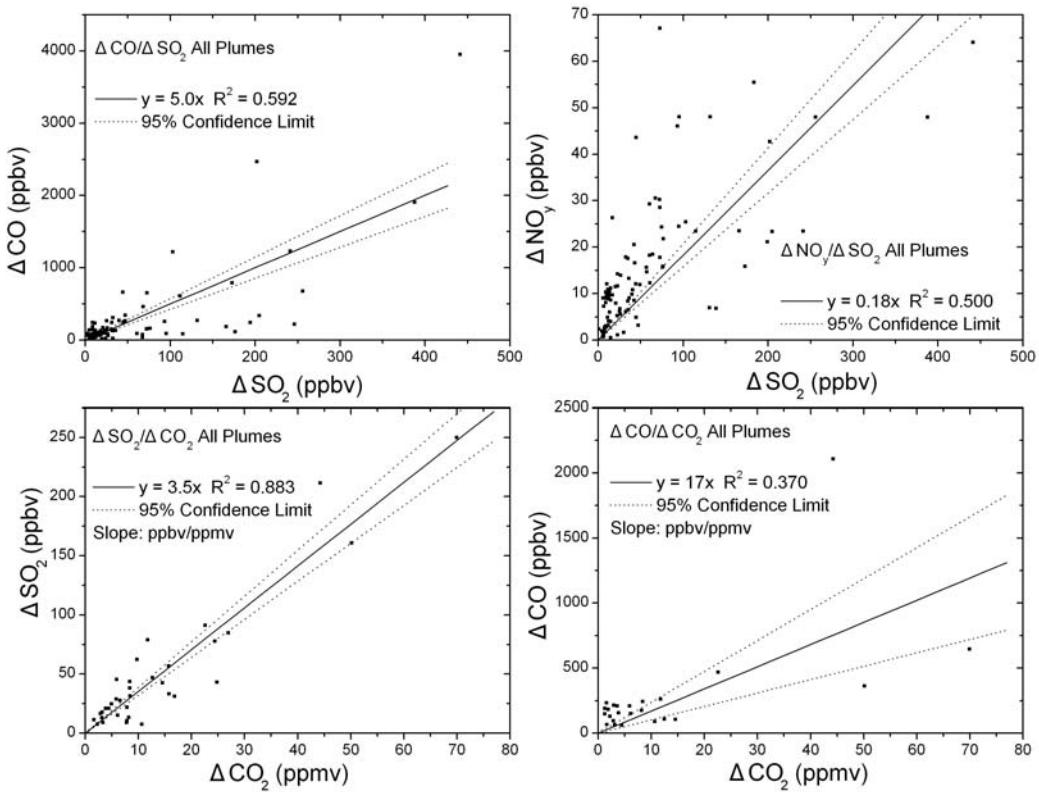

Figure 3.15. Correlations of ΔCO, ΔSO_2, ΔNO_y, and ΔCO_2 for all plume data. Dotted lines mark the 95% confidence interval for the correlation analysis. Note the slopes for $\Delta SO_2/\Delta CO_2$ and $\Delta CO/\Delta CO_2$ are in ppbv/ppmv.

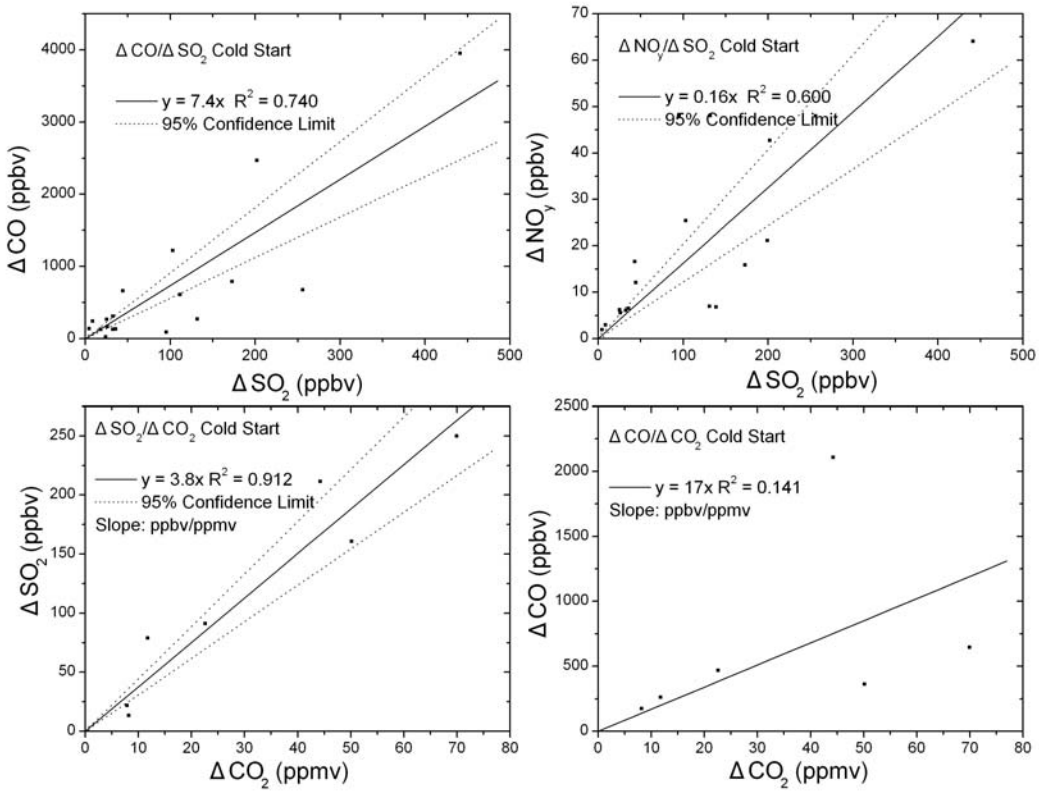

Figure 3.16. Same as Figure 3.15, but for cold start data.

ΔSO_2 and ΔCO_2 are well-correlated, with R^2 of 0.88 for all plume data and 0.91 for cold start data. The $\Delta SO_2/\Delta CO_2$ ratio does not change much in the two figures (3.5 (ppb/ppm) vs. 3.8), suggesting that SO_2 emissions from the boiler are not affected by burning conditions. The corresponding ratio in the emission inventory ranges from 1.1 to 20 (ppb/ppm) [*Streets et al.*, 2003]. In comparison, ΔCO and ΔCO_2 are only weakly correlated in all plume data (Figure 3.15), probably due to dependence of CO emissions on combustion conditions. For the few cold start data points, ΔCO and ΔCO_2 are not significantly correlated. Note that the inventory [*Streets et al.*, 2003] CO/CO_2 emission ratio for domestic coal burning in China is much higher at about 60 (ppb/ppm), compared to the ratio from this study (17 (ppb/ppm)). In 1-min data, ΔCO and ΔSO_2 are correlated in both all plume data and

cold start data, as are ΔNO_y and ΔSO_2. Comparing Figures 3.15 and 3.16, one can see that the cold start data have a greater $\Delta CO/\Delta SO_2$ ratio (7.4 vs. 5.0) but slightly smaller $\Delta NO_y/\Delta SO_2$ ratio (0.16 vs. 0.18) than all plume data. As SO_2 emissions vary little under different burning conditions, the change in $\Delta CO/\Delta SO_2$ ratio suggests that less-than-optimal conditions during the cold start stage may cause stronger CO emissions. NO_y emissions, on the other hand, remain about the same.

Assuming carbon makes up 80% of the mass of the coal and is all converted to CO_2 in combustion, burning 1 kg coal will emit 2.93 kg CO_2. From the $\Delta SO_2/\Delta CO_2$ ratio, I estimate that roughly 15.4 g SO_2 is emitted at the same time. If all the sulfur were released as SO_2, the sulfur content of the coal used in this boiler would be about 0.8%. Different assumptions concerning the carbon content of the coal and the percentage of sulfur released as SO_2 may lead to slightly different results. The overall relative uncertainty is about 30%; the SO_2 emission factor is 15.4 ± 4.6 g SO_2/kg coal (hereafter the units for emission factors are presented as g (species)/kg (fuel) unless otherwise noted), and the sulfur content of the coal is 0.8% ± 0.24%. The SO_2 emission factor from this analysis is lower than the value (46.7 g/kg) given by *Ge et al.* [2001], who used raw coal with sulfur content of 2.81%, but within the range of the factors used in emission inventories (3.29-54.8 g/kg for the domestic sector, [*Streets et al.*, 2003]). The average sulfur content of Chinese coal is 1.1-1.2% by weight [*He and Chen*, 2002]. According to the Beijing EPA's data, replacing small coal boilers in downtown Beijing has reduced coal usage by about 6 million tonne, and decreased SO_2 emissions by 56,000 tonne. This translates into an average SO_2 emission factor of about 9.3 g/kg for similar small coal-burning emission sources in

Beijing. If I assume, according to *Streets et al.* [2003], that the emission factor of CO_2 for domestic coal combustion in China is about 2 kg CO_2/kg coal, the SO_2 emission factor would be 10.5 g/kg.

Estimating the CO emission factor from the $\Delta CO/\Delta CO_2$ ratio is subject to greater uncertainty, as CO emissions are more variable, depending on combustion conditions. The CO emission factor is about 31.7 g CO/kg coal from this analysis, higher than the factor determined by *Ge et al.* [2001] for a larger automatic stoker (15 g/kg), but much lower than the values used in two emission inventories (74 g/kg, [*Streets et al.,* 2003]; EPA AP-42, 124 g/kg, [*Streets et al*., 2006]) for the domestic sector of China. Emission factors can also be derived with the correlations of $\Delta CO/\Delta SO_2$ and $\Delta NO_y/\Delta SO_2$. The CO emission factor calculated this way is 33.7 ± 13.5 g/kg for all plume data (49.6 ± 19.8 g/kg for cold start), consistent with the result from the $\Delta CO/\Delta CO_2$ ratio. Using the CO_2 emission factor from *Streets et al.* [2003] would give an even lower CO emission factor (23.6 g/kg for all plume, 34.7 g/kg for cold start). The NO_y emission factor is 2.0 ± 0.8 g/kg for all plume data and 1.8 ± 0.7 g/kg for cold start (assuming all NO_2), on the higher end of the range employed by *Streets et al.* [2003] (1.19-2.24 g/kg).

From March 2 to March 22, 2005, the boiler completed 66 runs for a total run time of about 88 hr (accumulated cold-start run time: 16.5 hr). The overall coal consumption was about 8800 kg, emitting roughly 135 kg SO_2, 300 kg CO, and 18 kg NO_y (assuming all NO_2). The heating season in this area usually lasts from mid-November through mid-March the following year. The actual running time of a heating unit depends on weather. A reasonable guess is that the boiler run time in

November is the same as in March, and December, January, and February each has twice as much run time. The total boiler running time would sum to about 350 hr for the entire heating season. Coal consumption of the season adds up to 35000 kg, emitting about 540 kg SO_2, 1200 kg CO, and 72 kg NO_y. *Streets et al.* [2006] estimated that in China, domestic boilers burnt about 80 million tonne of coal in 2001. If 25% or 20 million tonne were used by hand-fed boilers for heating, emissions from these small units in 2001 would include 308000 tonne SO_2, 674000 tonne CO, and 40000 tonne NO_y, applying the emission factors from this study. This is but a small fraction of the total emissions from China (1.5% of SO_2, 0.4% of CO, and 0.3% of NO_y, [*Streets et al.*, 2003, 2006]). But these small boilers are often located in densely populated communities (according to the author's experience living in the area); pollutants emitted to limited height by them are often trapped near ground as they run on cold winter nights. These factors may lead to heavy local pollution at times as observed in this study, and may cause severe adverse health effects.

3.5 Summary

Measurements of CO, SO_2, NO_y, O_3, aerosol scattering, aerosol absorption, and aerosol chemical composition have been made in Xianghe, a rural site about 70 km east-southeast and generally downwind of Beijing. Located in a rural area undergoing fast industrialization and in proximity to two mega cities, the Xianghe site allows us to look into China's air pollution issue from close distance.

During the experiment in March 2005, air pollution at the Xianghe site was characterized by high pollutant levels and fast transitions between clean and heavily

polluted periods. Cold front passages, repeating every 4-5 days, are the major mechanism driving these transitions, as they are associated with strong vertical motions and wind shear accompanying the change of air mass. The observed response of air quality to weather is similar to what has been found in the eastern U.S. What is different is that northern China is much drier in spring, and wet deposition is inefficient in removing pollutants at this time of the year. Some pollutants are probably lofted away from the surface during cold front passages, but pollutant transport and evolution afterwards need further investigation. The next chapter will analyze aircraft-measured pollutant profiles under a variety of weather conditions, and discuss the role of mid-latitude wave cyclones in pollutant lofting and transport. Synoptic variation of chemical processes involved in the production of secondary aerosols (sulfate and nitrate) is another interesting phenomenon observed in Xianghe, and will be discussed in more detail in Chapter 5.

The observed diurnal cycle of pollutants discloses the diverse nature of the emission sources near the Xianghe site. Pollutant levels are more variable in the normally stagnant morning, (7-9 am LST), as the instruments detect more "local" and fresh pollutants. Under strong winds in the afternoon hours (2-4 pm LST), the instruments see more "regional" and well-mixed aged pollutants. Low single scattering albedo (morning: 0.81, afternoon: 0.85) suggests that aerosols near the surface are light absorbing, as seen in previous experiments in eastern China [*Bergin et al.*, 2001; *Xu et al.*, 2002; *Andreae et al.*, 2005]. The ground SSA is much lower than the column integrated value (0.9) [*Z. Li et al*, 2007a]. Stronger aerosol

absorption at lower altitudes could have impacts on the local radiation budget as well as atmospheric stability. Further work is needed to quantitatively address these effects.

Using the CO emission data from *Streets et al.* [2006] and the BC/CO ratio from this experiment, black carbon emitted from China is estimated at 1300-2600 Gg/yr. This is in agreement with bottom-up estimates [*Streets et al.*, 2003], but both have substantial uncertainties. Enrichment factor analysis confirms that Al, Ca, Fe, Mg, and K are mainly from soil sources, although Ca, Fe, and K might also be related to anthropogenic activities in the region such as construction (Ca) and biomass burning (K). Pb is still highly enriched several years after leaded gasoline was supposed to be phased out in China, and likely comes from human sources as shown by the good correlation between Pb and CO. The enrichment of Cl^- ion with respect to sea water is correlated with ambient SO_2 level, probably a result of HCl released from extensive coal burning in the area.

Afternoon gas concentration ratios (CO/SO_2, CO/NO_x (NO_y)) were compared to inventories. With a 36% increase in estimated CO emissions from China, the updated CO inventory by *Streets et al.* [2006] agrees better with our observations than earlier estimates [*Streets et al.*, 2003; *X. Wang et al.*, 2005]; but a difference of a factor of two in CO/SO_2 ratios still exists. The CO/NO_x ratio derived from this experiment is close to *Streets et al.* [2003; 2006], but a factor of four higher than *X. Wang et al.* [2005]. A number of issues could contribute to the difference between observations and inventories, including but not limited to temporal and spatial coverage of measurements, release heights of pollutants, chemical and physical losses of pollutants, and inventory errors. But for air from the populated area to the W and

SW, the observation-derived CO/SO_2 ratios are consistently more than 100% higher than the inventory values [*Streets et al.*, 2003, 2006]. Even larger gaps between observations and inventories are found for plumes from downtown Beijing, where in-situ measurements also record a CO/SO_2 ratio much higher than inventories [*Wen et al.*, 2008]. It is also worth mentioning that CO/SO_x (~27) and CO/NO_y (~55) ratios from earlier measurements downwind of the Beijing area [*Carmichael et al.*, 2003] indicated a possible low bias in inventory CO emissions for the region as well. Neither chemical conversion of SO_2 nor different release heights of SO_2 and CO would explain the revealed discrepancy. While quantitatively evaluating emissions for a vast country like China is difficult with measurements from a single location, it is plausible that CO emitted from China could still be underestimated (or SO_2 might be overestimated or SO_2 emissions might have decreased in recent years) [*Streets et al.,* 2006], since the inventories have difficulty matching the observed CO/SO_2 ratios for more polluted areas. The inventory ratios of CO/SO_2 are generally low (around 10) in some biggest cities of China [*Streets et al.,* 2003, 2006]; emissions from mobile sources, biofuel, and small coal-fired boilers in China need to be further measured to reduce the uncertainties [*Streets et al.,* 2006].

Our conclusion that CO emissions from China might be underestimated, to a large extent, relies on the SO_2 inventory, and it is worthwhile to discuss the recent trend of emissions from China. Since 2001, a substantial fraction of coal-fired power plants in China have been equipped with flue-gas desulfurization (FGD) devices. From 2001 to 2006, the penetration of the FGD technique increased from 3% to 30%, reducing the average SO_2 emission factor for Chinese coal-fired power plants by 15%

[*Q. Zhang*, personal communication]. Despite this improvement in the emission controls, SO_2 emissions from China during the same period increased by ~30-50% [*Chinese CBS*, 2006; *Q. Zhang*, personal communication]. The uncertainty of SO_2 emission inventory for China is relatively small (within 20%, [*Streets et al.*, 2003; *Q. Zhang*, personal communication]). Therefore it is unlikely that SO_2 is overestimated or has decreased (in fact SO_2 emissions from China in 2005 are likely greater than in 2000, the base year of *Streets et al.* [2003]); and it is very plausible that CO emissions from China in 2005 are much higher than in 2000 and 2001 (base years of *Streets et al.* [2003, 2006]). Indeed a new emission inventory that is just becoming available [*Q. Zhang et al.*, A new inventory of anthropogenic emissions in Asia for the year 2006, *Atmos. Chem. Phys. Discuss.*, manuscript in preparation, 2008] estimates that CO (166889 Gg/yr), SO_2 (31020 Gg/yr), and NO_x (20830 Gg/yr) emissions from China in 2006 are all higher than in 2000 and 2001. The national inventory ratios of CO/SO_2 and CO/NO_x for China based on this new inventory are 12.3 and 12.6, respectively, still lower than our measurement-derived values. The CO/SO_2 and CO/NO_x inventory ratios for Beijing and Hebei (the province with strong emissions to the south and southwest of Xianghe) combined are 16.4 and 18.2, respectively. These are higher than the national values, but lower than our observations. It appears that although this updated emission inventory has attempted to account for some recent changes, it may still underestimate CO emissions from China.

Trace gas emissions from a small coal-fired boiler at the Xianghe site were characterized with ambient data. Our estimated SO_2 (15 g/kg) and NO_y (2 g/kg) emission factors are in line with inventories. But the CO emission factor (31 g/kg all

data, 50 g/kg cold start) is only one third of the values used in inventories [*Streets et al.*, 2003, 2006]. If the boiler in this study is representative, similar small boilers in China may be more efficient than previously thought, and would not account for the possible low bias in inventory CO. However, this conclusion needs to be verified by measuring emissions from more boilers under different running conditions. Mobile sources, on the other hand, are becoming more important in Chinese cities, and experiments characterizing their emissions are called for. Note that small coal boilers may have severe local environmental effects, as they are often in residential areas, run under stagnant weather conditions, and have low stacks with insufficient emission control measures.

In summary, in this chapter I have presented results from the Xianghe ground experiment. I evaluated some current emission inventories of China, and found substantial uncertainties in inventory CO emissions, which are likely biased low. Examining the plumes from a local coal-fired boiler suggested that emissions of CO from similar boilers in China are less intense than earlier estimates, and that emissions of mobile sources and biofuel need further studies. The observed day-to-day variations in air quality are closely related to frontal systems. The interaction between atmospheric chemistry and synoptic systems will be the focus of later chapters.

Chapter 4: Shenyang Aircraft Campaign

4.1 Overview of the Aircraft Campaign

Many of the results presented in this chapter have been published in the *Journal of Geophysical Research* special section on EAST-AIRE [*Dickerson et al.*, 2007]. Additional information on the meteorology and flights as well as day-to-day variation of air quality during the aircraft campaign is given in this section.

4.1.1 Weather

Weather in Shenyang area during the aircraft campaign was characterized by frequent passages of mid-latitude wave cyclones. During the 12-day experiment from April 1 to 12, 2005, four low pressure systems visited the region, two of which brought precipitation (April 6 and 9) including thunderstorms on April 6. Accompanying these low pressure centers and the associated fronts, as discussed in Chapter 3, were changes in pollutant levels and meteorological conditions such as wind speed, wind direction, temperature and RH. Ahead of cold fronts, winds were usually from the relatively warm and moist south; behind cold fronts, winds from the cold and dry north were more common. Figure 4.1 and Table 4.1 summarize weather conditions recorded during the experiment. Daily surface weather maps at 00 UTC (8 am LST) over East Asia, generated by the Korean Meteorological Administration (KMA), are given in Appendix I.

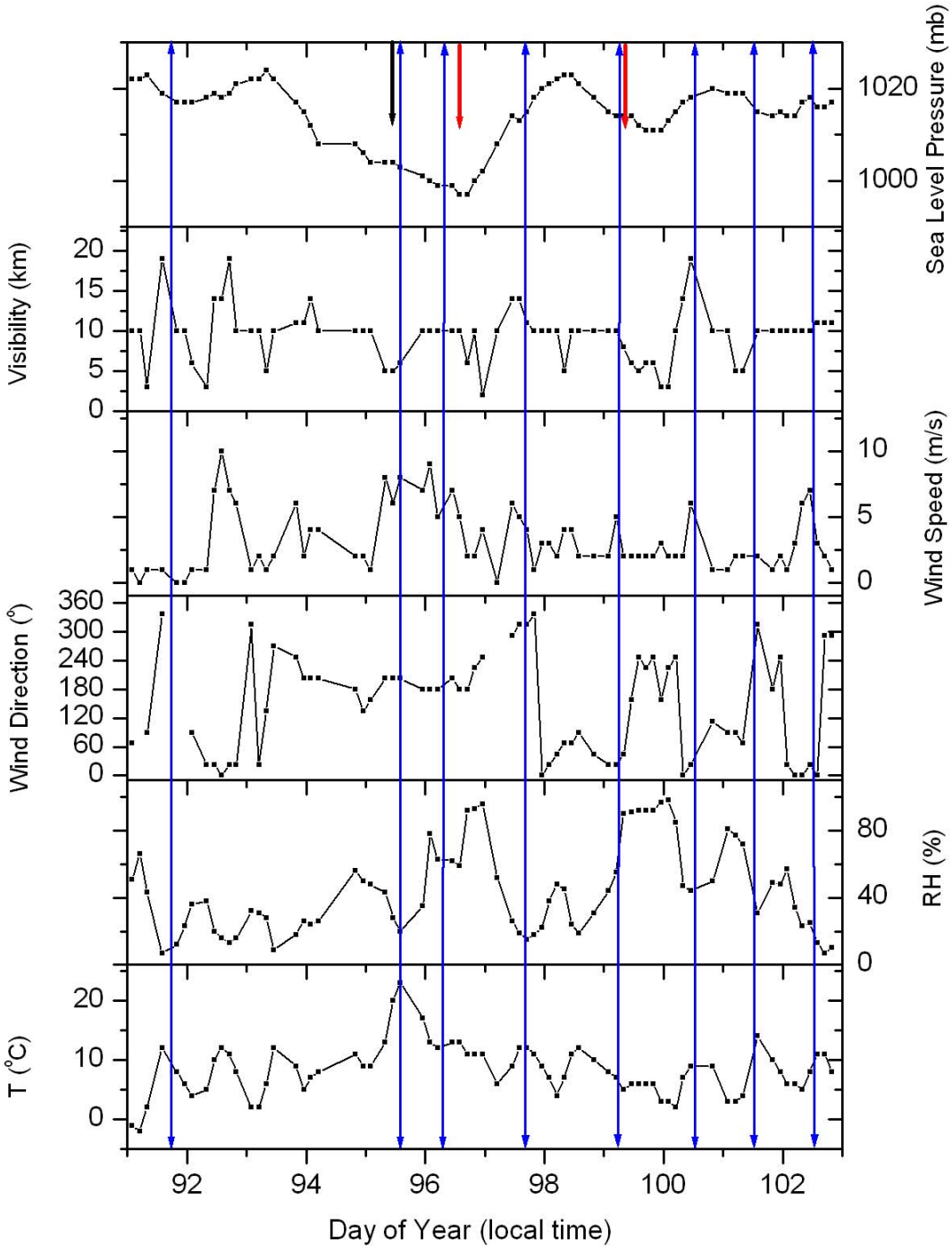

Figure 4.1. Meteorological records from the airport near Shenyang where the Y-12 research aircraft was deployed during the experiment. Blue lines with arrows roughly mark the time of flights. Red and black arrows in the top panel indicate rain and "blowing dust" observed by the meteorologist at the airport, respectively.

Table 4.1. Summary of weather conditions during the Shenyang aircraft campaign.

Date	Weather Conditions
April 1, 2005 (DOY 91)	A high over the region, a weak low to the SW but moving E, variable wind direction, low surface wind speed (< 1 m/s).
April 2, 2005 (DOY 92)	A low E of Shenyang over Korea, a high controls the region. Strong N winds in daytime (surface wind speed up to 10 m/s).
April 3, 2005 (DOY 93)	High over the region but moving E. A strong low sits NNW of the region, with its trough W of Shenyang near China-Mongolia border. Variable winds.
April 4, 2005 (DOY 94)	Two lows (N, and WNW of Shenyang) with a ridge sitting in between. Weak surface winds in daytime generally from S.
April 5, 2005 (DOY 95)	A strong low with its center to the NW, and its trough extending southward, W of Shenyang. Strong S winds up to 8 m/s. Local dust emissions and very low visibility.
April 6, 2005 (DOY 96)	The strong low passed the region on the day, bringing rain in the morning and strong thunderstorms in the afternoon.
April 7, 2005 (DOY 97)	The low moved to E of Shenyang; its cold front was over the Sea of Japan. Strong surface winds from NW (up to 6 m/s).
April 8, 2005 (DOY 98)	A high over the region. Winds mostly from NE up to 4 m/s. A weak low was NW of the region, just S of Lake Baikal.
April 9, 2005 (DOY 99)	The low on the previous day moved SE to the China-Mongolia border NW of Shenyang region. Another low about 1000 km to the S, near Shanghai. A high W of the two lows. Winds variable, with changing from generally N to generally S. Wind speed 2-5 m/s. Light rain during the day.
April 10, 2005 (DOY 100)	The low E of the region, over the Sea of Japan. High pressure system over the area. Winds from N during the day, with surface wind speed up to 6 m/s.
April 11, 2005 (DOY 101)	A weak low with its trough W of Shenyang. Variable winds from S, E, and W, surface wind speed no more than 2 m/s.
April 12, 2005 (DOY 102)	A high to the W dominated the region. Surface winds as strong as 7 m/s generally from N.

4.1.2 Flight routes

Different flight routes were chosen under various weather conditions. Spiral ascents were made over the same locations but on different days, as mid-latitude lows passed the region, to measure prefrontal and postfrontal pollutant profiles. In these profiling flights (April 5, 7, 10, and 11), the aircraft went up in spirals from ~300 m

to ~4000 m altitude (above sea level) over two locations roughly 100 km from Shenyang, one to the south and the other to the north. In two cloud seeding flights on April 7 and 9, the aircraft mostly flew through clouds at constant altitudes of about 3000-4000 m. Additionally there was a transit flight from the service facility to the airport on April 1, and a survey flight on April 12. Table 4.2 gives information for each flight. Maps of flight routes are available from the EAST-AIRE website at: http://www.meto.umd.edu/~zli/EAST-AIRE/station.htm. Flight height information can be found in Figure 4.2.

Table 4.2. Summary of the flights during the Shenyang aircraft campaign.

Date	Takeoff (LST)	Landing (LST)	Flight Description
April 1, 2005	13:45	15:51	Transit flight from the service facility in Harbin (45.71ºN, 126.65ºE) to Shenyang airport (41.64ºN, 123.49ºE). Flight altitude about 3000 m.
April 5, 2005	10:36	13:40	Research flight: one spiral of 300-4000 m at 11:30 over Liaozhong, S of Shenyang (41.37 ºN 122.61 ºE), and one spiral of 400-4000 m at 13:00 over Xiaoming, N of Shenyang (42.48ºN 123.61ºE)
April 6, 2005	07:28	09:34	Cloud seeding flight in the triangular area between Haicheng (40.85°N, 122.70°E), Benxi (41.30°N, 123.83°E), and Tieling (42.28°N, 123.83°E). Flight altitude about 3000 m.
April 7, 2005	14:43	18:13	Research flight: one spiral of 400-4000 m at 15:40 over Xiaoming, and one spiral of 300-4000 m at 17:10, over Liaozhong.
April 9, 2005	04:17	07:47	Cloud seeding flight E of Shenyang. Flight altitude about 3700 m.
April 10, 2005	10:05	13:30	Research flight: one spiral of 500-4000 m at 11:10 over Xiaoming, and one spiral of 300-4000 m at 12:30, over Liaozhong.
April 11, 2005	09:53	14:04	Research flight: one spiral of 80-4000 m at 11:30 over Liaozhong, and one spiral of 400-4000 m at 13:00 over Xiaoming.
April 12, 2005	11:00	12:54	Research flight surveying the region around Shenyang. Flight altitude about 1000-1500 m.

4.1.3 Synoptic variation of air pollution during the aircraft campaign

As can be seen from Figure 4.2, air pollution over Shenyang region features strong day-to-day variation. Below 1000-1500 m altitude, or generally within the daytime PBL, flights on April 1, 5, and 11 found SO_2 as much as 20 ppb near ground and up to 10 ppb around 1000 m, as stagnant conditions prevented dispersion (April 1 and 11) or strong surface winds blew from the populated and industrialized region to the south of Shenyang (April 5). Meteorological records (Table 4.1) suggest that these flights were conducted with a low pressure system approaching the area from W, and in general represent prefrontal atmosphere. Flights on April 7, 10, and 12 were under fairly strong N winds and high pressure systems. These postfrontal flights recorded little SO_2 near ground, mostly less than 5 ppb. Small legs of April 12 flight with high SO_2 were probably influenced by large point sources the aircraft flew over. Small SO_2 concentrations measured over the airport on April 6 and 9 were likely related to wet removal processes on the two rainy days. Above the PBL, SO_2 concentration is generally low (cf. section 4.2 for more detailed results). But substantial SO_2 was measured at 2000-3000 m altitude on April 5. Propelled by strong westerly winds in the free troposphere (FT), the observed SO_2 and other pollutants can potentially travel far downwind, and will be the major topic of discussion in section 4.2. Column integrated SO_2 varied from as little as 0.1-0.2 Dobson Unit (DU) on April 7 and 10 to as much as 1-2 DU on April 1 and 5 [*Krotkov et al.*, 2008], demonstrating a factor of 10 change in just days.

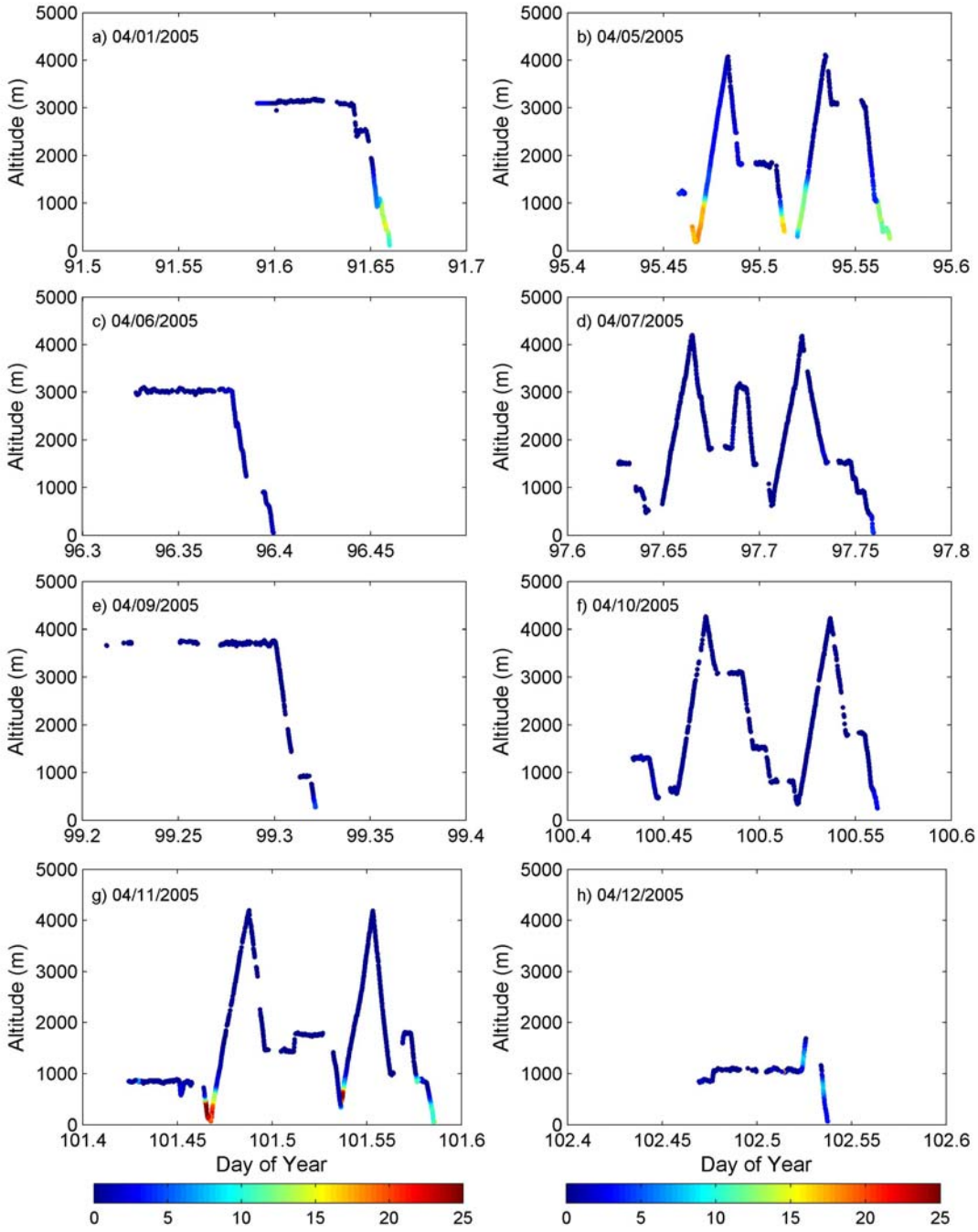

Figure 4.2. Flight altitudes and SO_2 concentrations (in color, unit: ppb) along the flight tracks during the Shenyang aircraft campaign. Gaps in data are mainly due to instrument zero mode.

Aerosol scattering data (Figure 4.3) show somewhat different day-to-day variability compared to SO_2. High aerosol loadings on April 5 (DOY 95), as will be shown later in this chapter and in Chapter 5, are mainly due to local and transported dust. Relatively abundant aerosols at around 2000 m altitude on April 7 are likely dust particles carried into the area by NW winds from arid desert regions. I attribute exceptionally high scattering at 1000-3000 m altitude on April 10 to possible cloud interference as the aircraft flew through a deck of fair weather cumulus. Slightly high aerosol levels near ground during the April 11 flight probably reflect the accumulation of anthropogenic pollutants under stagnant weather conditions. Aerosol optical thickness (AOT) at 500 nm, a measure of the column abundance of aerosol particles, observed from the surface using a hand-held (black squares, Figure 4.4, [*Xin et al.*, 2007]) and a Cimel sun photometers (red dots, Figure 4.4, [*Xia et al.*, 2007]) in the area also was also very variable during the aircraft campaign, ranging from 0.1-0.2 to above 1.0. The difference between the two sun photometers probably originates from different calibrations.

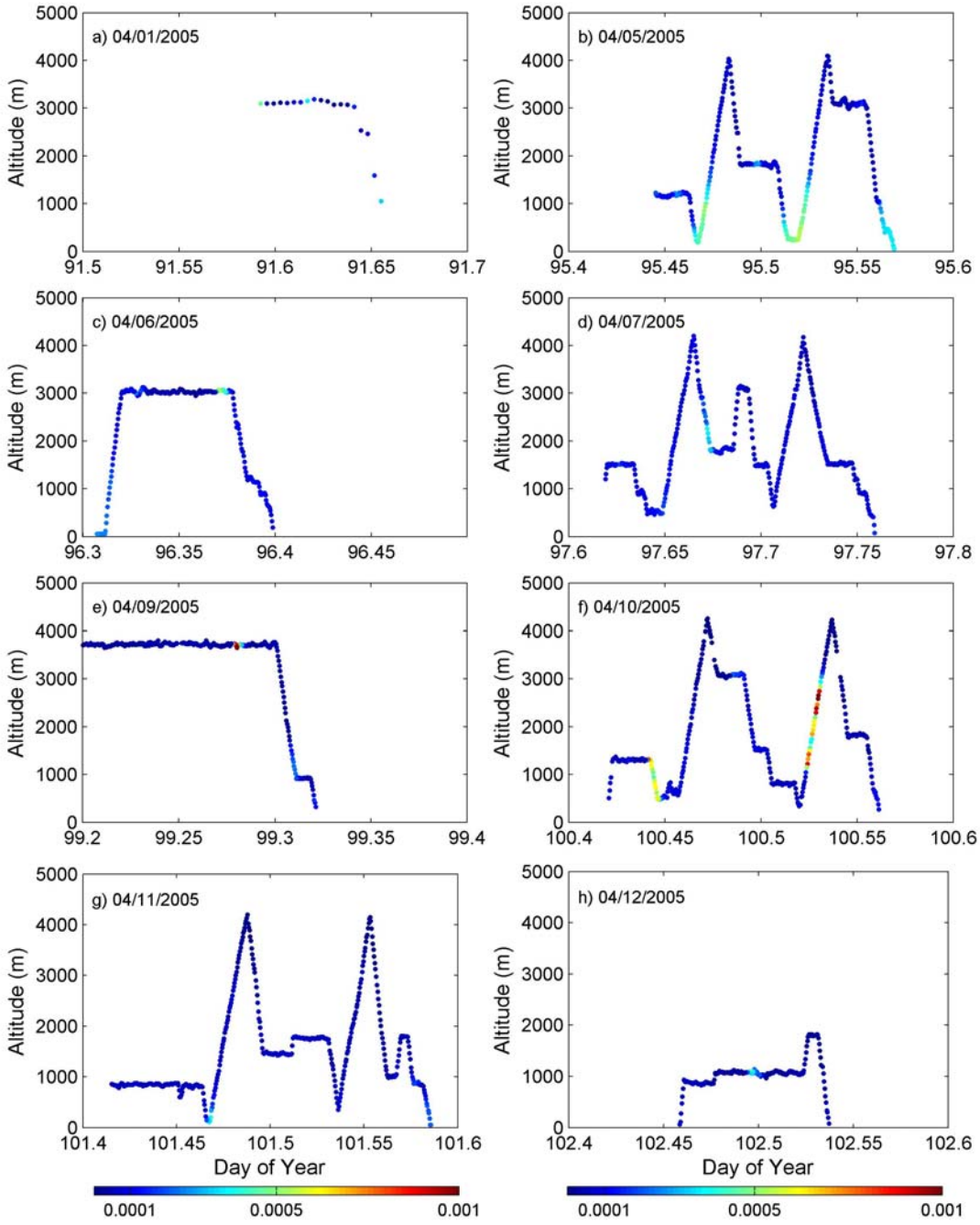

Figure 4.3. Flight altitudes and aerosol scattering at 550 nm (color, unit: m^{-1}) along the flight tracks during the Shenyang aircraft campaign.

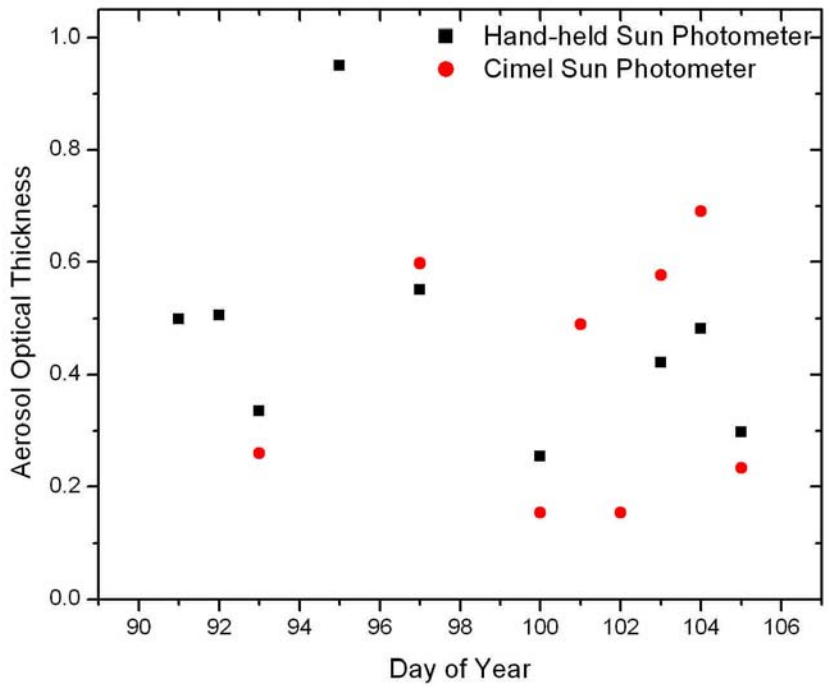

Figure 4.4. Hand-held (black squares) and Cimel (red dots) sun photometer measured aerosol optical thickness at 500 nm over Shenyang area, from April 1 to 15, 2005.

4.1.4 Vertical distribution of pollutants: comparison to the Northeastern U.S.

Here I compare the results from the Shenyang aircraft campaign to the chemical climatology amassed over the past decade through hundreds of flights over the northeastern U.S., with essentially the same bundle of instruments [*Hains et al.*, 2008; *Prados et al.*, 1999; *Taubman et al.*, 2006, 2007]. Detailed analyses on vertical profiles of pollutants from flights on April 5 and 7 are given in section 4.2. Vertical profiles from the other research flights (April 10, 11, and 12) are presented in Appendix II. Our data set from a single season in China is much smaller, but shows that concentrations of trace gases and aerosols over China are markedly greater than are typically measured over N America (Figure 4.5). Both data sets show that SO_2 is

more abundant in the lower PBL than at higher altitudes, but SO_2 in the lowest 500 m over the U.S. [*Taubman et al.*, 2006] is only about one third of that over China. The boundary layer in summer is deeper, and SO_2 over the U.S. around 1000 m altitude, measured mostly in summer, is comparable to the spring results over China from this study. But above the PBL, the mean SO_2 concentration over China is again sizably larger. For example, at 2500 m altitude over the U.S., the mean mixing ratio of SO_2 is 0.2 ppb (90^{th} percentile: 0.6 ppb) and over China the mean is greater at 0.6 ppb (90^{th} percentile: 2.3 ppb). The aerosol scattering over China in spring is greater than that under smoggy summer conditions over N America, and an order of magnitude larger than over the U.S. in spring. At 2500 m, the average b_{sp} over N America in summer is about 50 Mm^{-1} (10^{-6} m^{-1}); the average over China is about 250 Mm^{-1}. These results underscore the potential large-scale impacts emissions from China may have, but further flights are required to build a comprehensive chemical climatology over the region. Comparison of CO profiles is given in Figure 4.11, section 4.2.

Another interesting comparison that can be made between the U.S. and China data is about the Ångström exponents (AE), determined with the same nephelometer (Chapter 2) and sometimes used as a proxy of the overall particle size (Figure 4.6). The Ångström exponents over China are smaller than over the eastern U.S. at all levels. With exceptions at few altitudes, the 75^{th} percentiles of China data are smaller or comparable to the 25^{th} percentiles of the U.S. data. This suggests that using the same instrument, the overall size of aerosols sampled over N China is greater than over the NE U.S. Note there could be substantial sampling line losses of larger particles in both data sets, but particularly so over the dust-laden N China. Surface

measurements at three AERONET sites generally in the flight regions of China (Liaozhong and Xianghe) and the U.S. (Goddard Space Flight Center, GSFC, Greenbelt, MD), show similar differences in Ångström Exponents (Table 4.3). This comparison corroborates the importance of dust in aerosol loadings over N China in the dry spring months, as discussed in Chapter 3 and earlier in this chapter.

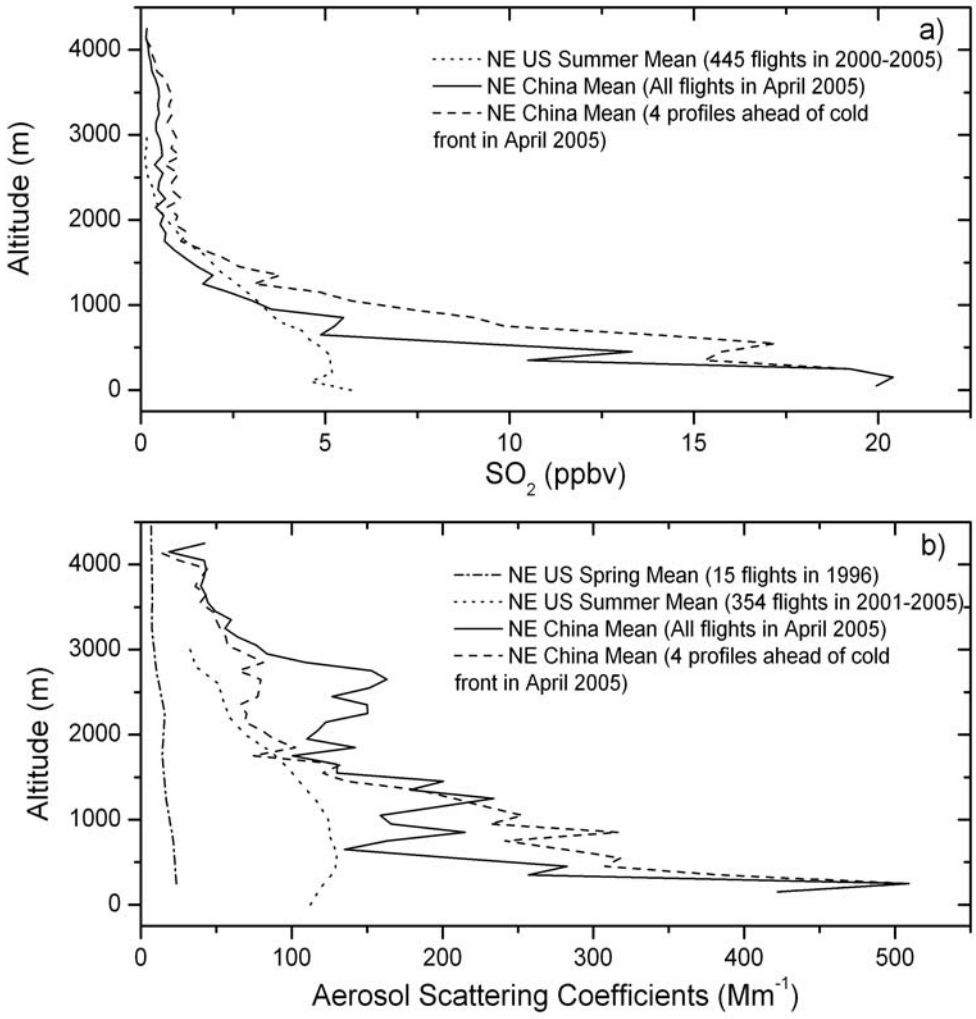

Figure 4.5. a) Mean vertical profiles of SO_2 for flights ahead of the front (dashed line) and all eight flights during the Shenyang experiment (solid line). For comparison, the mean SO_2 profile measured on smoggy summer days over the NE U.S. [*Taubman et al.*, 2006] is shown as a dotted line. **b)** Mean vertical profiles of aerosol scattering (b_{sp}) at 550 nm ahead of the front (dashed line) and for all eight flights conducted during the Shenyang experiment (solid line). For comparison, the mean b_{sp} profile measured

over the NE U.S. in spring 1996 is shown as a dot-dash line and the mean for smoggy summer days is shown as a dotted line [*Taubman et al.*, 2006, 2007].

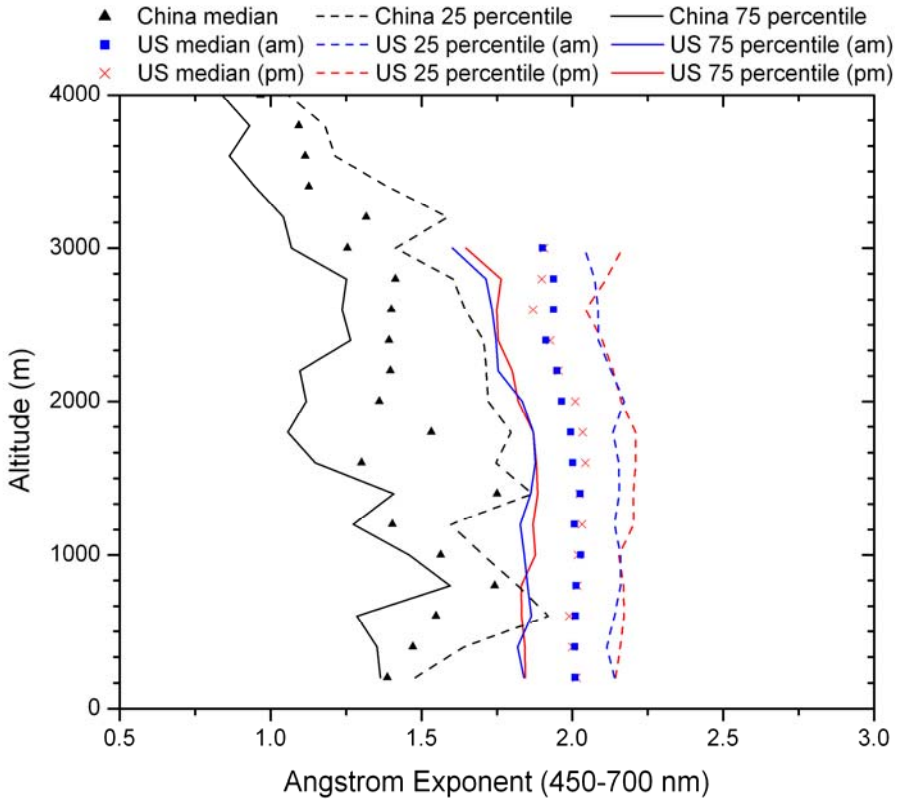

Figure 4.6. Vertical profiles of Ångström Exponents observed from aircraft flights over N China in spring and over the NE U.S. in summer with the same instrument. Note that overall the aerosols over China are larger and more variable in size. The aircraft measurements mainly represent fine particles due to line losses of coarse particles.

Table 4.3. Statistics of Ångström exponents (440-675 nm) in 2005 at three AERONET sites in China and the U.S.

Site	Period (DOY)	25th Percentile	Median	75th Percentile	Mean	Standard deviation
GSFC[a]		1.39	1.75	1.86	1.62	0.30
Liaozhong[b]	97-120	0.43	0.82	1.20	0.81	0.42
Xianghe[c]		0.60	0.86	0.97	0.78	0.28
GSFC		1.45	1.75	1.88	1.68	0.28
Liaozhong	97-186	0.78	0.97	1.23	0.96	0.32
Xianghe		0.82	1.06	1.22	1.00	0.30

[a] GSFC: 38.99°N, 76.84°W, AOT (500 nm) = 0.27 ± 0.17 (mean ± std. dev.) during DOY 97-186 in 2005;
[b] Liaozhong: 41.51°N, 122.70°E, AOT (500 nm) = 0.73 ± 0.62 (mean ± std. dev.) during DOY 97-186 in 2005;
[c] Xianghe: 39.75°N, 116.96°E, AOT (500 nm) = 0.76 ± 0.63 (mean ± std. dev.) during DOY 97-186 in 2005.

4.2 Upwind Dry Convection and Long-Range Transport: A Case Study

4.2.1 Prefrontal flight on April 5, 2005

The surface weather map and flight route on April 5 are given in Figure 4.7. The weather conditions for this prefrontal flight involved low-level flow from the southwest, some of the highly populated and polluted areas of China. Winds veered with altitude becoming westerly in the mid troposphere. In the area of the flights and to the south, few clouds were observed on that day; the system brought little rain to the flight region until April 6, and by April 7 only cirrus clouds were spotted. Strong surface winds (cf. section 4.1) from the polluted warm sector of the low pressure system brought heavy loadings of pollutants and dust (Figures 4.8 - 4.11). Sizable concentrations of trace gases and aerosols were observed not only in the PBL, but also in the free troposphere (Figures 4.8 – 4.11), where pollutants have relatively long lifetime, and stronger winds could potentially carry them far downwind, leading to possible large-scale impacts.

Aircraft measured temperature and RH profiles (Figure 4.8) indicate a strong inversion (7 °C at 11 am LST) layer at about 1000 m altitude, marking the top of the PBL. The ozone mixing ratios given in the same plot reflect moderate photochemical smog formation, and show a peak just above the inversion. Aerosol scattering coefficients (b_{sp}) also have a maximum at that altitude (Figure 4.9); for reference b_{sp}

of $4x10^{-4}$ m^{-1} corresponds to ~100 μg/m^3 particulate matter for a specific scattering coefficient of 4.2 m^2/g (3 m^2/g for dry ammonium sulfate and ammonium nitrate in the fine mode, 4 m^2/g for particulate organic matter, [*Boylan and Russell*, 2006]). Multiphase reactions in the aerosol rich PBL may suppress ozone formation [e.g., *Lary et al.*, 1997], while a layer of UV-scattering aerosols can inhibit photochemical production of ozone at low altitudes but accelerate it toward the top of the aerosol layer [*Dickerson et al.*, 1997]. These processes may contribute to the increase in ozone from the surface to 1000 m altitude. Concentrations of aerosols and trace gases fell off sharply above the strong inversion, but remained well above background values. Substantial pollutants and possibly mineral dust persisted to the highest altitudes sampled, ~4000 m. As will be discussed in Chapter 5, the heavy loadings of pollutants and dust detected during this flight were widespread and impacted large areas in China, Japan, and northern Pacific as they traveled eastward in the next few days.

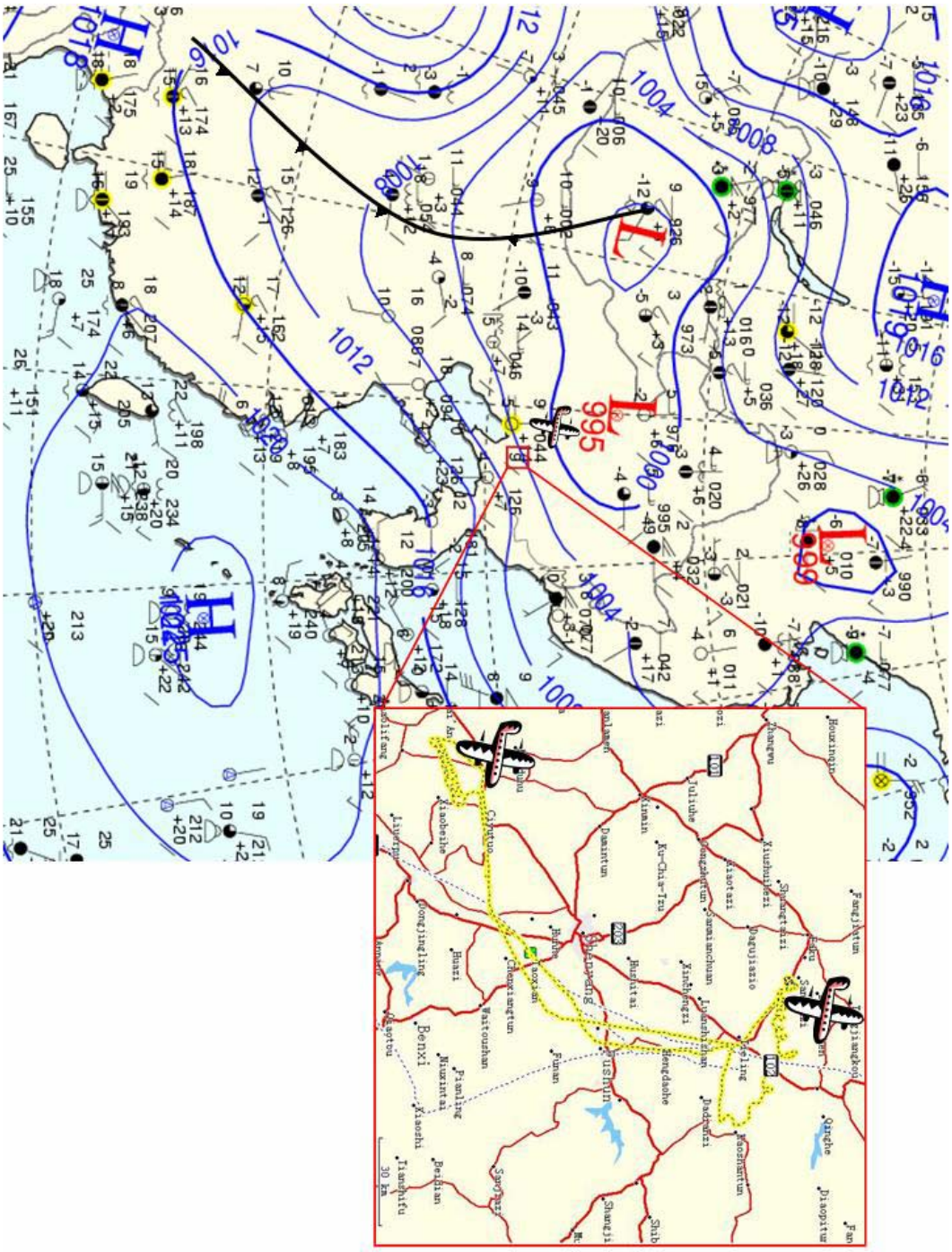

Figure 4.7. Surface analysis (Korean Meteorological Administration) for 00 UTC April 5, 2005 showing a low-pressure system (cyclone) moving towards Shenyang. The approximate location of the flights is shown by the symbol of an aircraft and the actual flight pattern is shown in the insert. Profiling spirals were conducted north and south of Shenyang (locations marked with aircraft symbols). Note little cloud cover or precipitation was reported in the vicinity of the flight and several hundred km to the south ahead of the surface cold front. Yellow circles indicate occurrence of fog.

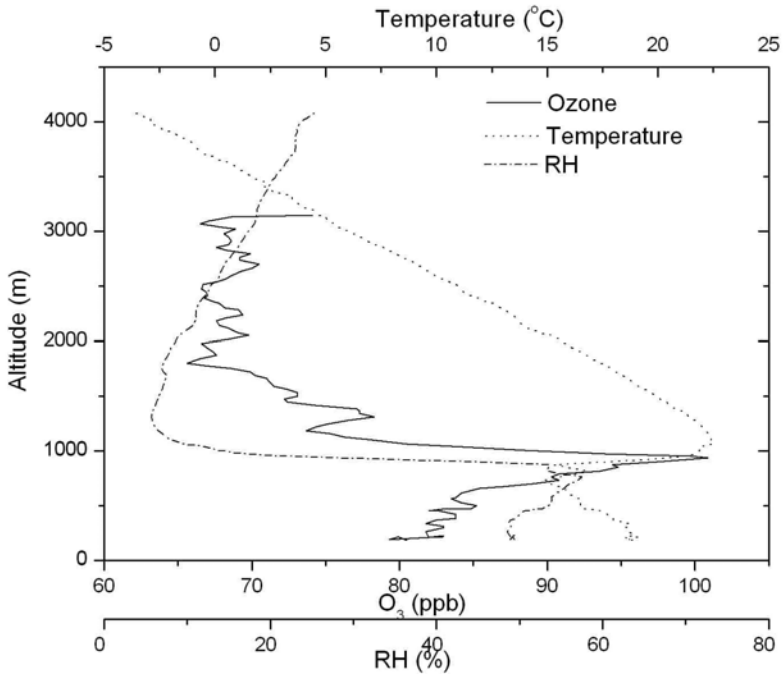

Figure 4.8. Vertical profiles of ozone, RH, and temperature measured south of Shenyang at 11:30 LST on April 5, 2005. Note maximum in RH and ozone near the strong temperature inversion (7˚C) around 1000 m altitude. In the lower free troposphere the air is dry and ozone concentrations are lower. See Appendix II for vertical profiles measured N of Shenyang on the same flight.

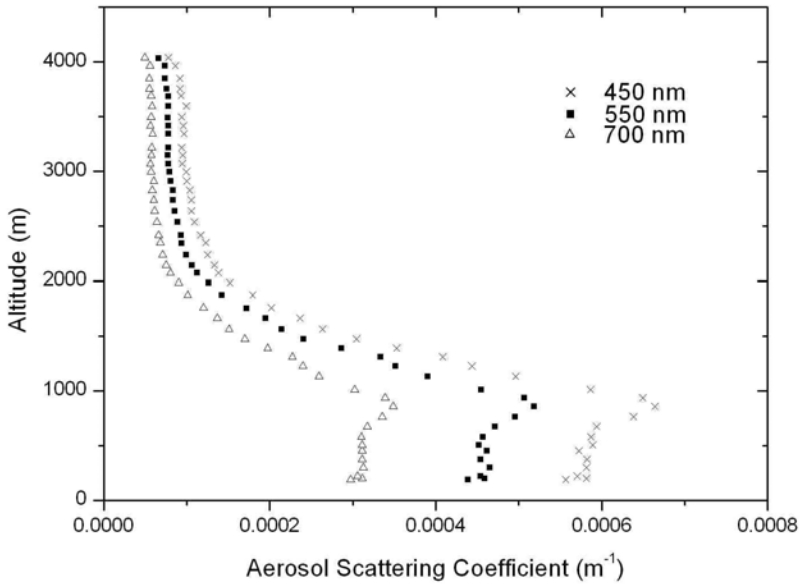

Figure 4.9. Vertical profile of aerosol scattering coefficients, b_{sp}, for the morning (11:30 LST) flight south of Shenyang on 5 April 2005.

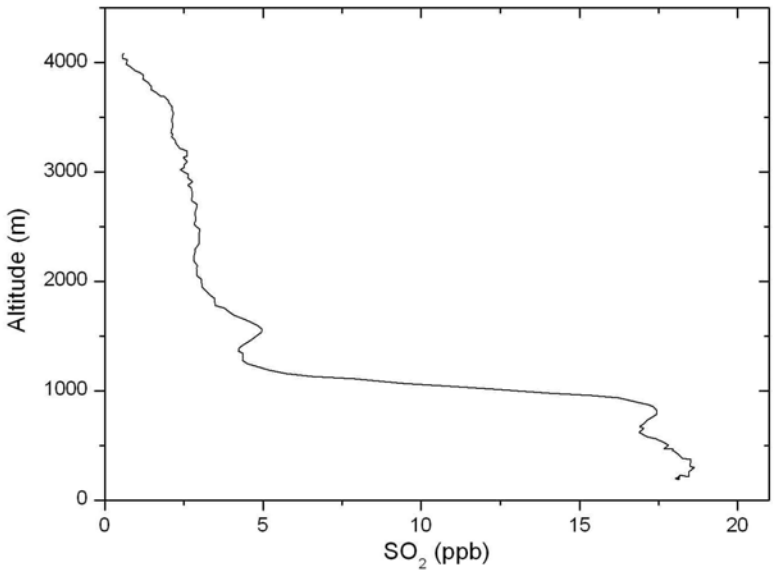

Figure 4.10. Vertical profile of SO_2, for the morning (~11:30 LST) flight S of Shenyang on April 5, 2005. Note the high SO_2 level in PBL. Above the inversion layer SO_2 drops off quickly but remains almost 3 ppb between 2000 and 3000 m. The profile north of Shenyang (Appendix II) shows less but still around 1 ppb of SO_2 at the same altitudes.

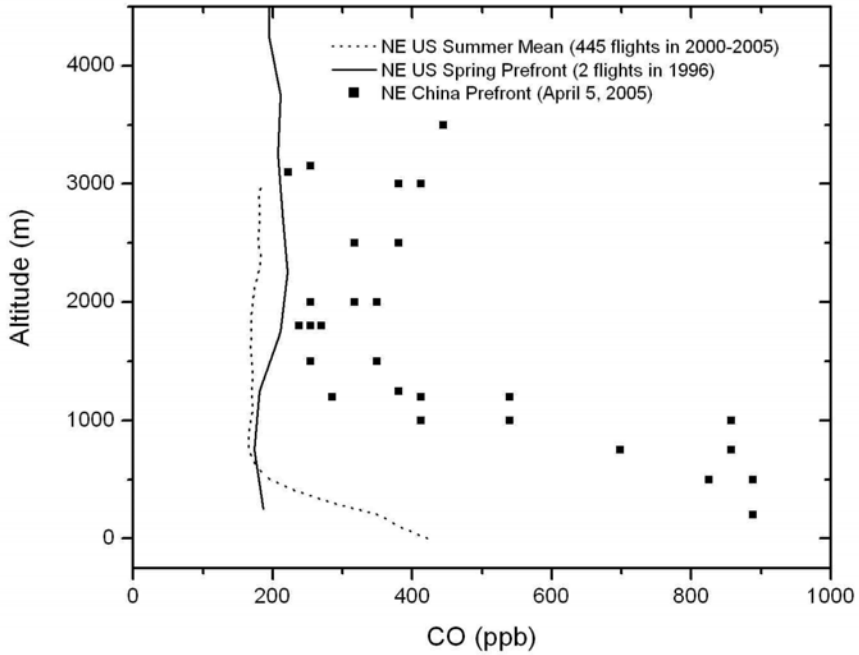

Figure 4.11. Vertical distribution of carbon monoxide from the flight of April 5, 2005 (squares). Mixing ratios over China drop off sharply above the inversion near 1000 m, but remain well above the background. The median CO profile from ~400 flights made on smoggy summer days during 2000-2004 over the NE U.S. [*Taubman et al.*, 2006] (dotted line) and the median for spring flights ahead of fronts over the U.S. [*Taubman et al.*, 2007] (solid line) are shown for reference.

To help identify the meteorological mechanism lifting the high concentrations of aerosols and trace gases above PBL, consider the backward trajectories (Figure 4.12) calculated with the HYSPLIT (Hybrid Single-Particle Lagrangian Integrated Trajectory) model and NCEP global reanalysis meteorological data. Flow at low levels, in agreement with the surface weather analysis (Figure 4.7), was from the southwest while flow at higher altitudes originated from the west. Little evidence of upward motion is seen in the pre-frontal zone along the east coast of China; in fact, back trajectories only indicate some weak upward motion, suggesting that in this case the WCB was not effective in lofting pollutants over the continent. The back-trajectory model and meteorological data used here cannot resolve small-scale vertical motions such as those caused by convective clouds. I examined GOES-9 satellite infrared images for April 3–5 2005 for clouds, and confirmed that in the warm sector where the low-level air originated, the sky was generally clear. Convection ahead of the cold front (associated with clouds) does not appear to have been the mechanism responsible for pollutant lofting in this event.

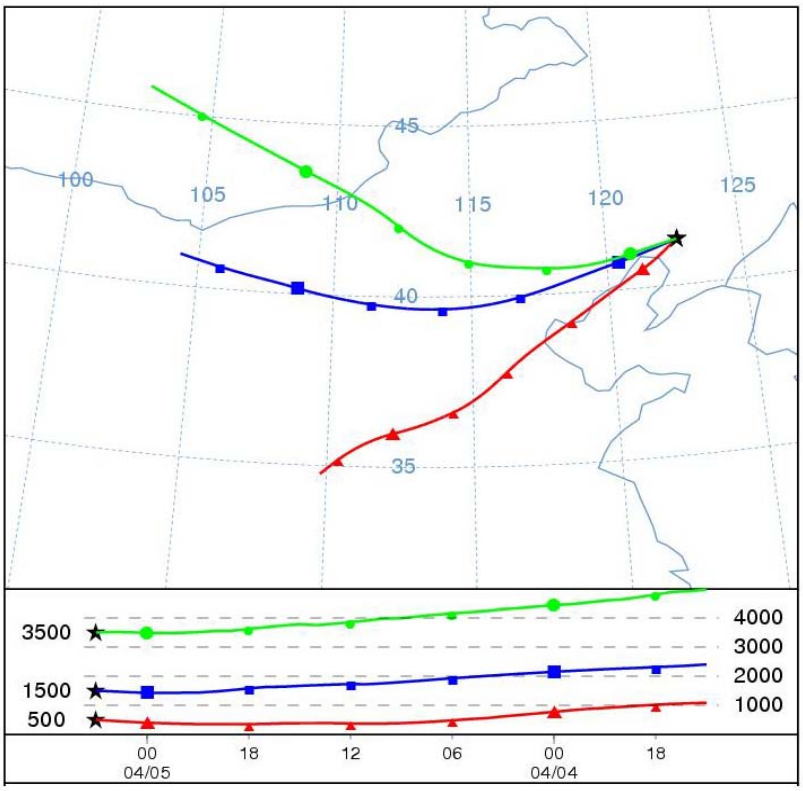

Figure 4.12. Backward trajectories calculated with the HYSPLIT model for air arriving at location of the southern spiral (41.4ºN, 122.7ºE, Figure 4.7) in the PBL (500 m above ground level) and in the FT (1500 and 3500 m) on April 5. The lower panel depicts vertical motions and shows little evidence of WCB lofting in the prefrontal zone for this episode. Back trajectories for the second spiral point, 200 km to the north and 2 hr later are similar.

Convective transport from west (upstream at higher altitudes) of the flight area likewise would not be captured by the backward trajectories, but deep clouds could lift pollutants and dust to high altitudes where they could travel in strong westerly winds to the Shenyang area. Satellite images (Figure 4.13) show strong convection over arid NW Mongolia (in the top left corner of the image). This part of the world is sparsely populated and unlikely the source of CO and SO_2 observed in the flight, but could be the source of dust. A smaller convective system is seen along the back trajectory (Figure 4.13) corresponding to the origin of the air 27 hr prior to

the flight. The MODIS IR cloud height analysis indicates that these cloud bands reached maximum heights of 6-12 km. They formed near the industrialized cities of Baotou and Hohhot with large steel mills, and could have detrained pollutants and dust to high altitudes, and caused the high concentrations of pollutants seen in the free troposphere during the prefrontal flight on April 5, ~ 1 day later (Figure 4.14).

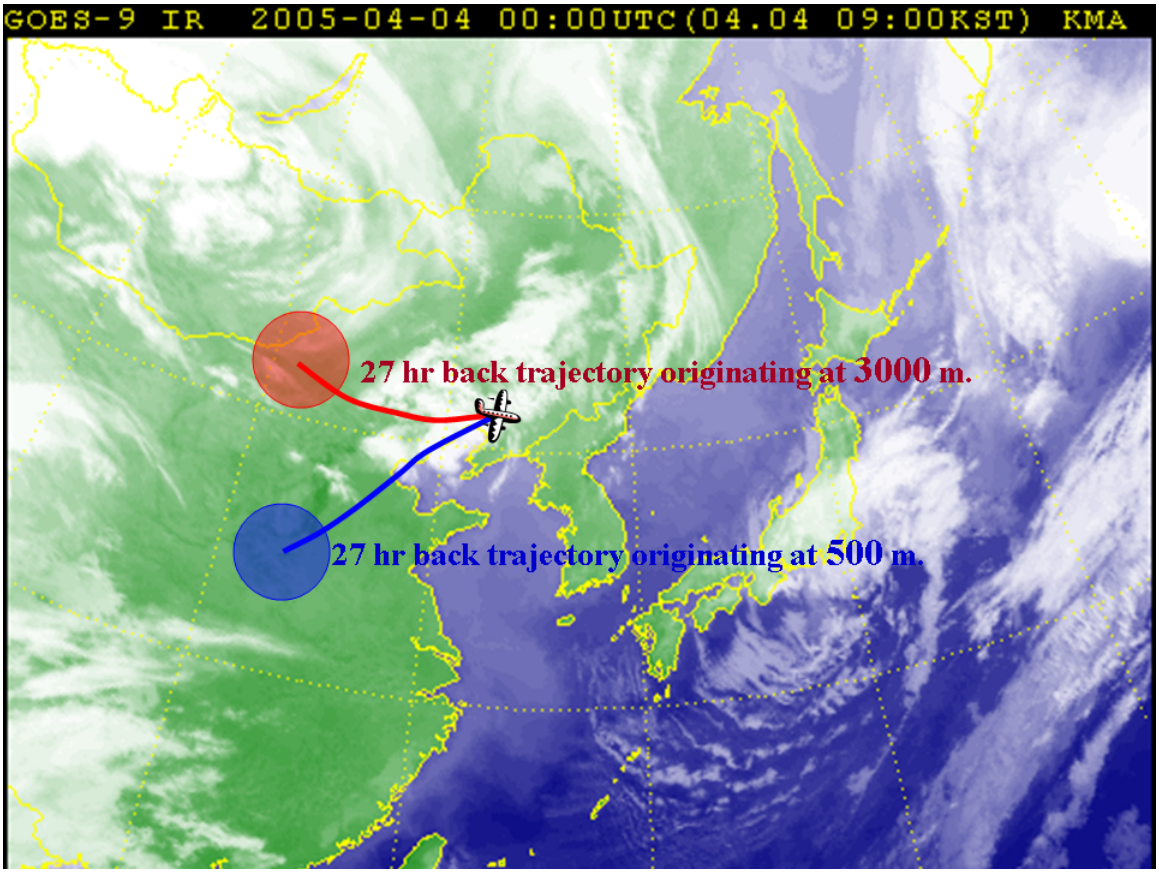

Figure 4.13. GOES-9 IR image for 00 UTC April 4, 2005, 27 hr prior to the flight depicted in Figure 4.7. Back trajectories originating at 500 m (blue line) and 3000 m (red line) are superimposed; the transparent red and blue disks show the approximate area of origin for air sampled on 5 April. Note deep convective clouds to the W and NW and clear skies to the SW.

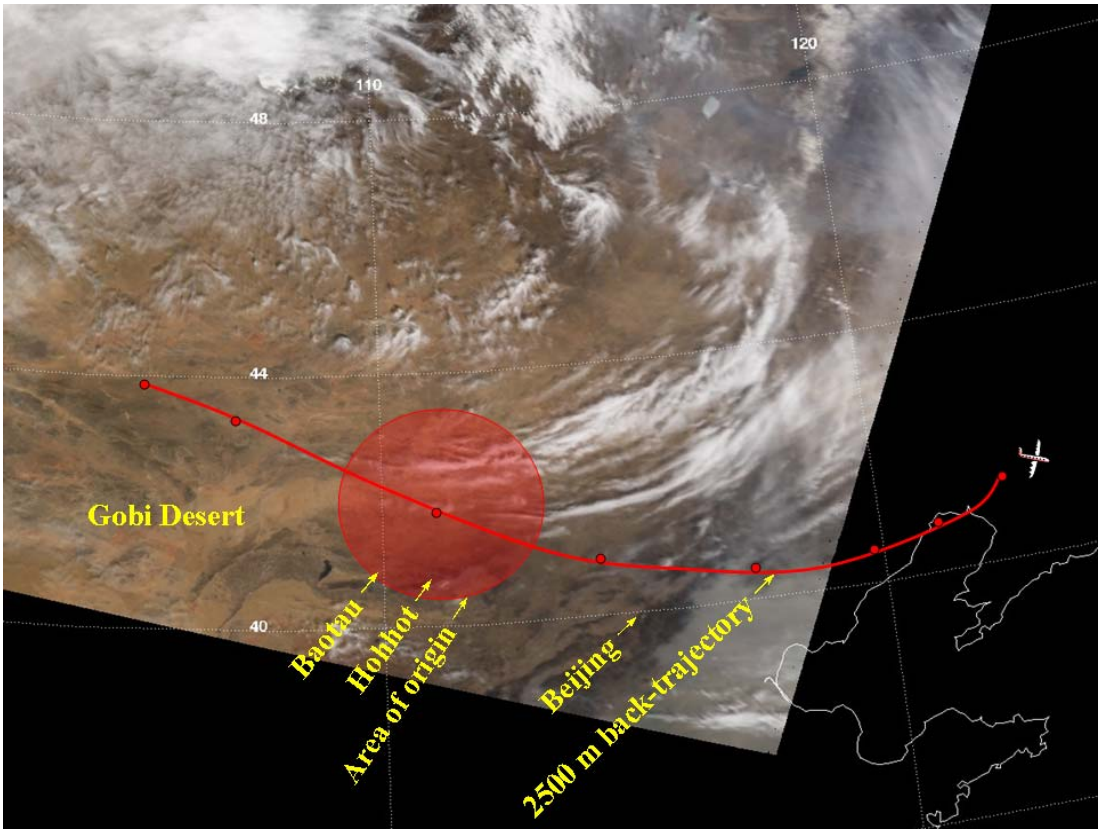

Figure 4.14. MODIS true color image for 04 UTC April 4, 2005 with 2500 m back trajectory superimposed. Heavy convection to NW was over sparsely populated, arid regions of Mongolia. The transparent red disk indicates the approximate origin of the air sampled ~24 h later on the flight of April 5. Baotou and Hohhot are industrial cities with substantial coal combustion and steel production.

4.2.2 Postfrontal flight on April 7, 2005

Following the flight of April 5, 2005, the cold front passed the Shenyang region; the dry, relatively warm continental tropical (cT) air mass moved off the coast and a continental polar (cP) air mass brought cooler, drier air (Figures 4.15 and 4.16). The flight route on April 7 was similar to that on April 5, but the composition of the atmosphere in this cP air mass was largely different (Figures 4.17 and 4.18). Pollutant levels were low, with SO_2 mixing ratios well below 1 ppb. Aerosol loading, however, was lower than on April 5 but still considerable with scattering coefficients of ~8 ×

10^{-5} m^{-1} (or ~80 Mm^{-1}). Bear in mind that the inlet employed for this study is inefficient at sampling coarse mode aerosols. The NASA OMI Aerosol Index shows a broad maximum over Shenyang on April 7, 2005. Ozone concentrations increased above the PBL, reaching a maximum of about 65 ppb, higher than expected for air with low concentrations of ozone precursors [e.g., *Logan*, 1999].

Backward trajectories (Figure 4.16) show rapid subsidence in the free troposphere and brisk flow from the NW – an arid and sparsely populated region of China and Mongolia. The high wind speed and low concentrations of pollutant gases suggest that this could be a dust event with surface material carried aloft from over the Gobi desert and other arid dust source regions. Ozone was likely transported downward from the upper troposphere/lower stratosphere (UT/LS) rather than locally produced in photochemical processes.

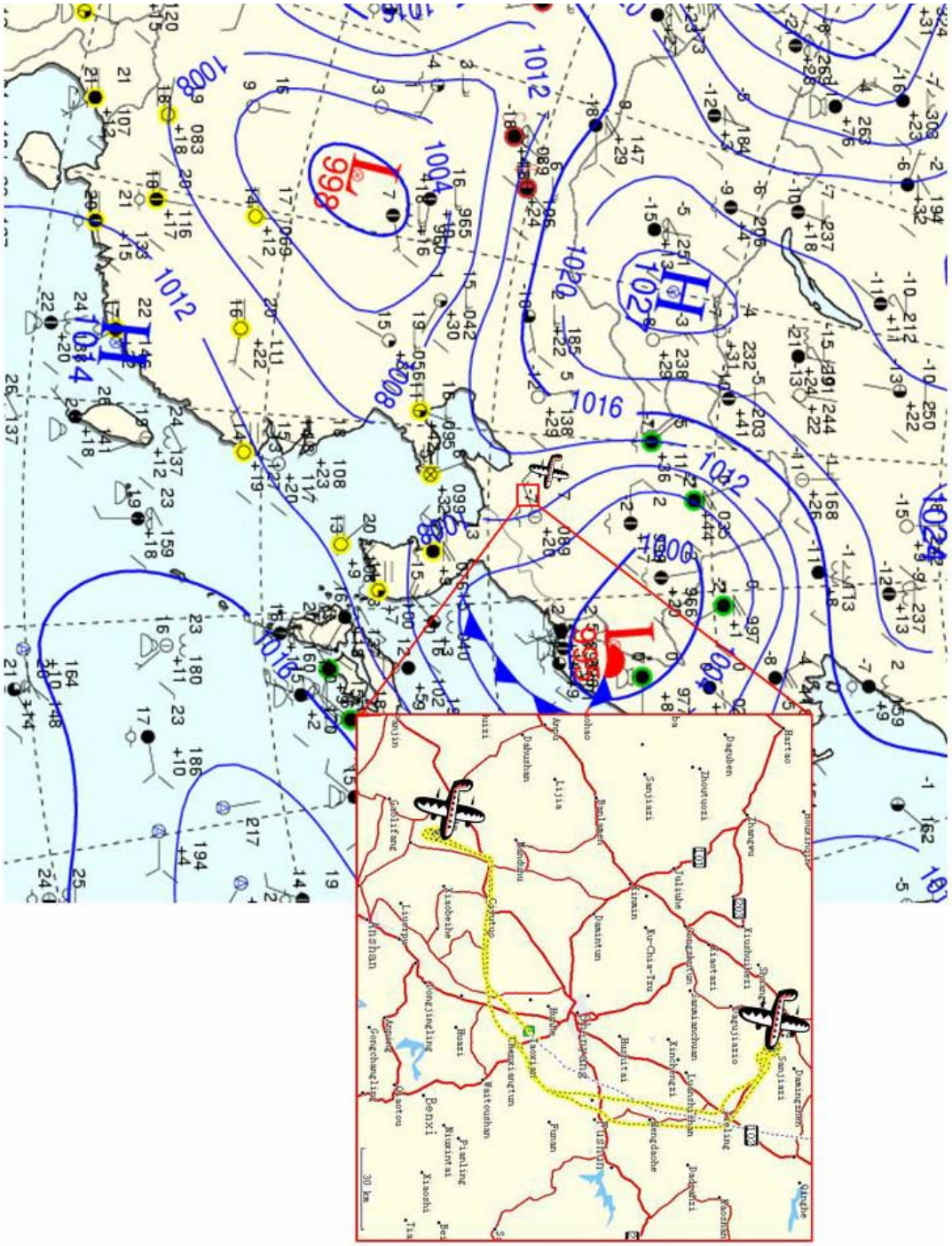

Figure 4.15. Surface weather analysis (Korean Meteorological Administration) for 00 UTC April 7, 2005 showing a cyclone NE of Shenyang. The flight was conducted behind the cold front in northerly flow. The approximate location of the flights is shown by the symbol of an aircraft and the actual flight pattern is shown in the insert. Profiling spirals were conducted north and south of Shenyang (locations marked with aircraft symbols). Yellow circles indicate occurrence of fog.

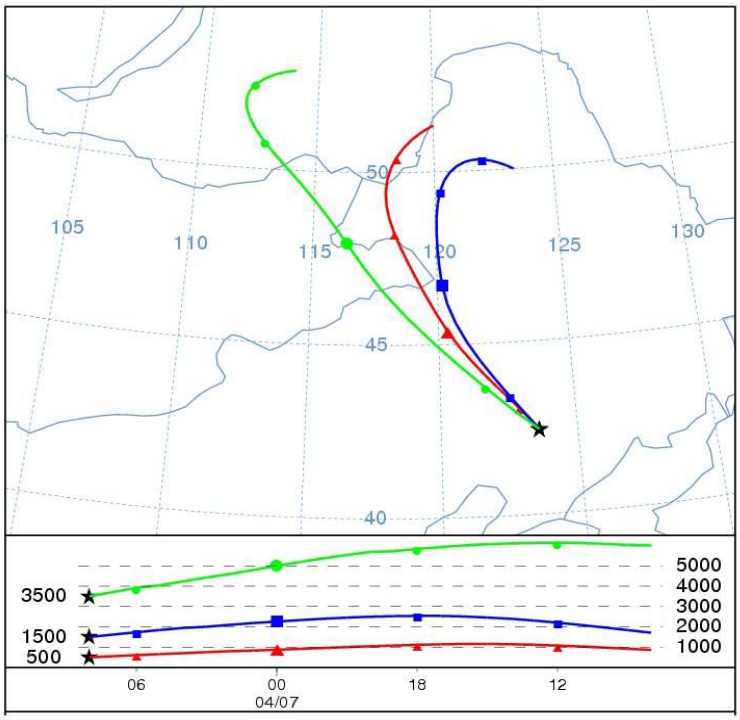

Figure 4.16. Backward trajectories calculated with the HYSPLIT model for air arriving at location of northern spiral (42.5ºN, 123.5ºE) on April 7 (Figure 4.18). The lower panel depicting vertical motions of the trajectories shows subsidence in this postfrontal air.

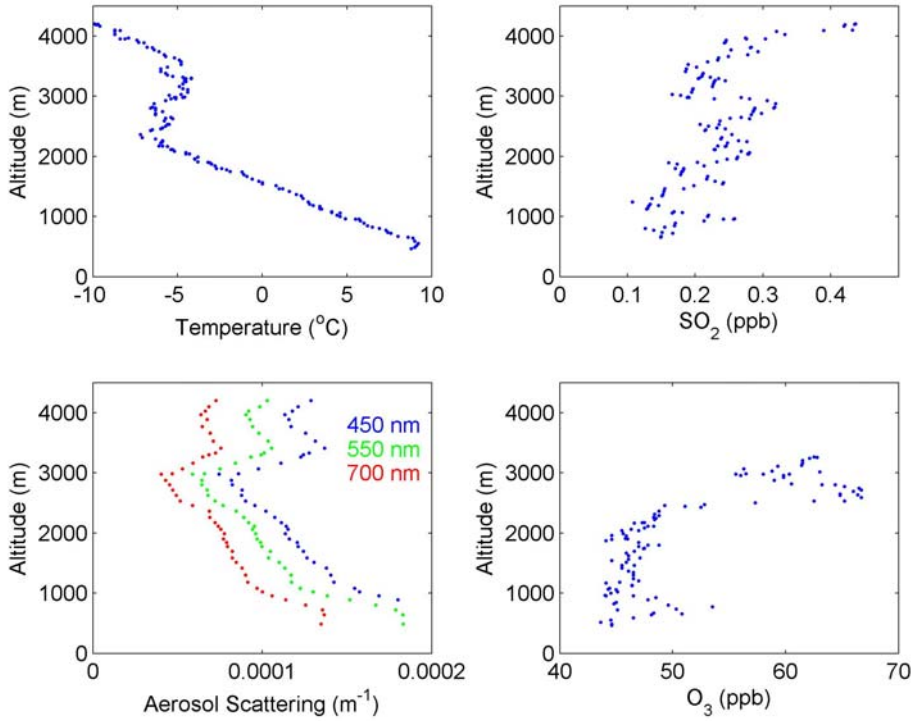

Figure 4.17. Profiles of temperature, trace gases and aerosol scattering north of Shenyang from the flight behind the cold front on April 7, 2005.

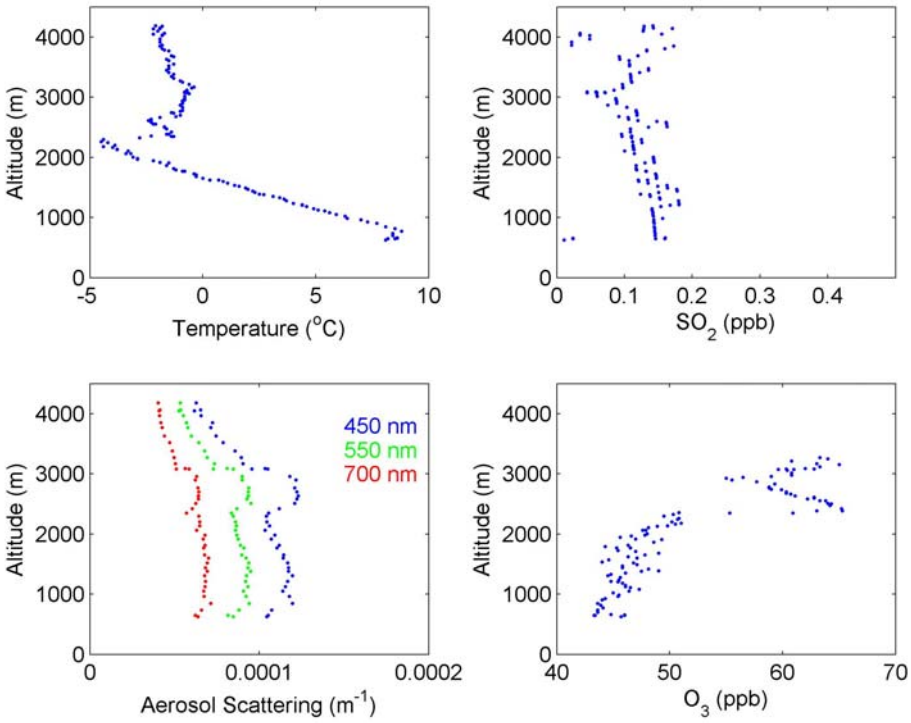

Figure 4.18. Profiles of temperature, trace gases and aerosol scattering south of Shenyang from the flight behind the cold front on April 7, 2005.

4.2.3 Discussion

Lofting of pollutants over North America and the resulting inter-continental transport have been studied more thoroughly than over China, and a comparison of the two regions can be enlightening. Cold front passage is prevalent over both continents, but spring in northern China is dry compared to North America (Figure 4.19). Over North America, cold fronts often demark the collision of maritime tropical (mT) and cP air masses, resulting in convective clouds and precipitation. Over northern China, the air mass in the warm sector generally has continental rather than maritime character; and the low humidities inhibit precipitation. Most of the precipitation in N China falls in the summer months (June to August), while precipitation in the NE U.S. falls more uniformly throughout the year. The area near

Beijing receives less than 20 mm of rain per month in March and April, while Baltimore, for example, receives about 80 mm per month in the two months. The total annual precipitation over N China is about half that over the NE U.S. (Figure 4.19).

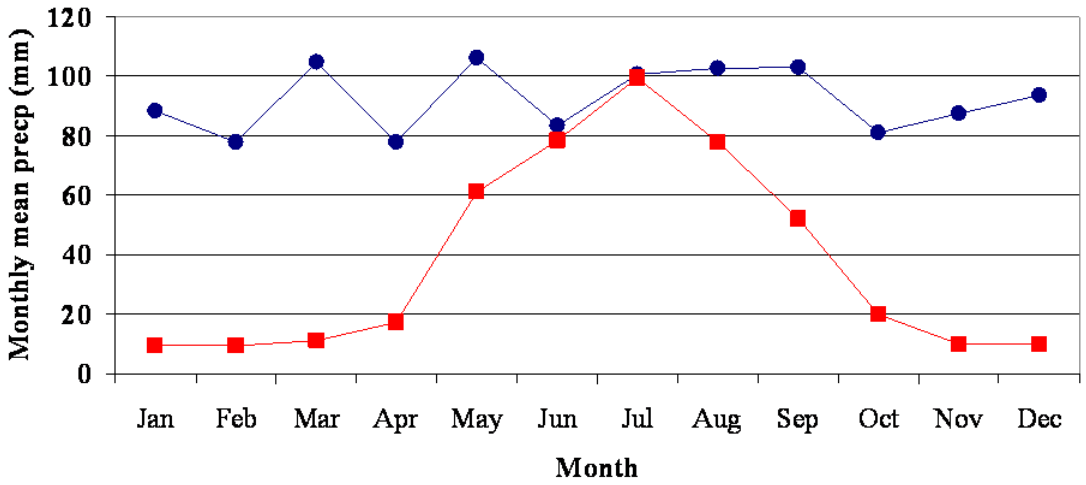

Figure 4.19. Climatology of precipitation near Baltimore and Beijing [*Arakawa*, 1969; *Bryson and Hare*, 1969]. Comparison between Baltimore and several other cities in the NE U.S. (e.g., New York, Philadelphia, and Boston) shows generally the same monthly change in precipitation (data source: National Climatic Data Center). Note that most of the rainfall over N China comes in the summer while over the NE U.S. it is more evenly distributed. In the spring, frontal passage and convection are common over both continents, but little rain is produced over NE Asia, thus dry convection may play a larger role in pollutant transport. N China has experienced severe drought recently, making the differences even greater [*Zou et al*, 2005].

In contrast to precipitation, the average cloud cover over the two continents is not as dramatically different. Over mid-latitudes (35 to 45˚N) the average total cloud cover in spring (MAM) is about 50% near and upwind of Beijing (115 to 130˚E) and 64% over the American Northeast (70 to 85˚W) [*Arakawa*, 1969; *Bryson and Hare*, 1969]. Cumulus clouds are reported about 7% of the time over N China and 9% over the NE U.S. The peak in the diurnal cycle in both places appears at 13:00-14:00 local time; cumulonimbus clouds are present in about 1% of the observations over both

continents. Aerosols might have reduced cloud cover over China in the past few decades, but not enough to change the basic climatology [*Qian et al.*, 2006; *U.S. DOE*, 1986]. In short, convective clouds form over China in spring, but little rain falls.

Pollutants over China even if emitted in great amounts, would have little impact on the global scale unless they are lofted above the PBL – rapid vertical transport of aerosols, NO_x and SO_2 increases their lifetimes and range of influence. As mentioned in Chapter 1, both WCB and convection play a role in pollutant lifting. The cyclone described here generated little precipitation on April 5, and over the continent, vertical transport associated with it appears to have been driven by dry (non-precipitating) convection well upwind. Dry convection, with minimal wet removal, may be especially effective at vertical transport of dust and pollutants.

The results from this April 5 flight, when combined with the climatology presented above, may have general implications for chemical transport models. Global-scale dynamical models can handle explicitly the transport along isentropes, such as in the WCB; for the case study presented here, this process was important after the cyclone moved eastward off the coast. Convection, in contrast, must be parameterized in large-scale models, and accurate representation of the aerosol and trace gas transport in dry convection poses a challenge to numerical models. Careful evaluation against observations and cloud resolving models is called for.

4.3 Summary

Both convection and WCB lofting associated with wave cyclones can play an important role in the springtime long-range transport of pollutants from East Asia.

Previous aircraft measurements in this region, mainly conducted off the Chinese coast, downwind of China's populated areas generally identify WCB lofting as the dominant meteorological mechanism driving transpacific transport events. Few observational studies have dealt with the convective lofting of pollutants over the E Asian continent. In this chapter, I investigate both mechanisms by analyzing a series of EAST-AIRE research flights in NE China.

In the PBL, aircraft-measured air quality responded to mid-latitude cyclones in a way similar to that observed on ground (Chapter 3). Transitions between polluted prefrontal (~10 ppb SO_2, ~1 × 10^{-4} m^{-1} aerosol scattering) and clean postfrontal (~2 ppb SO_2) conditions were recorded, but aerosol loading remained substantial behind the cold front probably due to strong dust emissions.

In the free troposphere at 1000-4000 m altitude, concentrations of trace gases and aerosols were much smaller than in the PBL. During the prefrontal flight on April 5, substantial pollution with ~300 ppb CO, ~2 ppb SO_2, and ~8 × 10^{-5} m^{-1} aerosol scattering was measured. Back trajectories show little or no WCB lifting over the continent; on the other hand, convective clouds formed near the industrial areas of Hohhot and Baotou, ~1000 km upwind, and a day before the flight might have lofted pollutants into the free troposphere. Pollutants uplifted can be carried in the westerly winds to the locations of aircraft spirals. Stronger convection to the northwest 48 hr prior to the flight occurred over sparsely populated regions of Mongolia, which may have contributed dust but likely not pollutant gases to the free troposphere. Up until this point, dry convection appears to have been the dominant mechanism of vertical pollutant transport in this case.

Behind the cold front on April 7, little SO_2 but abundant aerosols (likely mineral dust) and ozone were observed above the PBL. High winds in the cold sector of the cyclone (cP air mass) might have lofted dust from the surface and subsidence or tropopause folding might have brought ozone from the UT/LS to the middle troposphere.

Comparing the results from the Shenyang aircraft campaign to the chemical climatology over the NE U.S. shows that pollutant levels are greater at almost all altitudes over N China. Overall, the particle size over N China is larger, probably due to prevalence of dust in spring. The springtime meteorological mechanisms leading to long-range transport of pollutants are similar over eastern North America and East Asia – both involve the passage of wave cyclones and associated fronts. But one fundamental difference is that in the arid spring in N China, convection produces little rain – this makes convective lofting more efficient for pollutant transport and makes convection more difficult to simulate. Future studies of the global effects of emissions from China must account for dry convection; convective schemes of chemical transport models must be evaluated not only for their ability to match observed precipitation but also for their ability to simulate deep clouds that do not rain. Further aircraft flights in the region will help quantify the relative roles of dry convection and the WCB in large-scale atmospheric composition and climate.

The aircraft measurements discussed in this chapter were conducted over a relatively small region no more than 100 km from the city of Shenyang. In Chapter 5 I use satellite sensors to further study the April 5 pollution episode on a much larger

scale, and track the pollution plume as it moved eastward with the cyclone over the next few days.

Chapter 5: Evolution of Pollutants during Transport: A Perspective from Space

5.1 In-Cloud Processing of Upwind Sulfur Dioxide

5.1.1 The relative nitrate-to-sulfate ratio in Xianghe aerosol samples

One seemingly surprising result from the analysis of Xianghe aerosol samples (cf. Chapter 3) is that the average mass concentration of nitrate ($[NO_3^-]$) is higher than that of sulfate ($[SO_4^{2-}]$). Table 5.1 compares this study to some previous studies in the region near Beijing. A number of factors might affect the $[NO_3^-]/[SO_4^{2-}]$ ratio, for example sampling size range, sampling loss, interference of gaseous species, analysis method, and sampling time and location. PM_{10} or bulk aerosol samples often have higher $[NO_3^-]/[SO_4^{2-}]$ ratio than $PM_{2.5}$ or PM_1 samples, as the reaction between nitric acid and soil particles [*Seinfeld and Pandis*, 1998] may form nitrate compounds in the coarse mode. In N China, the winter $[NO_3^-]/[SO_4^{2-}]$ ratio (e.g., 0.5, *Sun et al.* [2004]; 0.2, *Hu et al.* [2002]) can be lower than that in springtime samples (e.g., 0.9, *Wang, Zhuang et al.* [2005]; 0.7, *He et al.* [2001]), due to extensive coal burning for heating. Growing emissions from vehicles and large point sources in the region [*Q. Zhang et al.*, 2007] may cause a larger $[NO_3^-]/[SO_4^{2-}]$ ratio in more recent samples [e.g., *Zhang et al.*, 2004]. If no denuder is employed in the sampling process, gaseous nitric acid can be absorbed by the aerosol filters, leading to a positive artifact in the nitrate concentration (e.g., this study).

Given the similarities in sampling season (spring), year (2005 vs. 2001-04), size range (bulk), and method (no denuder), I compare this study to *Wang, Zhuang et al.* [2006] to differentiate aerosol composition between rural (Xianghe) and urban (Beijing) locations in the region. An earlier study sampled both urban and rural aerosols in the area in autumn [*Huebert et al.*, 1988].

Higher average [NO_3^-] (17.9 μg/m^3) and [SO_4^{2-}] (20.8 μg/m^3) are found in more polluted downtown Beijing [*Wang, Zhuang et al.*, 2006]. The [NO_3^-]/[SO_4^{2-}] ratio in Xianghe, on the other hand, is greater than in Beijing. Both sites are influenced by nearby sources, but probably more so for Beijing, as in general cities have stronger local emissions and weaker surface winds due to friction. NO_x reacts faster to form NO_3^- than SO_2 does to from SO_4^{2-}; and therefore [NO_3^-]/[SO_4^{2-}] ratio at the downstream site in Xianghe may be greater than in upwind metropolitan Beijing when W or SW winds prevail. Additionally, the availability of NH_3 and soil particles, which neutralize HNO_3, differs between urban and rural atmospheres. Uncertainties in chemical analysis of the two studies may influence the ratio as well. *Huebert et al.* [1988] show a similar difference in the [NO_3^-]/[SO_4^{2-}] ratio between urban and rural sites under hazy conditions (Table 5.1).

Table 5.1. Average nitrate and sulfate concentrations from this study and some previous studies (μg/m^3).

Study	Time	Location	Size	NO_3^-	SO_4^{2-}	Remark
This study	Spring 2005	Xianghe	Bulk	9.5	7.2	No denuder, rural site near Beijing; Whatman 41 filters.
Hu et al. [2002]	Dec. 2000	Beijing	Not specified	5.6	28.0	Online ion chromatograph with gas measurements, urban site.
Sun et al. [2004]	Winter 2002 & 2003	Beijing	PM_{10}	18.7	34.5	Medium volume, Whatman 41 filters, urban site, usage of denuder not specified.
Yao et al. [2003]	1999-2000	Beijing	$PM_{2.5}$	10.3	18.4	Sampling during the whole year, with denuder, urban site.

Zhang et al. [2004]	1994-1995	Beijing	$PM_{2.5}$	5.2	15.2	Details of sampling and analysis not given.
	2000	Beijing	$PM_{2.5}$	5.6	9.9	
Wang, Zhuang et al. [2005]	Spring 2001-2003	Beijing	$PM_{2.5}$	11.9	13.5	Five urban and suburban sites, similar sampling and analysis as Sun et al. [2004]
He et al. [2001]	Spring 2000	Beijing	$PM_{2.5}$	7.3	10.2	Low-flow sampler with denuder, urban sites
Zheng et al. [2004]	Spring 2004	Beijing	$PM_{2.5}$	~20	~20	Sampling at 6-day interval, 5 urban and suburban sites in Beijing area, concentrations roughly read from the figure in paper, usage of denuder not specified.
Wang, Zhuang et al. [2006]	Spring 2001-2004	Beijing	Bulk	7.2	19.6	Similar sampling system as *Sun et al.* [2004], urban sites, 40 "dust" samples.
				47.1	48.9	Same study as above, 32 "haze" samples.
				13.6	13.6	Same study as above, 117 "clear" samples.
Huebert et al. [1988]	Oct. 1985	Beijing	Bulk	1450[a] 3.7[b]	2050[a] 8.2[b]	6 samples collected on two days under "hazy" and "slightly hazy" conditions.
		Xinglong	Bulk	50[a] 0.1[b]	150[a] 0.6[b]	Same study as above, 100 km NE of Beijing, N winds, clear
		Xinglong	Bulk	1440[a] 3.7[b]	1540[a] 6.2[b]	Same study as above, W winds, hazy.

[a] Unit: parts per trillion (ppt).
b Unit converted to μg/m^3 assuming 20°C, 101.325 kPa.

5.1.2 Synoptic change in $[NO_3^-]/[SO_4^{2-}]$

Figure 5.1 revisits the time series of nitrate and sulfate; the two secondary aerosol compounds are closely related to anthropogenic emissions and in correlation with CO (Figure 3.3). In Chapter 3 I have described in detail the synoptic variation of air quality seen in Xianghe. Briefly, weak S winds ahead of cold fronts allow pollutants to accumulate; strong winds from the less populated N/NW behind cold fronts ventilate local emissions, bringing relatively clean air.

In Figure 5.1, nitrate is more abundant than sulfate under polluted conditions, and vice versa under relatively clean conditions. This change of $[NO_3^-]/[SO_4^{2-}]$ ratio with pollutant level and synoptic conditions is qualitatively consistent with *Wang, Zhuang et al.* [2006]. Their "dust" samples are associated with strong winds (average wind speed: 8 m/s) and dry air (average RH: 20%) under postfrontal conditions (cf. Chapter 3). The corresponding nitrate concentration (7.2 $\mu g/m^3$) under these conditions is less than half of sulfate (19.6 $\mu g/m^3$). In contrast, the same ratio is almost one for "haze" samples, which comprise on average 47.1 $\mu g/m^3$ of nitrate and 48.9 $\mu g/m^3$ of sulfate. These "haze" samples were mostly collected under stagnant (average wind speed: 2.5 m/s) and relatively moist (average RH: 59%) conditions, usually found ahead of cold fronts. The "clear" samples [*Wang, Zhuang et al.*, 2006] may reflect both prefrontal and postfrontal conditions, and also the transition in between. Similarly, *Huebert et al.* [1988] found that as winds switched from generally N to generally W and brought pollutants to their site NE of Beijing, the observed nitrate-to-sulfate mole ratio went up from 0.33 to 0.93.

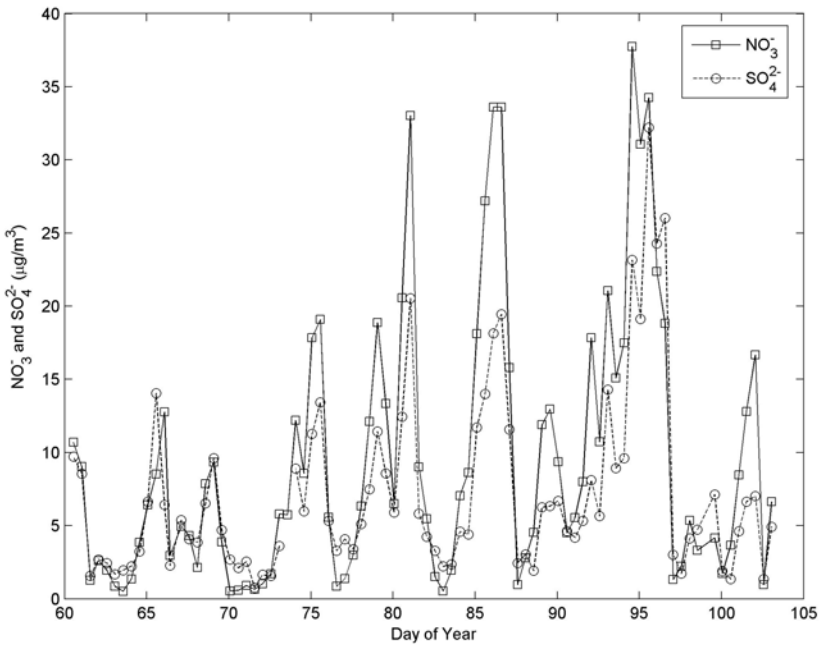

Figure 5.1. Concentrations of nitrate (squares) and sulfate (circles) in bulk aerosol samples from Xianghe, March 1 to April 13, 2005.

5.1.3 SO_4^{2-}/SO_x and NO_3^-/NO_y mole ratios

The mole ratio of SO_4^{2-}/SO_x, where $SO_x = SO_4^{2-} + SO_2$ (units: μmol/m^3), is plotted against the NO_3^-/NO_y mole ratio in Figure 5.2 as a function of CO concentration. Considering the positive artifact due to absorption of HNO_3 to filters, the calculated NO_3^-/NO_y ratio is better viewed as a proxy for the fraction of NO_x converted to secondary species including HNO_3. Relatively clean samples (CO < 500 ppb) mostly have higher SO_4^{2-}/SO_x ratio than NO_3^-/NO_y ratio, and vice versa for polluted samples (CO > 1000 ppb). The relative rates of sulfate and nitrate production may change with weather; and consequently so does the relative abundance of the two species.

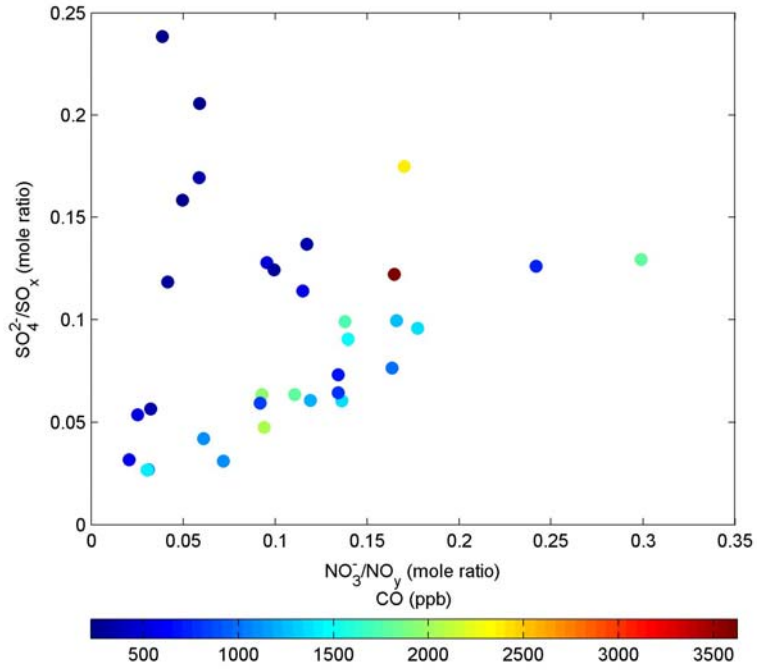

Figure 5.2. SO_4^{2-}/SO_x and NO_3^-/NO_y mole ratios as a function of CO concentration. Under relatively clean conditions, SO_4^{2-}/SO_x ratio is generally higher than NO_3^-/NO_y ratio, and vice versa under polluted conditions.

Scatter plots of SO_4^{2-}/SO_x and NO_3^-/NO_y mole ratios with various meteorological parameters in Figure 5.3 provide some insight into the conversion mechanisms of SO_2 and NO_x. The SO_4^{2-}/SO_x mole ratio shows little correlation with temperature (Figure 5.3b), implying an additional SO_2 conversion pathway besides the temperature-dependent gas-phase oxidation of SO_2. A fraction of sulfate may also form during transport (other than locally generated). The relationship between SO_4^{2-}/SO_x mole ratio and RH in Figure 5.3a largely reflects the distinct properties of air masses; SO_4^{2-}/SO_x is greater in the very dry but relatively clean postfrontal arctic air. Likewise, samples of high SO_4^{2-}/SO_x ratios are mostly related to strong northerly winds behind cold fronts (Figures 5.3c and 5.3d). The conversion of NO_x, in contrast, is temperature dependent and correlated with solar radiation (overall, daytime

samples more reacted) as shown in Figure 5.3f. The NO_3^-/NO_y ratio is low when it is cold and dark (lower ratio for night time samples shown as circles). The only nighttime sample with a relatively high NO_3^-/NO_y ratio had temperature of ~15ºC. The formation of nitrate is probably more through gas-phase photochemical process than through conversion from N_2O_5 to nitrate at night.

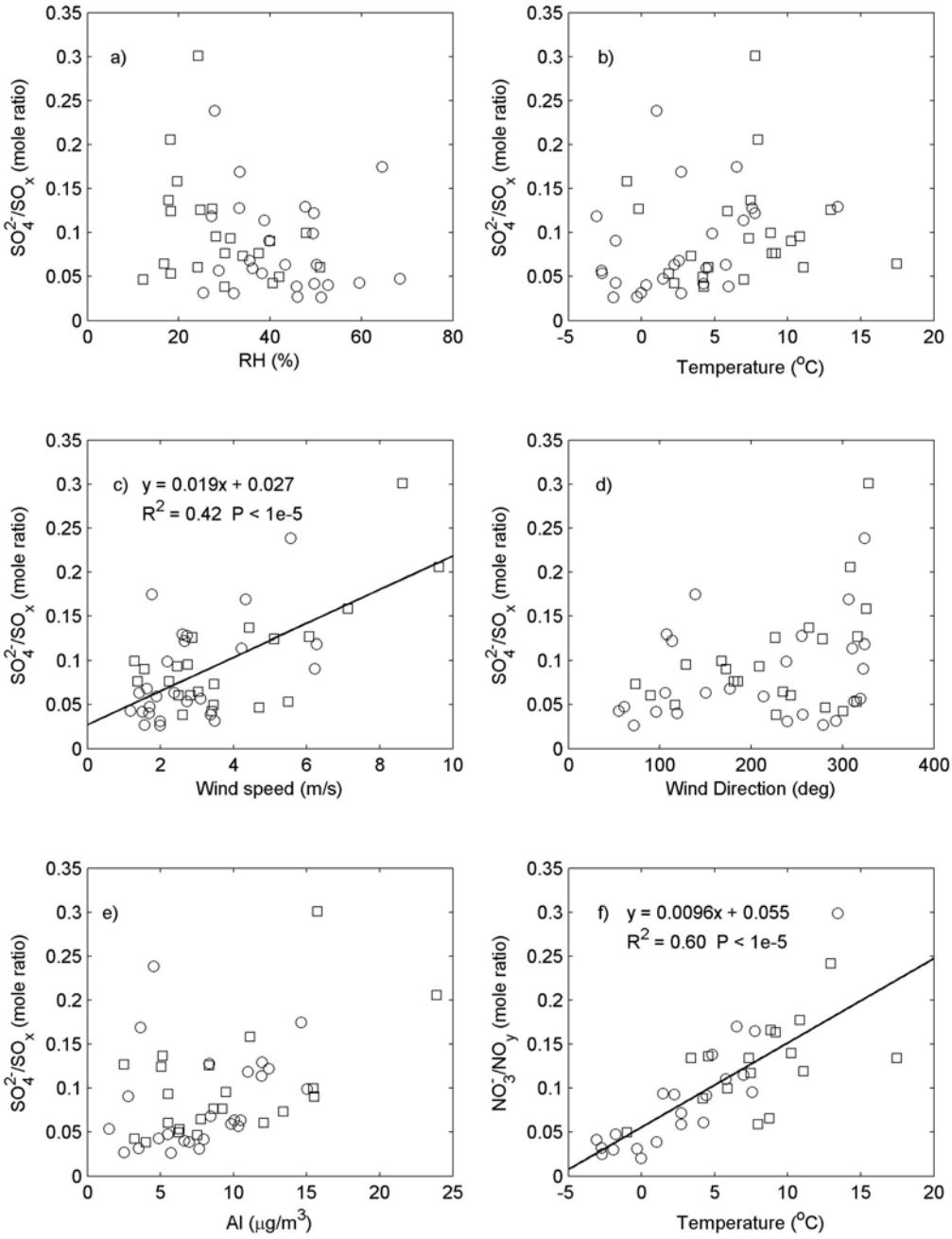

Figure 5.3. Scatter plots of SO_4^{2-}/SO_x mole ratio with a) relative humidity, with b) temperature, with c) wind speed, with d) wind direction, with e) Al concentration, and f) NO_3^-/NO_y mole ratio with temperature. Squares and circles represent daytime and nighttime samples, respectively. Solid lines are results of correlation analysis between SO_4^{2-}/SO_x mole ratio and wind speed (c), and between NO_3^-/NO_y mole ratio and temperature (f) for all samples.

Excluding locally emitted SO_2, which reacts slowly in the cold postfrontal environment (Chapter 3), I can approximate the SO_2 conversion ratio for "transported" sulfur species from the north. The abundance of local SO_2 is estimated assuming that its mixing ratio is 1/35.8 that of locally emitted CO. The value 35.8 comes from the correlation analysis between CO and SO_2 (Chapter 3), and presumably reflects the CO/SO_2 emission ratio from sources in the region. Local CO is calculated by subtracting the intercept of the same correlation analysis from the measured CO. This intercept (180 ppb) is also roughly the lowest CO recorded during the experiment, and is comparable to the "background" values at mid-latitude continental sites in northern hemisphere [*Novelli et al*, 1998]. Under windy conditions (mean surface wind speed > 4 m/s), 8 of 12 samples have "transported" SO_4^{2-}/SO_x mole ratio greater than 0.5 (2 with ratio of about 0.4). Note that this analysis is qualitative only, given our assumption of neglecting locally generated sulfate and the uncertainties in CO/SO_2 emission ratio that have been discussed in Chapter 3. The above analysis seems to indicate that the mixing of aged SO_x from distant sources may be the non-temperature dependent source of sulfate observed in Xianghe behind cold front.

One question that remains unanswered is why the SO_4^{2-}/SO_x ratio would be higher when winds blow from the cold north, where gas-phase photochemical reactions oxidizing SO_2 are likely slow? The interaction between dust particles and pollutants, particularly in dust storms, may accelerate sulfate formation, and has been the subject of numerous studies, [e.g., *Sun et al.*, 2005; *Wang, Zhuang et al.*, 2007; *Yuan et al.*, 2008], although some find little evidence of sulfate forming on dust [e.g.,

Zhang and Iwasaka, 1999]. Figure 5.3e is a scatter plot of the SO_4^{2-}/SO_x ratio and aluminum (Al), used here as a tracer for soil/dust particles. Recall that in Chapter 3 it was found that aluminum is a good tracer for transported dust, whereas some other crustal elements (e.g., calcium, iron, and potassium) are more related to local anthropogenic activities. Another possibility is that $CaSO_4$ in East Asian dust may contribute to sulfate in aerosol samples, although it is much less abundant than calcium carbonate ($CaCO_3$) [*Gao et al.*, 2007]. As can be seen in Figure 5.3e, several samples have a relatively high SO_4^{2-}/SO_x mole ratio but low Al or dust level; sulfate in these samples is not likely from $CaSO_4$ in dust or generated by interaction between SO_x and dust particles. Aqueous-phase oxidation of SO_2, for example through reaction with hydrogen peroxide (H_2O_2), is more efficient than gas-phase reactions [*Seinfeld and Pandis*, 1998]. In comparison, the aqueous-phase conversion from NO_x to nitrate probably contributes negligibly in this study [*Seinfeld and Pandis*, 1998]. Therefore in-cloud processing of SO_2, if occurs on the transport route from the north, can probably cause the relatively high SO_4^{2-}/SO_x but low NO_3^-/SO_4^{2-} ratios observed in the postfrontal air, and is probably the source of non-temperature dependent sulfate.

5.1.4 In-cloud processing of SO_2

To find out whether in-cloud processing may have occurred during postfrontal transport, I analyze backward trajectories and satellite data. Backward trajectories calculated using the HYSPLIT model and MODIS cloud properties are synchronized in time and space: I overlap each trajectory point (with time, latitude, longitude, and height in mb from the model) with MODIS-retrieved cloud top pressure (CTP) and

cloud optical thickness (COT) within ± 15 min, and ± 2.5º latitude/longitude. Thick clouds with top above the trajectory height, and clouds with top near trajectory height are more likely to interact with SO_x traveling alongside the trajectory. MODIS CTP and COT are used to identify such clouds. Given the uncertainties in satellite retrievals, particularly for multi-layer clouds (e.g., cirrus over low level clouds), additionally I use NCEP reanalysis RH along the trajectory to judge the existence of clouds.

As an example, the upper and middle panels of Figure 5.4 present the synchronized trajectory-cloud plot for the daytime sample on March 17, 2005. Over Lake Baikal, where the trajectories were at the level of 700-800 mb, MODIS retrieved thick clouds with COT ≥ 15 and CTP ~600-700 mb, suggesting possible interaction between clouds and air parcels. Note the high RH (over 80%) along the trajectory. The lower panels of Figure 5.4 are histograms of MODIS-retrieved CTP and COT around the position of the 500-m trajectory (55.312ºN, 108.117ºE, 794.8 mb, and RH ~87%), 48-hr prior to its arrival in Xianghe. To account for the uncertainties of trajectory computation, which is proportional to the distance traveled from the trajectory end point [*Stohl*, 1998], the histograms incorporate MODIS data within ±15 min of the trajectory time and the spatial uncertainty range of the trajectory (20% of the traveled distance from Xianghe). More than half of the clouds have CTP between 600 and 800 mb, close to the trajectory height. Some well-developed clouds exist, although relatively thin clouds with COT < 10 dominate. Based on Figure 5.4, I conclude that the air sampled during daytime on March 17 likely has a history of

cloud-interaction. The SO_4^{2-}/SO_x mole ratio of the sample is relatively high at 0.3, likely due to oxidation of SO_2 by H_2O_2 in the condensed phase.

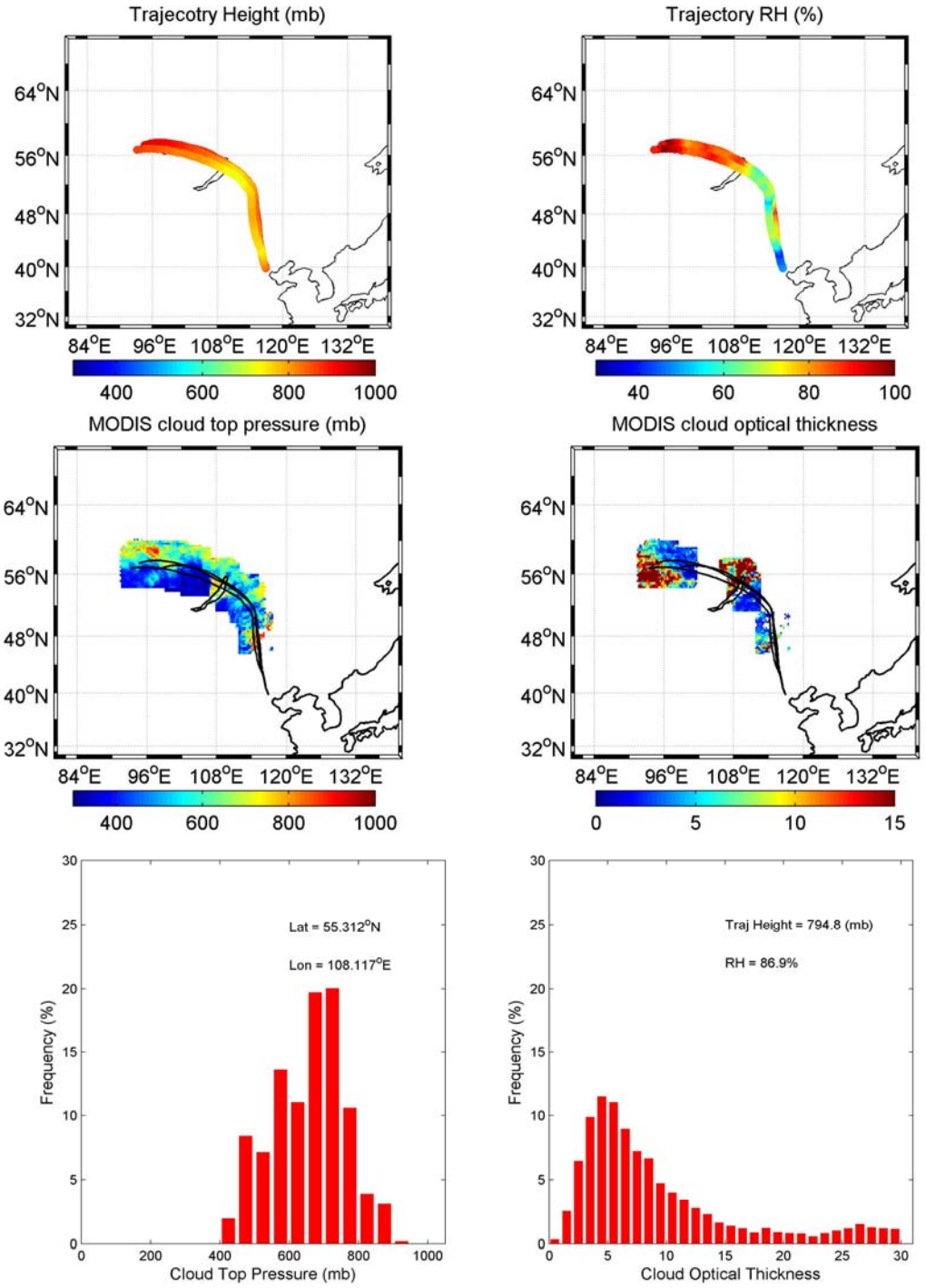

Figure 5.4. Upper: 72-hr backward trajectories starting at 200 m, 500 m, and 1000 m above ground from Xianghe at 04 UTC on March 17, 2005, with colors representing trajectory height (left) and NCEP reanalysis RH along the trajectories (right). **Middle**: MODIS-retrieved cloud top pressure (left) and cloud optical thickness (right) along

the trajectories, synchronized with trajectory waypoints in time (± 15 min) and space (± 2.5 º latitude/longitude). **Lower**: histograms of MODIS cloud top pressure (left) and cloud optical thickness (right) near the trajectory (500 m), 48 hr prior to its arrival. Position of the air parcel: 55.312ºN, 108.117ºE, 794.8 mb; RH: 86.9%.

Having examined similar plots on a case-by-case basis, I find that 16 out of 23 samples with NO_3^-/SO_4^{2-} mole ratio below 1.33 are related to trajectories with a history of possible cloud interaction, and 13 of the 23 samples have lower-than-average Al concentration and are relatively "dust-free". Among the 23 samples, 9 are possibly cloud-influenced and "dust free", and are defined as "cloud". Two with abundant dust are called "dust", 7 have both high dust levels and probable cloud interaction, and are named "cloud and dust", and 5 remain unaccounted for. Similarly, out of the 15 samples with SO_4^{2-}/SO_x mole ratio > 0.1, 6 are "cloud", 4 are "dust", and 4 are "cloud and dust". Additionally, 10 of 11 samples with $NO_3^-/SO_4^{2-} < 0.8$, and 5 of 6 samples with $SO_4^{2-}/SO_x > 0.15$ are "cloud" or "cloud and dust". Note that the fraction of cloud-related samples could be underestimated, as MODIS provides measurements only once a day (the daytime COT product is used). Figure 5.5 summarizes the results.

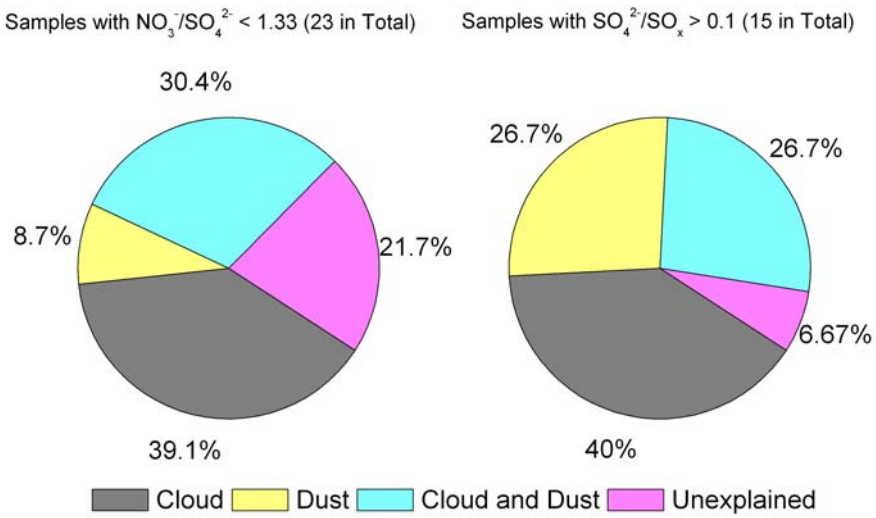

Figure 5.5. Percentage of "cloud", "dust", "cloud and dust", and "unexplained" events for samples with NO_3^-/SO_4^{2-} mole ratio below 1.33 (left), and samples with SO_4^{2-}/SO_x mole ratio over 0.1 (right).

5.1.5 Implications for regional atmospheric chemistry

As discussed in Chapter 3, SO_2 is the major SO_x species in N China in spring; its high abundance relative to other SO_x species is a combined result of strong local SO_2 emissions and slow photochemical processes. When a mid-latitude wave cyclone moves eastward, air flow behind its cold front carries pollutants away from northern China, usually within the PBL (cf. Chapter 1). Several such PBL transport episodes featuring high SO_x concentration were recorded in Cape Hedo, Japan, ~1000 km E of Xianghe, and a site of the Asian Brown Cloud (ABC) field campaign in coordination with EAST-AIRE [*Takami et al.*, 2007]. *Takami et al.* [2007] observed that the SO_x in these peaks was almost completely sulfate and proposed that only in-cloud processing would be fast enough for nearly complete conversion of SO_2 from China. Together, this study and *Takami et al.* [2007] show that under postfrontal conditions, aqueous oxidation may play an important role in the formation of sulfate aerosols, both

upwind and downwind of the strong emission sources in N China. Sulfate particles from the region N of China, although low in concentration, can be highly efficient cloud condensation nuclei (CCN), and may impact cloud systems over downwind areas [e.g., *Zhang et al.*, 2007] (and subsequently aqueous chemistry there). Chemical transport models need to properly treat both clouds and dust to accurately represent the regional sulfur chemistry in East Asia. In-cloud processing of SO_2 can also impact the distribution of sulfate aerosols and the regional radiation budget [e.g., *Takemura et al.*, 2003].

5.2 Transport and Evolution of a Pollution Plume from Northern China: A Satellite-Based Case Study

5.2.1 Introduction

As discussed in Chapters 3 and 4, mid-latitude wave cyclones play a central part in building up and venting pollution plumes over N China. These plumes with high concentrations of pollutants could travel far downwind off the Chinese coast, and potentially influence large areas (cf. Chapter 1 and the references therein). A key factor determining the large-scale impacts of a pollution plume is how the plume evolves over time and space. The SO_2-to-suflate conversion can supply cloud condensation nuclei and may greatly affect the aerosol-cloud system over the northern Pacific [*R. Zhang et al.*, 2007]. Diffusion and advection can dilute a plume, lessening but spreading its effects. Eulerian [e.g., *Carmichael et al.*, 2003] and Lagrangian [e.g., *Stohl et al.*, 2003] models can simulate the evolution of pollution plumes, but need observations for evaluation. By intercepting a plume a few times on

its path, Lagrangian or semi-Lagrangian airborne experiments can sample the plume at its different stages [e.g., *Methven et al.*, 2006; *Ramanathan et al.*, http://www.eol.ucar.edu/projects/pacdex/], but aircraft observations are costly and scarce.

The past several years have witnessed great progress in satellite remote sensing of pollutants in the troposphere. Satellite measurements have been used to track dust transport [e.g., *Hursar et al.*, 2001], characterize the chemical signature of frontal systems [e.g., *Liu et al.*, 2006], monitor long- [e.g., *Richter et al.*, 2005] and short-term [e.g., *Y. Wang et al.*, 2007] change in pollutant levels, evaluate emission inventories [e.g., *Akimoto et al.*, 2006], and constrain chemical transport models [e.g., *Allen et al.*, 2004]. With daily global coverage, finer resolution, and almost simultaneous observations of multiple pollutants, a series of satellite sensors in the "A-train" constellation provide unprecedented capacity in measuring air pollution from space.

This section can be viewed as a follow-up on the analysis on the April 5 research flight over N China given in Chapter 4. Taking advantage of the "A-train", I look at the air pollution episode at a regional scale, and track the evolution of the pollution plume as it moves to the east over the next few days, where and when in-situ measurements were not available.

5.2.2 Data and models

The Ozone Mapping Instrument (OMI) onboard NASA's Earth Observing System (EOS) Aura satellite retrieves SO_2 column content using UV spectral fitting

in the wavelength range of 310-380 nm [*Krotkov et al.,* 2006; 2008]. In the operational OMI PBL SO_2 product, the retrieved slant column SO_2 density (SCD) is converted to total SO_2 vertical column density (VCD) with a constant air mass factor (AMF, defined as the ratio between the slant column to the vertical column) of 0.36:

$$\text{total } SO_2 \text{ VCD} = \frac{SCD}{AMF} \qquad (5.1)$$

This operational AMF assumes cloud- and aerosol-free conditions, solar zenith angle of 30º, surface albedo of 0.05, surface pressure of 1013.13 mb, mid-latitude ozone profile of 325 DU, and a vertical SO_2 profile typically observed over the eastern U.S. in summer, with most of the SO_2 below 900 mb [*Taubman et al.,* 2006]. The PBL OMI SO_2 product has been validated against aircraft measurements during the EAST-AIRE campaign (Chapter 4), and could distinguish between polluted and background conditions over N China on a daily basis [*Krotkov et al.*, 2008]. The noise of the PBL SO_2 product is ~1.5 DU at the instrument's instantaneous field of view (FOV, 13 × 24 km at nadir), but can be greatly reduced through temporal and spatial averaging. Section 5.2.3 details the AMF corrections made in this case study.

Aerosol optical depth (AOD) retrieved from the MODerate resolution Imaging Spectrometer (MODIS) instrument aboard NASA's EOS/Aqua satellite provides aerosol information in this study, with a resolution of 10 × 10 km. The MODIS AOD retrieval algorithm derives aerosol properties over dark surfaces (cloud, ice, snow, sun-glint, and desert free), and is based on a "lookup table" approach, i.e., the observed radiation field is compared against the pre-computed radiative transfer calculations with a set of assumed aerosol and surface parameters [*Remer et al.*, 2005]. The best fit found through the comparison is the solution to the inversion.

Over oceans, the MODIS algorithm assumes that one fine and one coarse lognormal mode, if properly weighted, can combine to represent ambient aerosol properties. Over land, the surface reflectance can be derived from longer wavelength MODIS channels, as atmospheric extinction due to aerosols is generally low in the 2.12 μm band. An earlier version of the MODIS land algorithm assumed constant ratios between the surface reflectance at 0.47 and 0.66 μm and at 2.12 μm. The recently updated (collection 5: C005-L) MODIS land algorithm [*Levy et al.*, 2007] parameterizes this spectral surface reflectance relationship as a function of viewing geometry and surface type (NDVI: normalized difference vegetation index). The algorithm also employs new aerosol models derived from surface sun photometer measurements (AErosol RObotic NETwork: AERONET); and simultaneously retrieves surface reflectance, AOD, and fine mode aerosol weighting. The MODIS AOD product has been validated against sun photometer measurements over China [*Mi et al.*, 2007], and the collection 5 data show much improved agreement with surface observation. Both Aura and Aqua satellites are part of the "A-train" satellite constellation and pass over Shenyang region ~15 min apart at about 1 pm local time (05 UTC).

The HYSPLIT model along with NCEP global reanalysis data are used to calculate forward trajectories in this study. 72-hr forward trajectories from eight layers (every 500 m from 250 to 3750 m above ground level) are initiated from 0.5°×0.5° grid cells in the region of 35-49°N, 117-134°E (red rectangular boxes in Figure 5.11a), at 5 UTC, April 5, 2005. Each trajectory represents an air parcel 0.5°×0.5°×500m in size, and is tagged with AOD and SO_2 retrieved by MODIS and

OMI and weighted with aircraft profiles. AOD retrievals are missing in some grid cells; and trajectories originating from these grid cells are labeled with the mean AOD of adjacent grid cells. Grid cells with SO_2 below a certain threshold value (cf. section 5.2.5) are considered "non-detectable" by OMI. Trajectories from these grid cells are assigned half of the threshold SO_2. There is no special treatment for parcels with relatively low AOD, as MODIS appears to have good sensitivity even for low aerosol loadings [*Levy et al.*, 2007a]. Assuming that pollutants within each parcel are conserved, these "tagged" air parcels together can project and map the spatial distribution of SO_2 and AOD in the plume.

The aerosol extinction coefficient profile at 532 nm and depolarization ratio were measured in Sapporo, Japan (43.1 °N, 141.3°E), using a NIES (National Institute for Environmental Studies) lidar system. The extinction coefficients of non-spherical aerosols (dust) and spherical particles are computed following *Shimizu et al.* [2004]. Aerosol optical depth over the flight region was determined from the surface with a hand-held sun photometer on April 5 (Figure 4.4, measurement location: 41.5ºN, 123.6ºE).

This transport event was also reproduced in a Goddard Chemistry Aerosol Radiation and Transport (GOCART) model simulation. Driven by the assimilated meteorological fields of the Goddard Earth Observing System Data Assimilation System (GEOS DAS), GOCART is a global model with a horizontal resolution of 2 (latitude) by 2.5 (longitude) degrees and 20-55 vertical sigma layers [*Chin et al.* 2000]. The output of the GOCART model includes SO_2 as well as concentrations and

aerosol optical depth of sea salt, sulfate, organic and elemental carbonaceous compounds, and dust.

5.2.3 AMF correction for OMI operational SO_2 product

AMF is a function of SO_2 profile, surface albedo (R_s), viewing geometry (viewing angle: θ, solar zenith angle: θ_0, and relative solar azimuth angle: φ), total column ozone (Ω), aerosols, and clouds [*Krotkov et al.*, 2008]:

$$AMF = \int_0^\infty m(z, R_s, \Omega, \theta, \theta_0, \varphi) n_{SO_2}(z) dz \qquad (5.2)$$

$$m(z) = \frac{\partial \ln(I_{TOA})}{\partial \tau_{SO_2}(z)} \qquad (5.3)$$

where $m(z, R_s, \Omega, \theta, \theta_0, \varphi)$ is the vertically resolved OMI SO_2 sensitivity, I_{TOA} is the OMI measured reflectance at TOA (top of the atmosphere), $\tau_{SO2}(z)$ is the SO_2 absorption optical thickness at the layer z (km), and $n_{SO2}(z)$ is normalized SO_2 vertical profile. AMF can be obtained from a forward radiative transfer calculation; and the corrected SO_2 column amount would be:

$$SO_2(corrected) = \frac{0.36}{AMF(corrected)} SO_2(operational) \qquad (5.4)$$

Radiative transfer calculation of AMF for each pixel or grid cell is so computationally demanding that it is impractical. *Krotkov et al.* [2008] show that the viewing geometry correction of AMF can be parameterized through linear regression with respect to the slant column ozone (SCO):

$$AMF(corrected) = r_0 - r_1 \cdot SCO \qquad (5.5)$$

$$SCO = \Omega \cdot \left(\sec(\theta) + \sec(\theta_0)\right) \qquad (5.6)$$

where Ω is the total column ozone measured by OMI. The slope (r_1) and the intercept (r_0) of the linear regression depend on the normalized SO_2 vertical profile, the surface albedo (R_s), relative solar azimuth angle (φ), aerosols, and clouds. This linear regression could be further simplified, as R_s is normally small in the UV band for SO_2 retrieval, causing an error less than 15%, and changes of φ would result in typically ±10%, and in extreme cases no more than 20% error in AMF. In this study, AMF-SCO regression coefficients are derived under various assumptions concerning SO_2 profile, aerosols, and clouds. For example, on a given day, the clear-sky AMF-SCO relationship is derived with normalized SO_2 and aerosol vertical profiles and the average MODIS AOD around the core part of the plume, for two different aerosol types (industrial and dust):

$$AMF_{C,INDU} = r_{0,C,INDU} - r_{1,C,INDU} \cdot SCO \qquad (5.7)$$

$$AMF_{C,DUST} = r_{0,C,DUST} - r_{1,C,DUST} \cdot SCO \qquad (5.8)$$

where $AMF_{C,INDU}$ and $AMF_{C,DUST}$ stand for the corrected clear-sky AMF for industrial and dust aerosols, respectively. The retrieval assumes the same single scattering albedo (0.9) at 550 nm for both aerosol types, but each has a different size distribution and spectral dependence of absorption. $AMF_{C,INDU}$ and $AMF_{C,DUST}$ are then weighted with GOCART simulated dust ($AOD_{S,DUST}$) and total AOD (AOD_S) to obtain the clear-sky AMF (AMF_C):

$$W = \frac{AOD_{S,DUST}}{AOD_S} \qquad (5.9)$$

$$AMF_C = \left[(1-W)\cdot r_{o,C,INDU} + W \cdot r_{0,C,DUST}\right] - \left[(1-W)\cdot r_{1,C,INDU} + W \cdot r_{1,C,DUST}\right] \cdot SCO$$

(5.10)

The AMF under cloudy conditions can be calculated similarly for the same two aerosol types, using OMI measured reflectance (331 nm) and MODIS retrieved cloud top pressure. An assumption is that high clouds are mostly thin and have little influence on SO_2 retrieval. Low clouds on the other hand enhance OMI sensitivity to SO_2 above them. As a first-order approximation, in radiative transfer calculations for the two cloudy days (April 6 and 7), overcast conditions are assumed: a homogenous cloud "floor" with the mean reflectance of the region is placed at the average cloud top height of MODIS low clouds (Figure 5.6). The resulting AMF's are then combined using the weighting factor derived with Eq. 5.9. No correction was made for relatively clear sky conditions on April 5.

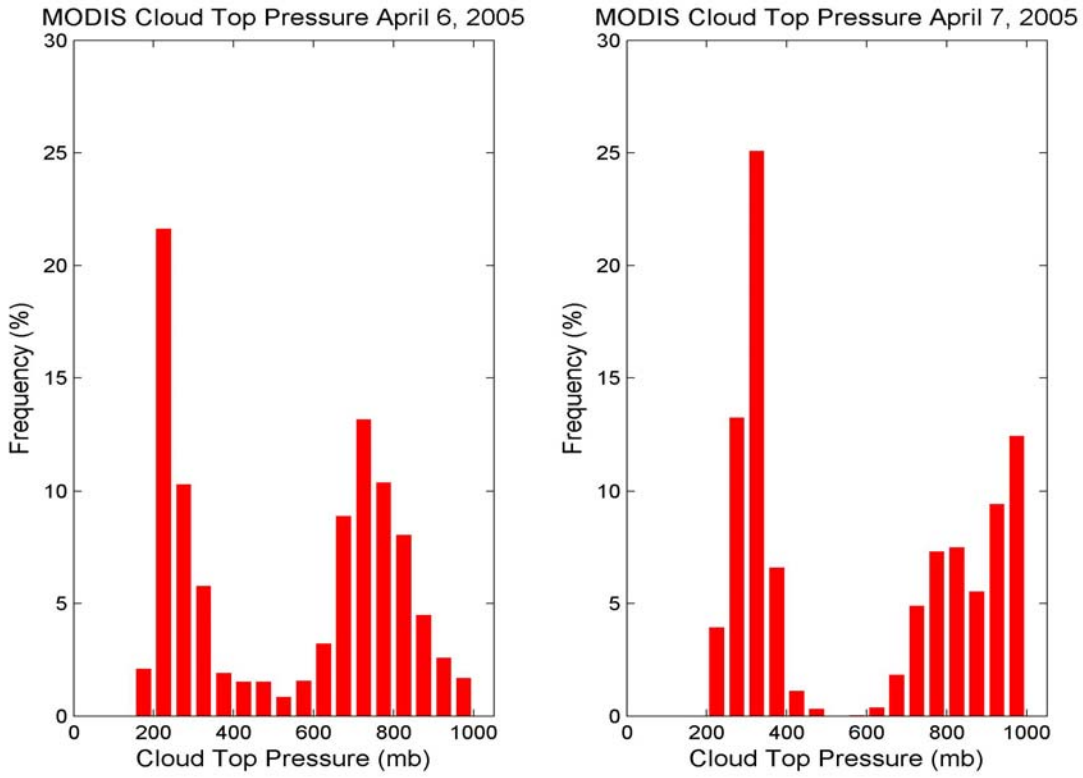

Figure 5.6. Histograms of MODIS cloud top pressure near the main body of the plume on April 6 (left) and 7 (right). Low clouds refer to those with cloud top pressure > 500 mb.

In this study, aircraft profiles of SO_2 and aerosols are used in the AMF calculation for April 5 (Figures 4.9 and 4.10). I calculate the trajectory-projected SO_2 and aerosol loadings at different heights (every 500 m, 0-6500 m) over the center of the plume (40-45ºN, 138-144ºE on April 6; 35-40 ºN, 160-165ºE on April 7). The normalized vertical distributions of SO_2 and aerosols are referred to as trajectory-projected profiles (Figures 5.7, 5.8, and 5.10). Trajectory-projected SO_2 profiles are employed for the AMF calculations for April 6 and 7, as aircraft measurements are not available. Lidar measurements over Sapporo, Japan (Figure 5.9) and trajectory

projection (Figure 5.10) provide aerosol profiling information for April 6 and 7, respectively.

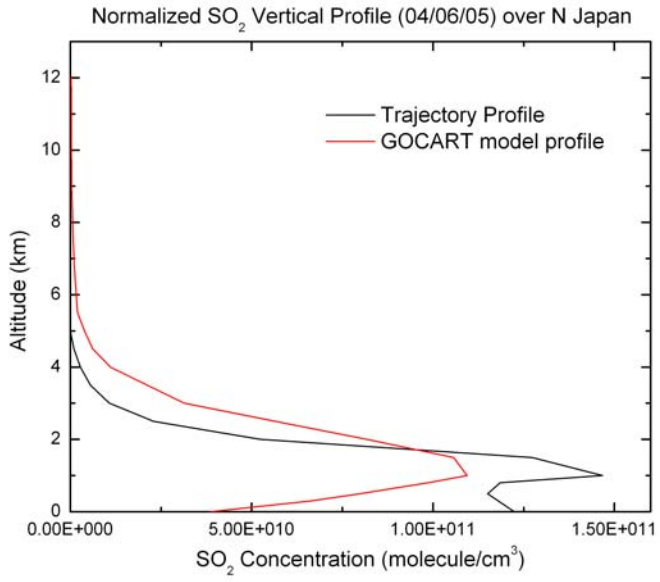

Figure 5.7. Normalized trajectory-projected and GOCART SO_2 vertical profile over N Japan on April 6, 2005.

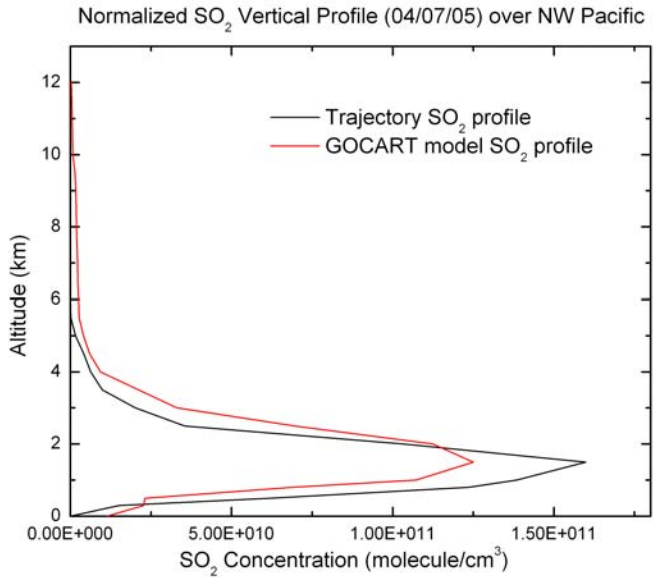

Figure 5.8. Normalized trajectory-projected and GOCART SO_2 vertical profile over N Pacific on April 7, 2005.

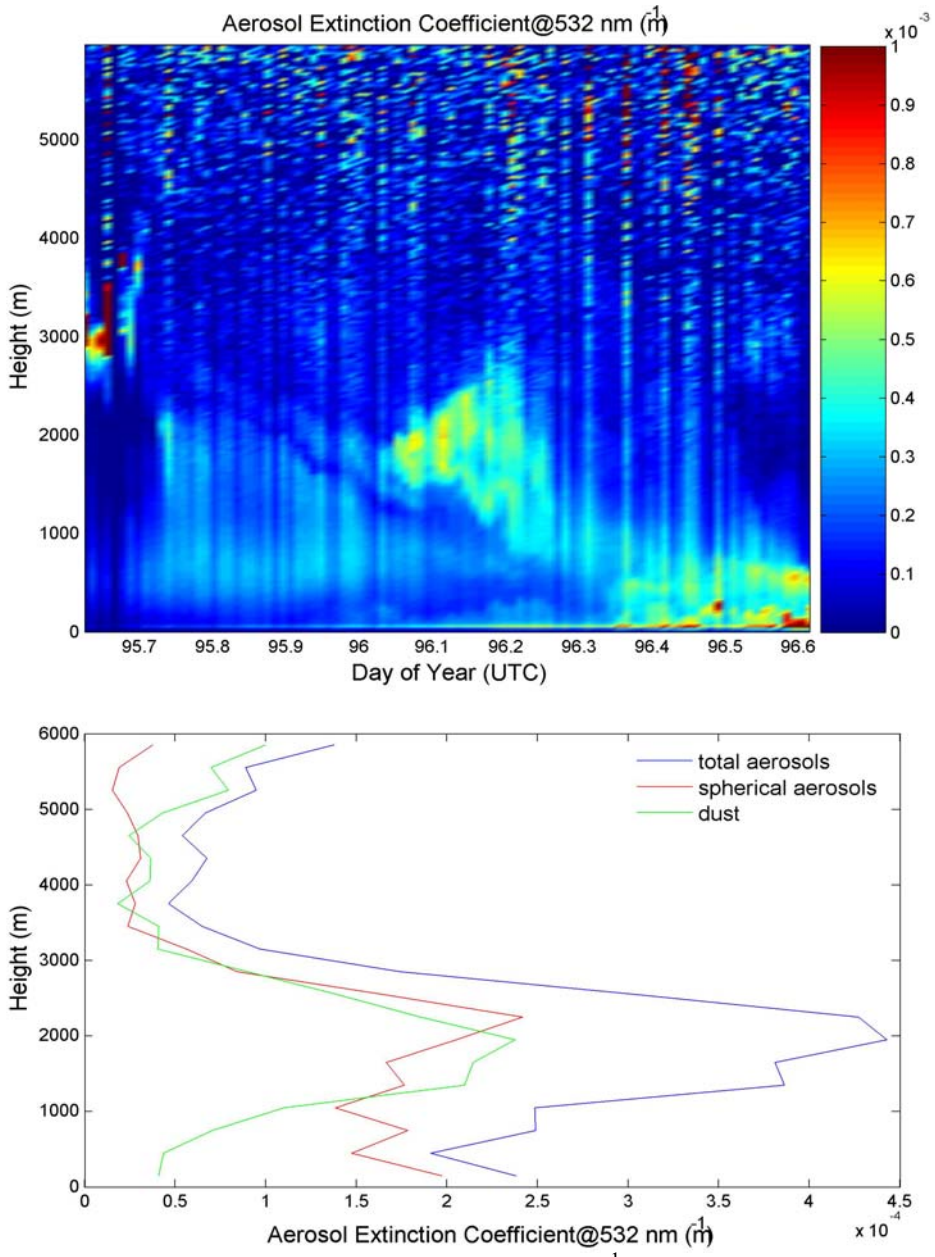

Figure 5.9. Upper: aerosol extinction coefficients (m^{-1}) in Sapporo, Japan on April 6, 2005; **Lower**: vertical profile of aerosol extinction by spherical (red), non-spherical (dust, green), and total (blue) aerosols, averaged from 0330 UTC to 0430 UTC. Note that using the wind speed at 2000 m (~20 m/s from local sounding data) and time the plume passed over the region (~5 hr), the size of the plume is estimated to be ~400 km along the wind direction (approximately from west to east). This is roughly the same as the satellite observed instantaneous plume size shown in Figures 5.11 and 5.12.

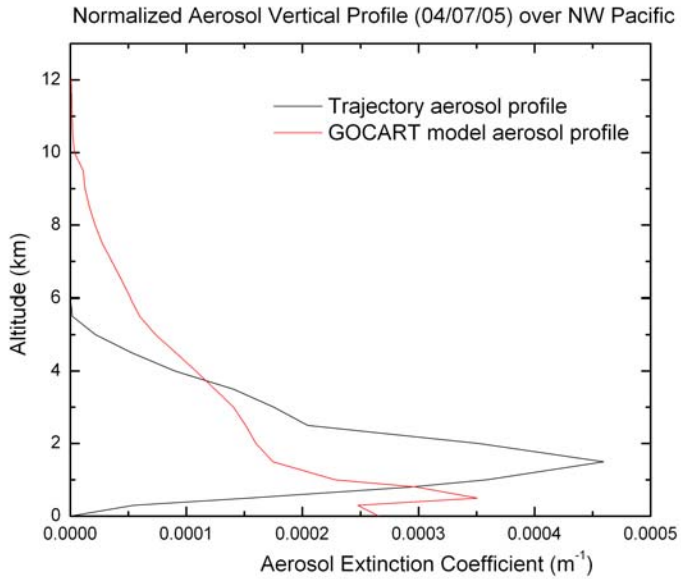

Figure 5.10. Normalized trajectory-projected and GOCART aerosol vertical profile over N Pacific on April 7, 2005.

5.2.4 Transport and evolution of the plume

The weather conditions and air quality measured by aircraft near Shenyang on April 5, 2005 have been discussed in detail in Chapter 4, and are only briefly reviewed here. Weather during this prefrontal flight featured strong surface winds from the south, local dust emissions and low visibility (4-5 km). Winds veered with altitude and became westerly in the middle troposphere. The aircraft detected ~20 ppb SO_2 within the PBL, and 1-3 ppb SO_2 in the FT, which translates into a vertical column amount of ~2 DU. The vertical distribution of aerosols was similar to that of SO_2, with ~500 Mm^{-1} scattering in the PBL and ~100 Mm^{-1} scattering in the FT. The aircraft-integrated and surface observed AOD (550 nm) were comparable at ~1. The Ångström Exponent (AE) from the surface AOD measurements was about 0.8, suggesting large overall size of particles. Single scattering albedo retrieved for the day is 0.87 [K-H. *Lee*, personal communication], indicating light-absorbing aerosols.

Satellite observations, in agreement with aircraft and surface measurements, detected high levels of SO_2 and aerosols on April 5, but over a much larger area. The average OMI SO_2 column content in the region near Shenyang (rectangular box, Figure 5.11a) was about 1.5 DU, with some "hot spots" exceeding 3 DU. The mean AOD (Fig 5.12a) in the same region was ~0.7, and higher values (~1.8) were found to the southwest. Fairly high OMI-observed Aerosol Index (AI, ~1.5, Figure 5.12d) in the region implied the existence of absorbing aerosols. Dust was likely the dominant aerosol compound according to high AI, low AE, meteorological records, and GOCART output (Figure 5.13).

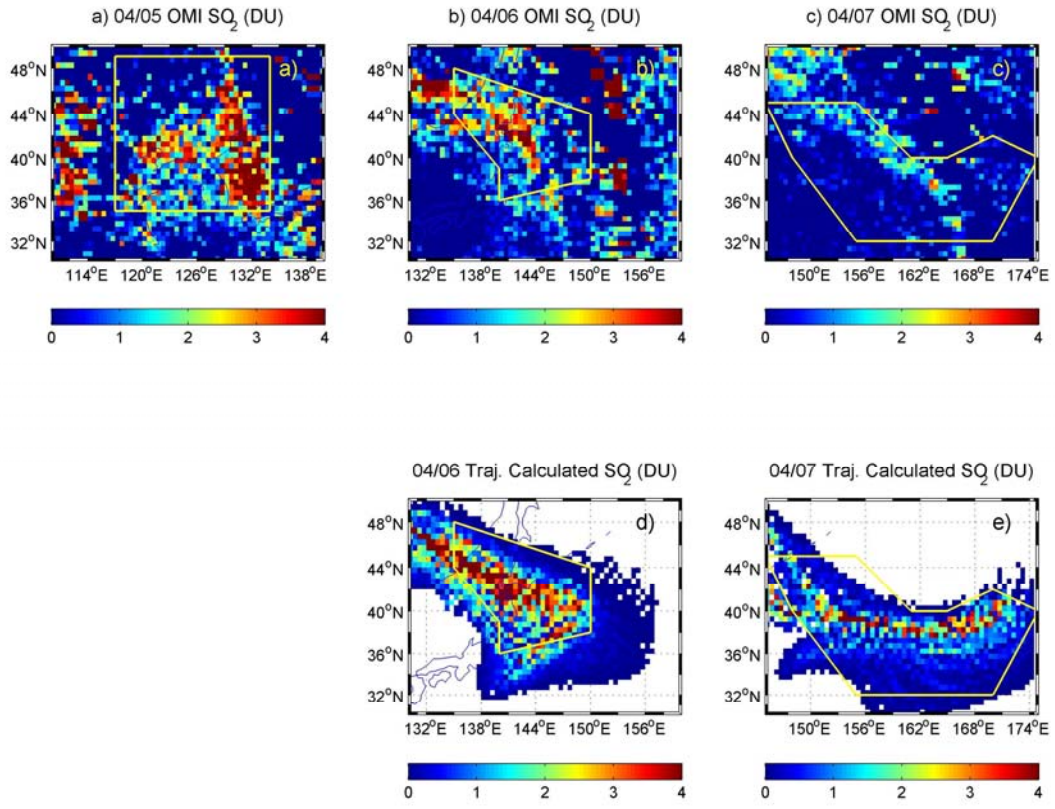

Figure 5.11. OMI-retrieved (a, b, and c) and trajectory-calculated (d and e) SO_2 from April 5 to 7 near the main part of the pollution plume.

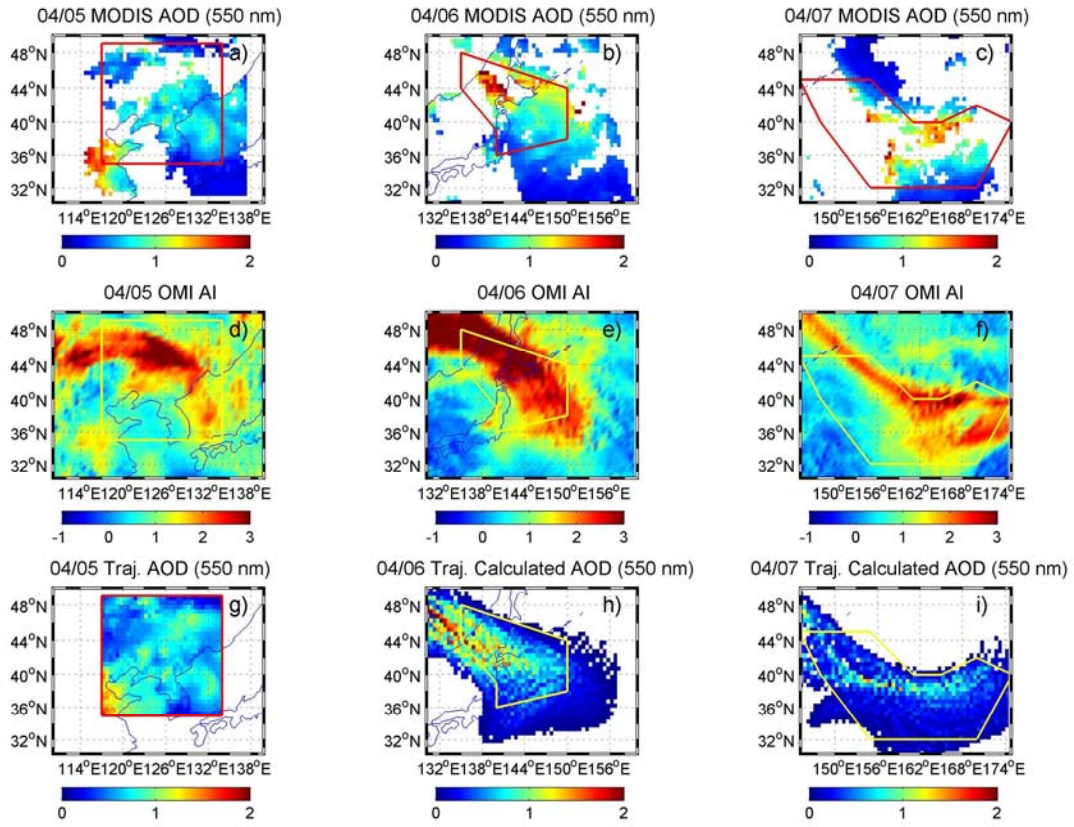

Figure 5.12. MODIS-retrieved AOD (a, b, c), OMI aerosol index (AI, d, e, f), and trajectory projected AOD (g, h, f) from April 5 to 7, 2005. The rectangular box in panel a (also d and g) indicates the area from which forward trajectories are initiated. Polygon boxes in b (e, h) and c (f, i) are examples of the boxes used to represent the core part of the plume, and to calculate the total SO_2 mass on April 6 and 7. Missing MODIS AOD retrievals in upper panels are mainly due to clouds, sun glint, or high surface reflectance (April 5). These grid cells are not included in the calculation of the average MODIS AOD.

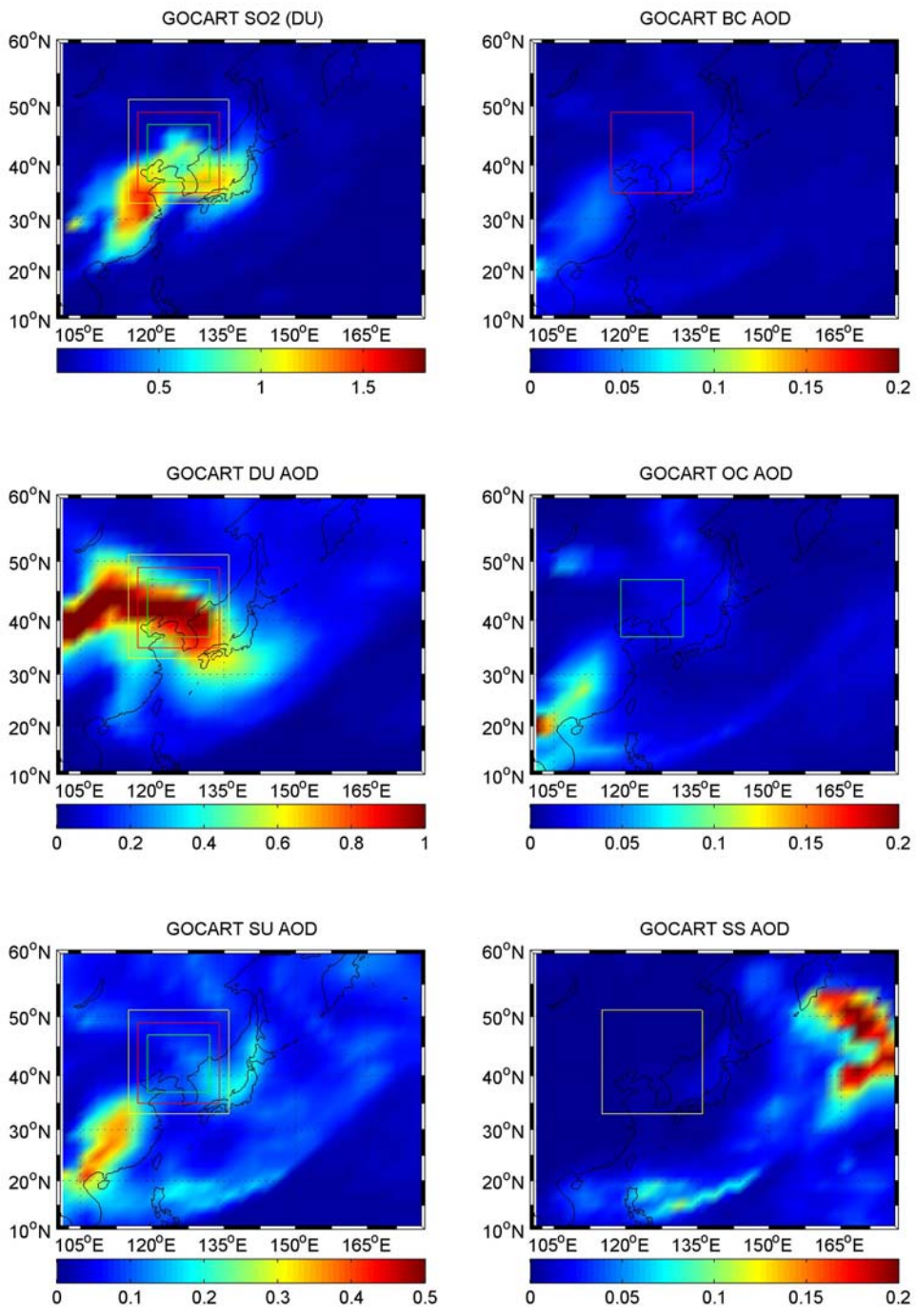

Figure 5.13. GOCART simulated SO_2 column amount (DU), and AOD of black carbon (BC), dust (DU), organic carbon (OC), sulfate (SU) and sea salt (SS) at 06 UTC, April 5, 2005. Red, green, and yellow boxes in the figure indicate domains for averaging GOCART output (results shown in Figure 5.20).

As shown in Figures 5.11 and 5.12, trajectory calculations indicate that the pollution plume in general traveled eastward, reaching N Japan on April 6 and the NW Pacific on April 7. OMI and MODIS successfully captured the pollutants on both days, taking "snapshots" of the plume (Figures 5.11d, e and 5.12h, i). The core part of the plume depicted by the OMI aerosol index (Figure 5.12e, f) resembles that mapped with trajectories (Figure 5.12h, i), suggesting that the forecast plume agrees with satellite observations and that AI could be a useful tool for tracking aerosol transport. GOCART simulated aerosol and SO_2 loadings over N Japan on April 6 (Figure 5.14) and over the NW Pacific (Figure 5.15) on April 7 also confirm the trajectory-projected movement of the plume. Based on Figure 5.9, the aerosol plume passed over the lidar site in ~5 hr on April 6. Using the wind speed at the plume center height (~20 m/s at 2000 m from sounding data), the size of the plume was estimated to be ~400 km along the wind direction (approximately from west to east). This is roughly the same as the satellite observed instantaneous plume size (Figure 5.12).

Bear in mind that the trajectory calculations use SO_2 and aerosols as "inert tracers" and therefore only account for the advection and dilution of the plume (Figures 5.11 and 5.12). OMI retrieved SO_2, on the other hand, reflects the combined effect of transport, chemical conversion, and change in satellite sensitivity and noise; as does MODIS retrieved AOD. Examining Figures 5.11 and 5.12 shows that near the major part of the plume, OMI SO_2 is considerably lower than trajectory SO_2 (e.g., Figure 5.11b vs. d), while MODIS AOD is greater than trajectory projection (e.g., Figure 5.12b vs. h). This seems to indicate that as the pollution plume moved downwind, SO_2, a precursor of sulfate aerosols, was lost whereas aerosols were

introduced (or the aerosol extinction was enhanced). Dust remained the dominant aerosol species throughout the three-day period, as evidenced by OMI AI (Figure 5.12d, e, f) and model simulated AOD (Figures 5.13-15), but sulfate became increasingly important over time (Figures 5.13-15). Is it possible that the satellite sensors detected signal of primary trace gas (SO_2) converting to secondary aerosols (sulfate)? Next I further discuss the evolution of the chemical properties of the plume.

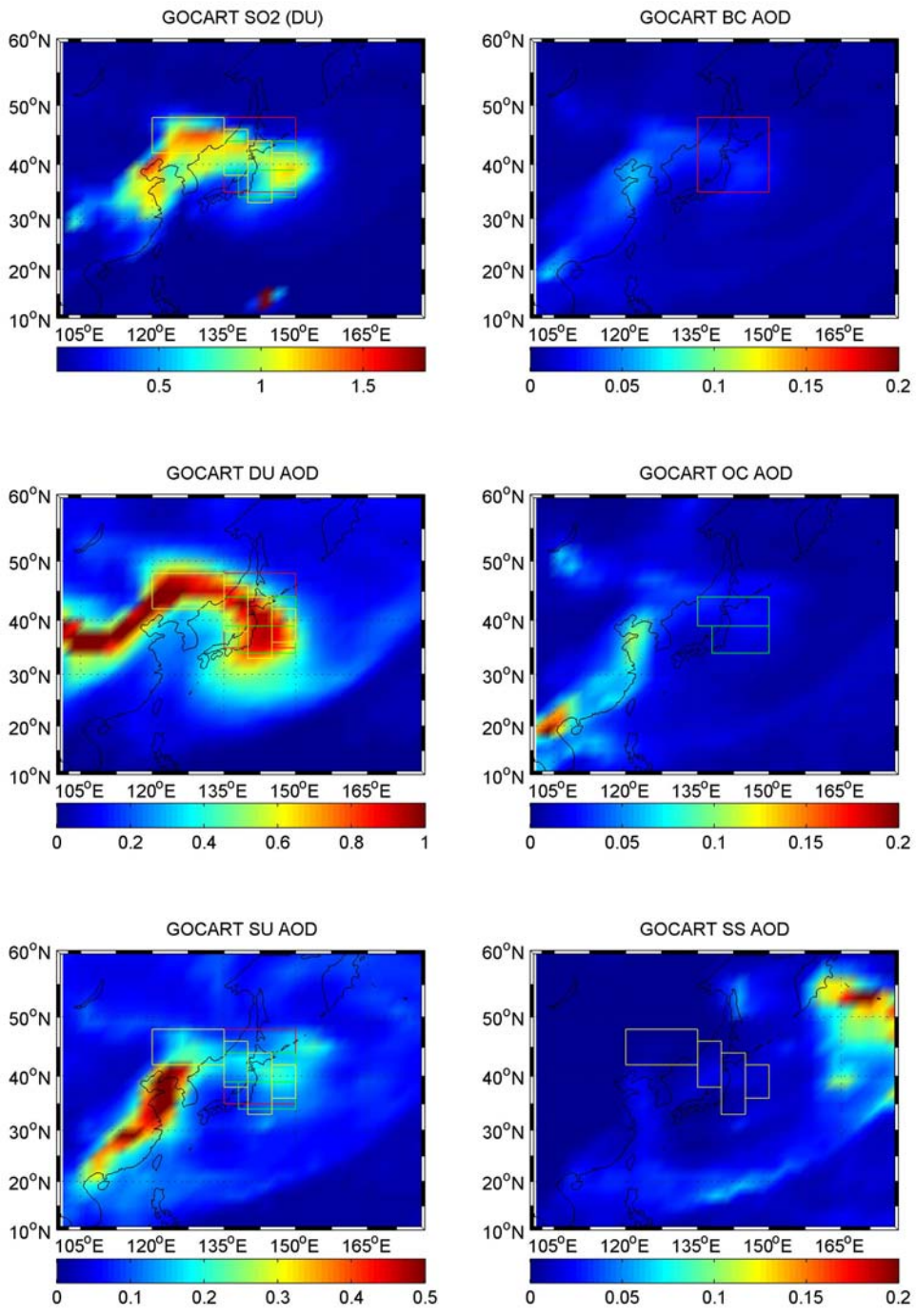

Figure 5.14. Same as Figure 5.13 but for 03 UTC, April 6, 2005

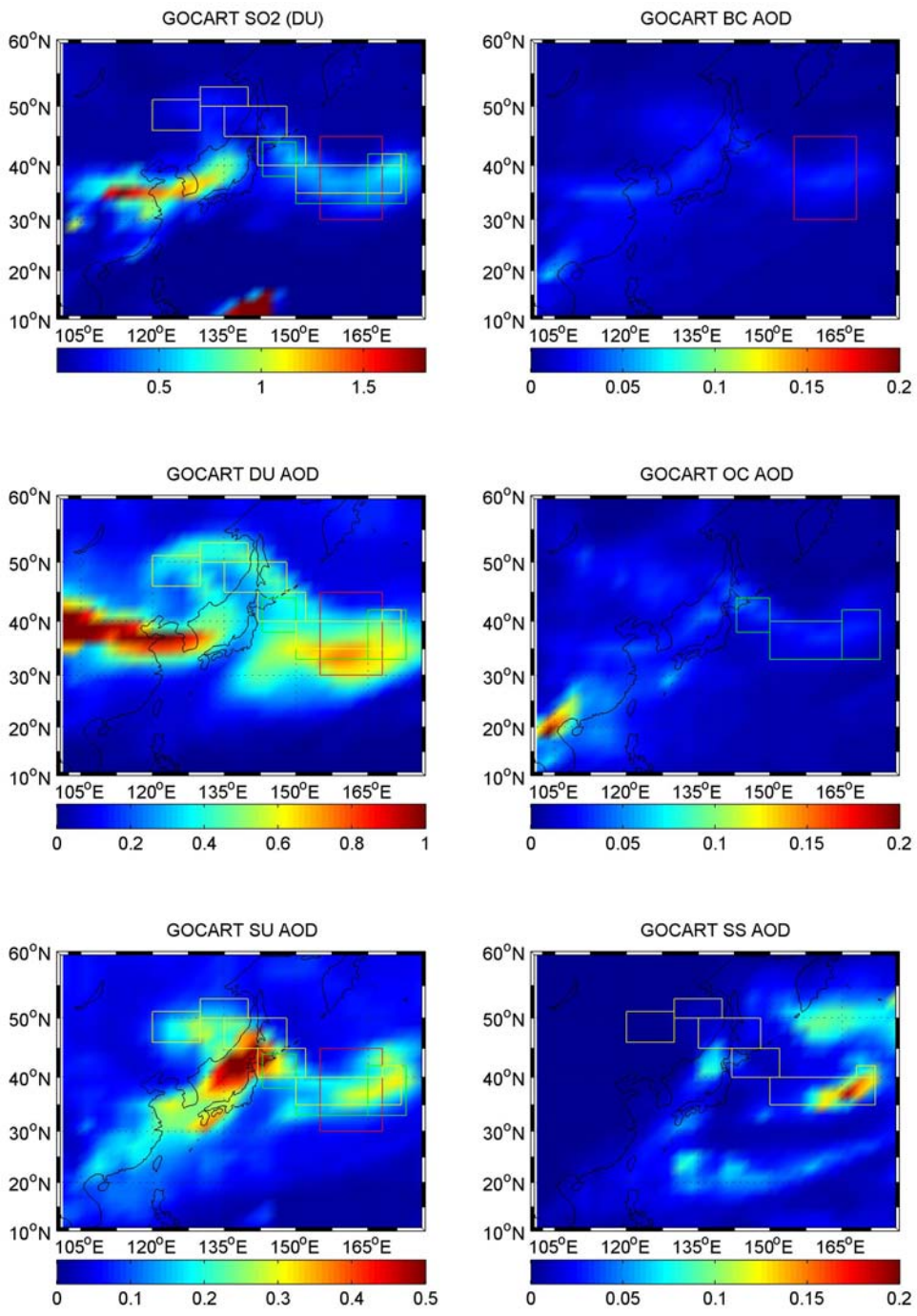

Figure 5.15. Same as Figure 5.13 but for 03 UTC, April 7, 2005

.

5.2.5 Changes in AOD and total mass of SO_2

Clouds, satellite orbit, surface reflectance, and the signal to noise ratio are some restraining factors limiting observation of pollution plumes from space. Dispersion and chemical/physical losses dilute SO_2, leading to the disappearance of the plume initially seen by OMI. On the other hand, OMI is more sensitive to SO_2 lofted to higher altitudes. Low-level clouds may enhance the OMI sensitivity to SO_2 above them, but can block the signal below them. In short, satellite sensors can picture the plume daily, but often only partially. To correct for the part of the plume not detected by the satellites, I define the dispersion weighting factor (DWF). Taking April 6 as an example, I first select a polygon box (P1) covering a good part of the plume with strong trajectory-projected SO_2 signal (e.g., Figure 5.11d). The DWF for this box (DWF_{P1}) is the ratio between trajectory-projected SO_2 mass within P1 ($M_{P1, TRAJ}$) and the initial total SO_2 of the plume (M_1), which is calculated from the OMI retrievals on April 5 (rectangular box, Figure 5.11a) and kept constant in trajectory calculations. Weighting the OMI-retrieved SO_2 mass within P1 ($M_{P1,SAT}$) with DWF_{P1} gives an estimate of the total SO_2 mass on April 6 ($M_{2, P1}$):

$$M_{2,P1} = \frac{M_{P1,SAT}}{DWF_{P1}} \qquad (5.11)$$

$$DWF_{P1} = \frac{M_{P1,TRAJ}}{M_1} \qquad (5.12)$$

In light of the uncertainties in trajectories and possible mismatch with satellite observations, five polygon boxes (P1 … P5) of different size and shape are selected each day for April 6 and 7 (see Appendix III for the polygon box selections). Each

has a corresponding estimated total SO_2 mass (e.g., $M_{2,P1}$ … $M_{2,P5}$). The average is taken as the estimated total SO_2 mass, for example on April 6:

$$M_2 = \sum_{i=1}^{5} M_{2,Pi} / 5 \qquad (5.13)$$

Pixels or grid cells with retrieved SO_2 under a certain threshold (presumed detection limit) are considered undetectable by OMI, and are assumed, on average, to contain half of the threshold column SO_2. Three threshold values (0.2, 0.5 and 1.0 DU) are chosen to approximate the variety of factors that might influence the OMI sensitivity to SO_2. Shown in Figure 5.16 are the estimated total SO_2 of the plume from April 5 to April 7, as well as the average AOD near the plume core (rectangular box in Figure 5.11a on April 5, various polygon boxes in Appendix III on April 6 and 7). The ~100000 tonne of SO_2 originally measured over the rectangular box in Figure 5.11a (35-49°N, 117-134°E) represents roughly 0.05% of the annual global emissions [*IPCC*, 2001]. As the SO_2 mass decays with time, the average AOD near the main body of the plume increases. The polygon boxes on April 6 and 7 mainly cover the core part of the plume while the rectangular box on April 5 encircles both polluted and clean areas. This sampling difference can explain part of the AOD increase, but not all, as suggested by the rising AOD/SO_2 ratio in our sampling areas (~0.3 to ~0.5 in the first two days). In fact, the average column SO_2 in two of the five polygon boxes on April 6 is greater than the plume-wide mean on April 5, reflecting the sampling difference. At least part of the growth in AOD with time is likely caused by introduction of aerosols and/or enhancement of aerosol extinction in the plume.

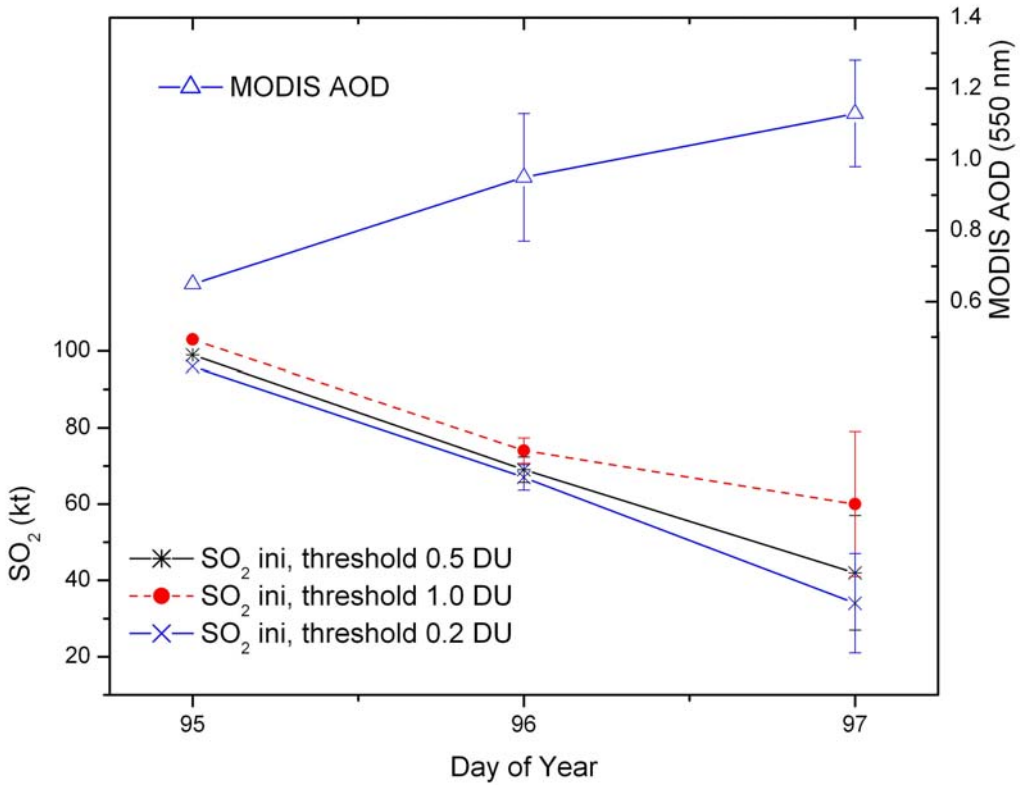

Figure 5.16. Total SO_2 mass of the plume and average AOD near the main body of the plume (within polygon boxes in Figure 5.12). Error bars represent the standard deviation of estimates using different polygon boxes. Note that the estimates of SO_2 mass with different assumptions are diverse on April 7, but much less so on April 6.

5.2.6 Discussion

Aerosols and SO_2 outside of the rectangular box on April 5 (initial plume area) might be carried into the polygon boxes on April 6 and 7, making an "outside contribution" to the estimated SO_2 mass and average AOD. The hygroscopic growth of aerosols may also enhance AOD. I conducted computational experiments to address these two factors. Forward trajectories similar to those described in section 5.2.2 are calculated over a larger area (30-49°N, 110-144°E). The hygroscopic growth

effect on AOD is estimated with NCEP reanalysis RH along trajectories and various growth factors (α):

$$\frac{AOD_{RH2}}{AOD_{RH1}} = \left(\frac{1-RH1}{1-RH2}\right)^{-\alpha} \qquad (5.14)$$

where RH1 and RH2 are the relative humidity at two different moments along a trajectory. Growth factor α when equal to zero represents aerosols with no hygroscopic growth; α of 0.5 corresponds to extremely hygroscopic aerosols. For reference, α is about 0.2-0.3 in summer months over the NE U.S. [*Taubman et al.*, 2004], where aerosols mainly consist of hygroscopic fine particles. Dust-dominated particles in this study are likely less hygroscopic. Figure 5.17 shows the trajectory projected AOD on April 6, with outside contribution and hygroscopic growth included. Compared to Figure 5.12h, aerosols initially outside of the plume area can enhance AOD in polygon boxes on April 6, particularly over the area E of Japan (around 40°N, 150°E, Figure 5.17). The effects of hygroscopic growth, in contrast, are relatively small except over the land W of the Sea of Japan. The trajectory projected AOD including outside contribution and aerosol swelling is compared to MODIS retrievals in Figure 5.18.

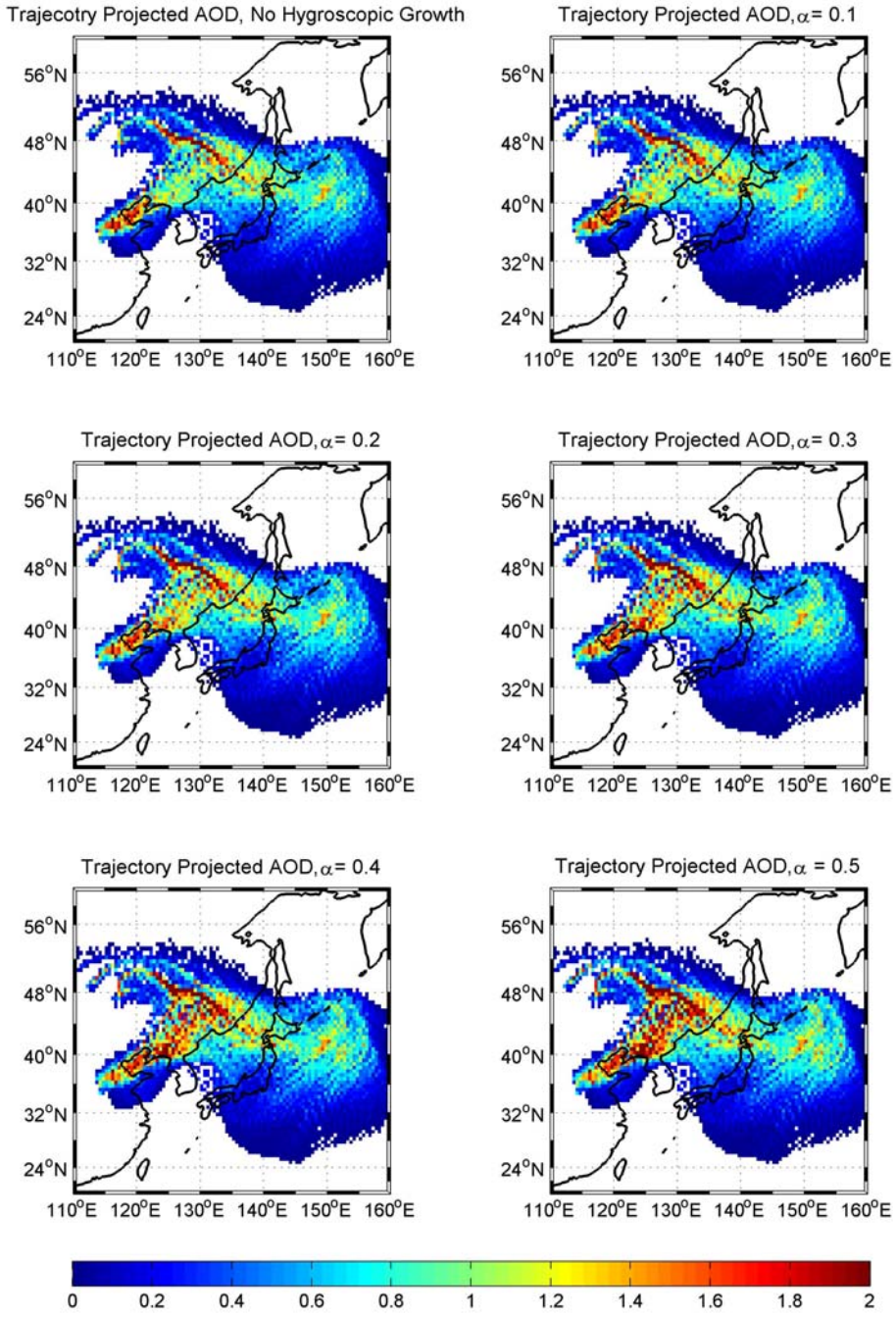

Figure 5.17. Trajectory-projected AOD on April 6 with contributions from outside of the initial plume area (rectangular box in Figure 5.12) and aerosol hygroscopic growth accounted for. Hygroscopic growth is calculated with NCEP reanalysis RH along forward trajectories and α of 0-0.5 (cf. Eq. 5.14).

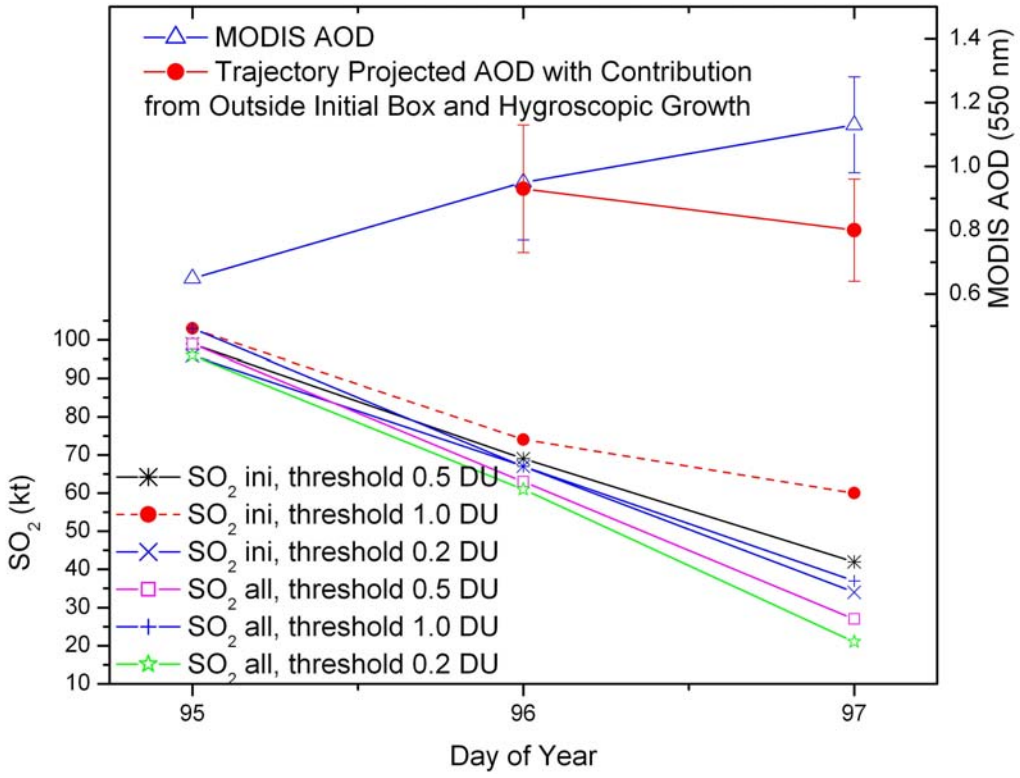

Figure 5.18. Total SO_2 mass of the plume with (SO_2 all) and without (SO_2 ini) outside contribution corrected for, and MODIS (blue triangle) and trajectory projected average AOD including outside contribution and effects of hygroscopic growth (red dot) near the core part of the plume.

To correct for the outside contribution to SO_2 mass, I first derive a different dispersion weighting factor, for example on April 6 for polygon P1:

$$DWF_{P1,all} = \frac{M_{P1,TRAJ,all}}{M_1} \qquad (5.15)$$

where M_1 is the same as in Eq. 5.12, $M_{P1,TRAJ,all}$ is the projected SO_2 mass using trajectories initiated from the larger area. Satellite determined SO_2 mass in P1 ($M_{P1,SAT}$) is then weighted with the new DWF to estimate the total SO_2 mass on this day ($M_{2,P1,all}$):

$$M_{2,P1,all} = \frac{M_{P1,SAT}}{DWF_{P1,all}} \qquad (5.16)$$

The assumption here is that SO_2 in the whole region (in and outside of the rectangular box in Figure 5.11a) decays at the same rate. The resulting total SO_2 mass of the plume ("SO_2 all", Figure 5.18) is generally smaller than that without the correction ("SO_2 ini", Figure 5.18), but the general decreasing trend in SO_2 remains largely unchanged.

From the decay in SO_2 mass, I can approximate the overall SO_2 lifetime in this plume. Assuming first order loss, the slope of the linear fit in Figure 5.19 gives the e-folding time or lifetime of SO_2. Our estimated SO_2 lifetime varies from 1.4 to 3.6 days, and is in the range of prior modeling studies [*Berglen et al.*, 2004; *Chin et al.*, 2000; *Koch et al.,* 1999]. Note that the calculated SO_2 mass on April 7 is far more diverse due to diluted signal. Excluding this day, the "best-guess" SO_2 lifetime is 2-3 days.

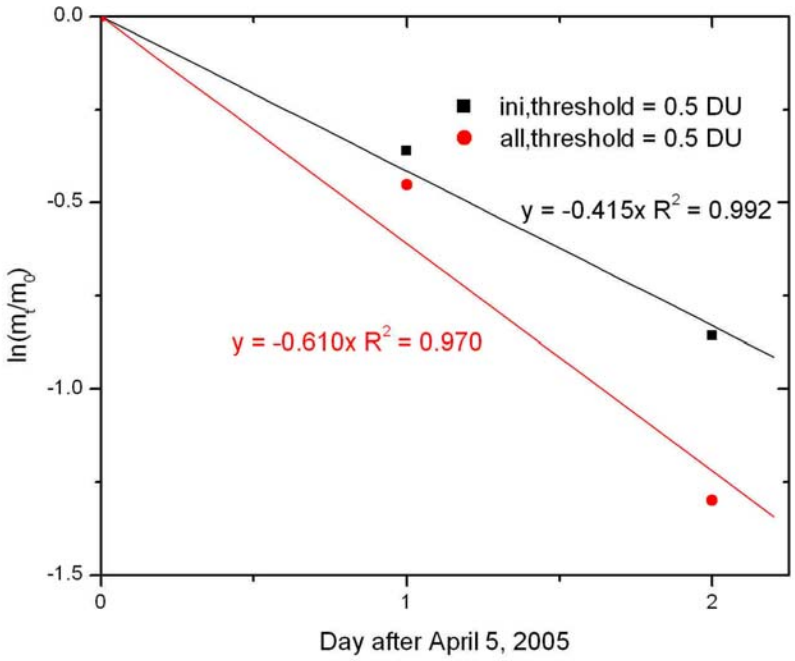

Figure 5.19. Decay plot of SO_2 in the plume from April 5 to 7, 2005. The slope of these two linear fits gives first-order removal rate of 0.42-0.61/day, which corresponds to an SO_2 overall lifetime of 1.6-2.4 days. Decay plots of SO_2 loading with other threshold values give slightly different estimates of SO_2 lifetime (1-4 days).

Supposing that all lost SO_2 converts to ammonium sulfate (assumed specific scattering coefficient: 4.2 g/m^2), the newly generated sulfate aerosols may add to ~0.1-0.2 average AOD over the polygon boxes on April 6, and ~0.2-0.4 in AOD on April 7. This is probably an overestimate, since a fraction of SO_2 can be removed by dry deposition; and the interaction with dust may produce larger particles that scatter light less efficiently. Little difference is found between the observed and projected AOD on April 6 (Figure 5.18); loss of dust from the plume probably cancels out the introduction of secondary aerosols. On the 7^{th}, the difference between trajectory-projected and observed AOD is about 0.3. Satellites cannot discern different aerosol species; the GOCART simulation (Figure 5.20) suggests that removal of dust and increase of sulfate are the most important processes controlling the change of aerosol

loading in this plume. Note that GOCART has a coarse horizontal resolution as compared to satellite observations; the boxes in Figures 5.13-15 indicate the domains for averaging GOCART AOD. They correspond roughly to the sampling areas (rectangular and polygon boxes) in Figures 5.12, but are not exact matches. In summary, in this case study two different satellite sensors OMI and MODIS successfully tracked this April 5 pollutant plume on its transport pathway, and measured the changes in its chemical properties. The loss of SO_2 and generation of sulfate appear to be detectable from space, although the uncertainty is high. A chemical transport model run could reduce the uncertainty. The method presented here could be employed to study other pollution transport episodes if SO_2 and aerosol loadings are heavy enough, but for each episode AMF correction to satellite product is needed for qualitative application of the data.

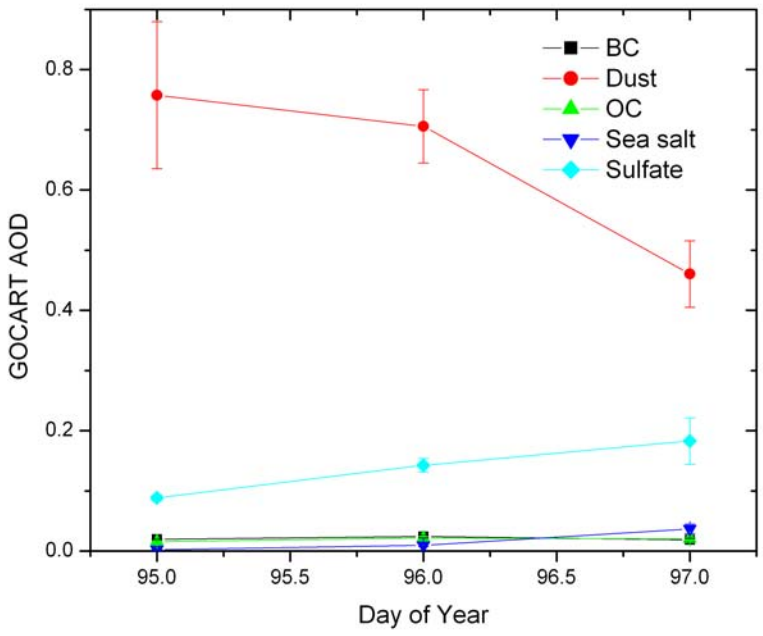

Figure 5.20. AOD of different aerosol species near the main body of the plume (boxes in Figures 5.13-5.15) in GOCART output from April 5 to 7, 2005.

Clouds may contaminate MODIS AOD retrievals, and might produce more marked errors on April 6 and 7, when cloud cover was greater. In a simple test, I discard MODIS pixels with high AOD (> 95th percentile) but small AE (< 0.2) to remove possible cloud-contaminated data. This results in lower average AOD of 0.61, 0.88, and 1.03 on the three days, but does not change the overall trend of AOD. Adjusting the threshold of AOD and AE to filter out cloud-contaminated pixels gives slightly different but qualitatively consistent results.

5.2.7 Summary

In this section I present a case study tracking and characterizing a pollutant plume from East Asia using satellite measurements. MODIS and OMI, two sensors of the "A-train" constellation successfully captured the regional-scale plume on three consecutive days along its transport pathway. The estimated SO_2 overall lifetime (e-folding time), derived from the decay of the SO_2 loading of the plume assuming first-order loss, is about 1-4 day and in line with previous modeling studies. Conversion from SO_2 to sulfate aerosols can generate AOD signal up to a few tenths, strong enough to be detected from space. Satellite retrieved average AOD near the core part of the plume is very close to the trajectory projected value (hygroscopic growth and outside contribution accounted for, but no loss of aerosols) over N Japan on April 6; to this point the introduction of secondary aerosols and loss of primary aerosols (dust) may have canceled out. MODIS AOD is greater than the trajectory AOD over NW Pacific on April 7. The GOCART model demonstrates that dust AOD decreases while sulfate AOD grows as the plume moves away from its source in N China.

Substantial uncertainties are associated with the quantitative application of satellite data. Errors in satellite retrievals stem from a priori assumptions and interferences. Cloud fraction changes quite a bit, and the plume becomes under-sampled, particularly for aerosols over the NW Pacific on April 7. Satellite sensitivity to SO_2 (and other trace gases) is controlled by various factors such as vertical distribution and surface reflectance, which would change as the plume evolves. In addition, SO_2 decays with time. Quantification of the temporal change of the SO_2 mass is therefore subject to sampling inconsistency. In this case study, errors of trajectory calculation grow over time with the distance traveled by the trajectories. Applying a few aircraft profiles to a large region is also probably an oversimplification. Nonetheless, as a first step, this case study provides a cost-effective alternative supplementing intensive semi-Lagrangian aircraft campaigns, and showcases the great potential in the fusion of data from multiple satellite sensors. With CO, NO_2, and cloud information from satellites, more can be done in the future to investigate the transport and evolution of pollution plumes and their interactions with weather and climate.

Chapter 6: Conclusions

6.1 Summary of Results

Measurements of trace gases (CO, NO_y, SO_2, and O_3), aerosol optical properties (scattering and absorption), and aerosol chemical composition were made in Xianghe, a rural site in N China about 70 km ESE of Beijing, in March 2005 under the auspices of the U.S.-China joint research project EAST-AIRE. Located in an area of mixed agriculture and light industry, in proximity to two mega cities (Beijing and Tianjin), this non-urban site featured high but variable pollutant loadings (CO: ~1 ppm, SO_2: ~20 ppb, NO_y: ~20 ppb, aerosol scattering: ~ 400 Mm^{-1}, aerosol absorption: ~50 Mm^{-1}, sulfate: ~8 $\mu g/m^3$, nitrate: ~10 $\mu g/m^3$) during the experiment. Springtime mid-latitude wave cyclones and the associated fronts, passing the region every 4-5 days, are the major mechanism behind the accumulation and removal of pollutants at the ground level. Strong northerly winds brought cold postfrontal air with little anthropogenic pollution but sometimes dust, while relatively warm and stagnant prefrontal conditions built up pollutants.

The observed ratios between different pollutants were compared to some contemporary emission inventories for China. The measurement-derived CO/SO_2 ratio (~35) is at least a factor of two greater than the national (10-17, [*Streets et al.*, 2003, 2006]) and regional (~8, [*X. Wang et al.*, 2005]) inventory ratios, suggesting substantial uncertainties in currently estimated CO (or less likely: SO_2) emissions from China. Representing a large area with measurements at a single location might

be problematic, but the observed CO/SO_2 ratio is consistently greater than *Streets et al.* [2003, 2006], when air was from the populated and polluted region to the southwest of Xianghe. The inventory CO/SO_2 ratio in metropolitan areas of China is in general very small (~10). Some other factors, for example the temporal mismatch between observations and inventories, pollutant release height, and chemical reactions may also contribute to our reported discrepancy, although the latter two are shown unlikely to contribute substantially in this study. To understand pollutant emissions from China better, especially those from the fast-developing eastern part, we need to make extensive observations near emission source regions and additionally, determine emission factors of various sources such as small boilers and automobiles [*Streets et al.*, 2006].

Trace gas emissions from a nearby hand-fed coal-fired boiler were studied. The derived SO_2 (15.4 g SO_2/kg coal) and NO_x (0.2 g NO_2/kg coal) emission factors fall in the range of the factors applied in some emission inventories [*Streets et al.*, 2003]. CO emissions, however, depend on combustion conditions; the CO emission factor from this study is at least a factor of two lower than the inventory values [*Streets et al.*, 2003, 2006]. Thus if this boiler is representative, small-scale coal boilers cannot explain the possible low bias in inventory CO; emissions from mobile sources need to be further investigated, but are beyond the scope of this research. In our ballpark estimate, similar small boilers altogether sum to less than 1% of China's annual gaseous pollutant emissions, but can cause severe local air quality issues, as these boilers with their low stacks are often located in densely populated communities, run under cold and stagnant conditions, and lack emission control measures.

Consistent with previous studies in eastern China, aerosols near the surface at the Xianghe site are found to be light-absorbing. The single scattering albedo calculated from the aerosol scattering and absorption data is 0.81 and 0.86 in the morning and in the afternoon, respectively. Assuming that black carbon is the dominant absorbing compound in the visible (specific absorption coefficient: 10 m^2/g), from aerosol absorption/CO correlation, I estimated the black carbon emissions from China at 1300-2600 Gg/yr, comparable to that from inventory [*Streets et al.,* 2003] but with large and ill-constrained uncertainties.

A considerable fraction of aerosol particles in Xianghe during the experiment were of soil origin, as indicated by the loadings of some crustal elements (e.g., Al: 9.6 $\mu g/m^3$; Fe: 6.5 $\mu g/m^3$, Ca: 9.8 $\mu g/m^3$). However high levels of Ca, Fe, and K under stagnant conditions hint at strong sources related to anthropogenic activities, for example construction and agricultural burning. Peak concentrations of Al on the other hand were mostly seen in the windy postfrontal environment, likely associated with transported or locally emitted dust. Compared to the Earth's crust, some trace elements (e.g., Zn, Cu, Ag, Pb, and As) in aerosol samples were enriched. Synoptic variations of these pollutant tracer elements were in phase with CO, implying their anthropogenic origins. Despite prohibition of leaded gasoline for an extended period, substantial Pb sources still exist in the area as evidenced by CO-correlated and highly enriched Pb (enrichment factor: 133). Chloride ion was enriched compared to sea water and in general more so when SO_2 was high, probably from heavy coal burning.

Our result that nitrate was more abundant than sulfate at the Xianghe site is in contradiction with a number of earlier studies conducted in the region. Size range of

aerosol sampling, interference of trace gases, analysis technique, sampling time and location are among the factors that complicate comparison of different aerosol composition data sets. Recent expansion in NO_x emission sources (large point sources and vehicle fleet) and progress in SO_2 emission abatement (e.g., replace coal with low-S fuels in downtown Beijing) might have increased the nitrate-sulfate ratio in the region. The ratio shows apparent synoptic variations: high in the warm and polluted prefrontal atmosphere, while low under cold and clean postfrontal conditions. NO_x-to-nitrate conversion appears temperature-dependent and probably is mainly through gas-phase reactions. The conversion from SO_2 to sulfate, in contrast, is more complete in air from the dry and cold north, where gas-phase reactions are likely suppressed. An analysis combining backward trajectories, assimilated meteorological data, and satellite-retrieved cloud properties suggests that during the experiment about 70% of the aerosol samples with relatively high SO_2 conversion ratio may have a history of potential cloud interaction. The in-cloud processes provide a fast pathway for SO_2 oxidization. The interaction between dust and sulfur compounds, widely studied in earlier research, may also contribute to the reaction of SO_2, but only in ~40% of the samples. Ground measurements in coordination with the EAST-AIRE Xianghe experiment carried out in Hedo, Japan, ~1000 km to the east, recorded surges in sulfate aerosols as wave cyclones passing the island brought continental flows from N China [*Takami et al.*, 2007] behind cold fronts. SO_2 in these postfrontal low-level transport events was almost completely reacted away, a fact that can only be explained with in-cloud processing [*Takami et al.*, 2007]. Together, the two studies demonstrate that, in contrast to some previous conclusions [e.g., *Yao et al.*, 2003],

under certain circumstances in-cloud processes can be important in the springtime sulfur chemistry over East Asia, both upwind and downwind of the strong emission sources in China. Chemical transport models need to properly treat clouds to accurately simulate the sulfur cycle in this part of the world.

The EAST-AIRE aircraft campaign conducted in April 2005 over the area near Shenyang (population: six million), the capital of China's industrialized northeastern province of Liaoning and ~600 km NE of Beijing, further investigated the interaction between mid-latitude wave cyclones and air pollution. The change in air quality in response to weather conditions during the aircraft experiment was similar to that in Xianghe. Within the PBL, prefrontal flights generally found great levels (~20 ppb SO_2) of anthropogenic pollutants associated with surface winds from the populated and polluted areas to the south; postfrontal flights on the other hand measured little SO_2 but sometimes dust (~60 Mm^{-1} aerosol scattering) in northerly winds. I contrast the results from this experiment to a chemical climatology amassed through hundreds of flights over the NE U.S. mainly on smoggy summer days [*Taubman*, 2004]. Pollutant levels over China are greater than over the U.S. at almost every altitude, indicating the potential large-scale impacts of pollutants from China. The overall particle size of aerosols sampled over China is larger than over the U.S., probably due to dust emissions, although line-losses of coarse particles in sampling could be large in both studies (in particular over China).

The prefrontal flight on April 5 recorded pollutants well above background levels (1-3 ppb SO_2, 300 ppb CO, 50 Mm^{-1} aerosol scattering) in the free troposphere, at 2000-3000 m altitude. Backward trajectory analysis shows little evidence of lofting

by a warm conveyor belt over the continent on previous days. However, satellites spotted some non-precipitating convective clouds near the industrial cities of Hohhot and Baotou roughly 1000 km to the west, along the backward trajectory and ~24 hr prior to the flight. This upwind convective process on April 4 might have lifted pollutants to the free troposphere, where strong westerly winds could carry them downwind in the next ~1 day to our area of flight. Pollutants lifted above the PBL could potentially travel over long distances, turning a local air pollution issue into a large-scale problem. Spring (MAM) cloudiness over N China is comparable to over the NE U.S., but it rains much less in N China. Dry (non-precipitating) convective processes over the emission source regions of China in spring can loft and export pollutants with great efficiency, but need further investigation and can be a great challenge to numerical models.

OMI and MODIS satellite sensors make it possible to look into the April 5 air pollution episode at a regional scale, and to track the transport and evolution of the pollution plume from China to as far as the northwestern Pacific on the following few days. The total SO_2 loading of the plume decayed with time. The overall SO_2 lifetime (e-folding time) based on the decay and assuming first-order loss, is 1-4 day, in the range of previous modeling studies. SO_2 to sulfate conversion would add up to ~0.1-0.2 and ~0.2-0.4 in AOD near the core part of the plume on April 6 and 7, respectively. The signal is however not easily detected in this dust-laden plume, as removal of dust and introduction of sulfate may cancel out. The GOCART model confirms that reduction of dust and formation of sulfate are the two major processes changing the aerosol loadings of this particular plume. This analysis showcases the

potential in combining different satellite sensors to trace major transport events and pollutant evolution, despite large uncertainties in quantitative application of satellite data.

6.2 Recommendations

In this dissertation I try to illustrate a few aspects of China's air pollution problem, by analyzing a data set collected during the first intensive field campaign of EAST-AIRE. This joint China-U.S. project focuses on measurements over inland China, close to some of the most populated and polluted regions in the world. Compared to experiments conducted downwind of China over the Pacific [e.g., *Carmichael et al.*, 2003], measurements near the emission source areas benefit from stronger signal and less chemical/physical losses, and can be directly used to evaluate emission inventories. However, as has been repeatedly stressed, this pilot study covers only a few locations over a short period of time, while emission inventories are in most cases compiled for a large region over much longer time (e.g., one year). Studying pollutant emissions from a country as massive and as diverse (e.g., modernized mega cities Beijing and Shanghai vs. rural areas) as China justifies long-term observations at much more representative locations. Combined with in-situ measurements, chemical transport models in forward, inverse, or assimilation modes can help estimate emissions from China in a more quantitative way, accounting for factors such as chemical reactions and pollutant release heights. One challenge in comparing modeling results to observations near emission sources would be to improve the spatial and temporal resolution of both models and emission inventories.

It was found in this study that some current emission inventories probably underestimate CO emissions from some of the largest metropolitan areas of China, for example, Beijing, Tianjin, Shanghai, and Guangzhou. A small coal-fired boiler studied appears to be more efficient than previously thought, but we probably need to test the results by sampling more similar boilers. A soaring vehicle fleet and deteriorating traffic conditions in these mega cities can lead to vast growth in CO emissions. To resolve this mystery of the "missing CO source", experiments directly determining emission factors of mobile sources in Chinese cities are needed.

The research flights conducted around the northeastern city of Shenyang are among some of the first efforts to measure the vertical distribution of pollutants over inland China. Some interesting comparisons have been made between results from the China flights and the chemical climatology of the northeastern U.S., but more flights in multiple seasons over China are necessary to build up a chemical climatology for more meaningful comparisons. The April 5 flight discloses the potential role that upwind dry convection may play in lofting and transporting pollutants in northern China's arid spring. Flights in proximity to similar non-precipitating convective clouds may provide direct evidence and more details for this lofting mechanism, but require careful planning and probably forecast modeling support. Additional profiling flights and chemical transport modeling are essential to determine the relative importance of convection and the warm conveyor belt lofting in long-range transport out of East Asia. Simulating dry convection processes may be particularly challenging, since the numerical model output cannot be graded against observed

precipitation. Instead, satellite-retrieved cloud properties may be useful for evaluating model-simulated convection.

In two case studies, I make use of some recently available satellite data to study the evolution of pollutants transported into and out of northern China by mid-latitude wave cyclones. These satellite products provide information concerning weather and pollution at a regional scale and on a daily basis. Substantial uncertainties restrict their quantitative applications, but there is room for improvement. Multi-layer cloud retrieving algorithms [e.g., *Chang and Li*, 2005] and later-launched CloudSat can resolve the vertical distribution of clouds, which may allow for a more accurate space-based account of cloud-pollutant interactions. As shown in the study tracking the April 5 pollution plume, the OMI SO_2 and AI products can be powerful tools tracing pollutant transport, and can be employed to identify pollution-influenced areas over the oceans in future studies on aerosol radiative forcing. The OMI SO_2 retrieval algorithm needs to be improved to estimate quantitatively anthropogenic emissions or study pollution episodes. The correction for clouds in this study assumes a homogeneous cloud deck; future studies will apply a cell-by-cell cloud correction scheme utilizing OMI-retrieved cloud information. Model simulated SO_2 and aerosol vertical profiles may help improve the OMI SO_2 algorithm as well. The ratio between satellite-retrieved relatively long-lived (e.g., CO) and short-lived (e.g., SO_2) gases may change as plumes move away from their sources. Using this differential decay of long- and short-lived gases, we may be able statistically evaluate the lifetime of short-lived gas. But enhancing sensitivity to

pollutants in the lower atmosphere especially in the boundary layer will be key to quantitatively applying satellite data in air pollution research.

In summary, research in this dissertation constitutes a first step towards better understanding China's air pollution issue and its large-scale impacts. Future efforts integrating in-situ observations, satellite retrievals, and numerical simulations will be crucial to appreciate and ultimately mitigate air pollution in China, a problem with roots in China but global effects.

Appendix I Surface Weather Maps during the Aircraft Campaign

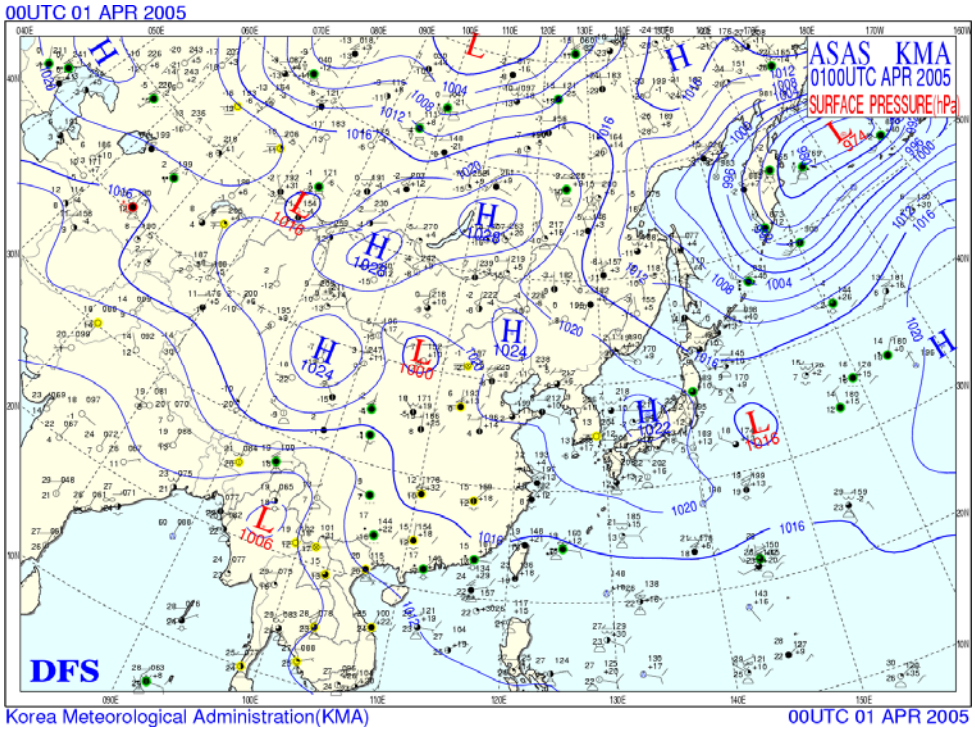

Appendix I.1. Surface weather analysis of East Asia at 00 UTC on April 1, 2005. (Source: *Korea Meteorological Administration*).

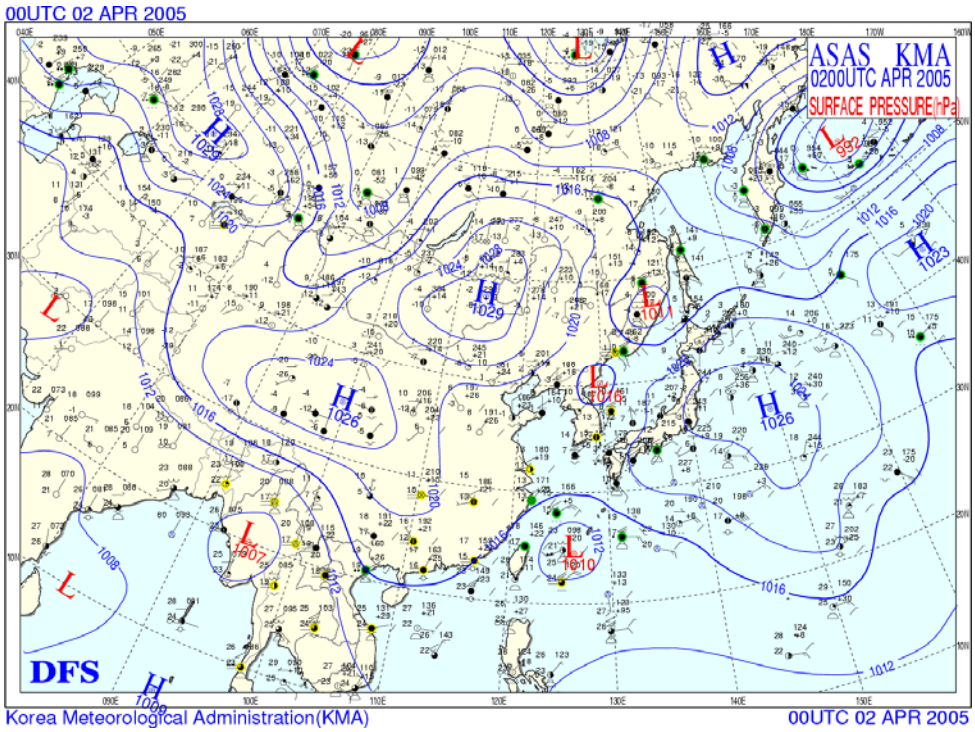

Appendix I.2. Surface weather analysis of East Asia at 00 UTC on April 2, 2005.

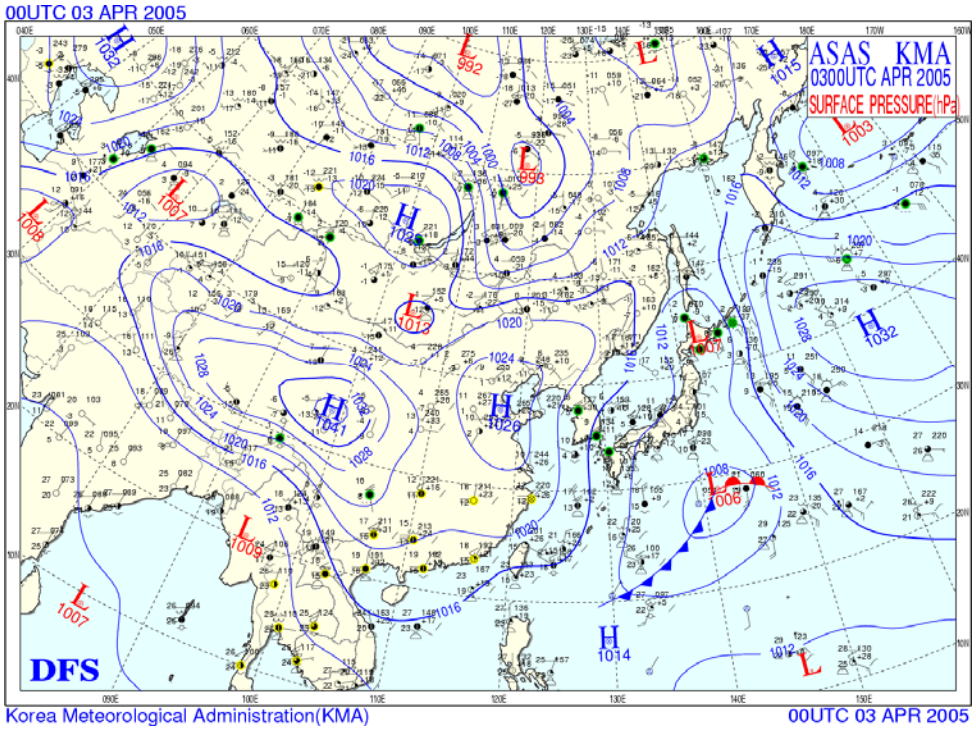

Appendix I.3. Surface weather analysis of East Asia at 00 UTC on April 3, 2005.

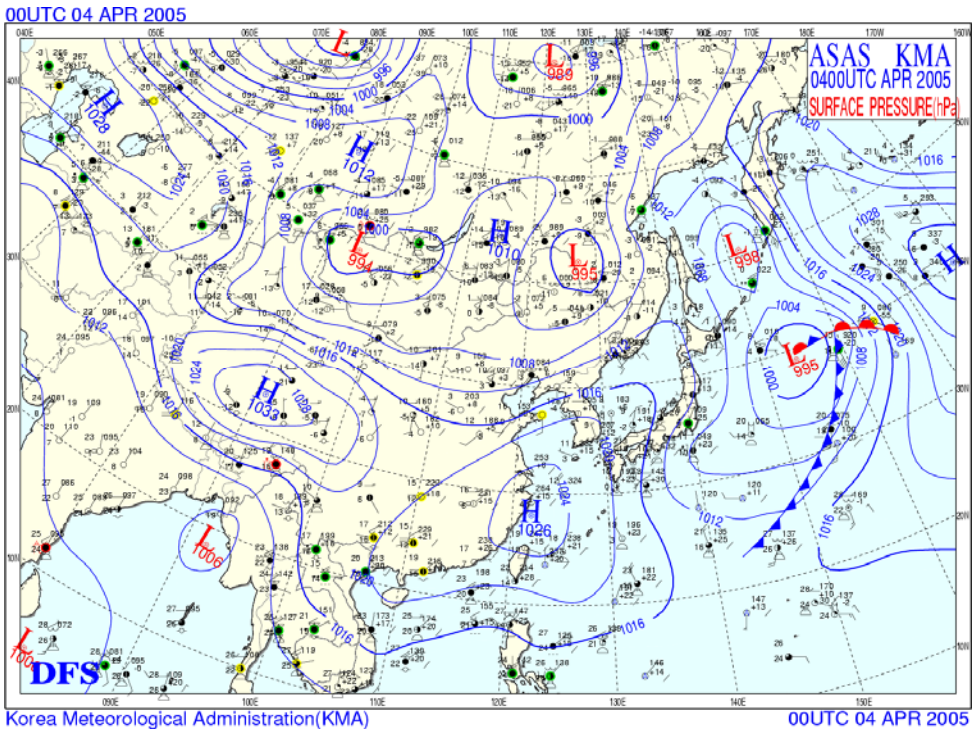

Appendix I.4. Surface weather analysis of East Asia at 00 UTC on April 4, 2005.

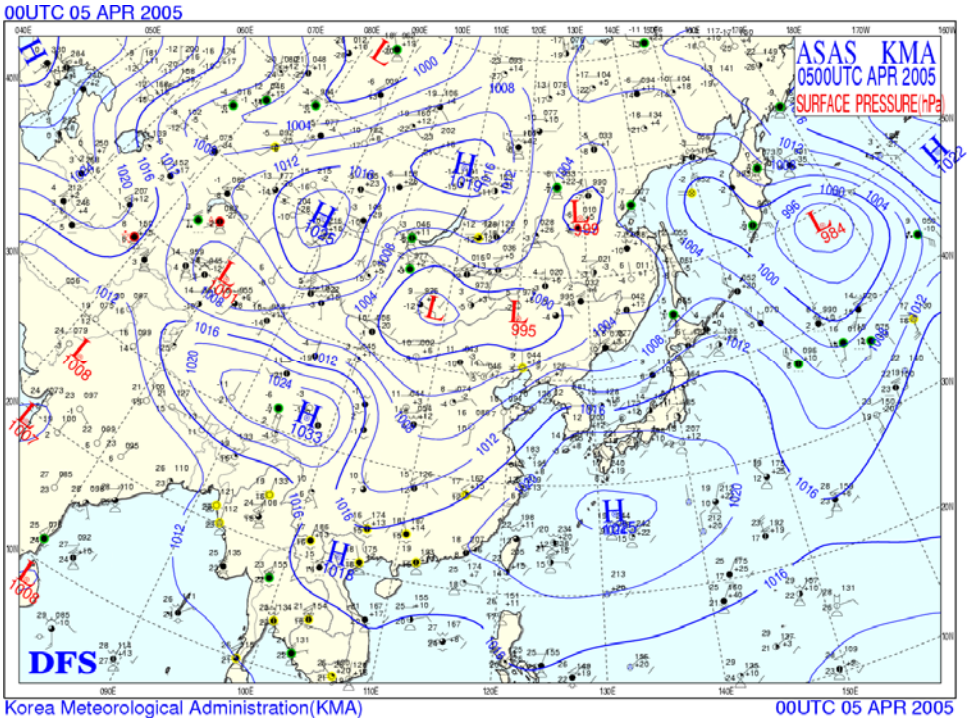

Appendix I.5. Surface weather analysis of East Asia at 00 UTC on April 5, 2005.

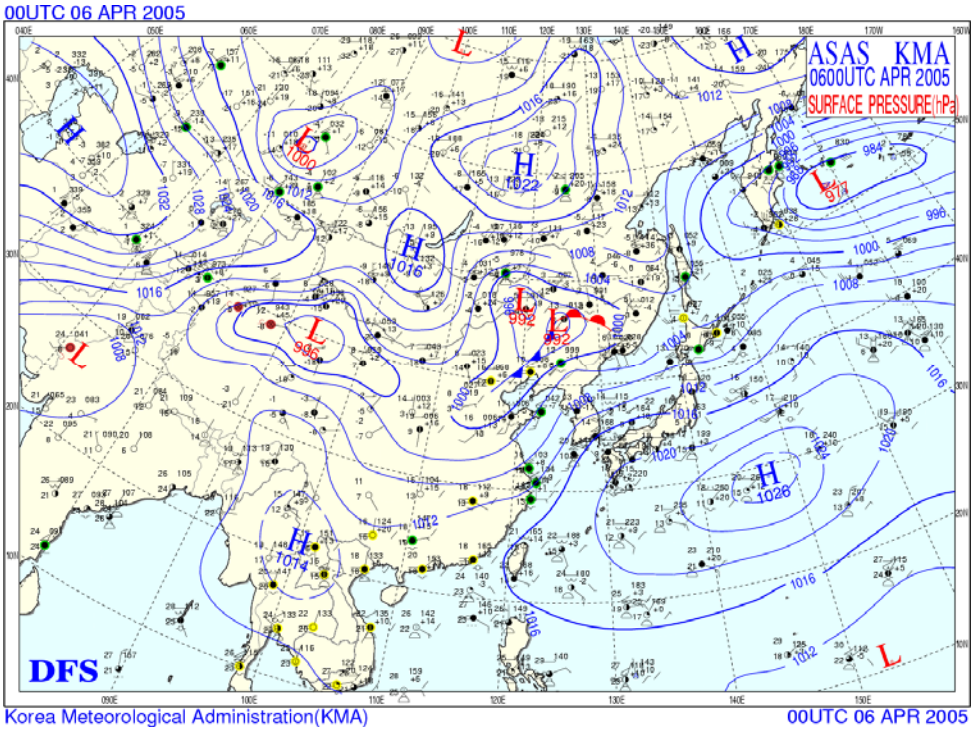

Appendix I.6. Surface weather analysis of East Asia at 00 UTC on April 6, 2005.

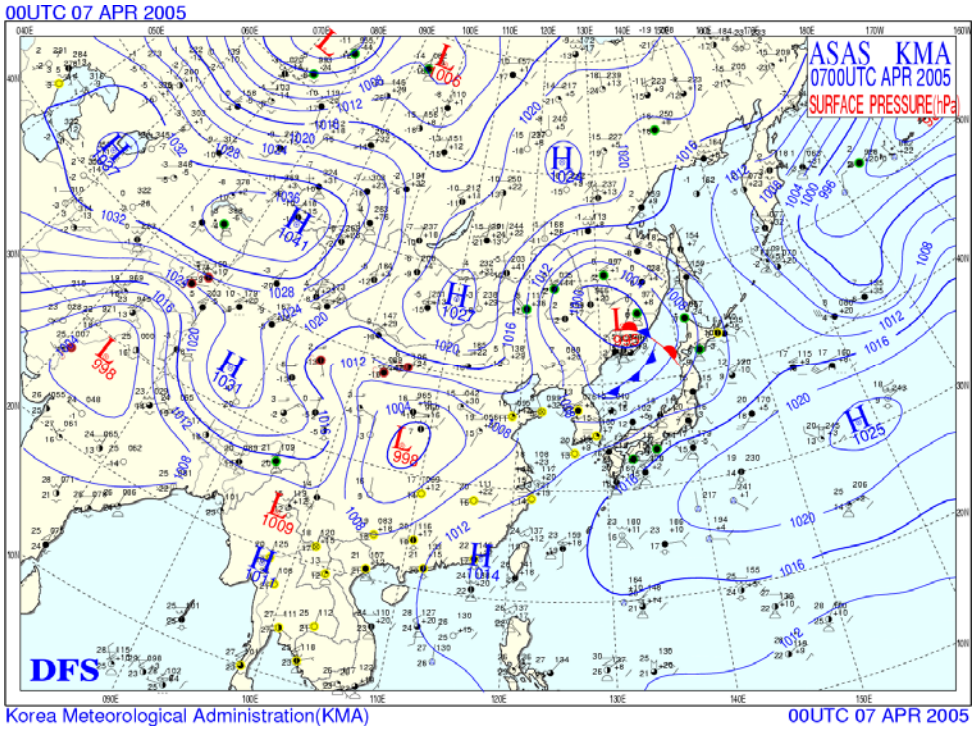

Appendix I.7. Surface weather analysis of East Asia at 00 UTC on April 7, 2005.

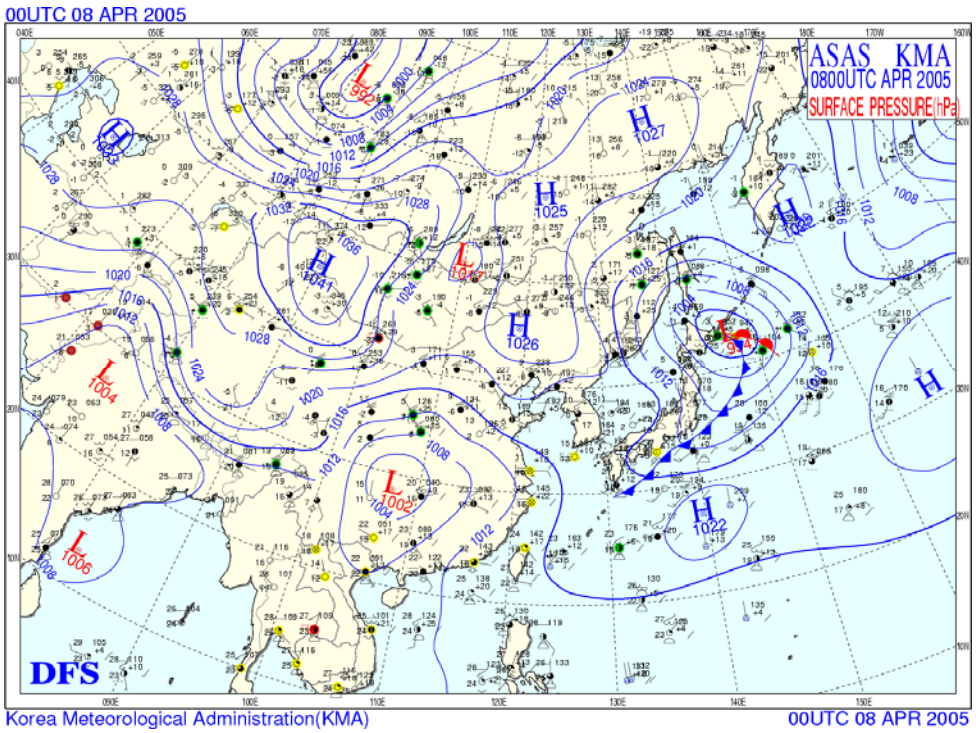

Appendix I.8. Surface weather analysis of East Asia at 00 UTC on April 8, 2005.

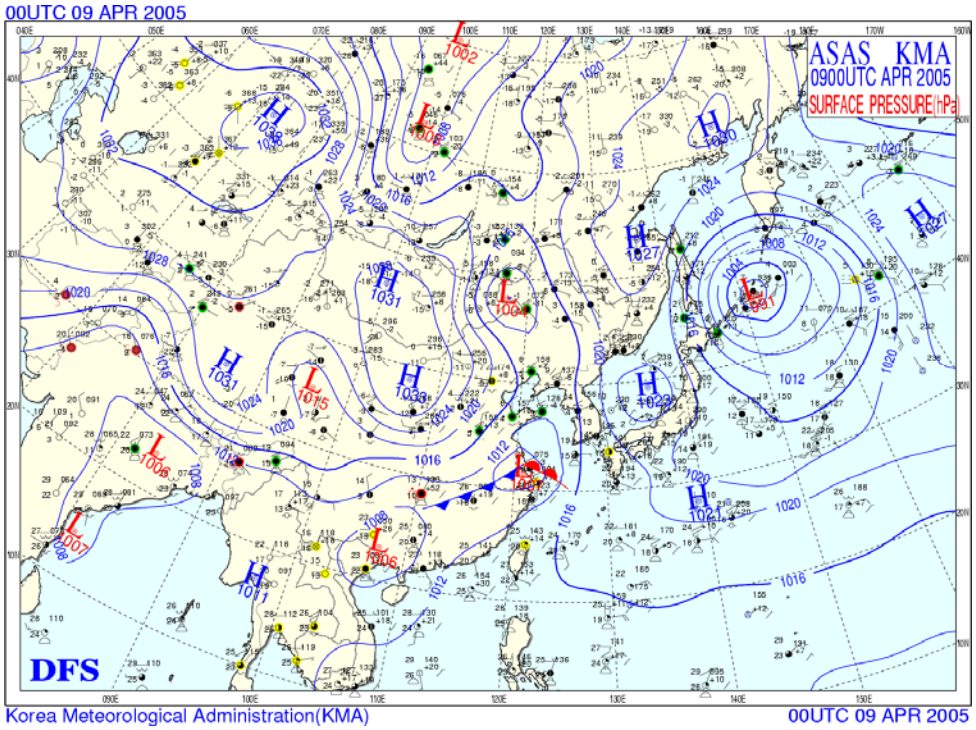

Appendix I.9. Surface weather analysis of East Asia at 00 UTC on April 9, 2005.

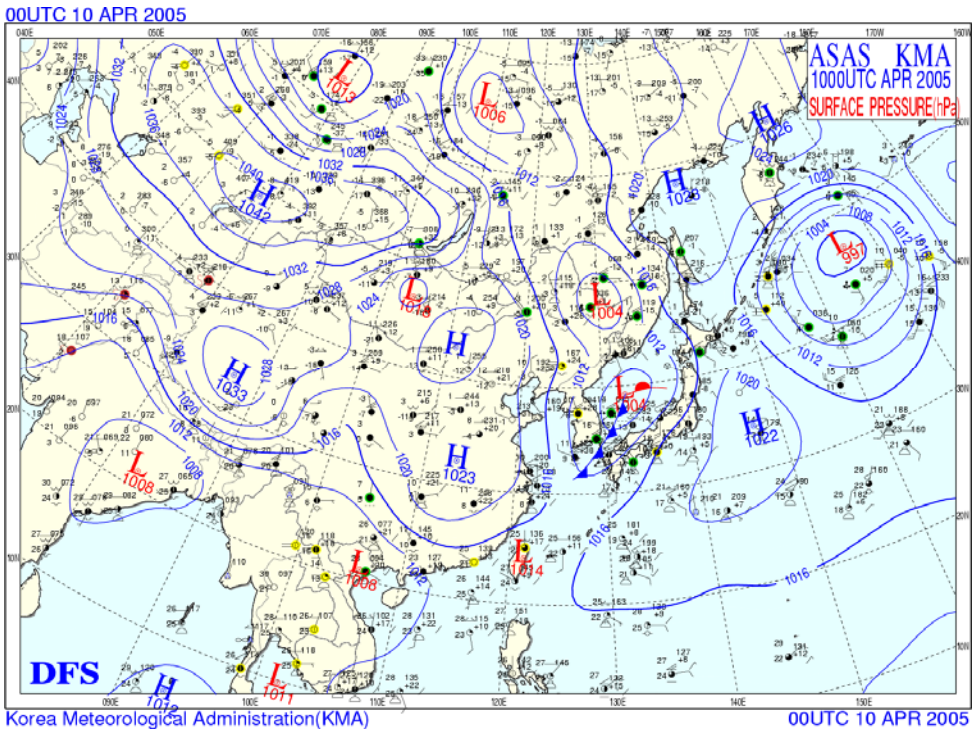

Appendix I.10. Surface weather analysis of East Asia at 00 UTC on April 10, 2005.

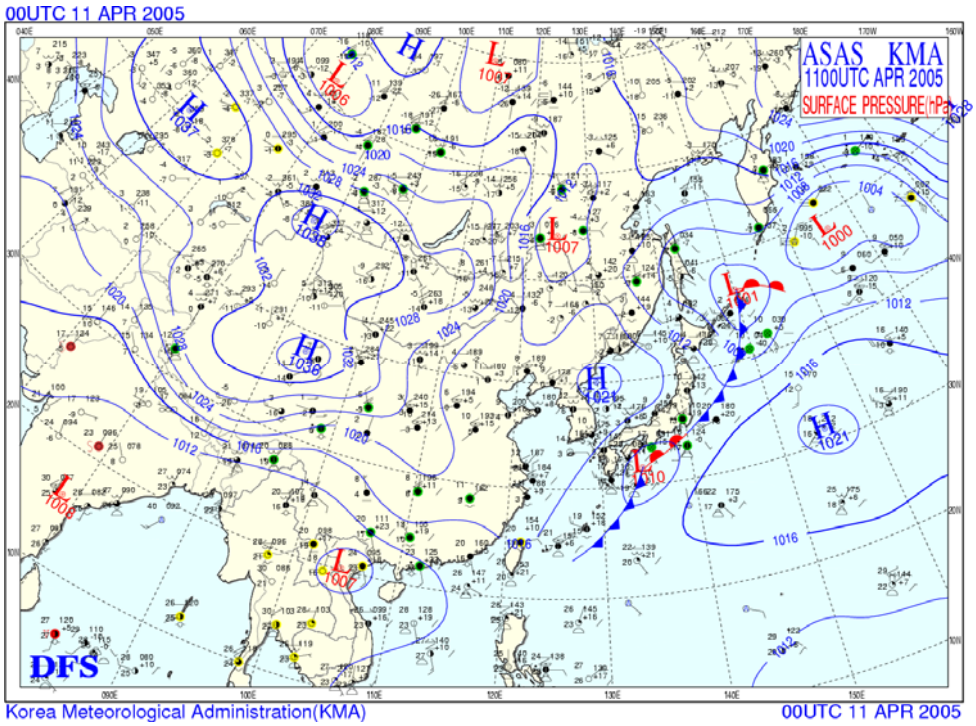

Appendix I.11. Surface weather analysis of East Asia at 00 UTC on April 11, 2005.

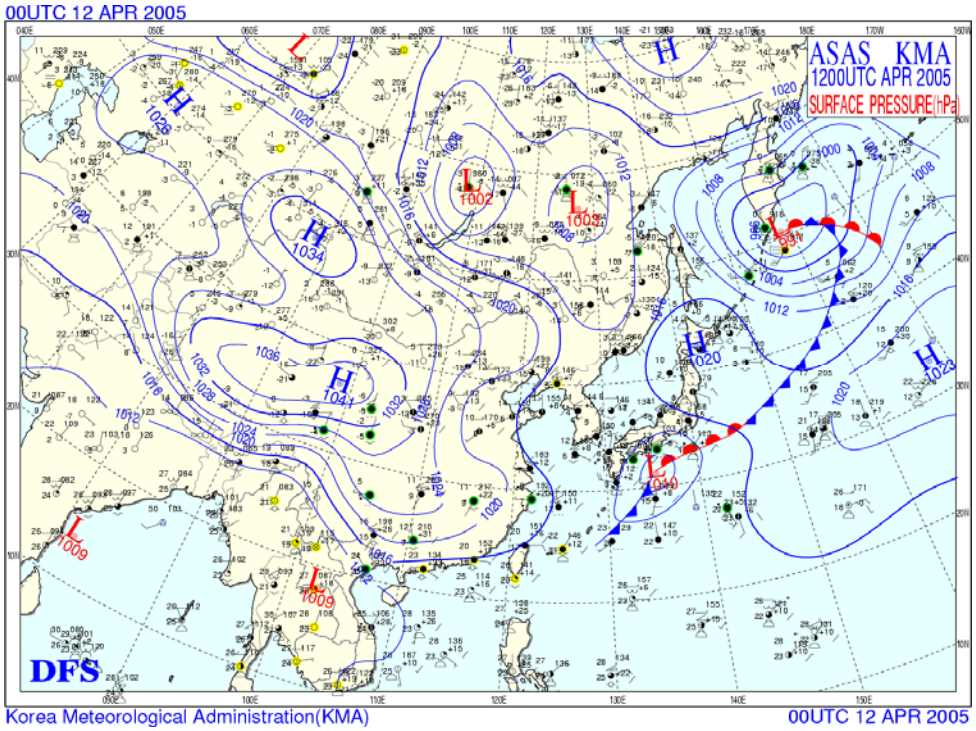

Appendix I.12. Surface weather analysis of East Asia at 00 UTC on April 12, 2005.

Appendix II: Vertical Profiles of Pollutants during the Aircraft Campaign

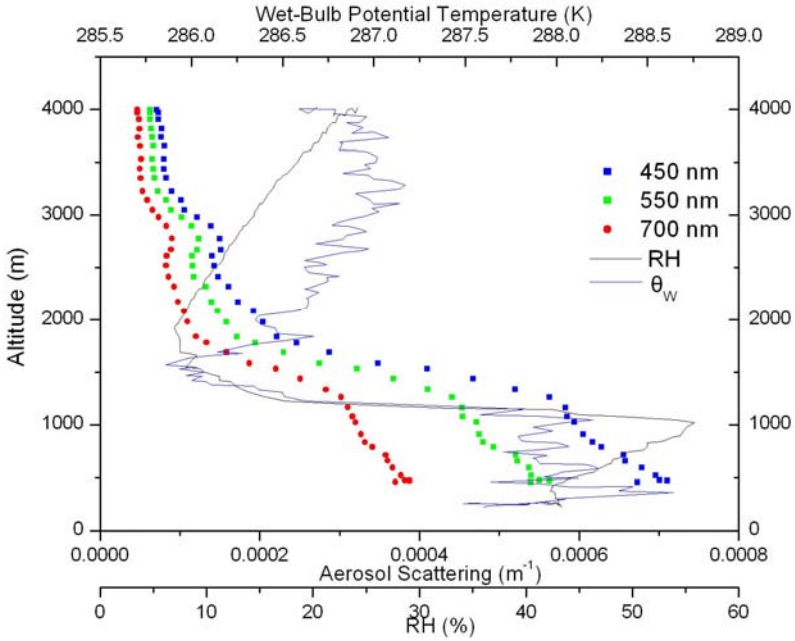

Appendix II.1. Vertical profiles of RH, aerosol scattering, and wet-bulb potential temperature north of Shenyang on April 5, 2005.

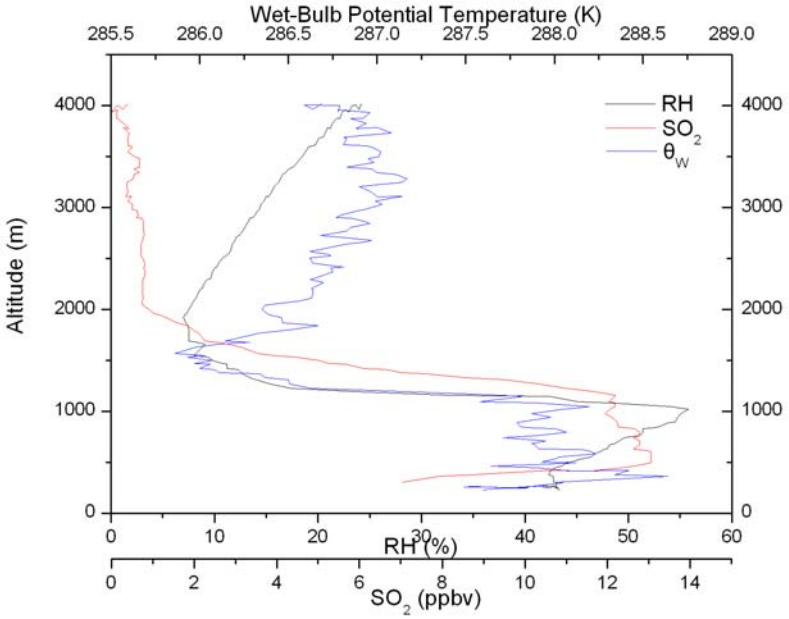

Appendix II.2. Vertical profiles of RH, SO_2, and wet-bulb potential temperature north of Shenyang on April 5, 2005.

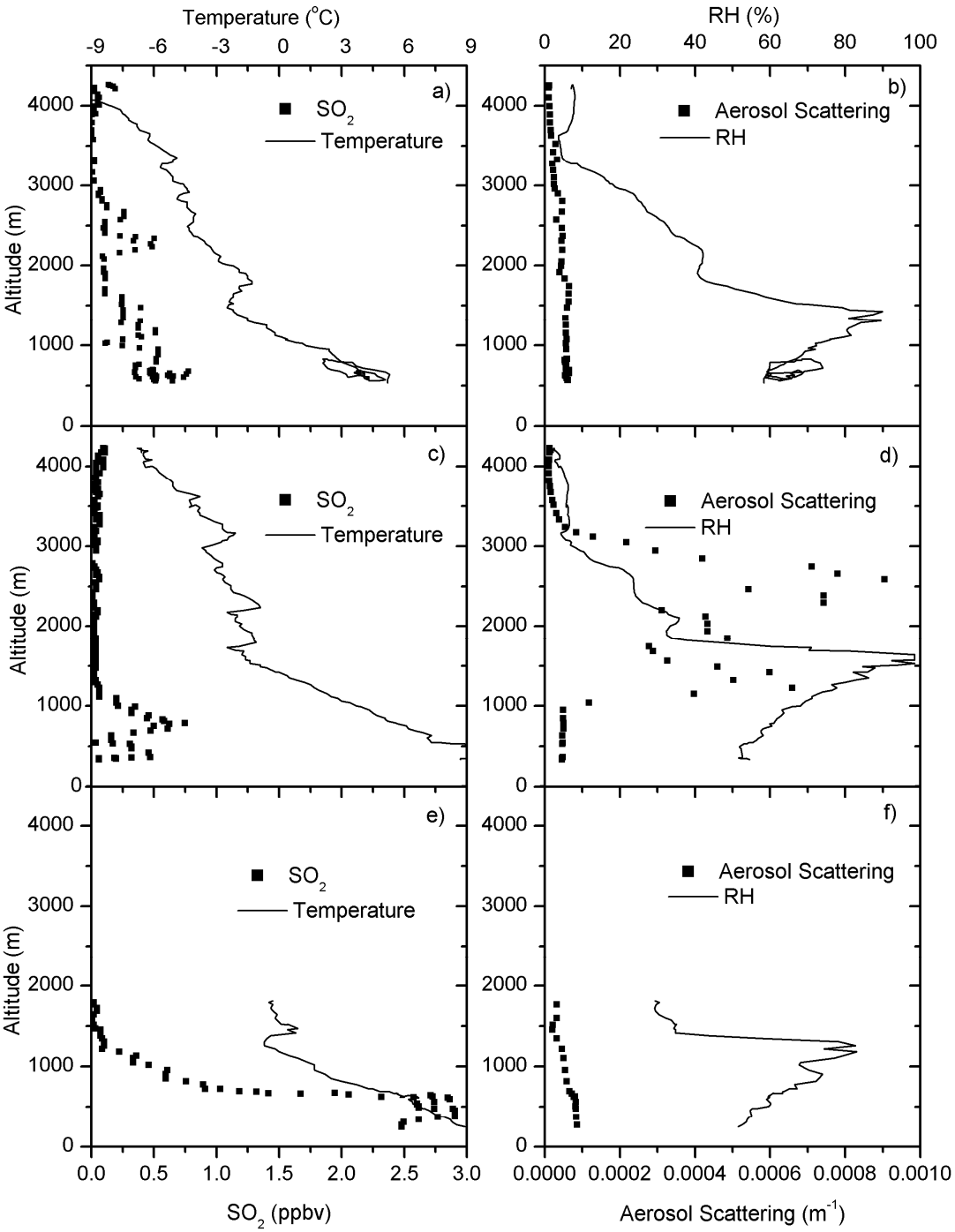

Appendix II.3. Vertical profiles of SO_2, temperature, aerosol scattering coefficients (550 nm) and relative humidity on April 10, 2005. Panels a) and b) present data obtained from a spiral ascend north of Shenyang (42.48ºN 123.61ºE). Panels c) and d) present data obtained from a spiral ascend south of Shenyang (41.37 ºN 122.61 ºE). Panels e) and f) present data obtained as when descending to the airport (41.64 ºN 123.49 ºE).

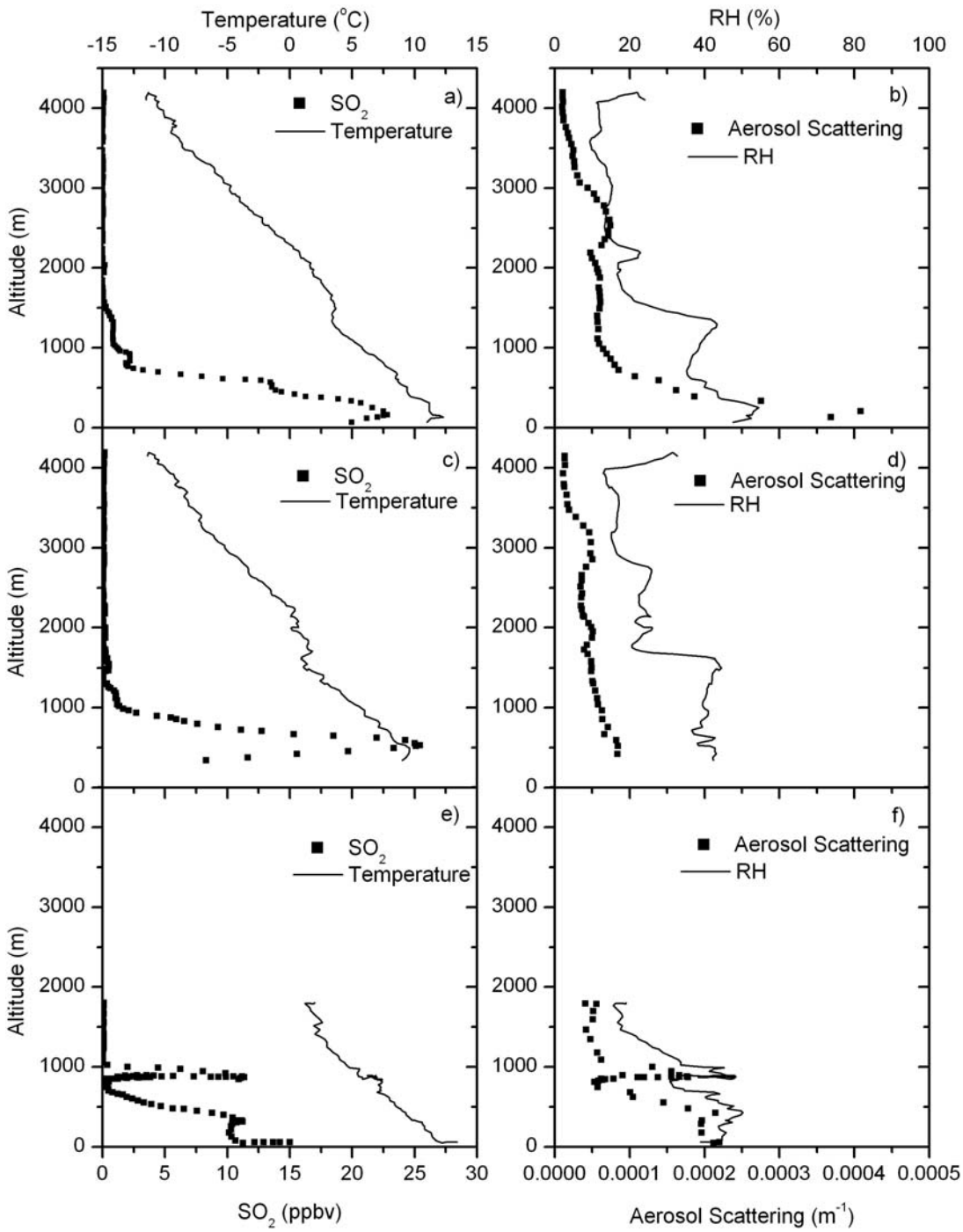

Appendix II.4. Vertical profiles of SO_2, temperature, aerosol scattering coefficients (550 nm) and relative humidity on April 11, 2005. Panels a) and b) present data obtained from a spiral ascend south of Shenyang (41.35ºN 122.65ºE). Panels c) and d) present data obtained from a spiral ascend south of Shenyang (42.45 ºN 123.61 ºE). Panels e) and f) present data obtained when descending to the airport (41.64 ºN 123.49 ºE).

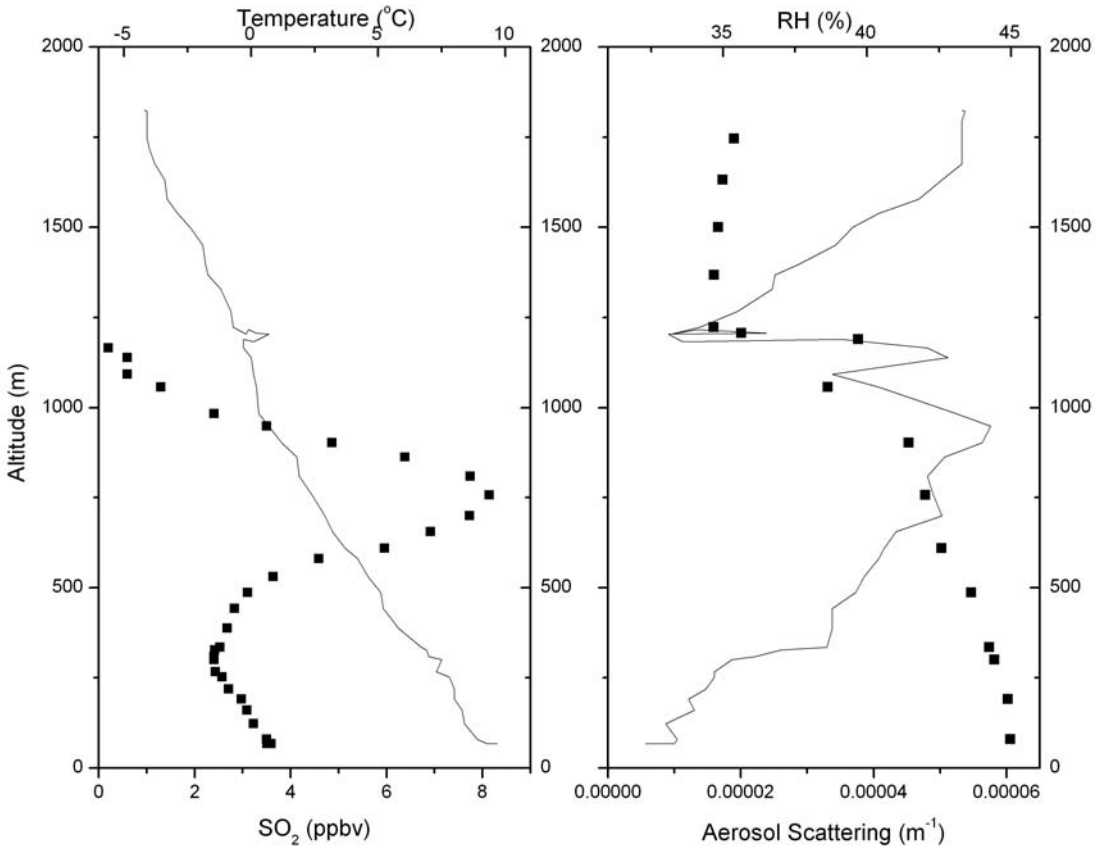

Appendix II.5. Vertical profiles of SO_2, temperature, aerosol scattering coefficients (550 nm) and relative humidity on April 12, 2005. Data were obtained as the aircraft was descending to the airport (41.64 ºN 123.49 ºE).

Appendix III Polygon Boxes Used to Calculate the Total SO_2 Loading of the Plume

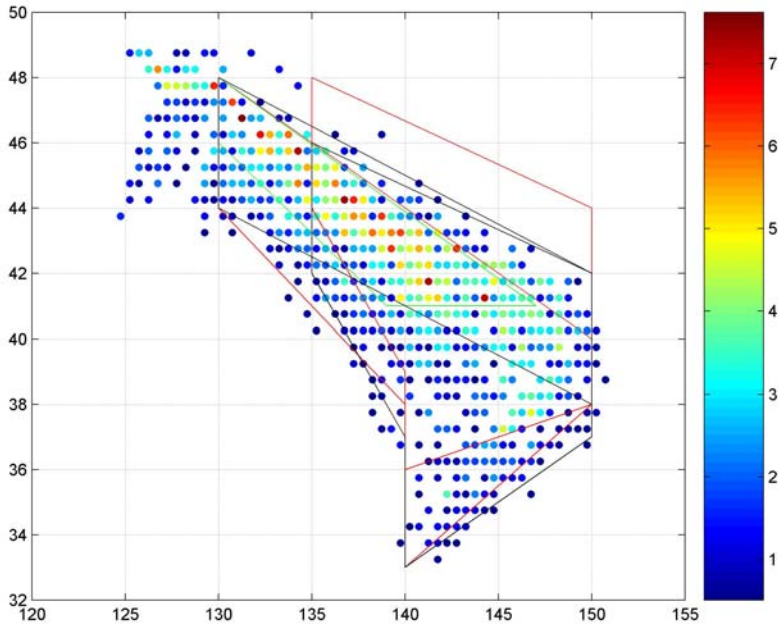

Appendix III.1. Polygon boxes used to sample pollution plume on April 6. Color represents trajectory projected SO_2 loading (DU).

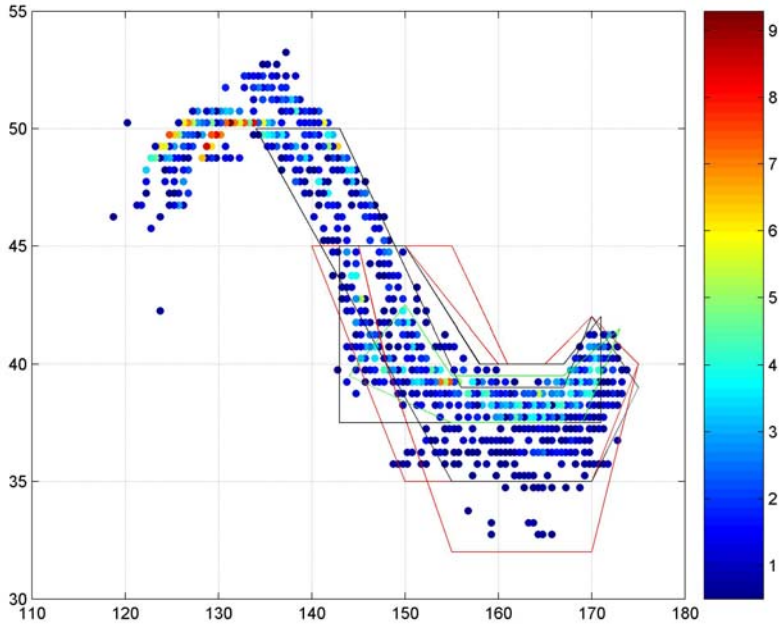

Appendix III.2. Polygon boxes used to sample pollution plume on April 7. Color represents trajectory projected SO_2 loading (DU).

Bibliography

Akimoto, H., T. Ohara, J. Kurokawa, and N. Horii (2006), Verification of energy consumption in China during 1996–2003 by using satellite observational data, *Atmos. Environ.*, 40, 7663-7667.

Allen, D., K. Pickering, and M. Fox-Rabinovitz (2004), Evaluation of pollutant outflow and CO sources during TRACE-P using model-calculated, aircraft-based, and Measurements of Pollution in the Troposphere (MOPITT)-derived CO concentrations, *J. Geophys. Res.*, 109, D15S03, doi:10.1029/2003JD004250.

Anderson, T. L., et al. (1996), Performance characteristics of a high-sensitivity, three-wavelength, total scatter/backscatter nephelometer, *J. Atmos. Oceanic Technol.*, 13967-13986.

Anderson, T. L., and J. A. Ogren (1998), Determining aerosol radiative properties using the TSI 3563 Integrating Nephelometer, *Aerosol Sci. Technol.*, 29, 57-69.

Andreae, M. O., and P. Merlet (2001), Emission of trace gases and aerosols from biomass burning, *Global Biogeochemical Cycles*, 15, 955–966.

Andreae, M. O., O. Schmid, H. Yang, D. Chand, J. Yu, Y. Zhang, and L. Zeng (2005), Aerosol optical and chemical properties in urban Guangzhou, China, *Eos Trans. AGU, 86*(18), Jt. Assem. Suppl., Abstract A21A-23.

Arellano, A. F., P. S. Kasibhatla, L. Giglio, G. R. van der Werf, and J. T. Randerson (2004), Top-down estimates of global CO sources using MOPITT measurements, *Geophys. Res. Lett.*, 31, L01104, doi:10.1029/2003GL018609.

Arakawa, H. (1969), *Climates of Northern and Eastern Asia*, Elsevier, New York,

USA.

Arimoto, R., et al. (2006), Characterization of Asian dust during ACE-ASIA, *Global and Planetary Change*, 52, 23-56.

Aunan, K., T. K. Berntsen, and H. M. Seip (2000), Surface ozone in China and its possible impact on agricultural crop yields, *Ambio*, 29(6), 294-301.

Barnard, J. C., E. I. Kassianov, T. P. Ackerman, S. Frey, K. Johnson, B. Zuberi, L. T. Molina, M. J. Molina, J. S. Gaffney, and N. A. Marley (2005), Measurements of black carbon specific absorption in the Mexico City metropolitan area during the MCMA 2003 field campaign, *Atmos. Chem. Phys. Discuss.*, 5, 4083-4113.

Beijing EPA (2002), *Integrated emission standard of boiler pollutants*, DB11/139-2002, Beijing, China (in Chinese).

Bergin, M., et al. (2001), Aerosol radiative, physical, and chemical properties in Beijing during June 1999, *J. Geophys. Res.*, 106(D16), 17969-17980.

Berglen, T. F., T. K. Berntsen, I. S. A. Isaksen, J. K. Sundet (2004), A global model of the coupled sulfur/oxidant chemistry in the troposphere: The sulfur cycle, *J. Geophys. Res.*, 109, D19310, doi:10.1029/2003JD003948.

Berkowitz, C. M., P. H. Daum, C. W. Spicer, and K. M. Busness (1996), Synoptic patterns associated with the flux of excess ozone to the western North Atlantic, *J. Geophys. Res.*, 101(D22), 28923-28934, 10.1029/95JD03274.

Berntsen, T. K., S. Karlsdóttir, and D. A. Jaffe (1999), Influence of Asian emissions on the composition of air reaching the North Western United States, *Geophys. Res. Lett.*, 26(14), 2171–2174.

Bertram, T. H., et al. (2007), Direct measurements of the convective recycling of the upper troposphere, *Science*, 315, 816-820.

Bethan, S., G. Vaughan, C. Gerbig, A. Volz-Thomas, H. Richer, and D. A. Tiddeman (1998), Chemical air mass differences near fronts, *J. Geophys. Res.*, 103(D11), 13413-13434, 10.1029/98JD00535.

Bey, I., D. J. Jacob, J. A. Logan, and R. M. Yantosca (2001), Asian chemical outflow to the Pacific in spring: Origins, pathways, and budgets, *J. Geophys. Res.*, 106(D19), 23097-23114, 10.1029/2001JD000806.

Bond, T. C., T. L. Anderson, and D. Campbell (1999), Calibration and intercomparison of filter-based measurements of visible light absorption by aerosols, *Aerosol Sci. Technol.*, 30, 582-600.

Boylan, J. W., and A. G. Russell (2006), PM and light extinction metric, goals, and criteria for three-dimensional air quality models, *Atmos. Environ.*, 40, 4946-4959.

Brajer, V., and R. W. Mead (2003), Blue skies in Beijing? Looking at the Olympic effect, *J. Environ. Development*, 12(2), 239-263.

Bryson, R. A., and F. K. Hare (1969), *The climates of North America*, Elsevier, New York, USA.

Cao, J. J., S. C. Lee, K. F. Ho, X. Y. Zhang, S. C. Zou, K. Fung, J. C. Chow, and J. G. Watson (2003), Characteristics of carbonaceous aerosol in Pearl River Delta Region, China during 2001 winter period, *Atmos. Environ.*, 37, 1451-1460.

Carmichael, G. R., et al. (2003), Evaluating regional emission estimates using the TRACE-P observations, *J. Geophys. Res.*, 108(D21), 8810, doi:10.1029/2002JD003116.

Chameides, W. L, P. S. Kasibhatla, J. Yienger, H. Levy II (1994) Growth of continental-scale metro-agro-plexes, regional ozone pollution, and world food production, *Science*, 264, 74–77.

Chameides, W. L., et al. (1999a), Is ozone pollution affecting crop yields in China?, *Geophys. Res. Lett.*, 26(7), 867-870, 10.1029/1999GL900068.

Chameides, W. L., et al. (1999b), Case study of the effects of atmospheric aerosols and regional haze on agriculture: An opportunity to enhance crop yields in China through emission controls?, *Proceedings of the National Academy of Sciences*, 96, 13626-13633.

Chan, C. Y., X. D. Xu, Y. S. Li, K. H. Wong, G. A. Ding, L. Y. Chan, and X. H. Cheng (2005), Characteristics of vertical profiles and sources of $PM_{2.5}$, PM_{10}, and carbonaceous species in Beijing, *Atmos. Environ.*, 39, 5113-5124.

Chang, F.L., and Z. Li (2005), A new method for detection of cirrus overlapping water clouds and determination of their optical properties, *J. Atmos. Sci.*, 62, 3993-4009.

Charlson, R. J., S. E. Schwartz, J. M. Hales, R. D. Cess, J. A. Coakley, J. E. Hansen, and D. J. Hofmann (1992), Climate forcing by anthropogenic aerosols, *Science*, 255, 423-430.

Chatfield, R. B., and P. J. Crutzen (1984), Sulfur dioxide in remote oceanic air: Cloud transport of reactive precursors, *J. Geophys. Res.*, 89(D5), 7111–7132.

Chen, J., F. Wei, C. Zheng, Y. Wu, and D. C. Adriano (1991), Background concentrations of elements in soils of China, *Water Air and Soil Pollution*, 57/58, 699-712.

Chen, L., Y. Duan, Y. Zhuo, L. Yang, L. Zhang, X. Yang, Q. Yao, Y. Jiang, and X. Xu (2007), Mercury transformation across particulate control services in six power plants of China: The co-effect of chlorine and ash composition, *Fuel*, 86, 603-610.

Chen, L. W. A. (2002), Urban fine particulate matter: Chemical composition and possible origins, *Ph.D. Dissertation*, Chemical Physics Program, University of Maryland.

Chen, L-W. A., B. G. Doddridge, R. R. Dickerson, J. C. Chow, P. K. Mueller, J. Quinn, and W. A. Butler (2001), Seasonal variations in elemental carbon aerosol, carbon monoxide and sulfur dioxide: Implications for sources, *Geophys. Res. Lett.*, 28(9), 1711-1714.

Chen, L. W. A., B. G. Doddridge, R. R. Dickerson, J. C. Chow, and R. C. Henry (2002), Origins of fine aerosol mass in the Baltimore-Washington corridor: Implications from observation, factor analysis, and ensemble air parcel back trajectories, *Atmos. Environ.*, 36, 4541-4554.

Chen, T-B. et al. (2005), Assessment of heavy mental pollution in surface soils of urban parks in Beijing, China, *Chemosphere*, 60, 542-551.

Chen, Y., G. Zhi, Y. Feng, J. Fu, J. Feng, G. Sheng, and B. R. T. Simoneit (2006), Measurements of emission factors for primary carbonaceous particles from residential raw-coal combustion in China, *Geophys. Res. Lett.*, 33, L20815, doi:10.1029/2006GL026966.

Chin, M., D. Jacob, G. Gardner, M. Foreman-Fowler, P. Spiro, and D. Savoie (1996), A global three-dimensional model of tropospheric sulfate, *J. Geophys. Res.*, 101(D13), 18667-18690.

Chin, M., D. Savoie, B. Huebert, A. Bandy, D. Thornton, T. Bates, P. Quinn, E. Saltzman, and W. De Bruyn (2000), Atmospheric sulfur cycle simulated in the global model GOCART: Comparison with field observations and regional budgets, *J. Geophys. Res.*, 105(D20), 24689-24712.

Chinese CBS (2005), *China statistical yearbook 2005*, China Statistics Press, Beijing, China.

Chinese EPA (1999), Online document in Chinese available at their website: http://www.zhb.gov.cn/law/fg/gwyw/199809/t19980902_81940.htm

Chinese EPA and Chinese CBS (2006), *China green national accounting study report 2004 (public version)*, Beijing, China.

Cooper, O. R., J. L. Moody, D. D. Parrish, M. Trainer, T. B. Ryerson, J. S. Holloway, G. Hübler, F. C. Fehsenfeld, S. J. Oltmans, and M. J. Evans (2001), Trace gas signatures of the airstreams within North Atlantic cyclones: Case studies from the North Atlantic Regional Experiment (NARE'97) aircraft intensive, *J. Geophys. Res.*, 106(D6), 5437-5456, 10.1029/2000JD900574.

Cooper O. R., et al. (2004), A case study of transpacific warm conveyor belt transport: Influence of merging airstreams on trace gas import to North America, *J. Geophys. Res.*, 109, D23S08, doi:10.1029/2003JD003624.

Delene, D. J., and J. A. Ogren (2002), Variability of aerosol optical properties at four North American surface monitoring sites, *J. Atmos. Sci.*, 59, 1135-1150.

Dickerson, R. R., A. C. Delany, and A. F. Wartburg (1984), Further modification of a commercial NO_x detector for high sensitivity, *Rev. Sci. Instrum.*, 55(12), 1995-1998.

Dickerson, R. R., et al. (1987), Thunderstorms: An important mechanism in the transport of air pollutants, *Science,* 235, 460-465.

Dickerson, R. R., and A. C. Delany (1988), Modification of a commercial gas filter correlation CO detector for enhanced sensitivity, *J. Atmos. Oceanic Technol.*, 5, 424-431.

Dickerson, R. R., S. Kondragunta, G. Stenchikov, K. L. Civerolo, B. G. Doddridge, and B. N. Holben (1997), The impact of aerosols on solar ultraviolet radiation and photochemical smog, *Science, 278*, 827-830.

Dickerson, R. R., M. O. Andreae, T. Campos, O. L. Mayol-Bracero, C. Neususess, and D. G. Streets (2002), Analysis of black carbon and carbon monoxide observed over the Indian Ocean: Implications for emissions and photochemistry, *J. Geophys. Res.*, 107, 8017, doi:10.1029/2001JD000501.

Dickerson, R. R., et al. (2007), Aircraft observations of dust and pollutants over NE China: Insight into the meteorological mechanisms of long-range transport, *J. Geophys. Res., 112, D24S90, doi:10.1029/2007JD008999.*

Donnell, E. A., D. J. Fish, E. M. Dicks, and A. J. Thorpe (2001), Mechanisms for pollutant transport between the boundary layer and the free troposphere, *J. Geophys. Res.*, 106(D8), 7847-7856, 10.1029/2000JD900730.

Draxler, R.R., and G.D. Rolph, (2003), HYSPLIT (HYbrid Single-Particle Lagrangian Integrated Trajectory) Model access via NOAA ARL READY

Website htttp://www.arl.noaa.gov/ready/hysplit4.html). *NOAA Air Resources Laboratory*, Silver Spring, MD.

Dzubay, T. G., R. K. Stevens, C. W. Lewis, D. H. Hern, W. J. Courtney, J. W. Tesch, and M. A. Mason (1982), Visibility and aerosol composition in Houston, Texas, *Environ. Sci. Technol.*, 16, 514-525.

Ehrman, S. H.; Pratsinis, and S. E.; Young (1992), J. R. Receptor modeling of the fine aerosol at a residential Los Angeles site, *Atmos. Environ.*, 26B, 473-481.

Esler, J. G., P. H. Haynes, K. S. Law, H. Barjat, K. Dewey, J. Kent, S. Schmitgen, and N. Brough (2003), Transport and mixing between airmasses in cold frontal regions during Dynamics and Chemistry of Frontal Zones (DCFZ), *J. Geophys. Res.*, 108 (D4), 4142, doi:10.1029/2001JD001494.

Fairlie, T. D., D. J. Jacob, and R. J. Park (2007), The impact of transpacific transport of mineral dust in the United States, *Atmos. Environ.*, in press.

Fehsenfeld, F. C., et al. (1987), A ground-based intercomparison of NO, NO_x, NO_y measurement techniques, *J. Geophys. Res.,* 92(12), 14710-14722.

Fiore, A. M., D. J. Jacob, I. Bey, R. M. Yantosca, B. D. Field, A. C. Fusco, and J. G. Wilkinson (2002), Background ozone over the United States in summer: origin, trend, and contribution to pollution episodes, *J. Geophys. Res.*, 107(D15), 10.1029/2001JD000982.

Fuelberg, H. E., C. M. Kiley, J. R. Hannan, D. J. Westberg, M. A. Avery, and R. E. Newell (2003), Meteorological conditions and transport pathways during the Transport and Chemical Evolution over the Pacific (TRACE-P) experiment, *J. Geophys. Res.*, 108(D20), 8782, doi:10.1029/2002JD003092.

Gao, Y., and J. Anderson (2001), Characteristics of Chinese aerosols determined by individual-particle analysis, *J. Geophys. Res.*, 106(D16), 18037-18045.

Gao, Y., J. R. Anderson, and X. Hua (2007), Dust characteristics over the North Pacific observed through shipboard measurements during the ACE-Asia experiment, *Atmos. Environ.*, 41, 7907-7922.

Ge, S., Z. Bai, W. Liu, T. Zhu, T. Wang, S. Qing, and J. Zhang (2001), Boiler briquette coal versus raw coal: Part 1. Stack gas emissions, *J. Air Waste Manage. Assoc*., 51, 524– 533.

Ge, S., X. Xu, C.J. Chow, J. Watson, Q. Sheng, W. Liu, Z. Bai, T. Zhu, and J. Zhang (2004), Emissions of air pollutants from household stoves: Honeycomb coal vs. coal cake, *Environ. Sci. Technol.*, 38, 4612-4618.

Gregory, G. L., A. S. Bachmeier, D. R. Blake, B. G. Heikes, D. C. Thornton, A. R. Bandy, J. D. Bradshaw, and Y. Kondo (1996), Chemical signatures of aged Pacific marine air: Mixed layer and free troposphere as measured during PEM-West A, *J. Geophys. Res.*, 101(D1), 1727-1742, 10.1029/95JD00410.

Gregory, G. L., J. T. Merrill, M. C. Shipham, D. R. Blake, G. W. Sachse, and H. B. Singh (1997), Chemical characteristics of tropospheric air over the Pacific Ocean as measured during PEM-West B: Relationship to Asian outflow and trajectory history, *J. Geophys. Res.*, 102(D23), 28275-28286, 10.1029/97JD02292.

Guttikunda, S. K., Y. Tang, G. R. Carmichael, G. Kurata, L. Pan, D. G. Streets, J.-H. Woo, N. Thongboonchoo, and A. Fried (2005), Impacts of Asian megacity

emissions on regional air quality during spring 2001, *J. Geophys. Res.*, 110, D20301, doi:10.1029/2004JD004921.

Hains, J. C., B. F. Taubman, A. M. Thompson, L. T. Marufu, J. W. Stehr, and R. R. Dickerson (2008), Origins of chemical pollution derived from Mid-Atlantic aircraft profiles using a clustering technique, *Atmos. Environ.,* 42, 1727-1741.

Hannan, J. R., H. E. Fuelberg, J. H. Crawford, G. W. Sachse, and D. R. Blake (2003), Role of wave cyclones in transporting boundary layer air to the free troposphere during the spring 2001 NASA/TRACE-P experiment, *J. Geophys. Res.*, 108(D20), 8785, doi:10.1029/2002JD003105.

Hao, J., and L. Wang (2005), Improving urban air quality in China: Beijing case study, *J. Air & Waste Manage. Assoc.*, 55, 1298-1305.

Harris, A. R., and C. I. Davidson (2005), The role of resuspended soil in lead flows in the California South Coast Air Basin, *Environ. Sci. Technol.*, 39, 7410-7415.

Hatakeyama, S., A. Takami, W. Wang, and D. Tang (2005), Aerial observation of air pollutants and aerosols over Bo Hai, China, *Atmos. Environ.*, 39, 5893–5898.

Hartmann, D.L. (1994), *Global Physical Climatology*, Academic Press, San Diego, CA, USA, 411 pp.

He, B. S., and C. H. Chen (2002), Energy ecological efficiency of coal fired plant in China, *Energy Conver. Mgmt.*, 43, 2553-2567.

He, K., F. Yang, Y. Ma, Q. Zhang, X. Yao, C. K. Chan, S. Cadle, T. Chan, and P. Mulawa (2001), The characteristics of $PM_{2.5}$ in Beijing, China, *Atmos. Environ.*, 35, 4959-4970.

He, K., H. Huo, and Q. Zhang (2002), Urban air pollution in China: Current status, characteristics, and progress, *Annu. Rev. Energy Environ.*, 27, 397–431.

He, P., P. Liu, X. Chen, and X. Chen (1999), Investigation on atmospheric pollution of Zhengzhou in 1998, *J. Henan Medical Univ.*, 34, 64-67 (in Chinese).

Heald, C. L., et al. (2003), Asian outflow and trans-Pacific transport of carbon monoxide and ozone pollution: An integrated satellite, aircraft, and model perspective, *J. Geophys. Res.*, 108(D24), 4804, doi:10.1029/2003JD003507.

Heald, C. L., D. J. Jacob, D. B. A. Jones, P. I. Palmer, J. A. Logan, D. G. Streets, G. W. Sachse, J. C. Gille, R. N. Hoffman, and T. Nehrkorn (2004), Comparative inverse analysis of satellite (MOPITT) and aircraft (TRACE-P) observations to estimate Asian sources of carbon monoxide, *J. Geophys. Res.*, 109, D23306, doi:10.1029/2004JD005185.

Holzer, M., I. G. McKendry, and D. A. Jaffe (2003), Springtime trans-Pacific atmospheric transport from east Asia: A transit-time-pdf approach, *J. Geophys. Res.*, 108(D22), 4708, doi:10.1029/2003JD003558.

Holzer, M., T. M. Hall, and R. B. Stull (2005), Seasonality and weather-driven variability of transpacific transport, *J. Geophys. Res.*, 110, D23103, doi:10.1029/2005JD006261.

Hu, M., F. Zhou, K. Shao, Y. Zhang, X. Tang, and J. Slanina (2002), Diurnal variations of aerosol chemical compounds and related gaseous pollutants in Beijing and Guangzhou, *J. Environ. Sci. Health*, A37, 479-488.

Hudman, R.C., et al. (2004), Ozone production in transpacific Asian pollution plumes and implications for ozone air quality in California, *J. Geophys. Res.*, 109, D23S10,10.1029/2004JD004974.

Huebert, B. J., M.-X. Wang, and W.-X. Lu (1988), Atmospheric nitrate, sulfate, ammonium, and calcium concentrations in China, *Tellus*, 40B, 260-269.

Huebert, B. J., T. Bates, P. B. Russell, G. Shi, Y. J. Kim, K. Kawamura, G. Carmichael, and T. Nakajima (2003), An overview of ACE-Asia: Strategies for quantifying the relationships between Asian aerosols and their climatic impacts, *J. Geophys. Res.*, 108 (D23), 8633, doi:10.1029/2003JD003550.

Husar, R. B., et al. (2001), Asian dust events of April 1998, *J. Geophys. Res.*, 106(D16), 18317-18330, 10.1029/2000JD900788.

Igarashi, Y., Y. Sawa, K. Yoshioka, H. Takahashi, H. Matsueda, and Y. Dokiya (2006), Seasonal variations in SO_2 plume transport over Japan: Observations at the summit of Mt. Fuji from winter to summer, *Atmos. Environ.*, 40 (36), 7018-7033.

IPCC (2001), *Climate change 2001: The scientific basis*, Cambridge University Press, Cambridge, United Kingdom and New York, NY, USA, 881 pp.

IPCC (2007), *Climate change 2007: The scientific basis*, Cambridge University Press, Cambridge, United Kingdom and New York, NY, USA, 996 pp.

Jacob, D. J., J. H. Crawford, M. M. Kleb, V. S. Connors, R. J. Bendura, J. L. Raper, G. W. Sachse, J. C. Gille, L. Emmons, and C. L. Heald (2003), Transport and Chemical Evolution over the Pacific (TRACE-P) aircraft mission: Design,

execution, and first results, *J. Geophys. Res.*, 108(D20), 9000, doi:10.1029/2002JD003276.

Jaffe, D. A., et al. (1999), Transport of Asian air pollution to North America, *Geophys. Res. Lett.*, 26, 711-714.

Jaffe, D. A., I. McKendry, T. Anderson, and H. Price (2003a), Six 'new' episodes of trans-Pacific transport of air pollutants, *Atmos. Environ.*, 37, 391-404.

Jaffe, D. A., D. Parrish, A. Goldstein, H. Price, and J. Harris (2003b), Increasing background ozone during spring on the west coast of North America, *Geophys. Res. Lett.*, 30(12), 1613, doi: 10.1029/2003GL017024.

Jaffe, D. A., E. Prestbo, P. Swartzendruber, P. Weiss-Penzias, S. Kato, A. Takami, S. Hatakeyama, and Y. Kajii (2005), Export of atmospheric mercury from Asia, *Atmos. Environ.*, 39, 3029-3038.

Jeong, M.-J., Z. Li, E. Andrews, and S.-C. Tsay (2007), Effect of aerosol humidification on the column aerosol optical thickness over the Atmospheric Radiation Measurement Southern Great Plains site, *J. Geophys. Res.*, 112, D10202, doi:10.1029/2006JD007176.

Kaneyasu, N., K. Takeuchi, M. Hayashi, S. -I. Fujita, I. Uno, and H. Sasaki (2000), Outflow patterns of pollutants from East Asia to the North Pacific in the winter monsoon, *J. Geophys. Res.*, 105(D13), 17361-17378, 10.1029/2000JD900138.

Karlsdóttir, S., and I. S. A. Isaksen (2000), Changing Methane Lifetime: Possible Cause for Reduced Growth, *Geophys. Res. Lett.*, 27(1), 93–96.

Kiley, C. M., and H. E. Fuelberg (2006), An examination of summertime cyclone transport processes during Intercontinental Chemical Transport Experiment (INTEX-A), *J. Geophys. Res.*, 111, D24S06, doi:10.1029/2006JD007115.

Kim, B., J. Han, and S. Park (2001), Transport of SO_2 and aerosol over the Yellow Sea, *Atmos. Environ.*, 35, 727-737.

Kim, J. Y., C. H. Song, Y. S. Ghim, J. G. Won, S. C. Yoon, G. R. Carmichael, and J.-H. Woo (2006), An investigation on NH_3 emissions and particulate NH_4^+–NO_3^- formation in East Asia, *Atmos. Environ.*, 40, 2139-2150.

Koch, D., D. Jacob, I. Tegen, D. Rind, and M. Chin (1999), Tropospheric sulfur simulation and sulfate direct radiative forcing in the Goddard Institute for Space Studies general circulation model, *J. Geophys. Res.*, 104(D19), 23799-23822.

Krotkov, N. A., et al. (2006), Band residual difference algorithm for retrieval of SO_2 from the Aura Ozone Monitoring Instrument (OMI), *IEEE Transactions on Geoscience and Remote Sensing*, 44, 1259-1266.

Krotkov, N. A., et al. (2008), Validation of SO_2 retrievals from the Ozone Monitoring Instrument over NE China, *J. Geophys. Res.*, 113, D16S40, doi:10.1029/2007JD008818.

Kurata, G., G. R. Carmichael, D. G. Streets, T. Kitada, Y. Tang, J.-H. Woo, and N. Thongboonchoo (2004), Relationships between emission sources and air mass characteristics in East Asia during the TRACE-P period, *Atmos. Environ.*, 38, 6977–6987.

Larssen, T., et al. (2006), Acid rain in China, *Environ. Sci. Technol*, 40, 418-425.

Lary, D., A. Lee, R. Toumi, M. Newchurch, M. Pirre, and J. Renard (1997), Carbon

aerosols and atmospheric photochemistry, *J. Geophys. Res.*, 102(D3), 3671-3682.

Levy, R. C., L. A. Remer, S. Mattoo, E. Vermote, and Y. J. Kaufman (2007a), Second-generation operational algorithm: Retrieval of aerosol properties over land from inversion of Moderate Resolution Imaging Spectroradiometer spectral reflectance, *J. Geophys. Res.*, 112, D13211, doi:10.1029/2006JD007811.

Levy, R. C., L. A. Remer, and O. Dubovic (2007b), Global aerosol optical models and application to MODIS aerosol retrieval over land, *J. Geophys. Res.*, 112, D13210, doi:10.1029/2006JD007815.

Li, C., L.T. Marufu, R. R. Dickerson, Z. Li, T. Wen, Y. Wang, P. Wang, H. Chen, and J. W. Stehr (2007), In-situ measurements of trace gases and aerosol optical properties at a rural site in northern China during EAST-AIRE IOP 2005. *J. Geophys. Res.*, D22S04, doi:10.1029/2006JD007592.

Li, Z., et al., (2007a), Aerosol optical properties and its radiative effects in northern China, *J. Geophys. Res.,* 112, D22S01, doi:10.1029/2006JD007382.

Li, Z., et al., (2007b), Preface to special section: Overview of the East Asian Study of Tropospheric Aerosols: an International Regional Experiment (EAST-AIRE), *J. Geophys. Res.* D22S00, doi:10.1029/2007JD008853.

Liang, Q., L. Jaegle´, D. A. Jaffe, P. Weiss-Penzias, A. Heckman, and J. A. Snow (2004), Long-range transport of Asian pollution to the northeast Pacific: Seasonal variations and transport pathways of carbon monoxide, *J. Geophys. Res.*, 109, D23S07,doi:10.1029/2003JD004402.

Liang, Q., L. Jaegle´, and J. M. Wallace (2005), Meteorological indices for Asian outflow and transpacific transport on daily to interannual timescales, *J. Geophys. Res.*, 110, D18308, doi:10.1029/2005JD005788.

Lide, D. R. (1998), *CRC handbook of chemistry and physics*, 79th Edition, CRC Press LLC., Boca Raton, FL, USA, 2496 pp.

Lin, C.-Y. C., D. J. Jacob, J. W. Munger, and A. M. Fiore (2000), Increasing background ozone in surface air over the United States, *Geophys. Res. Lett.*, 27(21), 3465-3468, doi:10.1029/2000GL011762.

Liu, H., D. J. Jacob, I. Bey, R. M. Yantosca, B. N. Duncan, and G. W. Sachse (2003), Transport pathways for Asian pollution outflow over the Pacific: Interannual and seasonal variations, *J. Geophys. Res.*, 108, 8786, doi 10.1029/2002JD003102.

Liu, J., J. R. Drummond, D. B. A. Jones, Z. Cao, H. Bremer, J. Kar, J. Zou, F. Nichitiu, and J. C. Gille (2006), Large horizontal gradients in atmospheric CO at the synoptic scale as seen by spaceborne Measurements of Pollution in the Troposphere, *J. Geophys. Res.*, 111, D02306, doi:10.1029/2005JD006076.

Liu, J., and D. L. Mauzerall (2005), Estimating the average time for intercontinental transport of air pollutants, *Geophys. Res. Lett.*, 32, L11814, doi:10.1029/2005GL022619.

Liu, J., D. L. Mauzerall, and L. W. Horowitz (2005), Analysis of seasonal and interannual variability in transpacific transport, *J. Geophys. Res.*, 110, D04302, doi:10.1029/2004JD005207.

Liu, X., and M. Shao (2004), The analysis of sources of ambient light extinction coefficient in summer time of Beijing city, *Acta Scientiae Circumstantiae*, 24(2), 185-190 (in Chinese).

Liu, L., and W. Song (2001), Atmosphere pollution feature analysis and countermeasure, *J. Hebei Academy of Sciences*, 18, 61-64 (in Chinese).

Logan, J. A. (1999), An analysis of ozonesonde data for the troposphere: Recommendations for testing 3-D models and development of a gridded climatology for tropospheric ozone, *J. Geophys. Res.*, 104, 16115–16149.

Luke, W. T. (1997), Evaluation of a commercial pulsed fluorescence detector for the measurement of low-level SO_2 concentrations during the Gas-Phase Sulfur Intercomparison Experiment, *J. Geophys. Res.,* 102**,** 16255–16265.

Lun, X., X. Zhang, Y. Mu, A. Nang, and G. Jiang (2003), Size fractionated speciation of sulfate and nitrate in airborne particles in Beijing, China, *Atmos. Environ.*, 37, 2581-2588.

Ma, J., and J. A. van Aardenne (2004), Impact of different emission inventories on simulated tropospheric ozone over China: A regional chemical transport model evaluation, *Atmos. Chem. Phys.*, 4, 877–887.

Ma, Y., H. Yang, Z. Fang, and Y. Zhang (2003), Analysis of status and trends on the air pollution in the center multi-cities of Liaoning, *Urban Environ. Urban Ecology,* 16, 89-91 (in Chinese).

Mari, C., M. J. Evans, P. I. Palmer, D. J. Jacob, and G. W. Sachse (2004), Export of Asian pollution during two cold front episodes of the TRACE-P experiment, *J. Geophys. Res.*, 109, D15S17, doi:10.1029/2003JD004307.

Martin, B. D., H. E. Fuelberg, N. J. Blake, J. H. Crawford, J. A. Logan, D. R. Blake, and G. W. Sachse (2002), Long-range transport of Asian outflow to the equatorial Pacific, *J. Geophys. Res.*, 107, 8322, doi:10.1029/2001JD001418.

Menon, S., J. Hansen, L. Nazarenko, and Y. Luo (2002), Climate effects of black carbon aerosols in China and India, *Science*, 297, 2250-2253.

Methven, J., et al. (2006), Establishing Lagrangian connections between observations within air masses crossing the Atlantic during the International Consortium for Atmospheric Research on Transport and Transformation experiment, *J. Geophys. Res.*, 111, D23S62, doi:10.1029/2006JD007540.

Mi, W., Z. Li, X. Xia, B. Holben, R. Levy, F. Zhao, H. Chen, and M. Cribb (2007), Evaluation of MODIS aerosol products at two AERONET stations in China, *J. Geophys. Res.*, 112, D22S08, doi:10.1029/2007JD008474.

Mickley, L. J., D. J. Jacob, B. D. Field, and D. Rind (2004), Effects of future climate change on regional air pollution episodes in the United States, *Geophys. Res. Lett.*, 31, L24103, doi:10.1029/2004GL021216.

Miyazaki, Y., et al. (2003), Synoptic-scale transport of reactive nitrogen over the western Pacific in spring, *J. Geophys. Res.*, 108(D20), 8788, doi:10.1029/2002JD003248.

Nadim, F., P. Zack, G. E. Hoag, S. Liu (2001), United States experience with gasoline additives, *Energy Policy*, 29, 1-5.

Newell, R. E., and M. J. Evans (2000), Seasonal changes in pollutant transport to the North Pacific: The relative importance of Asian and European sources, *Geophys. Res. Lett.*, 27(16), 2509-2512, 10.1029/2000GL011501.

Ning, D., L. Zhong, and Y. Chung (1996), Aerosol size distribution and elemental composition in urban areas of Northern China, *Atmos. Environ.*, 30, 2355-2362.

Novelli, P., K. Masarie, and P. Lang (1998), Distributions and recent changes of carbon monoxide in the lower troposphere, *J. Geophys. Res.*, 103(D15), 19015-19033.

Pacyna, J.M., (1998), Source inventories for atmospheric trace metals. In: Harrison, R.M. and van Grieken, R.E., Editors, 1998. *Atmospheric Particles, IUPAC Series on Analytical and Physical Chemistry of Environmental Systems,* Vol. 5, Wiley, Chichester, UK, pp. 385–423.

Palmer, P. I., D. J. Jacob, D. B. A. Jones, C. L. Heald, R. M. Yantosca, J. A. Logan, G. W. Sachse, and D. G. Streets (2003), Inverting for emissions of carbon monoxide from Asia using aircraft observations over the western Pacific, *J. Geophys. Res.*, 108(D21), 8828, doi:10.1029/2003JD003397.

Park, R. J., D. J. Jacob, B. D. Field, R. M. Yantosca, and M. Chin (2004), Natural and transboundary pollution influences on sulfate-nitrate-ammonium aerosols in the United States: implications for policy, *J. Geophys. Res.*, 109, D15204, 10.1029/2003JD004473.

Parrish, D. D., Y. Kondo, O. R. Cooper, C. A. Brock, D. A. Jaffe, M. Trainer, T. Ogawa, G. Hübler, and F. C. Fehsenfeld (2004), Intercontinental Transport and Chemical Transformation 2002 (ITCT 2K2) and Pacific exploration of Asian Continental Emission (PEACE) experiments: An overview of the 2002 winter and spring intensives, *J. Geophys. Res.*, 109, D23S01, doi:10.1029/2004JD004980.

Pekney, N. J., C. I. Davidson, K. J. Bein, A. S. Wexler, and M. V. Johnston (2006), Identification of sources of atmospheric PM at the Pittsburgh supersite, Part I: single particle analysis and filter-based positive matrix factorization, *Atmos. Environ.*, 40, S411-S423.

Pickering, K. E., R. R. Dickerson, G. J. Huffman, J. F. Boatman, and A. Schanot (1988), Trace gas transport in the vicinity of frontal convective clouds, , *J. Geophys. Res.,* 93(1), 759-773.

Pickering, K. E., A. M. Thompson, R. R. Dickerson, B. S. Gockel, W. T. Luke, D. P. McNamara, J. P. Greenberg, and P. R. Zimmerman (1990), Model calculations of tropospheric ozone production potential following observed convective events, *J. Geophys. Res.,* 95(9), 14,049-14062.

Pike, S. M., and S. B. Moran (2001), Trace elements in aerosol and precipitation at New Castle, NH, USA, *Atmos. Environ.*, 35, 3361-3366.

Pope III, C. Arden, David V. Bates, and Mark E. Raizenne (1995), Health effects of particulate air pollution: time for reassessment?, *Environ. Health Perspect*., 103, 472-480.

Prados, A. I., R. R. Dickerson, B. G. Doddridge, P. A. Milne, J. L. Moody, and J. T. Merrill (1999), Transport of ozone and pollutants from North America to the North Atlantic Ocean during the 1996 AEROCE Intensive Experiment, *J. Geophys. Res.,* 104(21), 26219-26234.

Prospero, J. M., D. L. Savoie, and R. Arimoto (2003), Long-term record of nss-sulfate and nitrate in aerosols on Midway Island, 1981–2000: Evidence of increased

(now decreasing?) anthropogenic emissions from Asia, *J. Geophys. Res.*, 108(D1), 4019, doi:10.1029/2001JD001524.

Qian, Y., D. P. Kaiser, L. R. Leung, and M. Xu (2006), More frequent cloud-free sky and less surface solar radiation in China from 1955 to 2000, *Geophys. Res. Lett.*, 33, L01812, doi:10.1029/2005GL024586.

Qiu, J., and L. Yang (2000), Variation characteristics of atmospheric aerosol optical depths and visibility in North China during 1980–1994, *Atmos. Environ.*, 34, 603-609.

Rahn, K. A., (1981), The Mn/V ratio as a tracer of large-scale sources of pollution aerosol for the Arctic, *Atmos. Environ.*, 15, 1457-1464.

Reay, D. S., F. Dentener, P. Smith, J. Grace, and R. A. Feely (2008), Global nitrogen deposition and carbon sinks, *Nature Geoscience*, 1, 430-437.

Remer, L. A., et al. (2005), The MODIS aerosol algorithm, products and validation, *J. Atmos. Sci.*, 62, 947–973.

Richter, A., J. P. Burrows, H. Nüß, C. Granier, and U. Niemeier (2005), Increase in tropospheric nitrogen dioxide over China observed from space, *Nature*, 437, 129-132.

Rosenfeld, D., U. Lohmann, G. B. Raga, C. D. O'Dowd, M. Kulmala, S. Fuzzi, A. Reissell, and M. O. Andreae (2008), Floor or drought: How do aerosols affect precipitation, *Science*, 321, 1309-1313.

Seinfeld, J. H., and S. N. Pandis (1998), *Atmospheric chemistry and physics: From air pollution to climate change*, John Wiley & Sons, New York, USA, 1326 pp.

Seiler, W., and C. Junge (1970), Carbon monoxide in the atmosphere, *J. Geophys. Res.*, 75(12), 2217–2226.

Shao, M., X. Tang, Y. Zhang, and W. Li (2006), City clusters in China: air and surface water pollution, *Frontiers in Ecology and the Environment*, 7(4), 353-361.

Shimizu, A., N. Sugimoto, I. Matsui, K. Arao, I. Uno, T. Murayama, N. Kagawa, K. Aoki, A. Uchiyama, and A. Yamazaki (2004), Continuous observations of Asian dust and other aerosols by polarization lidars in China and Japan during ACE-Asia, *J. Geophys. Res., 109*, D19S17, doi:10.1029/2002JD003253.

Sinton, J. E., (2001), Accuracy and reliability of China's energy statistics, *China Econ. Rev.*, 12, 373– 383.

Stehr, J. W., R. R. Dickerson, K. A. Hallock-Waters, B. G. Doddridge, and D. Kirk (2000), Observations of NO_y, CO, and SO_2 and the origin of reactive nitrogen in the eastern United States. *J. Geophys. Res.*, 105(D3), 3553-3563.

Steiner, A. L., S. Tonse, R. C. Cohen, A. H. Goldstein, and R. A. Harley (2006), Influence of future climate and emissions on regional air quality in California, *J. Geophys. Res.*, 111, D18303, doi:10.1029/2005JD006935.

Stohl, A., (1998), Computation, accuracy and applications of trajectories—A review and bibliography, *Atmos. Environ.*, 32, 947-966.

Stohl, A., S. Eckhardt, C. Forster, P. James, and N. Spichtinger (2002), On the pathways and timescales of intercontinental air pollution transport, *J. Geophys. Res.*, 107(D23), 4684, doi:10.1029/2001JD001396.

Stohl, A., C. Forster, S. Eckhardt, N. Spichtinger, H. Huntrieser, J. Heland, H. Schlager, S. Wilhelm, F. Arnold, and O. Cooper (2003), A backward modeling study of intercontinental pollution transport using aircraft measurements, *J. Geophys. Res.*, 108(D12), 4370, doi:10.1029/2002JD002862.

Streets, D. G.., and S. T. Waldhoff (2000), Present and future emissions of air pollutants in China: SO_2, NO_x, and CO, *Atmos. Environ.,* 34, 363-374.

Streets, D. G., et al. (2003), An inventory of gaseous and primary aerosol emissions in Asia in the year 2000, *J. Geophys. Res.*, 108(D21), 8809, doi:10.1029/2002JD003093.

Streets, D. G., Q. Zhang, L. Wang, K. He, J. Hao, Y. Wu, Y. Tang, and G. R. Carmichael (2006), Revisiting China's CO emissions after the Transport and Chemical Evolution over the Pacific (TRACE-P) mission: Synthesis of inventories, atmospheric modeling, and observations, *J. Geophys. Res.*, 111, D14306, doi:10.1029/2006JD007118.

Sullivan, R. C., S. A. Guazzotti, D. A. Sodeman, and K.A. Prather (2007), Direct observations of the atmospheric processing of Asian mineral dust, *Atmos. Chem. Phys.*, 7, 1213-1236.

Sun, Y., G. Zhuang, Y. Wang, L. Han, J. Guo, M. Dan, W. Zhang, Z. Wang, and Z. Hao (2004), The air-borne particulate pollution in Beijing – concentration, composition, distribution and sources, *Atmos. Environ.*, 38, 5991-6004.

Sun, Y., G. Zhuang, Y. Wang, X. Zhao, J. Li, Z. Wang, and Z. An (2005), Chemical composition of dust storms in Beijing and implications for the mixing of mineral

aerosol with pollution aerosol on the pathway, *J. Geophys. Res.*, 110, D24209, doi:10.1029/2005JD006054.

Sun, Y., G. Zhuang, W. Zhang, Y. Wang, and Y. Zhuang (2006), Characteristics and sources of lead pollution after phasing out leaded gasoline in Beijing, *Atmos. Environ.*, 40, 2973-2985.

Takami, A., T. Miyoshi, A. Shimono, N. Kaneyasu, S. Kato, Y. Kajii, and S. Tatakeyama (2007), Transport of anthropogenic aerosols from Asia and subsequent chemical transformation, *J. Geophys. Res.*, 112, D22S31, doi:10.1029/2006JD008120.

Takemura, T., T. Nakajima, A. Higurashi, S. Ohta, and N. Sugimoto (2003), Aerosol distributions and radiative forcing over the Asian Pacific region simulated by Spectral Radiation-Transport Model for Aerosol Species (SPRINTARS), *J. Geophys. Res.*, 108, 8659, doi:10.1029/2002JD003210.

Tan, Q., W. L. Chameides, D. Streets, T. Wang, J. Xu, M. Bergin, and J. Woo (2004), An evaluation of TRACE-P emission inventories from China using a regional model and chemical measurements, *J. Geophys. Res.*, 109, D22305, doi:10.1029/2004JD005071.

Tang, X., J. Li, X. Su, and D. Chen (1990), *Atmospheric Environmental Chemistry*, Higher Education Press, Beijing, China, 343 pp (in Chinese).

Taubman, B. F. (2004), Airborne characterization of regional aerosol origins and optical properties, *Ph.D. Dissertation*, Department of Chemistry, University of Maryland.

Taubman, B. F., L. Marufu, B. Vant-Hull, C. Piety, B. Doddridge, R. Dickerson, and Z. Li (2004), Smoke over haze: Aircraft observations of chemical and optical properties and the effects on heating rates and stability, *J. Geophys. Res.*, 109, D02206, doi: 10.1029/2003JD003898.

Taubman, B. F., J. C. Hains, L. T. Marufu, B. G. Doddridge, A. M. Thompson, J. W. Stehr, C. A. Piety, and R. R. Dickerson (2006), Aircraft vertical profiles of trace gas and aerosol Pollution over the Mid-Atlantic U.S.: Statistics and meteorological cluster Analysis, *J. Geophys. Res.,* 111(D10), D10S07, 10.1029/2005JD006196.

Taubman, B. F., et al. (2007), Aircraft observations over the Mid-Atlantic U.S. and North Atlantic Ocean during the 1996 Atmosphere/Ocean Chemistry Experiment: Evidence for linked transport of natural and anthropogenic ozone over Bermuda, *J. Geophys. Res.*, in preparation.

Thomas, V. M. (1995), The elimination of lead in gasoline, *Annu. Rev. Energy Environ*., 20, 301-324.

Twomey, S. A., (1959), The nuclei of natural cloud formation. Part II: The supersaturation in natural clouds and the variation of cloud droplet concentrations, *Pure Appl. Geophys.,* 43, 243–249.

UNEP (2000), *The Montreal protocol on substances that deplete the ozone layer*, Ozone Secretariat, United Nations Environment Programme, Nairobi, Kenya (ISBN: 92-807-1888-6).

U.S. DOE (1986), Global distribution of total cloud cover and cloud type amounts over land, Tech. Rep. DOE/ER/60085-H1, Natl. Cent. for Atmos. Res., Boulder, CO, USA.

U.S. EPA (2006), *Air Quality Criteria for Lead*, EPA/600/R-5/144aF.

Venkataraman, C., and G. U. M. Rao (2001), Emission factors of carbon monoxide and size-resolved aerosols from biofuel combustion, *Environ. Sci. Technol.*, 35, 2100– 2107.

Virkkula, A., N. C. Ahlquist, D. S. Covert, W. P. Arnott, P. J. Sheridan, P. K. Quinn, and D. J. Coffman (2005), Modification, calibration and a field test of an instrument for measuring light absorption by particles, *Aerosol Sci. Technol.*, 39, 68-83.

Wang, T., T. F. Cheung, Y. S. Li, X. M. Yu, and D. R. Blake (2002), Emission characteristics of CO, NO_x, SO_2 and indications of biomass burning observed at a rural site in eastern China, *J. Geophys. Res.*, 107(D12), doi:10.1029/2001JD000724.

Wang, T., et al. (2004), Relationships of trace gases and aerosols and the emission characteristics at Lin'an, a rural site in eastern China during spring 2001, *J. Geophys. Res.*, 109, doi:10:1029/2003JD004119.

Wang, T., A. Ding, J. Gao, and W. S. Wu (2006), Strong ozone production in urban plumes from Beijing, China, *Geophys. Res. Lett.*, 33, L21806, doi:10.1029/2006GL027689.

Wang, W., and T. Wang (1995), On the origin and the trend of acid precipitation in China, *Water, Air, & Soil Pollution*, 85, 2295-2300.

Wang, W., and T. Wang (1996), On acid rain formation in China, *Atmos. Environ.*, 30, 4091-4093.

Wang, X., Z. Han, and X. Lei (2003), Study on ozone concentration change of Guangzhou district, *Acta Scientiarum Naturalium Universitatis Sunyatseni*, 42, 106-109 (in Chinese).

Wang, X., D. L. Mauzerall, Y. Hu, A. G. Russell, E. D. Larson, J.-H. Woo, D. G. Streets, and A. Guenther (2005), A high-resolution emission inventory for eastern China in 2000 and three scenarios for 2020, *Atmos. Environ.*, 39, 5917-5933.

Wang, X., and D.L. Mauzerall (2006), Evaluating impacts of air pollution in China on public health: Implications for future air pollution and energy policies, *Atmos. Environ.*, 40, 1706-1721.

Wang, Y., M. B. McElroy, T. Wang, and P. I. Palmer (2004), Asian emissions of CO and NO_x: Constraints from aircraft and Chinese station data, *J. Geophys. Res.*, 109, D24304, doi:10.1029/2004JD005250.

Wang Y., M. B. McElroy, K. F. Boersma, H. J. Eskes, and J. P. Veefkind (2007), Traffic restrictions associated with the Sino-African summit: Reductions of NO_x detected from space, *Geophys. Res. Lett.*, 34, L08814, doi:10.1029/2007GL029326.

Wang, Y., G. Zhuang, A. Tang, H. Yuan, Y. Sun, S. Chen, and A. Zheng (2005), The ion chemistry and source of $PM_{2.5}$ aerosol in Beijing, *Atmos. Environ.*, 39, 3771-3784.

Wang, Y., G. Zhuang, Y. Sun, and Z. An (2006), The variation of characteristics and formation mechanisms of aerosols in dust, haze, and clear days in Beijing, *Atmos. Environ.*, 40, 6579-6591.

Wang, Y., G. Zhuang, A. Tang, W. Zhang. Y. Sun, Z. Wang, and Z. An (2007), The evolution of chemical components of aerosols at five monitoring sites of China during dust storms, *Atmos. Environ.*, 41, 1091-1106.

Wang, Z., H. Akimoto, and I. Uno (2002), Neutralization of soil aerosol and its impact on the distribution of acid rain over East Asia: Observations and model results, *J. Geophys. Res.*, 107(D19), 4389, doi:10.1029/2001JD001040.

Wen, T., R. R. Dickerson, Y. Wang, Y. Sun, M. Xue, D. Streets, and Z. Li (2006), Trace gases and aerosol observations in Beijing: 1, evaluations of emission inventories, in preparation.

Westerling, A.L., H.G. Hidalgo, D.R. Cayan, and T.W. Swetnam (2006), Warming and earlier spring increases western U.S. forest wildfire activity, *Science*, 313: 940-943

WHO and UNDP (2001), *Environment and people's health in China*, World Health Organization, Geneva, Switzerland, 76 pp.

Williamson, S. J. (1973), *Fundamentals of air pollution*, Addison-Wesley Publication Company, Inc. Philippines, 472 pp.

World Bank (1997), *Clear water, blue skies: China's environment in the new century*, World Bank, Washington DC, USA, 122 pp.

World Bank (2006), *2006 World Development Indicators database*, World Bank, Washington DC, USA, 242 pp.

Wu, X., J. Sun, B. Shi, and W. Liu (2002), The source of nitrogen oxide and its characters in the air of Urumqi, *Arid Environ. Monitoring*, 16, 137-139 (in Chinese).

Xia, X., H. Chen, Z. Li, P. Wang, and J. Wang (2007), Significant reduction of surface solar irradiance induced by aerosols in a suburban region in northeastern China, *J. Geophys. Res.*, 112, D22S02, doi:10.1029/2006JD007562.

Xin, J., et al. (2007), Aerosol optical depth (AOD) and Ångström exponent of aerosols observed by the Chinese Sun Hazemeter Network from August 2004 to September 2005, *J. Geophys. Res.*, 112, D05203, doi:10.1029/2006JD007075.

Xu, H., Y. Wang, T. Wen, and X. He (2007a), Size distributions and vertical distributions of water soluble ions of atmospheric aerosol in Beijing, *Environ. Sci.*, 28, 14-19 (in Chinese).

Xu, H., Y. Wang, T. Wen, and X. He (2007b), Size distributions and vertical distributions of metal elements of atmospheric aerosol in Beijing, *Environ. Chem.*, 26, 675-679 (in Chinese).

Xu, J., M. H. Bergin, X. Yu, G. Liu, J. Zhao, C. M. Carrico, and K. Baumann (2002), Measurement of aerosol chemical, physical, and radiative properties in the Yangtze delta region of China, *Atmos. Environ.*, 36, 161-173.

Xu, J., M. H. Bergin, R. Greenwald, J. J. Schauer, M. M. Shafer, J.-L. Jaffrezo, and G. Aymoz (2004), Aerosol chemical, physical and radiative characteristics near a desert source region of Northwest China during ACE-Asia, *J. Geophys. Res.*, 109, D19S03, doi:10.1029/2003JD004239

Xu, L., K. Okada, Y. Iwasaka, K. Hara, Y. Okuhara, Y. Tsutsumi, and G. Shi (2001), The composition of individual aerosol particle in the troposphere and stratosphere over Xianghe (39.45°N, 117.0°E), China, *Atmos. Environ.*, 35, 3145-3153.

Xu, M., C.-P. Chang, C. Fu, Y. Qi, A. Robock, D. Robinson, and H. Zhang (2006), Steady decline of East Asian monsoon winds, 1969–2000: Evidence from direct ground measurements of wind speed, *J. Geophys. Res.*, 111, D24111, doi:10.1029/2006JD007337.

Xu, Q. (2001), Abrupt change of the mid-summer climate in central east China by the influence of atmospheric pollution, *Atmos. Environ.*, 35, 5029-5040.

Yan, P., J. Tang, J. Huang, J. T. Mao, X. J. Zhou, Q. Liu, Z. F. Wang, and H. G. Zhou (2008), The measurements of aerosol optical properties at a rural site in Northern China, *Atmos. Chem. Phys.*, 8, 2229-2242.

Yang, F., K. He, B. Ye, X. Chen, L. Cha, S. H. Cadle, T. Chan, and P. A. Mulawa (2005), One-year record of organic and elemental carbon in fine particles in downtown Beijing and Shanghai, *Atmos. Chem. Phys.*, 5, 1449-1457.

Yang, L., B. Qin, and R. Wu (2001), Preliminary study for potential impacts on the aquatic environment of Lake Taihu by acid rain, *J. Lake Sci.*, 13(2), 135-142.

Yao, X., A. P. S. Lau, M. Fang, C. K. Chan, and M. Hu (2003), Size distributions and formation of ionic species in atmospheric particulate pollutants in Beijing, China: 1—inorganic ions, *Atmos. Environ.*, 37, 2991-3000.

Yienger, J. J., M. Galanter, T. A. Holloway, M. J. Phadnis, S. K. Guttikunda, G. R. Carmichael, W. J. Moxim, and H. Levy II (2000), The episodic nature of air

pollution transport from Asia to North America, *J. Geophys. Res.*, 105(D22), 26931-26946, 10.1029/2000JD900309.

Yu, H., S. C. Liu, and R. E. Dickinson (2002), Radiative effects of aerosols on the evolution of the atmospheric boundary layer, *J. Geophys. Res.*, 107(D12), doi:10.1029/2001JD000754.

Yuan, H., G. Zhuang, J. Li, Z. Wang, and J. Li (2008), Mixing of mineral with pollution aerosols in dust season in Beijing: Revealed by source apportionment study, *Atmos. Environ.*, 42, 2141-2157.

Yumimoto, K., and I. Uno (2006), Adjoint inverse modeling of CO emission over the East Asian region using four dimensional variational data assimilation, *Atmos. Environ.*, 40, 6836-6845.

Zhang, D., and Y. Iwasaka (1999), Nitrate and sulfate in individual Asian dust-storm particles in Beijing, China in spring of 1995 and 1996, *Atmos. Environ.*, 33, 3213-3223.

Zhang, J., K. R. Smith, R. Uma, Y. Ma, V. V. N. Kishore, K. Lata, M. A. K. Khalil, R. A. Rasmussen, and S. T. Thorneloe (1999), Carbon monoxide from cookstoves in developing countries: 1. Emission factors, *Chemosphere*, 1, 353– 366.

Zhang, Q., et al. (2007), NO_x emission trends for China, 1995–2004: The view from the ground and the view from space, *J. Geophys. Res.*, 112, D22306, doi:10.1029/2007JD008684.

Zhang, R., R. Arimoto, J. An, S. Yabuki, and J. Sun (2002), Ground observations of a strong dust storm in Beijing in March 2002, J. Geophys. Res., 110, D18S06, doi:10.1029/2004JD004589.

Zhang, R., G. Li, J. Fan, D. L. Wu, and M. J. Molina (2007), Intensification of Pacific storm track linked to Asian pollution, *Proceedings of the National Academy of Sciences*, 104, 5295-5299.

Zhang, X. Y., S. L. Gong, Z. X. Shen, F. M. Mei, X. X. Xi, L. C. Liu, Z. J. Zhou, D. Wang, Y. Q. Wang, and Y. Cheng (2003), Characterization of soil dust aerosol in China and its transport and distribution during 2001 ACE-Asia: 1. Network observations, *J. Geophys. Res.*, 108(D9), 4261, doi:10.1029/2002JD002632.

Zhang, Y., X. Zhu, S. Slanina, M. Shao, L. Zeng, M. Hu, M. Bergin, and L. Salmon (2004), Aerosol pollution in some Chinese cities, *Pure Appl. Chem.*, 76. 1227–1239.

Zhao, C., X. Tie, and Y. Lin (2006), A possible positive feedback of reduction of precipitation and increase in aerosols over eastern central China, *Geophys. Res. Lett.*, 33, L11814, doi:10.1029/2006GL025959.

Zheng, M., L. G. Salmon, J. J. Schauer, L. Zeng, C. S. Kiang, Y. Zhang, and G. R. Cass (2005), Seasonal trends in $PM_{2.5}$ source contributions in Beijing, China, *Atmos. Environ.*, 39, 3967-3976.

Zou, X., P. Zhai, and Q. Zhang (2005), Variations in droughts over China: 1951–2003, *Geophys. Res. Lett.*, 32, L04707, doi:10.1029/2004GL021853.